University of Nottingham
UK | CHINA | MALAYSIA

Influencing the degradation rate of recombinant spider silk in the presence of matrix metalloproteinases

by

Thomas G. J. Coekin, BSc

Thesis submitted to the University of Nottingham for the degree of Doctor of Philosophy

January 2021

Abstract

Understanding the degradation behaviour of extracellular matrix (ECM) scaffolds is essential for predicting and advancing wound healing. Spider-silk based proteins are one type of biomaterial with the potential to be used as a matrix to improve would healing. In addition to good biocompatibility and low-pyrogenicity, silk-based biomaterials have displayed the capacity for controlled degradation, a characteristic that is investigated in this study.

In silico studies took target sequences of human matrix metalloproteinase 2 and 9 (MMP2 and MMP9) and compared them to sequences of silk major ampullate spidroin 1 (MaSp1) termini of spider genera: *Araneus, Argiope, Cyrtophora, Dolomedes, Euprosthenops* and *Nephila* and the recombinant synthetic mini-spidroin 4RepCT to identify locations for potential mutations to influence the protein's degradation. Proteolytic degradation has been carried out *in vitro* with dragline silk fibres of a range of species from distantly related spider families namely *Cyrtophora citricola*, *Dolomedes fimbriatus*, *Pisaura mirabilis*, *Pholcus phalangioides* and *Nephila madagascarensis* to confirm the predicted degradation seen from *in silico* studies.

Based on the MaSp1 of *Euprosthenops australis*, 4RepCT was recombinantly expressed and degraded by human neutrophil elastase (ELNE), MMP2 and MMP9. From the MMP profiles of 4RepCT, 14 mutation sites were identified, with a final seven being carried forward to experimentation due to location within the structured spidroin. Of these seven, two mutations located near the thrombin cleavage site and within the structured C-terminus were successfully expressed in DL41 and BL21 *E. coli,* respectively.

Successfully expressed mutant spidroins were subjected to MMP2 (>1000 pmol/min/µg protein) and MMP9 (>1300 pmol/min/µg protein) concentrations that were approximately 10% of that typically seen in chronic wounds. Spidroins with a mutation in the amorphous region of the spidroin gene increased the degradation rate, degrading 1 mg/mL protein in 30 minutes with both proteases, whereas mutations within the structured C-terminus did not degrade in the same way. This suggests that while introducing target sites can influence the rate of degradation, the sites must be accessible to the protease in question.

Contents

List of Figures

Introduction

Chapter 3

Chapter 4

Chapter 5

Appendix

List of Tables

Introduction

Methods

Chapter 3

Chapter 5

List of Schematics and Schemes

Acknowledgements

This dissertation would not have been possible without the help of many people. I am greatly appreciative of my supervisors Prof. Neil R. Thomas and Prof. Sara L. Goodacre, for their patient help and invaluable guidance throughout the course of this project. I have learnt so much from their knowledge, teaching and support.

It is with thanks to the BBSRC and the University of Nottingham DTP that I have been able to carry out this important and exciting research.

This work would not have been possible without the generous help of those in the School of Life Sciences Image and Microscopy lab (SLIM) who taught and guided me, especially Dr Tim Self and Ian Ward. I would like to extend this thanks to those in 'Ye Old Arachnarium' spider lab (University of Nottingham) for their help and expertise in spider handling and advice in the natural silk sections of this thesis.

I would like to thank Dr David Harvey for his support and ideas throughout the four years, giving his valuable time and insight into this project. This thanks is extended to all those in the Thomas Lab, friends and colleagues that I have shared my office with over the last four years. It is hard to believe this is all now coming to an end, and I wish you all the best with each of your projects.

Finally, I have my greatest thanks to my amazing wife and family. To Esther, for her unwavering encouragement, love and support throughout this journey. We have achieved this as much together than as two individuals, I would never have managed this without you. To my parents, thank you for always being just a phone call away, supporting and loving, not being afraid to give the tougher advice in the latter years.

'For the Lord gives wisdom; from his mouth comes knowledge and understanding' – Proverbs 2:6

Glossary of terms and abbreviations

Aggregation – The visible clumping of insoluble protein.

Araneidae (family) – 'orb-weaving' spiders containing 25 genera and 185 species. [1,2]

Araneus (genus) – 'round-shouldered orb-weaver' spider, of the family Araneidae. [3]

Argiope (genus) – 'garden orb-weaver' spider, of the family Araneidae. [4]

Biocompatibility – the property of a (bio)material defined as fit for its intended use, not harmful or toxic to living tissue.

Biomaterial – a biological or synthetic substance that can be introduced into body tissue as part of a medical device or used to replace an organ or bodily function. [5]

Birefringence – an optical property of a material having a refractive index that depends on the polarization and direction of the light source. [6]

Bright Field – an illumination technique used for subject illumination during transmission light microscopy. [7]

Cyrtophora (genus) – 'tent-web' spiders, of the family Araneidae. [8]

Dark Field – a specialised illumination technique that uses oblique illumination to enhance contrast in specimens that are not imaged well under normal brightfield illumination conditions. [9]

Degradation – the breakdown of an object or material through physical or enzymatic means resulting in the loss of mechanical properties or material.

Degumming – the process by which the silkworm silk protein fibroin is separated from its immunologically active auxiliary protein sericin.

Dolomedes (genus) – 'fishing/raft' spider, of the family Pisauridae. [10]

Ecribellate – a prey-capture technique that utilises multiple different silks and their properties to capture prey.

Euprosthenops (genus) – 'Australian nursery-web' spider, of the family Pisauridae. [11]

Fibre – a macroscopic spidroin polymer with a significant longitudinal axis.

Flowing fibre – a term used to describe where a silk fibre crosses the microscope stage without overlapping itself.

MaSp – Major Ampullate Spidroin.

MMP – Matrix Metalloproteinase.

Nephila (genus) – 'golden silk orb-weaver' spider, of the family Araneidae. [12]

Pholcidae (family) – 'cellar' spiders. [13]

Pholcus (genus) – genus of spiders of the family Pholcidae. [14]

Pisaura (genus) – genus of spiders of the family Pisauridae. [15]

Pisauridae (family) – 'nursery-web' spiders. [16,17]

Polymer – used to describe the polymeric nature by which fibres are formed from the regular combination of monomeric units (e.g. spidroins).

Precipitation – the observable result of soluble proteins becoming insoluble, often seen as white aggregated clumps.

Pyrogenicity – the ability to induce an inflammatory response.

Recombinant – a protein expression technique that uses components from two or more different sources to express proteins. For example, a gene from a spider introduced into bacterial *E.coli* and expressed with the bacterial expression system.

RGD – arginine-glycine-aspartate peptide

SDS-PAGE – sodium dodecyl sulphate-polyacrylamide gel electrophoresis

Covid-19 impact statement

The impact of COVID-19 has been unforeseen and significant. From March 2020, I have been unable to re-enter the laboratory to collect any additional supplementary data and images. Despite this, every effort has been made to meet the amendments advised by examiners. The unprecedented situation surrounding COVID-19 prevented the collection of further data since the *viva voce* examination. This has particularly impacted the number of representative images available for the *in vitro* degradation of natural spider silks. As a result, the total number of images collected are shown in the text of the thesis and conclusions were drawn that reflected the views and experience of my examiners. Although additional images would have further supported the conclusions that were made, I believe the results that were collected before submission continue to support these claims.

1. General Introduction

1.1 An overview of silk, natural and recombinant

Silk is naturally spun fibre utilised by a large variety of arthropods including spiders, silkworms and mites. The most utilised silk is that of the *Bombyx mori* silkworm due to its ease of cultivation and use in human clothing. The traditional practise of farming, harvesting and spinning silkworm silk has been carried out in Ancient China since the Neolithic era, 4000BC [18]. The continued demand for silk as a commodity has encouraged the automation and industrialisation of silk production, contributing to predicted industry value of USD $16.94 billion in 2021 worldwide [19].

1.1.1 Natural silk, its properties and uses in nature

The silk fibre is produced using spinning apparatus to convert the stored liquid spinning dope to a linear fibre with immense tensile strength [20]. Silk-producing spiders are either cribellate or ecribellate depending on the method used to capture prey with their silk [21]. While cribellate spiders utilise a cribellum comb-like structure to produce extremely fine fibres to increase the silk's adhesion to prey, ecribellate spiders use a combination of silks with different mechanical properties to enable prey capture [21].

In addition to the major ampullate silk (dragline), ecribellate spiders also produce flagelliform, aggregate, minor ampullate, aciniform, pyriform and cylindriform silk as illustrated in **Schematic 1** [22,23]. Dragline silk is used in the frame and radial spokes of a spider's web, allowing the web to maintain its shape and strength during high impact prey collisions [24]. As its name suggests, dragline silk is also used as a safety line for the spider when descending or escaping [24]. Despite the varieties of silk in nature, most literature has focused on the more easily available and abundant dragline (major ampullate) or flagelliform silks, resulting in a lack of structural and mechanical data for the alternative silks. The development of recombinant silk has therefore predominantly focused on dragline silk for its desirable mechanical properties and available information [24,25].

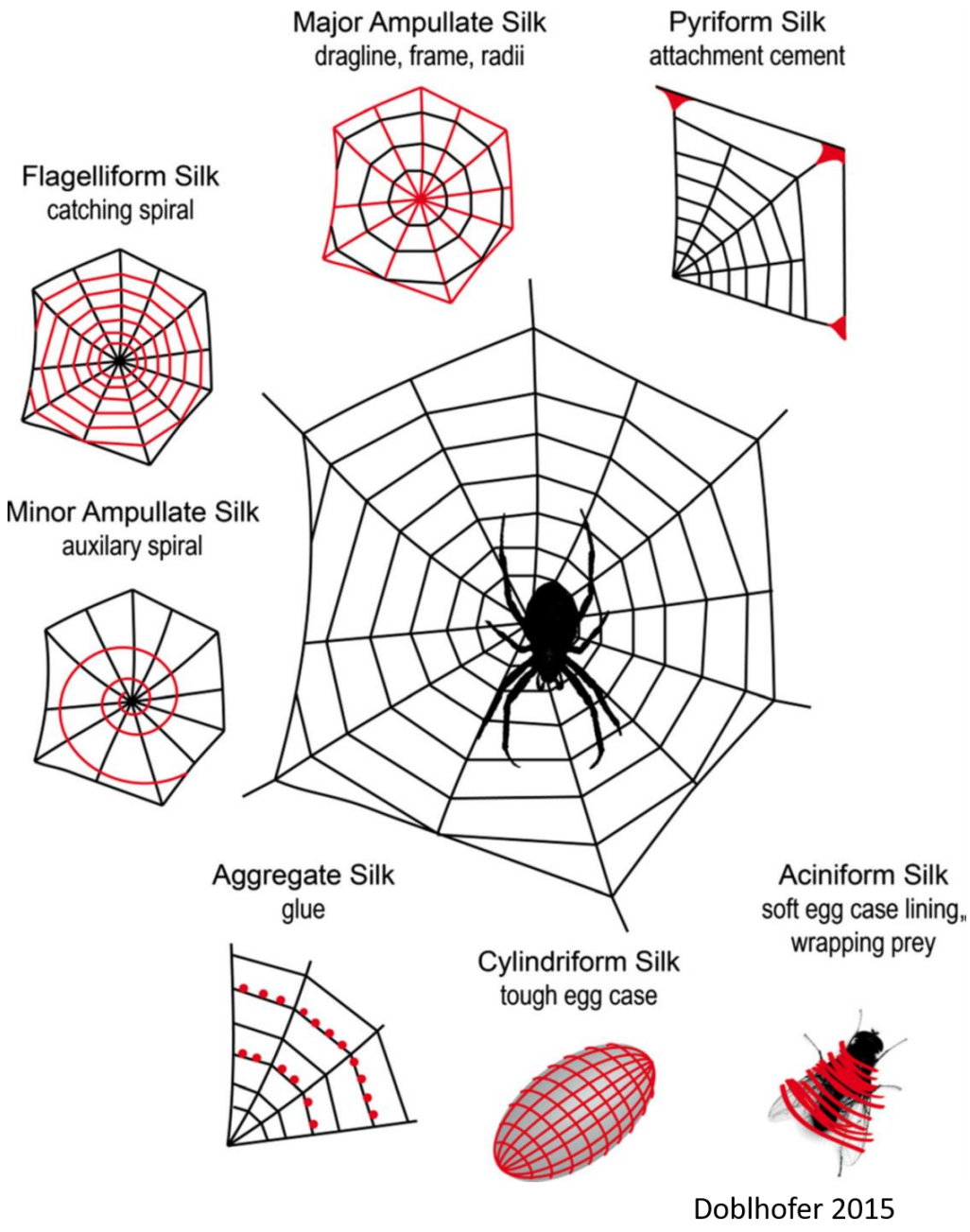

Schematic 1. An overview of the different types of silk produced by female orb weaving spiders (Araneae); each silk type (highlighted in red) is tailored for a specific purpose as depicted. Image taken from 'To spin or not to spin: spider silk fibers and more', Doblhofer 2015.

1.1.2 Organisation of silk fibres

Native dragline silk has been studied with a variety of techniques in order to determine its internal structure. Although many theories exist around the hierarchical organisation of silk fibres, the exact structure of silk fibres is still under discussion [25]. A popular theory is that silk fibres

consist of three distinct levels of molecular organisation [20]. The macroscopic structure reveals a core-shell structure encompassing the whole silk fibre bundle which protects the individual fibrils from damage, maintaining the integrity of the fibre over time as shown in **Figure 1** [20]. The shell structure is thought to attach biomolecules such as lipids and glycoproteins, although the reason for this is not yet known. On a mesoscopic scale the individual fibres appear to be aligned along the horizontal fibre axis to form a core structure, similar to individual strands of fibre in a rope. Within the individual fibres, crystals of repeated alanine residues are intermixed with larger crystalline regions that contain repeated glycine residues, although the size of these crystals is not always agreed on [20,25]. The high percentage of crystalline regions provides the silk fibril with extreme tensile strength, whilst the interlinking amorphous regions contribute to the silk's flexibility and extensibility [26].

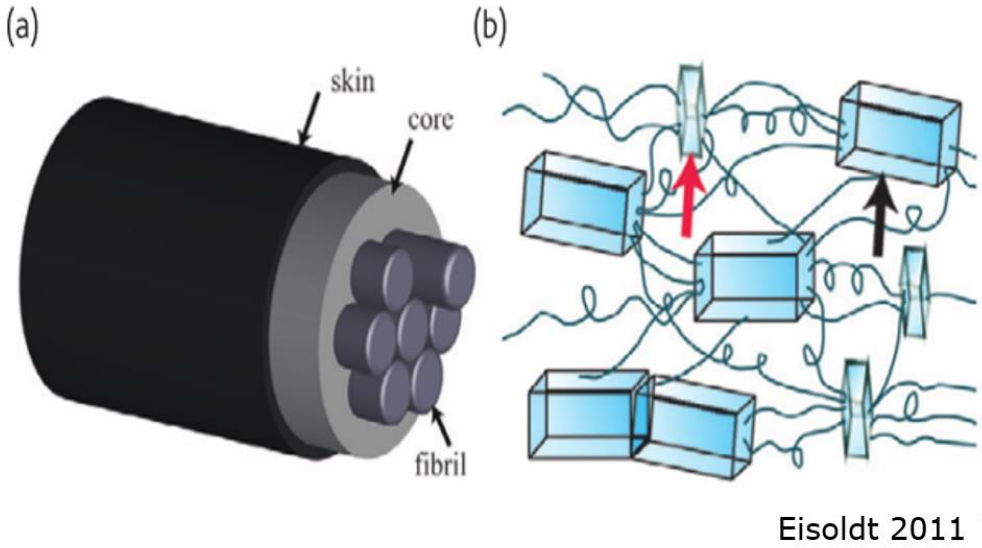

Figure 1. Illustration of the hierarchical spider silk structure demonstrating the fibre skin-core structure with fibrils forming the core (**a**). At the nano-structural level the fibrils comprise small tightly packed β-sheet crystals (red arrow) and larger crystalline regions (black arrow) interconnected by an amorphous matrix (**b**). Image taken from 'Decoding the secrets of spider silk', Eisoldt 2011.

Dragline silk is comprised of two major classes of proteins from which they receive their names: Major Ampullate Spidroin 1 and 2 (MaSp1/2). Each MaSp is comprised of a repetitive core with each repeat

containing 40 – 100 amino acids, flanked by highly conserved non-repetitive domains (NRDs) [20,27–31]. The core can be repeated over 100 times within a single spidroin and varies depending on spidroin and species, with some residues conserved throughout. MaSp1 contains the highly conserved sequences – $(Ala)_{4-14}$, $(GlyAla)_n$, GGX –, whilst MaSp2 contains the residue sequence GPGXX (where X can be Q, G or Y), greatly increasing the proline content of MASP2. The ratio of MaSp1 and the more hydrophobic MaSp2 within a fibre enables the silk to undergo supercontraction, maintaining the strength and structure of the web when loaded with rain or dew [30,32–34]. During supercontraction, the secondary structure of the silk is proposed to re-arrange, causing a rotation of the β-sheet crystals. This movement contracts the poly(glycine) regions and the whole fibre is shortened dramatically in length [35].

While the repetitive core provides strength, toughness and elasticity to the silk fibre, the non-repetitive domains are involved in spidroin storage and polymerisation [25,36]. Although both termini are highly conserved, the N-termini is conserved across different silk types and spider species [37]. Both termini are made up of five α-helices but differences in charged and exposed residues within each domain enables termini-specific roles [38–41].

The N-termini acts as a pH-sensitive switch during storage to enable the transition to polymeric spidroin in increasing acidic conditions [38,42]. Under these conditions, the termini exist as an antiparallel dimer which, through the exposure of a single tryptophan, enables dimerisation [39,43]. As the pH continues to decrease in the silk gland the spidroin dimerisation is further lineated by the gland tapering and shear forces [20]. The N-termini also serve to solubilise the monomeric spidroin which, when lost, quickly becomes insoluble.

The C-terminus exists as a parallel dimer and contains a single disulphide bond [31]. Seen in **Figure 2**, the C-termini of *A. diadematus, N. madagascarensis* and *A. aurantia* were modelled by Ittah *et al.*, comparing the homology of the conserved domain [44]. Ittah identified a

single cysteine residue within the four α-helices through which the homodimer is thought to form [44]. The C-terminus is less pH-sensitive than its amino counterpart, providing a stable dimer interface through which subsequent fibre formation is possible [45]. The C-terminus is also highly conserved across spidroin termini, but to a lesser extent than N-termini [46].

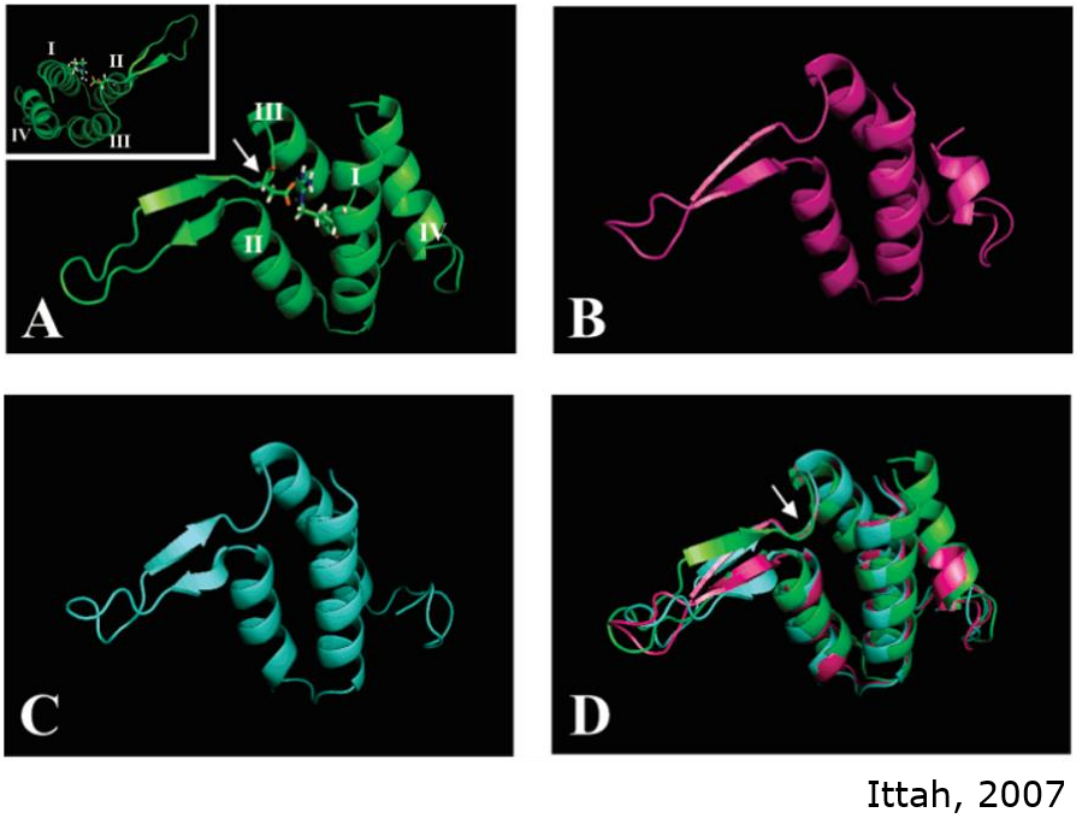

Figure 2. A proposed structure for the C-terminal domain of MaSp silk proteins. (**a**) Predicted tertiary structure for C-terminal domain of *A. diadematus* ADF-4. Inset: A different angle of the structure showing the circular arrangement of the helices in the imaginary barrel structure. The cysteine-containing loop that is N-terminal to helix III is marked by an arrow, and the D and R residues that are involved in a salt bridge between this loop and helix I are shown in a ball and stick format. (**b**) Model of *N. madagascarensis* MaSp1. (**c**) Model of *A. aurantia* MaSp2. Notice that this protein has no helix IV. (**d**) Superimposition of all three predicted structures. The conserved loop mentioned in panel A is marked by an arrow. All tertiary structures were generated using the ORCHESTRAR homology modelling program. Image taken from 'A Model for the Structure of the C-Terminal Domain of Dragline Spider Silk and the Role of Its Conserved Cysteine', Ittah *et al.* 2007.

1.1.3 Diversity and breakdown of natural silk

Inhabiting every continent except Antarctica, spiders use their silks to adapt to their different habitats. Under laboratory conditions spider silk is considered non-degradable by US Pharmacopeia owing to its conservation of mechanical properties *in vivo* [47,48]. However, in the field, webs must survive an onslaught of wind, debris, dust and wetting. A number of these impacts result in physical damage, which the spider must choose to repair or replace the web, both options resulting in a high energy cost for the spider [49,50].

The degradation of native spider silk has been studied by Agnarsson *et al.* over 4 years. Agnarsson reported that whilst the ultimate tensile strength of the aged silk fibres did not improve, the yield strength increased by 217% as the silk fibres reduced in diameter. It was therefore suggested that a rearrangement within the β-sheet crystals had resulting in an increase of yield strength [51].

However, the ability to withstand physical deterioration over time does not determine a web's degradation properties when exposed to enzymatic proteolysis. As many spiders consume their own silk, it is possible that those spidroins could be susceptible to proteolytic degradation [52,53]. By comparing the protein sequence of silks from different species it may enable us to consider them 'naturally occurring mutants', selected to work by evolution over millions of years. Therefore, variation between typical silk sequences will allow researchers to identify adaptations between species, especially those that may originate from differing ecosystems or habitats [53,54].

Unlike silkworms, spiders cannot be farmed because their cannibalistic behaviour prevents the storage of numerous individuals in one place [55]. In addition, the process of obtaining silk from spiders, force-reeling, is not able to be scaled, making it inappropriate for industrial production. Therefore, recombinant silk production is required to provide a cheap and readily available biomaterial. Recombinant silks also allow for genetic manipulation, editing the spidroin gene sequence to produce variations within the silk fibre, enhancing the silk's mechanical

and biocompatibility properties [56]. Although native-sized spidroins have been expressed recombinantly by supplementing the bacterial tRNA pool during expression, the majority of recombinant spidroin expression is carried out with proteins between 30 – 90 kDa [57–59].

A recombinant protein, 4RepCT, was proposed by Stark *et al.* based on the MASP1 of *Euprosthenops australis*, the African nursery web spider [28,60]. Stark discovered that a minimum of four poly(alanine) tracts flanked by poly(glycine) tracts were required for successful polymerisation and fibre formation as well as a conserved Asn-Arg-Asp amino acid motif at its C-terminus required for dimerisation. However, a recent study by Andersson *et al.* discovered that recombinant silk fibres could be developed that contained only two repetitive tracts, suggesting that the N- and C-termini were the most important domains required for fibre formation [58]. Stark showed that BL21 *E. coli* could overexpress the 4RepCT protein as a soluble protein [28]. To aid purification and solubility, hexa-histidine and thioredoxin tags were added respectively to form a 39 kDa fusion protein. 4RepCT was purified by Ni^{2+} immobilised metal affinity chromatography (IMAC) before the solubilisation tag was removed by a thrombin protease that cleaves at the specific target peptide sequence '-Lys-Val-Pro-Arg-Gly-Ser-' [61–64]. A report by Jastrzebska *et al.* found that introduction of purification tags resulted in brittle fibres after polymerisation and suggested a new method of purification was required [65]. They proposed the use of thermal or acidic extraction as a means of purification, relying on the natural stability of spider silk to ensure sufficient purification. However, because the tags of 4RepCT were removed during fibre formation, an additional purification step was not required.

eADF4(C16) is another synthetic miniaturised spidroin based on the dragline fibroin of *Araneus diadematus* [66]. eADF4(C16) contains 16 repeated poly(alanine/glycine) tracts compared to 4RepCT's four as seen in **Figure 3**, and has demonstrated toughness, a combination of tensile strength and elasticity, higher than that of most native spider silks [67]. eADF4(C16) was also recombinantly expressed in *E. coli* before purification by thermal extraction. Heated to 80 °C, the recombinant silk

proteins were not denatured, and subsequently extracted by 20% (w/v) ammonium sulphate precipitation. [68]. Unlike 4RepCT however, eADF4(C16) does not form silk fibres spontaneously owing to its insolubility, requiring its use in high concentrations of guanidinium thiocyanate after expression. It must therefore be mechanically electrospun [69,70].

Figure 3. Structural diagram of eADF4(C16) (left) and 4RepCT (right) demonstrating the repeated poly(alanine/glycine) tracts and non-repetitive C terminus of 4RepCT. Images adapted from 'Cell adhesion and proliferation on RGD-modified recombinant spider silk proteins', Wohlrab 2012 and 'Macroscopic fibres self-assembled from recombinant miniature spider silk proteins', Stark 2007.

Although the primary amino acid sequence of spider silk can be replicated *in vitro*, synthetic silk fails to compare in tensile strength to natural silk [28]. The difference in strength between native and synthetic spidroins results from the vast difference in size leading to a reduction in van der Waals interactions and possible intramolecular salt bridges that occur within smaller synthetic silks. The ultimate tensile strength of 4RepCT fibres was recorded with an average yielding tensile stress of 150 MPa compared to 1.5 GPa of the native dragline silk of *Euprosthenops* [28]. Despite the reduction in ultimate tensile strengths however, 4RepCT and eADF4(C16) are still extraordinarily strong for their size and maintain incredible toughness, advertising their use in biomaterial applications [28,29,71,72]. Most importantly, recombinant production of both 4RepCT and eADF4(C16) is scalable, providing enough material for future industrial uses and manufacture. Companies such as SPIBER INC™ (www.spiber.jp/en) and AMSILK™ (www.amsilk.com/home) both produce recombinant silk on an industrial scale while Bolt Threads™ (https://boltthreads.com/) uses recombinant silk to produce fabrics that exhibit excellent mechanical performance but are also biodegradable after use. To decrease the price of production further, Kraig Labs (https://kraiglabs.com/) have combined with the more prolific silkworm production technique, extracting the natural spider

silk from silk cocoons in vast quantities, enabling production costs as low as $300 / kg [73].

In addition to differences in size, spinning is crucial for the strength and performance of natural silks [74]. Unlike 4RepCT, which forms fibres spontaneously after purification, eADF4(C16) requires electrospinning for fibre formation. In an attempt to replicate the silk gland, a series of ionic gradients were used with increased tapering shear forces to encourage fibre formation. Passed through an electrically charged needle-tip, the silk is attracted to an electrode placed a determined distance away, polymerising as it does so [75–78]. Despite attempts to replicate natural spinning apparatus, eADF4(C16) fibres fail to display the same tensile capabilities as natural silks [72,74,79].

1.2 Silk in therapeutic use

1.2.1 Why spider silk?

A biomaterial is a biological or synthetic substance that can be introduced into body tissue as part of a medical device or used to replace an organ or bodily function [5]. The term biocompatibility includes several different properties including host response upon implantation, host and biomaterial response during the time the biomaterial is present, and the mechanism of degradation or deterioration at the end of a biomaterial's use. In addition to high tensile strength and toughness, recombinant spider silk has excellent biocompatibility properties, including low immunogenicity and pyrogenicity while displaying biodegradability, making it an attractive candidate for use in biomaterials [25,80].

Silk from the commercial silkworm *Bombyx mori* has also been utilised as a biomaterial, resulting in the silk-based material Mersilk™ produced by Ethicon™ (Johnson & Johnson) [81]. However, the presence of the auxiliary protein sericin in silkworm silk caused an immune response forcing companies to remove it before the silk could be utilised medically, greatly increasing the cost of production [82]. Like eADF, Mersilk™ could not be functionalised after production, further identifying 4RepCT as an attractive alternative for silk-based biomaterials [83].

Silkworm film degradation has been investigated *in vitro* by Brown *et al.*, subjecting 3% (w/v) films to several digestive serine proteases such as α-chymotrypsin and proteinase K, as well as MMP1 and MMP2 [84]. By standardising the observed rate of degradation, it may be possible to make a direct comparison between both kinds of silk.

Silkworm silk also possesses the ability to be processed into a wide range of morphologies. Reviewed in a paper by Jao *et al*., silkworm silk is an attractive option for drug delivery, utilising two methods of drug delivery: diffusion of payload and degradation of the delivery vesicle [85–87]. Unlike silkworm silk, which generates an immune response upon implantation due to the presence of the auxiliary protein sericin, spider silk is non-pyrogenic eliciting no increased host immune inflammation upon implantation [48,88–90]. Before silkworm silk can be incorporated into *in vivo* studies, the silk must first be subjected to severe 'degumming' process to remove the aggravating sericin protein [82,89,91]. This additional step consequently favours the use of spider silk over silkworm silk for the development of biomedical applications. While the development of enzymatic degumming techniques have reduced the price of this necessary procedure, the absence of this step during spider silk production highlights the latter for biomaterial use [92].

1.2.2 Drug delivery

In the development of improved drug delivery routes, silk of both silkworm and spider has been investigated by many groups [87]. eADF4(C16) particles and microspheres less than 10 μm have also been used to transport drug molecules to target sites [71,93,94]. The lipophilicity of the silk particle allows it to be loaded with the drug molecule before RGD (arginine-glycine-aspartate) peptides fused to the silk particle interact with the cell surface to allow drug release. However, due to limiting charge or lipophilicity, only small drug molecules are capable of being loaded onto the silk particles, preventing wide-spread application [66].

One solution to this is to ensure that drug release occurs as close to its target as possible. The expression of recombinant fusion proteins containing site-specific substrate tags at one terminus could allow for

selective drug delivery systems. This hypothesis was investigated by Florczak *et al*. using recombinant Her2 recognising peptide–fused MaSp1 and MaSp2 proteins from *N. clavipes* [95]*.* Florczak demonstrated that hybrid silk spheres could be produced that increased uptake of charged drug molecules and released them at specific target locations.

Drug uptake and release can also be influenced during the formation of the microspheres, shown by a study by Brüm *et al*. Produced with eADF4, Blüm identified a link between cross-linking in sphere production with resulting drug uptake and release [96]. This was developed further by Kucharczyk *et al*. who developed microspheres from recombinant modified MaSp2 protein from *N. clavipes*. Glutamic acid residues were introduced in to the recombinant protein to introduce an overall negative charge, ultimately increasing drug uptake in the presence of the positively charge mitoxantrone. However, although the drug uptake was improved, the release of the charged drug was too rapid for therapeutic use [97].

Recombinant silk particles have also been proposed for gene therapy and delivery by Numata *et al* [98]. Acting as a transfection vector silk particles containing multiple RGD peptides and cationic poly(L-lysine) residues on its opposite face were shown to complex both luciferase-containing plasmid DNA (pDNA) and integrin receptors simultaneously. RGD-integrin binding enabled the cellular uptake of silk particle-pDNA complexes by endocytosis. Upon reaching the interior of the cell, the pDNA was released allowing transfection to occur, assessed by the presence of the luciferase reporter gene [99].

Anti-microbial peptides have also been successfully fused to spider silk proteins, suggesting an application in drug delivery or wound healing. In 2011, Gomes successfully expressed three recombinant silk fusion proteins containing different antimicrobial peptides in *E. coli*: human neutrophil defensin 2 (HNP-2), human neutrophil defensin 4 (HNP-4) and hepcidin. Antimicrobial activity was assessed visually by zone of inhibition assays before dynamic light scattering was used to analyse protein aggregation. Gomes confirmed that the fusion of these peptides to the

silk fibres had no effect on the secondary structure, whilst the β-sheet conformations interacted with the antimicrobial peptides, enabling activity without the introduction of chemical cross-linking [100]. The area of inhibition was also relatively small as the active molecules are fused directly to the silk protein, a significant downside to genetic functionalisation. The ability to release drug moieties upon arrival at target sites would greatly increase the effectiveness of drug delivery applications.

1.2.3 Spider silk in wound healing

Native silk fibres have been used to guide nerve regeneration *in vivo.* Implanted into rats containing sciatic nerve defects, spider silk vein grafts were compared to isogenic grafts and left to regenerate over 6 months [101]. A similar study by Radtke *et al.* was conducted using decellularised vein grafts of adult sheep, evaluated after 6 - 10 months implantation, Radtke concluded that spider silk enhanced Schwann cell migration, axonal regrowth and remyelination over a 6 cm tibial nerve defect [102]. As neuronal cell growth was similar across all grafts and axons were aligned regularly with a healthy appearance, the studies concluded that spider silk was a suitable biomaterial for tissue engineering and guidance, supporting cell proliferation and migration during neuronal regeneration.

In addition to fibres and particles, recombinant silks can also be processed into films, hydrogels and non-woven meshes, each with distinct biomedical applications [25,103,104]. Films can be obtained by gradual evaporation of solvent, whilst spheres and particles can be formed from nucleation at low silk concentrations in the presence of kosmotrophic ions [65,71]. A recent review by Schacht and Scheibel presented several possible applications for the recombinant spidroin eADF4(C16), proposing that hydrogels and non-woven meshes could be self-assembled before being incorporated into an *in vivo* tissue scaffold to enable invasive fibroblast cell growth [30]. Non-differentiated neuronal embryonic stem cells have also been grown on recombinant 4RepCT films *in vitro* by Lewicka *et al.* When compared to positive controls of fibronectin and poly-L-ornithine,

4RepCT films facilitated similar levels of cell growth and supported stem cell differentiation when induced [105].

To promote cell migration and adhesion, arginine-glycine-aspartic acid (RGD) amino acid peptides have been attached to eADF4(C16) by genetic modification or by post-translational chemical conjugation of cysteine side chains as shown in **Schematic 2**. Interacting with the naturally present integrin receptors on cell surfaces, migrating cells used spider silk as guidance scaffolds, providing positive contact signals required for sustained cell growth [66,71,72,76]. However, genetically functionalising the protein primary sequence of silk proteins prevented further adaptation, suggesting a limit to their overall use.

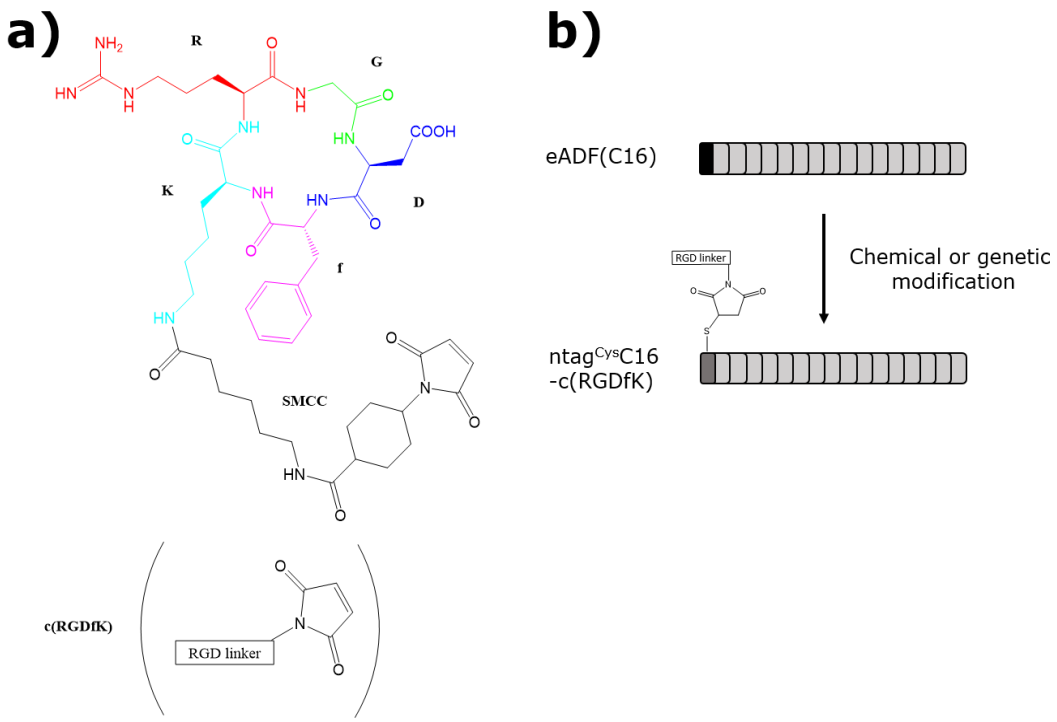

Schematic 2. Chemical structure of the synthetic cyclic RGD peptide c(RGDfK) employed for chemical modification of ntagCysC16 **a)**. eADF4(C16) and the RGD-containing variant ntagCysC16-c(RGDfK) (chemically modified) **b)**. For ntagCysC16-c(RGDfK), c(RGDfK) was covalently coupled to the thiol group of a cysteine residue of ntagCysC16. Image adapted from 'Cell adhesion and proliferation on RGD-modified recombinant spider silk proteins' Wohlrab 2012.

Antibiotic functionalisation has also been developed by Harvey *et al.* by conjugating levofloxacin via copper catalysed azide-alkyne cycloaddition (CuAAC) or 'click chemistry'. Expressing 4RepCT in the methionine auxotrophic *E. coli* (DL41) to enable uptake of unnatural amino acids, Harvey proceeded to conjugate the broad-spectrum antibiotic to methionine analogue L-azidohomoalanine (L-Aha). To demonstrate that the antibiotic had not just been absorbed by the fibres, each fibre was washed intensely to ensure only covalently conjugated antibiotic remained. Once washed, 4RepCT fibres were transferred to zone-inhibition agar plates before exhibiting antimicrobial activity for up to 5 days. The labile ester linker allowed the antibiotic to be released to the surrounding environment over the course of the experiment, demonstrating the potential for wound dressing applications and as tissue regeneration scaffolds [83]. As the name suggests, 'click' chemistry conjugation is an efficient, high yielding process, enabling the conjugation of numerous antibiotic compounds with relative ease. The flexibility of this conjugation method provides further applications if incorporated into biomaterials. Unlike chemically synthesised materials such as nylon, 4RepCT fibres can be functionalised with the conjugation of medically relevant antibiotics whilst remaining non-toxic to eukaryotes [83]. The chemical modification approach investigated with 4RepCT ensured that repeated functionalisation could be possible even after protein expression [106].

The role of silk in the application of wound healing has been identified by many researchers. Both silkworm fibroin and native spider silk have been investigated as a result of attractive biocompatibility in the form of macrophagic cytokine release and recruitment of migrating fibroblasts [107,108]. Artificial skin alternatives for burn wound healing were attempted with silkworm fibroin and native spider silk by Gholipourmalekabadi and Liebsch, respectively. Gholipourmalekabadi produced 3 dimensional bilayer of decellularised human amniotic membrane and electrospun nanofibers from silk fibroin [107]. Seeded with adipose-tissue derived mesenchymal stem cells (MSCs), Gholipourmalekabadi reported recruitment of inflammatory cells and

upregulation of angiogenic factors such as vascular endothelial growth factor and basic fibroblast growth factor as the wound returned to the remodelling phase of repair [109]. Unlike silkworm fibroin, native spider silk induced minimal release of inflammatory cytokine release from macrophages and neutrophil granulocytes. Critically for wound healing the presence of spider silk encouraged the ingrowth of single capillaries and migration of keratinocytes and fibroblasts, presenting itself as highly biocompatible [108].

Use in wound healing has also been investigated with recombinant silk or both silkworm and spider silk (4RepCT) [110–113]. By incorporating cell binding motifs as fusion proteins or additional functionalised attachments, recombinant silk structures can be used to develop biocompatible skin substitutes, reproducing the basil membrane for cell migration. This was investigated by Chouham *et al.* with silk scaffold bilayers consisting of a keratinised epidermal layer fixed with bulk silkworm scaffold material [110]. While the functionalised 4RepCT layer enabled cellular interaction, binding and proliferation, the inactive silkworm base provided a strong and malleable base to be introduced into the wound site [110]. Crucially, it is the ability to choose the function of recombinant silk that highlights its flexibility of use as a biomaterial [111–113]. The breadth of this research mentioned in this summary is summarised in **Table 1**. The potential of recombinant spider silk in therapeutic use has been highlighted and the research into its medical role will continue to develop.

Title	Silk origin	Area of research	Summary of findings	Year	Ref
Protein-based drug-delivery materials	Silkworm (native)	Drug delivery	Review	2017	54
Silk for Drug delivery applications: Opportunities and Challenges	Silkworm (native)	Drug Delivery	Review	2013	55
Recombinant spider silk particles as drug delivery vehicles	Spider silk (recombinant)	Drug Delivery	Charged recombinant spider silk particles can be produced that enable drug delivery with biodegradable properties	2010	57
Cell adhesion and proliferation on RGD-modified recombinant spider silk proteins	Spider silk (recombinant)	Drug delivery	The drug delivered is limited in choice by size and lipophilicity of silk particle	2012	31
Functionalised spider silk spheres as drug carriers for targeted cancer therapy	Spider silk (recombinant)	Drug delivery	Her-2 receptor fused spidroins enabled targeted delivery of delivery of doxorubicin to cancer cells overexpressing Her-2	2014	58
Control of drug loading and release properties of spider silk sub-microparticles	Spider silk (recombinant)	Drug delivery	Crosslinking within microspheres reduces drug loading but increases drug release.	2012	59
Bioengineering the spider silk sequence to modify its affinity for drugs	Spider silk (recombinant)	Drug delivery	Modifying the sequence of MaSp2 spidroin greatly increased its drug loading capabilities while retaining its self-assembling capabilities.	2018	60
Bioengineered silk protein-based gene delivery systems	Spider silk (recombinant)	Drug delivery	Silk particles containing RGD peptides and poly(L-lysine) residues enabled binding to integrin receptors for cellular up-take and the effective delivery of pDNA within	2009, 2010	61,62
Antimicrobial functionalised genetically engineered spider silk	Spider silk (recombinant)	Anti-microbial	Recombinantly fused human neutrophil defensin (HNP-2) and human neutrophil defensin 4 (HNP-4) spidroins enabled localised anti-microbial properties	2011	63
Spider silk fibres in artificial nerve constructs promote peripheral Nerve regeneration in long nerve defects in sheep	Spider silk (native)	Wound regeneration	Nerve cell regeneration was observed with spider silk constructs and grafts with integrated Schwann cell migration and proliferation	2007, 2011	64,65
Processing of recombinant spider silk proteins into tailor-made materials for biomaterials applications	Spider silk (recombinant)	Wound scaffold	Recombinant eADF4 can be processed into hydrogels and non-woven meshes for incorporation as in vivo tissue scaffolds that encourage fibroblast proliferation	2014	12
Recombinant spider silk matrices for neural stem cell cultures	Spider silk (recombinant)	Wound regeneration	4RepCT matrices enabled non-differentiated neuronal stem cells to proliferate, remaining undifferentiated throughout	2012	66
Antibiotic spider silk: site-specific functionalisation of recombinant spider silk using 'Click' chemistry	Spider silk (recombinant)	Anti-microbial	Functionalisation of 4RepCT can be targeted through use of selective mutation to enable controlled release of anti-microbial peptides	2017	47
Silk fibroin/amniotic membrane 3D bi-layered artificial skin	Silkworm (native)	Wound scaffold	Use of silk fibroin/amniotic membrane scaffold encourages wound healing with upregulation of angiogenic factors and the facilitation of remodelling phase	2018	67,69
Preliminary investigations of spider silk wounds in vivo – implications for an innovative wound dressing	Spider silk (native)	Wound scaffold	Spider silk scaffolds encouraged capillary growth and migration of keratinocytes and fibroblasts with minimal cytokine release	2018	68
Recombinant spider silk functionalised silkworm silk matrices as potential bioactive wound dressings and skin grafts	Spider silk (recombinant)	Wound scaffold	Dual silk approach combined selective functionalisation (keratinised spider silk) with readily available bulk material (silkworm silk) for the scaffold	2018	70
Osteoinductive recombinant silk fusion proteins for bone regeneration	Spider silk (recombinant)	Wound scaffold	Recombinantly fused hydroxyapatite binding domain spidroins induced osteogenesis while providing material stability and selective functionalisation.	2016	71
Studies on the use of recombinant spider silk protein/polyvinyl alcohol electrospinning membrane as wound dressing	Spider silk (recombinant)	Wound scaffold	Unique recombinant spidroin fibres (pNSR16) were constructed that encouraged fibroblast migration and basic fibroblast factor expression	2017	73
Tissue response to subcutaneously implanted recombinant spider silk: An in vivo study	Spider silk (recombinant)	Wound scaffold	When introduced subcutaneously, 4RepCT and Mersilk™ implants degraded over a similar time while only 4RepCT supported ingrowth of fibroblasts and new capillaries	2009	51

Table 1. Both silkworm and spider silk has been investigated for its biomedical and biocompatible properties.

1.3 How polymers break down

1.3.1 Polymer degradation

Put simply, polymers are molecules of repeating units and are often classified by their original material [114,115]. Understanding the internal structure and properties of various polymers allows us to better predict the properties of future polymeric materials. Whilst many naturally occurring polymers can now be synthetically crafted, synthetic polymers typically refers to materials from which their respective monomers were produced through the petrochemical industry. Polymers in this family include polypropylene (PP), polyvinylchloride (PVC), polybutadiene (PBD), polysulfone (PES, PSU), polyetherketones (PEEK) and polysiloxanes (silicones). Naturally occurring polymers include deoxyribonucleic acid (DNA) and proteins as silk and hair that exhibit an overall increase in mechanical performance compared to their monomeric units [116]. Naturally, the internal structure of these polymers influences their subsequent breakdown and deterioration.

The process of natural fibre and polymer breakdown is often regarded in three stages: biodeterioration, biofragmentation and assimilation, illustrated in **Figure 4** [117]. Although these stages do not have to follow in order, all three are observed as a fibre degrades. Biodeterioration refers to the change in mechanical, physical and chemical properties that materials may undergo as a result of exposure to abiotic factors such as compression, light, temperature and chemicals [117,118]. Depending on the conditions and rate of deterioration, this is sometimes paralleled with biofragmentation [119].

Biofragmentation sees the beginning of the lytic process within the polymer chains. Cleaving of the polymer bonds to generate oligomers and monomers may be achieved by either abiotic factors or enzymatic processing. Fragmentation is usually influenced by the presence or absence of oxygen as microorganisms allow further enzymatic degradation to take place [119]. A lack of oxygen forces anaerobic degradation, releasing methane as a by-product in addition to carbon dioxide, water and new biomass. As a result, anaerobic biofragmentation

is often slower but more thorough than aerobic degradation where no methane is produced [120].

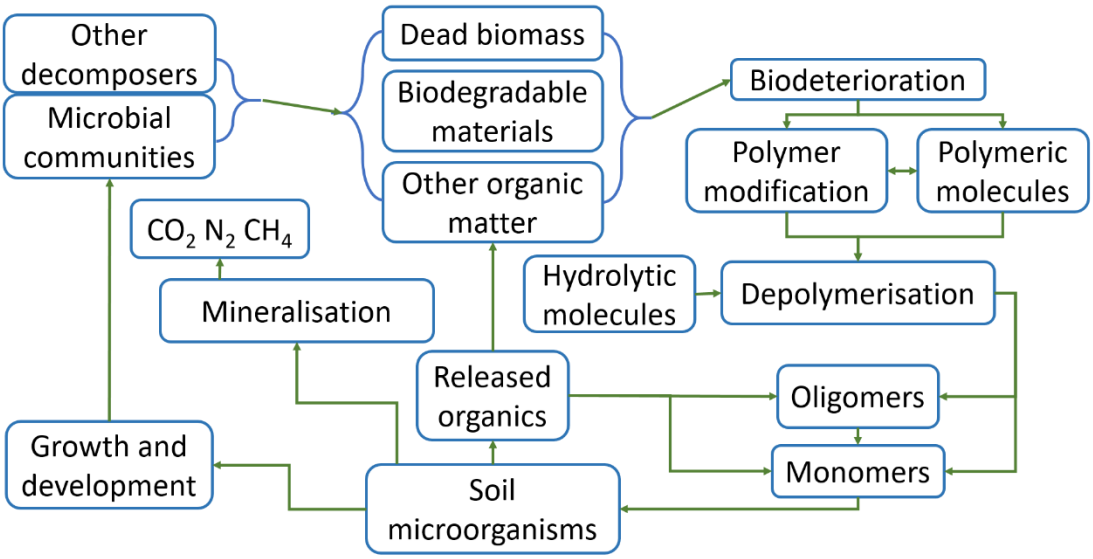

Figure 4. Polymer biodegradation diagram illustrating the complex pathways that polymers undertake in the process of biodegradation. Image recreated from 'Polymer degradation: Mechanisms and estimation techniques', Lucas 2008.

Assimilation describes the process of by-products of the original polymer being taken up into surrounding cells. For smaller chemical products this process can be achieved using membrane carriers while larger material undergoes further biotransformation reactions to reduce the size of waste products to allow cellular assimilation [117]. Once inside, many chemicals enter catabolic pathways to be used in the production of adenosine triphosphate (ATP) or become integral to cell structure. The rate of biodegradation varies greatly between materials, although nearly all chemical compounds will biodegrade with enough time, often relying on the accumulation of bioavailability to allow significant degradation to take place [118].

Natural molecules such as protein and hydrolysable starch can also be included to increase the rate of synthetic polymers breakdown [121]. The presence of enzymes within the cell and organism, causes the natural material to degrade first, increasing the available surface area for further biofragmentation. Utilising the cell's need to repair and grow, materials can be designed to integrate protein fibres within their structures. Using the high processivity of bacterial proteases, the materials are degraded

faster than the synthetic material would be alone. Cellulose is often combined with synthetic compounds like acetate or nitrate to give highly biodegradable materials.

However, the presence of proteolytic enzymes within the body can cause issues for the medical profession [122]. A break in the protective barrier of skin, whether by the surgeon's knife or by trauma, causes an immediate immunological response by the host organism [123]. During this time, the expressed levels of proteases increased rapidly to remove broken and damaged tissue and to allow repair of the new ECM. Materials introduced into the wound site are immediately surrounded by highly processive proteases. These proteases often have a broader range of substrates than typical cellular proteases as they are required to degrade multiple different objects. As a result, proteinaceous materials introduced by surgeons often undergo severe degradation, reducing their medical effectiveness and increasing their cost.

For this reason, it is important to first attempt to understand the wound environment and allow it to influence the way we design our materials [122]. Similar to biodegradation of synthetic materials, medical textiles undergo the same three stages of breakdown namely: biodeterioration, biofragmentation and assimilation or waste product release.

1.3.2 Natural polymer degradation

Collagen

The most prominent protein component of animal connective tissues is that of collagen [124]. Composed of approximately 33% glycine, 25% proline and 25% hydroxyproline, collagen polypeptides form triple helices as large as 300 kDa and 300 nm in length [125]. In addition to connective tissues, collagen is also present in the ECM, alongside other fibrous proteins such as fibrinogen, to produce the basal membrane, facilitating cell migration and remodelling [124].

The ability to be enzymatically degraded has given rise to interest in using collagen as a biodegradable biomaterial. A number of studies have identified the degradation behaviour of the protein in the presence

of specific collagenases and metalloproteinases [125–128]. The degradation rate of collagen can also be prolonged by chemical or enzymatic crosslinking, shown by Rothamel *et al*. when five different collagens with different crosslinking were degraded *in vivo* over a course of 24 week healing period [127]. Rothamel reported a decrease in biodegradation and vascularisation in the presence of glutaraldehyde cross-linked collagen compared to non-cross-linked porcine collagen type I and type III [127].

The tuneable degradation exhibited by collagen coupled with its ability to be functionalised and cross-linked makes it an attractive tool in sustained drug delivery and tissue engineering. Many biomaterials have been developed that utilise the protein's excellent biocompatibility and are currently in or have recently passed FDA clinical trials [125]. These uses include skin substitutes such as Integra® Dermal Regeneration Template, Biobrane® and Alloderm® [129,130], ECM replacements such as TransCyte® [125] and wound dressings for use in chronic wounds such as Orcel® and Apligraf® [131].

Unfortunately collagen-based materials are limited by mild immunogenicity that is produced from the release of its terminal regions and antigenic regions within its triple helix as a result of being animal-derived [125]. Therefore much investigation is currently ongoing to develop recombinant human collagen to overcome this limitation [132].

Cellulose

The plant-derived cellulose protein may provide a solution to the immunogenicity caused by animal-derived proteins. Cellulose is a polysaccharide made up of repeating units of cellobiose, illustrated in **Schematic 3.**

Insoluble and crystalline in all organic solvents, cellulose must be first transformed before it is processable [133]. Once processed however, cellulose-associated products are biodegradable through enzymatic oxidation by fungal oxidases and bacteria [134,135]. By increasing the number of hydroxyl groups within each repeating unit ethers, ester and acetal derivatives are possible. From these, many cellulose-based polymers have been produced, Tenite® (Eastman, USA), Bioceta®

(Mazzuchelli, Italy), Fasal® (IFA, Austria) and Natureflx® (UCB, Germany) to name a few [124].

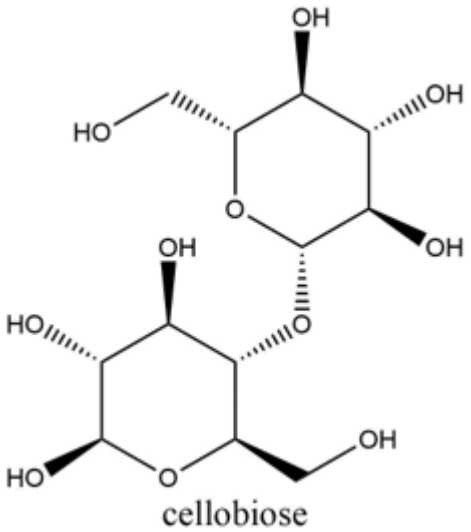

Schematic 3. Cellobiose, the monomeric unit of cellulose can be hydrolysed enzymatically or in the presence of acid to form two glucose molecules.

Cellulose acetate (CA) is amongst the most common cellulose-derivative, with strength similar to that of polystyrene. CA is used in a variety of consumer products such as textiles, cigarette filters and plastic films. Its biodegradability was assessed by Puls *et al.*, investigating its biological, chemical and photochemical degradation mechanisms [136]. Puls reports that CA must undergo deacetylation before the polymer backbone undergoes rapid and significant breakdown in the presence of enzymes or chemical hydrolysis [136]. However, it is still unclear how cellulose-derived biomaterials would function in complex wound environments.

Fibrin and fibrinogen

Other natural polymers include fibrinogen and its derived protein fibrin as well as keratin and β-amyloid fibrils. Similar to collagen, fibrin is involved in natural blood clotting after cleavage by the protease thrombin [124]. Composed of three pairs of polypeptide chains, the 360 kDa protein forms fibrin clots that are subsequently degraded by additional thrombin proteolysis [137].

Due to its excellent biocompatibility, biodegradability and ability to be injected, fibrin was one of the earliest biopolymers used in biomaterials [124,138]. Developed as a sealant, fibrin was used as a haemostasis and tissue sealant for surgery. Growth factors have also been incorporated into fibrin matrices, enabling prolonged release over time [139]. Products have also been developed to aid the recovery of chronic wounds. Bioseeds® is a fibrin-based treatment that utilises a combination of keratinocytes and fibrin to allow remodelling of the lost ECM [140]. Fibrin has also been shown to undergo degradation in the presence of some bacterial proteases, namely two cysteine proteases from *Staphylococcus aureus* which cleaved the C-terminus of fibrin while also displaying collagenase activity [141].

Not all biopolymers readily undergo enzymatic proteolysis, however. The predominant structural protein in hair, horns, nails and feathers, keratin is resistant to most proteases. However, in the presence of specific keratinases, keratin does undergo enzymatic proteolysis. The strength of keratin resides in the repetitive α-helical structure, maintained by multiple disulphide bridges. A report by Navone *et al.* suggested that the degradation rate of keratin could be increased by 90% in the presence of reducing agents, disrupting the disulphide bond formation within the proteins [142]. The reduction of the disulphide bonds is also the method utilised by two keratinolytic serine proteases isolated from *Stenotrophomonas sp.* strain D1 in deer fur [143].

As extraction of keratin from natural sources requires harsh chemical treatment, much interest has been had in enzymatic extraction techniques [144–146]. However, the limited enzymes with high efficiency with diverse substrates prevents commercialisation [147].

1.4 Acute and chronic wound environments

1.4.1 Acute wound site behaviour

During normal or acute wound healing, the surrounding tissue responds in a balanced and controlled process, during which many cellular activities are conducted. These include phagocytosis, chemotaxis, mitogenesis, collagen synthesis and the synthesis of other ECM components. These processes are grouped into four well defined stages: haemostasis, inflammation, proliferation and remodelling to return the tissue to its normal anatomical structure, illustrated in **Figure 5** [148,149].

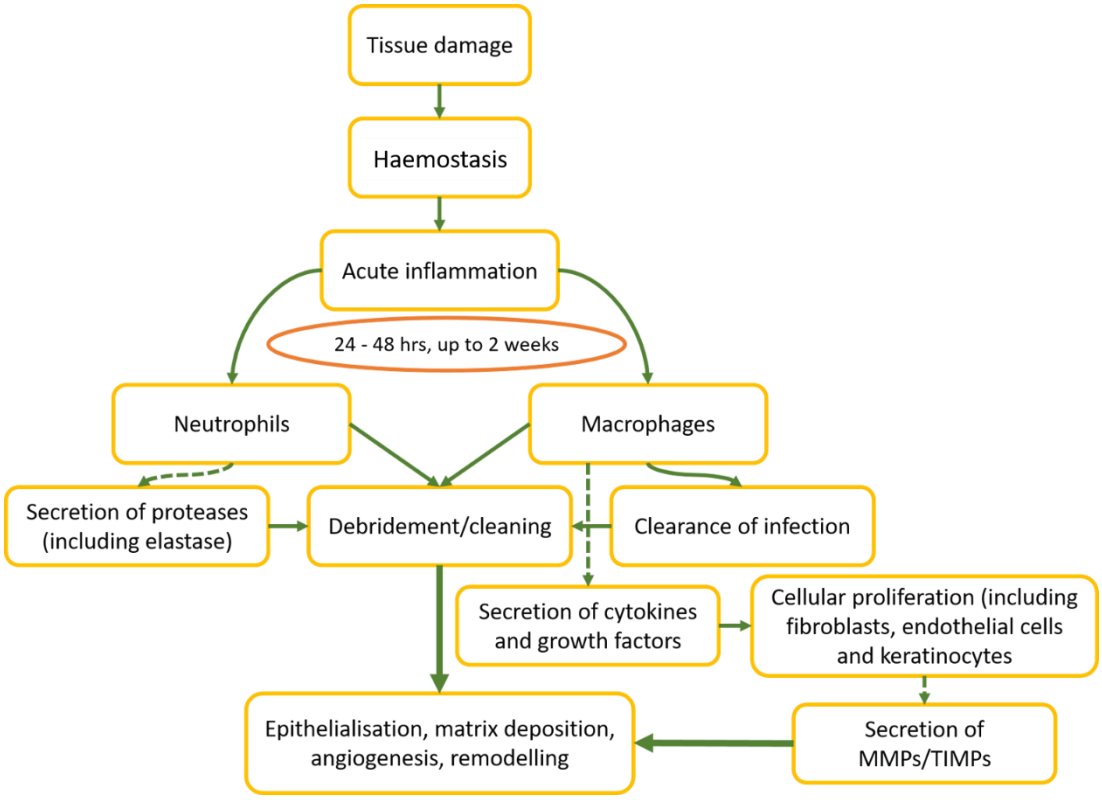

Figure 5. Following initial tissue injury, haemostasis occurs resulting a fibrin clot formation. Inflammation then proceeds and leads to debridement and cleaning of the wound area before cellular proliferation and migration. Macrophages and neutrophils act to further debride and clean the wound area by removing contaminating microorganism and foreign material. Proteases aid in the remodelling of the ECM. ECM deposition and degradation are delicately balanced by maintaining the secretion of both MMPs and their TIMPs. Image recreated from 'Proteases and Delayed wound healing' McCarty and Percival, 2012.

When designing biomaterials involved in wound repair, the evolving environment of wound conditions must be taken into consideration. Understanding the complexities of these processes allows researchers to design effective tools whilst reducing the likelihood of serious side effects, as seen in **Figure 6** [150,151]. This is especially important where loss of material could result in life-threatening complications such as thrombus or stroke [152]. After wound healing however, the role of the implant may become superfluous, at which point the material may be designed to undergo predictable degradation into harmless by-products at a controlled rate. As a result, it is increasingly common for biomaterials to be left inside a patient to reduce the need for a further operation and risking wound recovery complications.

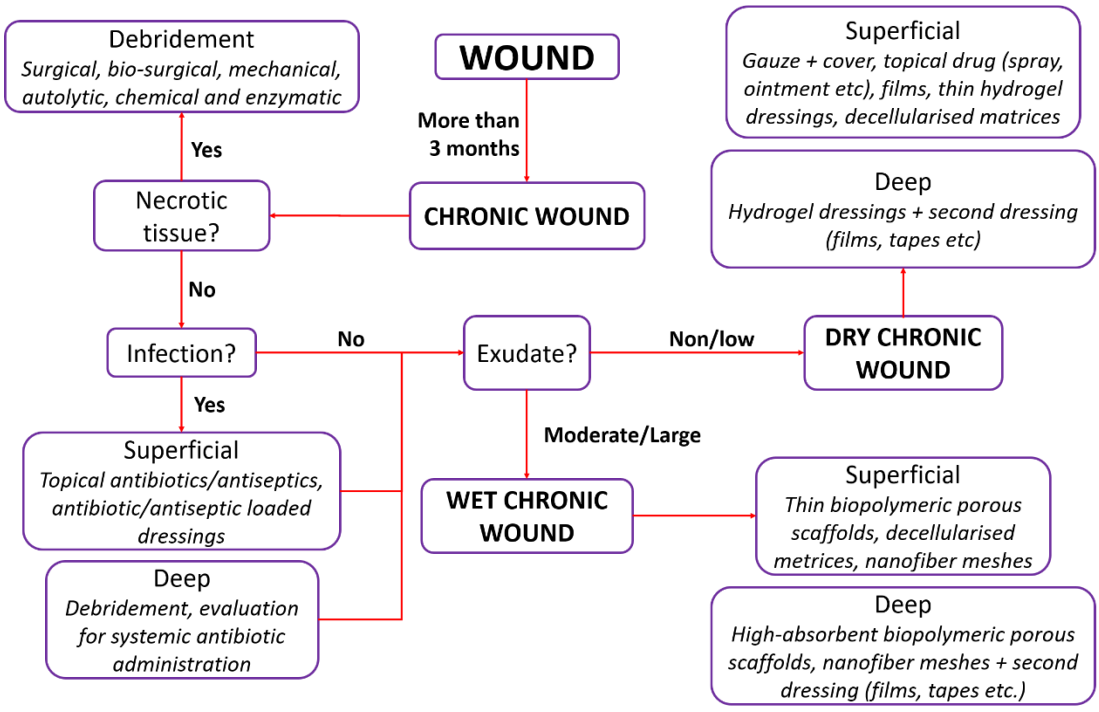

Figure 6. Wound assessment and dressing selection criteria. Image recreated from Chronic wounds: Current status, available strategies and emerging therapeutic solutions' Las Heras *et al*. 2020**.**

Considered a foreign body, the material will undergo granulation as part of the natural wound inflammatory response [153,154]. During this stage, platelet aggregation recruits granulocytes and polymorphonuclear leucocytes (PMNLs). When present, PMNLs release a vast array of degrading enzymes and free-radical species in an attempt to remove the

offending object. As the presence of bacteria is reduced, PMNLs are replaced with macrophages as regulators of the wound healing process, releasing cytokines and growth factors to recruit fibroblasts, keratinocytes and endothelial cells [155]. At this point, the surrounding environment begins to be dismantled and rebuilt through the careful expression and secretion of structural proteins such as collagen and proteolytic MMPs. Biomaterials that have survived to this stage would then allow fibroblast infiltration, integrating the non-self with self [151]. Controlled degradation at this point allows the resulting ECM to maintain the local environment while the biomaterial is removed in the presence of macrophages.

1.4.2 Pressure ulcers and chronic wounds

In chronic wounds, the process of healing is disrupted during one or more of the four healing stages (haemostasis, inflammation, proliferation or remodelling) [151,156]. This is most common in the inflammatory or proliferative phases due to the high level of cytokine and signalling molecules present and interacting with each other, as shown in **Figure 7**. Impaired healing can be contributed to a change in activity of one of many ECM elements, such as growth factors, cytokines, proteases and cellular elements. Wound healing can also be compromised in the presence of oxidative damage or neuropathy of the tissue, preventing the cells responsible for removing debris from reaching their targets, the build-up of which further accelerates both oxidative damage and neuropathy of the surround tissue. Diseases that result in the restriction of mobility often lead to the development of chronic wounds as blood flow becomes limited to the affected area, resulting in the death of the tissue. Eventually, breakage in the skin leads to sores and the development of severe pressure ulcers [157–159]. It is suspected that up to 15% of Type 2 diabetic sufferers may be affected. As a result, national expenditure associated with chronic pressure ulcers for the year of 2012 was reported as £11.7 billion according to NHS England, increasing annually [160–162].

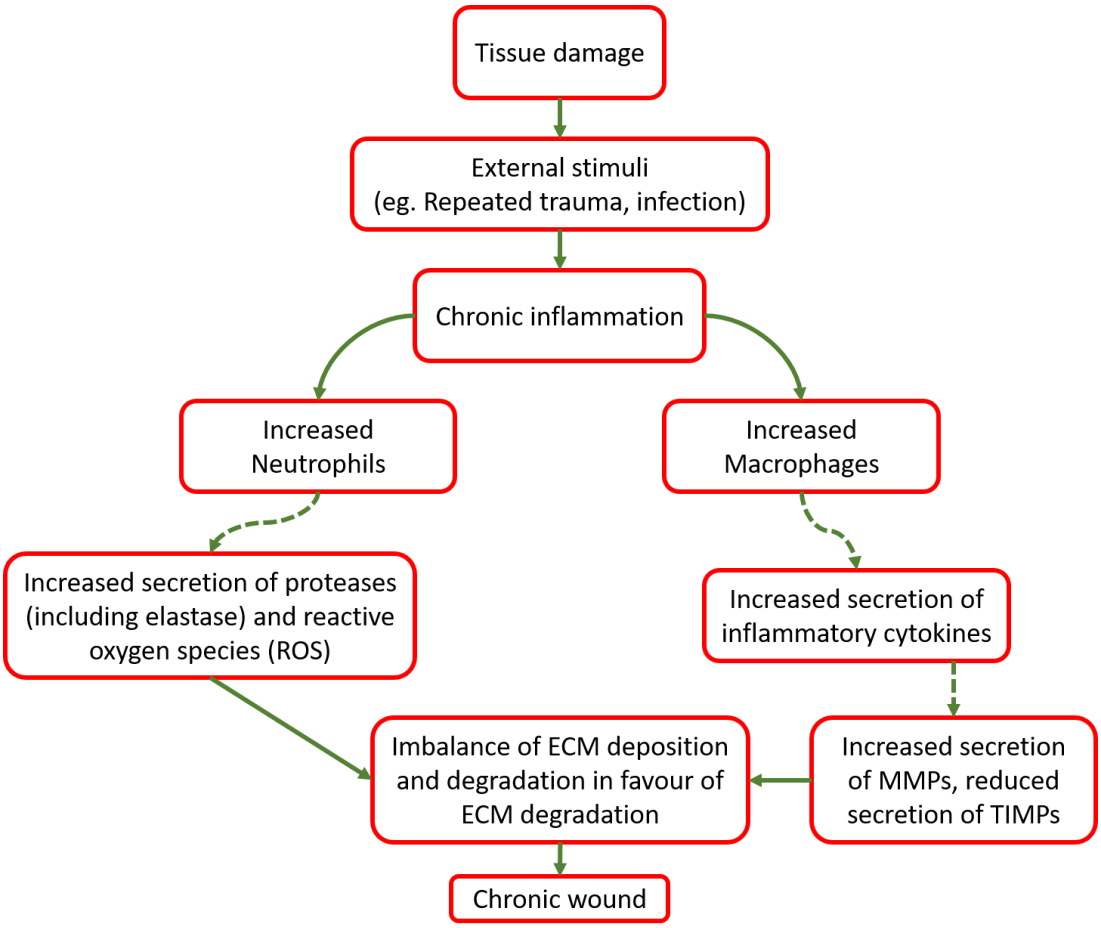

Figure 7. Stages of chronic cutaneous wound development. After the initial tissue injury, prolonged and augmented inflammatory response is caused by external stimuli, including bacterial contamination and infection. This can lead to elevation of inflammatory cytokine and protease release. As the deposition and degradation of the ECM is unbalanced, the wound enters a state of chronicity. Figure recreated from 'Protease and Delayed wound healing' McCarty and Percival 2012.

For many chronic wounds, the concentrations of matrix metalloproteinases (MMPs) are sustained at an elevated level and prevent wound closure [163,164]. Substrates of MMPs include the collagen bundles, produced during the remodelling phase of acute wound healing. In the presence of elevated MMPs however, the collagen is degraded rapidly, preventing the wound from closing. In acute wound healing, the formation of the new ECM allows an influx of migrating epithelial cells and a reduction in MMP production. Paired with an increased release of tissue inhibitors of metalloproteinases (TIMPs), the concentration of active MMPs are further reduced.

TIMP release and expression is thought to be mediated by the growth factor TGF-β. However, if the level of TGF-β is reduced, whether

by elevated MMPs or lack of angiogenesis from poor circulation, the release of essential TIMPs into the environment is reduced and wound remodelling is slowed. This is especially problematic if the wound is in a location on the body that poses a high risk of introducing infecting bacteria. While invading bacteria may be removed by host macrophages, the wound is returned to the inflammation phase of recovery, preventing further wound remodelling and subsequent healing. As a result, the repair of chronic wounds are unable to progress as the time required for inflammation and remodelling phases allows bacteria to invade multiple times and the elevated concentrations of MMPs is never reduced.

For biomaterials to function in these conditions, they must provide solutions to these issues. The introduction of MMP target sites to an implant material may act as a diluting effect at the wound site, allowing adequate collagen synthesis to facilitate the migration of epithelial cells and expression of TIMPs to reduce the MMP concentration. The presence of materials with antibacterial properties could speed up the phase of inflammation, in turn reducing the release of inflammatory cytokines, enabling the subsequent recovery of the wound [151,165].

Chronic wounds are often characterised by high free iron concentrations, a significant contributor to hyperactivation of MMP9 [166]. It is possible that functionalising 4RepCT with an iron-chelating ligand would reduce the free iron concentration, reducing the level of MMP9 activation and relieving the chronic wound environment. However, the large quantity of chelates required to noticeably reduce the iron concentration prevents silk from being utilised in this way. As a result, this route was not explored further during the course of this project.

Critically, recombinant silks have the potential to be degraded by host proteases present in the ECM [29,151]. However, before a silk-based biomaterial can be manufactured, its degradation over time must be investigated, specifically when subjected to proteases expressed at chronic wound sites [149,163,167].

1.4.3 Replication of wound conditions *in vitro*

If recombinant silks are to be incorporated into tissue engineering scaffolds and accelerated wound healing scenarios, the performance of these materials must be studied in representative physiological conditions. Although previous work has been performed to recreate accurate wound conditions, it is difficult to reproduce exact concentrations of the relevant enzymes present in a wound. As laboratory concentrations of enzymes are often in great excess of that present biologically, *in vivo* studies would provide the most accurate data regarding silk implant activity at an active wound site [168]. However, *in vivo* results are often complex to interpret, providing information on every protein. To study individual enzymes, knockout mice are required, increasing the expense of the investigation.

Two studies have taken different approaches when investigating the degradation of recombinant silks in the presence of enzymes found at sites of trauma. An *in vitro* study by Susanne Müller-Herrmann and Thomas Scheibel attempted to recreate concentrations at normal and wound conditions of various MMPs (MMP2, MMP8, MMP9, MMP13) and PMN elastase in the presence of eADF4(C16) [72]. Collagenase IA and digestive enzyme Protease type XIV were also investigated to compare to natural collagen breakdown as a positive control. To simulate a trauma cascade response, the enzyme concentration was increased by around five times its resting value for its 'wound value' (total enzyme mass was increased from 351 ng/ml to 1050 ng/ml). Müller-Herrmann and Scheibel agree that although the concentrations were in excess of realistic wound conditions, the elevated protein was essential for quantifiable data [169,170]. As a result, their data should be treated with caution. Each enzyme was also investigated in isolation, unlike the environment found at a wound site. Despite this, Müller-Herrmann and Scheibel observed that eADF4(C16) showed no degradation when exposed to MMP8 or MMP9, whilst complete degradation was noticed when introduced to MMP2 and PMN elastase overnight. Müller-Herrmann and Scheibel also proposed the introduction of MMP9 active sites into the recombinant silk's peptide sequence, increasing the rate of protein degradation. Interestingly, a 35 kDa intermediate was observed after MMP2 and PMN elastase mixture

degradation but was subsequently degraded when exposed to Protease XIV suggesting that eADF(C16) was suspectable to digestive protease degradation. This is thought to occur because some spiders consume their own silk during repair, resulting in rapid breakdown when exposed to Protease XIV [72,171].

In comparison, Camilla Fredriksson *et al.* investigated the degradation of 4RepCT *in vivo*, by observing the histological changes in tissue surrounding recombinant silk implants in rats as shown in **Figure 8** [90]. Degradation was analysed seven days after implantation, revealing little to no increased immune response, whilst the implant itself appeared intact of proteolytic degradation. Fredriksson compared six different implants, each with different preparation steps, a commercial degummed silkworm silk implant (Mersilk™) as a positive control and 'sham' cut as a negative control. Histological results were compared to that of a normal injury and foreign body response, concluding that no significant increase in leukocyte activity could be observed, a typical indication of aggravated immune response. At a macroscopic evaluation, a third of the implants showed slight reddening, although two of these were later associated with small capillary haemorrhage. A second histological evaluation suggested that partial degradation of the 4RepCT fibres had occurred, indicated by the increase of multinucleated giant cells displaying fibre remnants. Throughout all implants, fibroblast-like elongated cells were seen in close proximity to the implants indicating that fibroblast infiltration had occurred. Interestingly, Mersilk™ fibres did not appear to have undergone degradation, occupying less space in the tissue. However, the surrounding fibrotic capsule (indicating an aggregation of macrophage cells) was denser for the Mersilk™ implant, whilst newly formed capillaries were clearly visible for 4RepCT.

Fredricksson goes on to suggest that silk fibres may encourage angiogenesis as new capillary formation was observed surrounding all 4RepCT implants. If controlled, angiogenesis is a favourable property in tissue engineering, ensuring a constant supply of oxygen, nutrients and biochemical cues to the growing cells. The ability to stimulate

angiogenesis without amplifying inflammation is essential for successful wound healing. This demonstrated that 4RepCT was therefore superior to Mersilk™ in supporting and promoting physiological fibroblast and angioblast migration and growth.

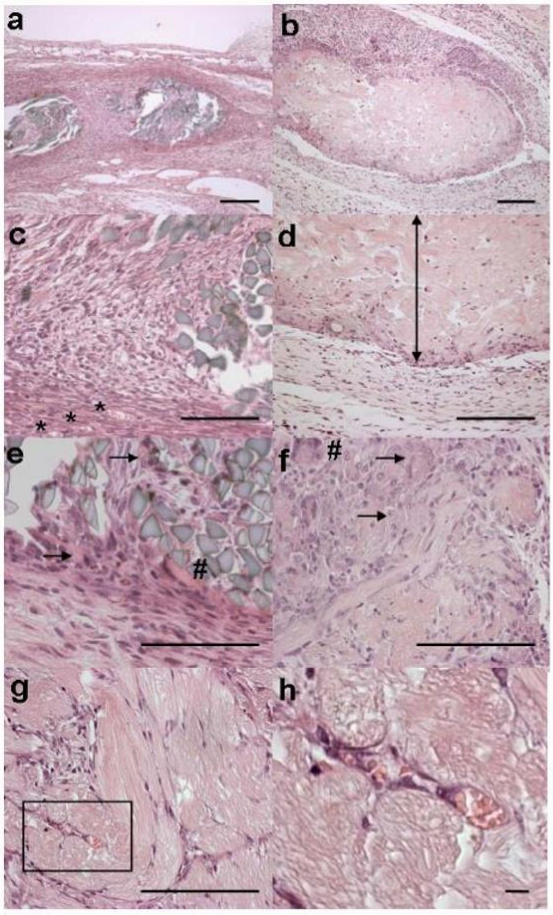

Fredricksson, 2009

Figure 8. Microscopic appearances of implants. The Mersilk™ implant from rat no. 3 is shown in (**a**), (**c**) and (**e**). 4RepCT fibre implants are shown in (**b**), (**d**) and (**f**) (C3 from rat no. 2), and in (**g**) and (**h**) (C2 from rat no. 2). Scale bars are 100 µm in **a-g**, and 10 µm in **h**. (**a**) A fibrous capsule surrounds bundles of regular refringent fibres of the Mersilk™ implant. (**b**) A polar infiltrate surrounds the 4RepCT implant, where one side evokes practically no response, at the bottom of the figure, while the opposite side, in the upper part of the figure, shows a moderate foreign body reaction with macrophages and multinucleated giant cells. (**c**) Capillaries are present in the fibrous capsule surrounding Mersilk™ (*****). Inside of the capsule, cells have populated the implant. (**d**) The side of the 4RepCT that evokes almost no inflammatory response is shown. The location of the 4RepCT implant is indicated by a double edged arrow. (**e**) The reaction in close contact with the Mersilk™ implant displays macrophages (**arrows**) and multinucleated giant cells (**#**). (**f**) The side of the 4RepCT implant that evokes a moderate foreign body response is shown. The cell reaction adjacent the 4RepCT implant exhibit macrophages (**arrows**) and multinucleated giant cells (**#**). (**g**) The centre of a 4RepCT fibre bundle displays delicate septae with elongated cells, resembling fibroblasts, angioblasts and newly formed capillaries. The square box (magnified in **h**) encloses capillaries in the 4RepCT fibre bundle. (**h**) Magnification of square box in (**g**) shows erythrocytes in the lumen of tubular structures indicating capillaries present (and newly developed) in the centre of a 4RepCT fibre bundle. Image taken from 'Tissue response to subcutaneously implanted recombinant spider silk: An *In vivo* study', Fredricksson et al. 2009.

1.5 ECM proteases

The ECM is comprised of numerous structural proteins, growth factors and matrix remodelling proteases. These components work in balance to grow, replace and repair the surrounding environment for cell migration and to enable cytokine signalling. As the composition of the ECM is tissue specific, biomaterials must be investigated in a variety of different environments and enzyme concentrations. For the purpose of this study, MMP2, MMP9 were used to reflect the overexpression of gelatinases observed in chronic wound environments. As these enzymes are highly cited in the literature, reliable proteomic data for each enzymatic degradation profile could be utilised [164,172,173].

1.5.1 Serine proteases

Serine proteases are a super-family of endopeptidases, so called because they utilise a serine residue within their active site. Found ubiquitously across both eukaryotes and prokaryotes, they are categorised by structure being either chymotrypsin-like or subtilisin-like. In addition to extracellular remodelling, they also contribute to digestion, immune response and blood coagulation. Serine proteases have a distinct structure, consisting of two β-barrel domains that converge towards the catalytic active site. These proteases can also be categorised by substrate specificity as trypsin-like, chymotrypsin-like, thrombin-like, elastase-like and subtilisin-like. Despite the various substrate specificities, the catalytic mechanism and catalytic triad (His57, Ser195 and Asp102) remains similar regardless.

α-Chymotrypsin is a digestive enzyme found in pancreatic juice and duodenum. It utilises its serine proteases activity to breakdown proteins and polypeptides on the carboxyl side of relatively large aromatic residues such as tyrosine, phenylalanine and tryptophan [174]. The large side chains fit into the specificity pocket of chymotrypsin and provides the enzyme's substrate specificity. Chymotrypsin is also capable of hydrolysing other peptide bonds such as leucine and methionine, but at a slower rate. Although not present at wound sites, investigations into 4RepCT degradation by high-specificity α-chymotrypsin would serve as a

comparison to previous studies by Brown *et al.* with silkworm silk films [84].

1.5.2 Catalytic mechanism

Located at the active site of the enzyme, the catalytic triad consisting of His57, Ser195 and Asp102 residues, serves to activate, stabilise, and cleave the incoming substrate peptide. As the substrate peptide comes into proximity with the enzyme, an ordered 'ping-pong' mechanism takes place to generate a series of unstable intermediates and final cleavage product, shown in **Scheme 1**.

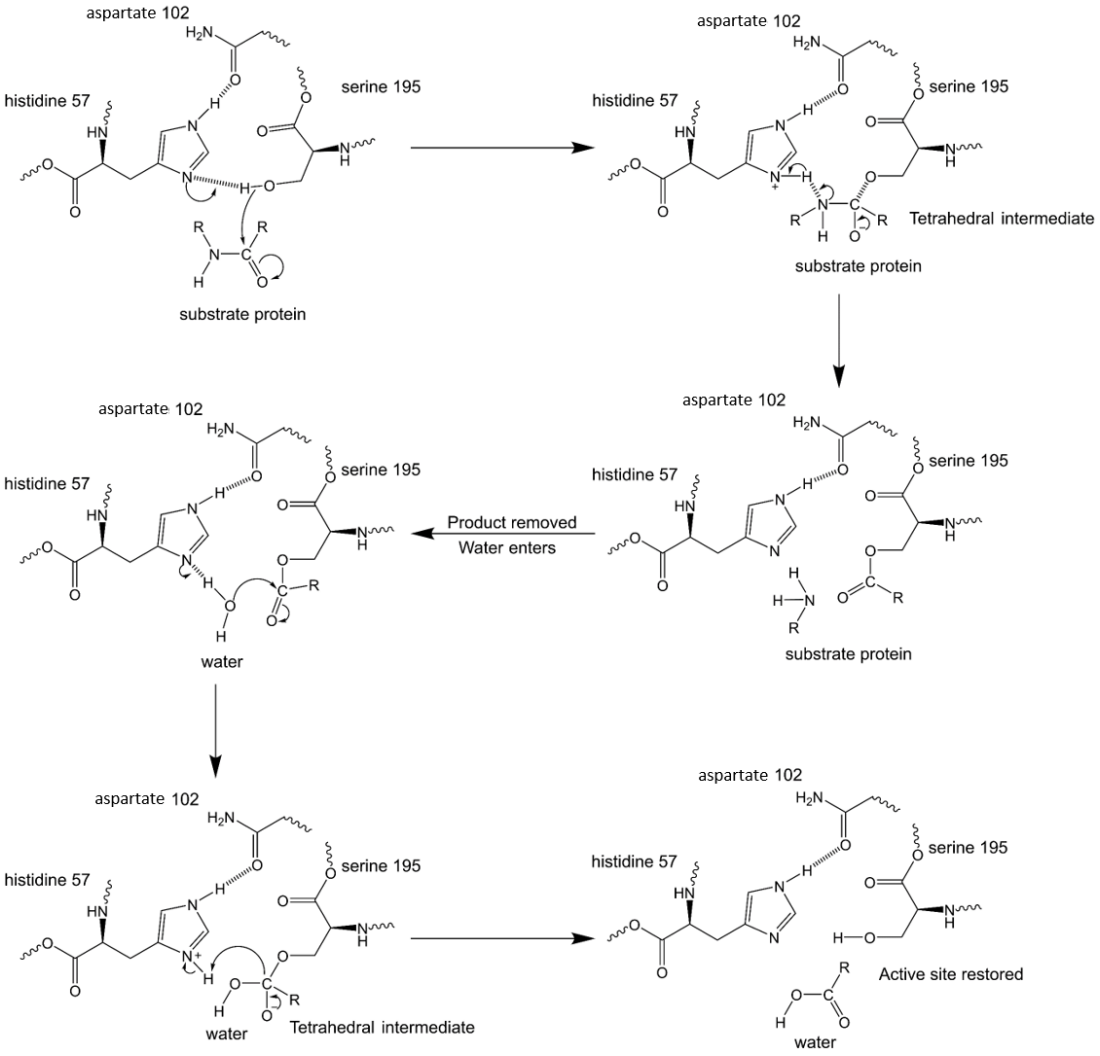

Scheme 1. Catalytic 'ping pong' mechanism of serine proteases. Image recreated from 'Serine Protease Mechanism and Specificity', Hedstrom 2002.

By use of a nucleophilic serine (S195) and tautomeric histidine (H57), two tetrahedral intermediates are produced in the process of peptide backbone cleavage. The movement of electrons to and from the carbonyl oxygen double bond earns its name 'ping-pong'. The imidazole ring of the histidine is maintained in its tautomeric state by hydrogen bonding with the aspartate (A102), enabling the histidine to accept an additional hydrogen from the -OH of the serine [175].

1.5.3 MMPs

MMPs are classified as calcium-dependent zinc-containing endopeptidases. The majority of MMPs can be divided into four main groups: the collagenases, stromelysins, gelatinases and membrane-type MMPs (MT-MMPs) and refer to the substrate specificity of the enzymes. Shown in **Figure 9**, MMPs are expressed as inactive zymogens before catalytic cleavage of the inhibiting pro-domain is signalled by the release of activating proteases at the onset of wound repair [149]. MMP2 (gelatinase A) is also involved in the controlled breakdown of the ECM in normal physiological processes.

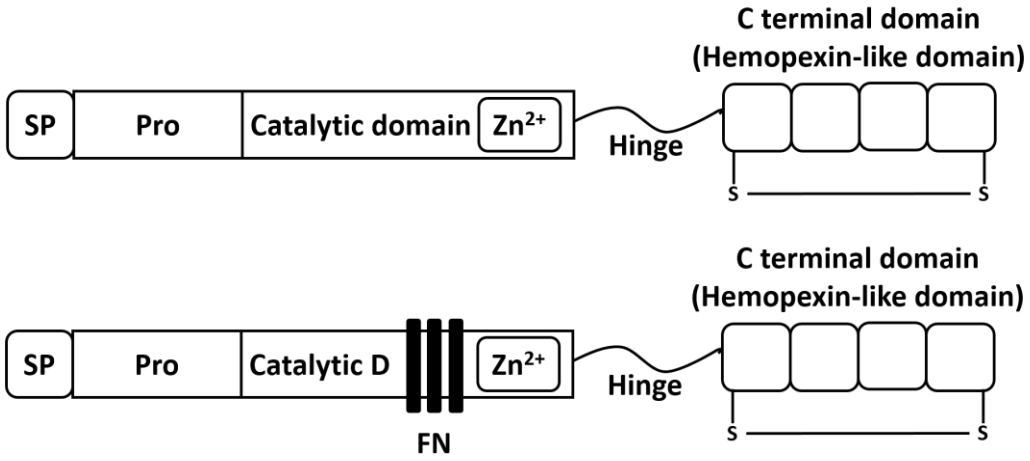

Figure 9. The simplified domain structure of MMPs involved in cutaneous wound healing. The upper image represents simple hemopexin domain-containing MMPs (collagenases and stromelysins). The lower image represents gelatinases (MMPs and MMP9). All MMPs consist of a signal peptide (SP) and are expressed as a zymogen to prevent catalytic activity in the presence of a pro-domain (Pro). Catalytic activity is carried out in the catalytic domain, utilising zinc-binding site and hemopexin-like C terminal domains. The hemopexin-like domain consists of four repeated subunits and is connected by a disulphide bridge. The hemopexin-like C terminal and catalytic domains are connected by a hinge region. Three fibronectin type II repeats (FN) within the catalytic domain differentiates gelatinases from the rest of the MMP family. Figure recreated from 'Proteases and Delayed wound healing' McCarty & Percival 2012.

Like many MMPs, MMP2 requires proteolytic processing before it is activated. Activation occurs at the cell surface membrane by the membrane-bound MMP1 (MT-MM1) and a MMP2-tissue inhibitor. MMP2 is also activated in the presence of integrin clustering, indicating that cell migration may be about to take place. Like other MMPs, MMP2 cleaves at specific glycine residues, specifically: X-Gly-Ile, X-Gly-Leu, X-Gly-Val, X-Gly-Phe, X-Gly-Asn and X-Gly-Ser where X is any neutral amino acid [176,177]. The recognition sequence of MMP9 has been constructed from cleavage alignments from a vast array of substrate proteins [178–182]. From the substrate libraries produced by the literature, three subsets of target sequences were compiled. The broadest contained a P-X-X-Hy-(Ser/Thr) motif (where X is any residue and Hy is a hydrophobic residue) in positions P3 – P2 [183]. This motif is recognised by many MMPs and is thought to resemble that of structural collagen. The second substrate group contained G-L-(K/R) motif at P1 - P2 [183]. Interestingly, the third set of substrates is unique as it consists of Arg residues in both P1 and P2 of the hexamer sequence. Together, these sequences can be combined to produce substrate profiles that can be applied to known peptide sequences to allow accurate predictions of protein cleavage.

Illustrated in **Schematic 4**, the MMP reaction mechanism occurs when a catalytic water molecule is strongly polarized by the negatively charged Glu116 residue, enabling the positively charged zinc cation to act as a nucleophile. This then attacks the carbonyl carbon of the scissile bond in the substrate. The Glu116 side chain then accepts a proton from the water molecule to transfer it to the scissile-bond nitrogen atom. Finally, the peptide C-N bond in the substrate is cleaved. The role of Glu116 was found to be critical in facilitating this reaction, as replacing it for an Ala removed the protease activity [184,185].

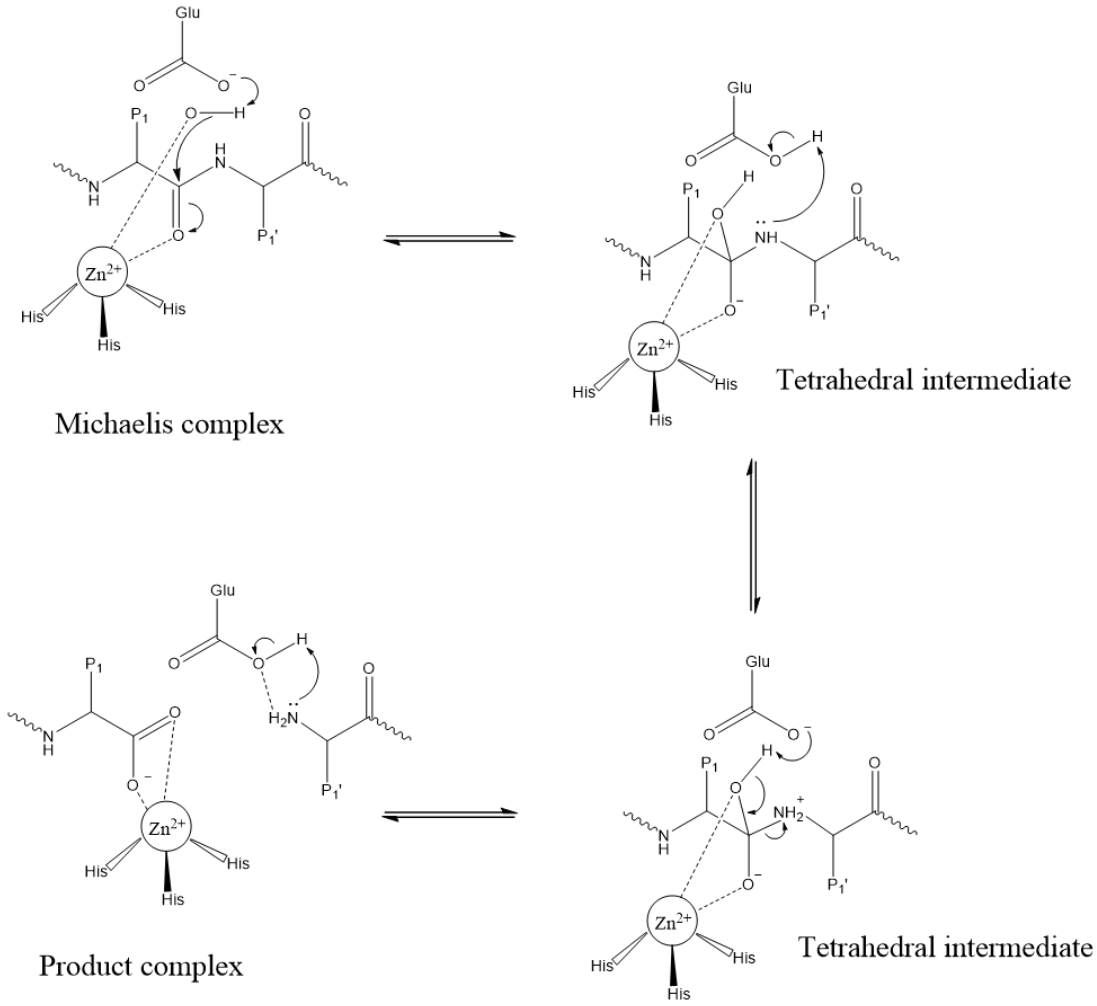

Schematic 4. General features of the proposed metalloprotease reaction mechanism. Image recreated from 'Mechanism of Proteolysis in Matrix Metalloproteinase-2 Revealed by QM/MM Modeling' Vasilevskaya, 2015.

1.5.4 Introduction of MMP target sequences into 4RepCT

In the literature, multiple MMP target sequences have been determined by heat mapping which provided a library of possible substrate sequences that individual MMPs recognised [172,173]. 4RepCT's primary amino acid sequence was then screened for any pre-existing substrate sequences in addition to any that could be accessed within one or two point mutations. However, conservation within the α-helical C-terminus restricted the number of viable mutation sites, avoiding amino acids that were thought to facilitate soluble expression and function [45,186,187]. As a result, this novel approach granted new insight into the potential biocompatible properties of 4RepCT as a biomaterial.

As the complex environment within the ECM is difficult to replicate *in vitro*, it is therefore necessary to produce isolated 'snapshots' of protein behaviour when degraded in specific proteases. With this in mind, profiles of predicted enzymatic coverage of 4RepCT can be produced to better understand the protein's degradation behaviour.

If synthetic spidroins are to be used for functional tissue engineering, their functional life and subsequent rate of deterioration must be determined and controlled [104,188]. While the introduction of MMP target sequences into the spidroin amino acid sequence may increase the rate of degradation, mutating the sequence may disrupt the material's biocompatibility or disrupt spidroin folding and prevent polymerisation and fibre formation. For this reason, mutations should be located within the repetitive domains of the sequence ensuring the conserved non-repetitive domains (NRDs) are not disturbed. Müller-Herrmann and Scheibel suggested introduction of specific MMP9 target sequences to achieve controllable degradation [72]. MMP9, also known as gelatinase B, is expressed in leukocytes, macrophages, osteoclasts and other cell types present in the surrounding wound environment [189]. Gelatinase B cleaves collagen type I, II and III after triple helices at the target sequence G/PA/-/G#L/-/G/- 47. The selective introduction of MMP9 cleavage sites into 4RepCT or eADF4(C16) by site-directed mutagenesis could allow the degradation of implants to be controlled, reducing the time of recovery.

1.5.5 Summarising developments to improve silk-based biomaterials

While spider silk has begun to be incorporated into many medical procedures and roles, there remains the ever-constant need to improve the tools that are produced using this unique material. For this to happen, the concept of 'improvement' must be considered for each application, of which there may be several. Some aspects of improvement may be similar for all applications, such as maintaining (or further improving) desired physical properties, host responses, material use and reducing the price of manufacture. However, the design of biomaterials located within the ECM scaffolds must also consider how the

biomaterial's behaviour might be improved during breakdown in varying environmental conditions.

For use in chronic wounds, the biomaterial should act to return the host environment to that of an acute wound environment. At this point, the multiple entities involved in wound repair would be balanced and appropriate feedback within the system could be re-established. Once achieved, the implant should undergo eventual breakdown and assimilation into the surrounding cells. One advantage of using proteinaceous material is that it can be degraded by proteases within the wound environment and ECM.

By engineering a biomaterial such as 4RepCT with these properties, it provides a platform that can be utilised for further tuneable properties. In the development of ever-improved tissue scaffolds, the opportunity for functionalised silk-inspired biomaterials with predictable degradation rates may be achievable soon.

2. General Methods

2.1 MASP sequence alignments

2.1.1 Gathering sequence data

Both MASP 1 coding gene sequences and subsequent translations were collected from GenBank® database (https://www.ncbi.nlm.nih.gov/genbank/) and compiled using Notepad++. Only MASP1 sequences were collected and included entries from the arachnid genera *Argiope, Araneus, Cyrtophora, Dolomedes, Euprosthenops* and *Nephila*.

2.1.2 Aligning multiple sequences

Gathered sequences were first aligned using an online MAFFT algorithm against sequences of the same species to identify amino termini, carboxyl termini and repetitive regions [190]. All alignments were viewed using JalView 2.11.0 and identified variation within spidroin termini within a single species [191]. A single consensus sequence was produced for each species spidroin termini and used for subsequent *in silico* investigations. Accession numbers are recorded in descending order in the respective images.

2.1.3 *In silico* analysis of natural and recombinant spidroins

Proteolytic target sequences for MMP2 and MMP9 were gathered from the literature and compiled to produce series of six amino acid sequences that were expected to be cleaved by active MMP2 and MMP9 [172,173,192]. These sequences were then cross examined against the protein sequences of natural spidroin termini and TRX_4RepCT. Amino acid residues that matched these target sequences across the cleavage point were identified and highlighted to match the number of residues that the cleavage site contained. To better identify protein sequences that contained a higher coverage of proteolytic sites, the highlighted regions were scored with increasing weighting towards 6-residue sequences.

The protein sequences were also submitted to the online prediction software PROSPER to identify expected cleavage sites, complimenting the manually conducted *in silico* studies.

2.2 Preparation of enzyme solutions

α-Chymotrypsin
The assay concentration of α-chymotrypsin (Type II, bovine pancreas, Sigma Aldrich) was prepared in line with a method developed by Brown *et al.*, dissolving the enzyme powder in dH_2O with an activity of 40 units/mg protein [84].

Human neutrophil elastase (ELNE)
The activity of human neutrophil elastase was determined by FRET fluorescence spectroscopy using an Amplite universal fluorometric protease activity kit at Ex/Em = 490/525 nm. ELNE activity (20 µmol/min/mg protein) was corrected to 160 RFU^{-1} as suggested by Brown *et al.* to give comparable results [84] until concentrations were reduced 34 nM to reflect concentrations observed *in vivo* [193].

2.2.1 Activating MMPs

Recombinant inactive MMP2 (gelatinase A, CHO-derived human MMP2 protein, specific activity >1000 pmol/min/µg protein) and MMP9 (gelatinase B, CHO-derived human MMP9 protein, specific activity >1300 pmol/min/µg protein) were purchased from RnD systems (Bio-techne, Minneapolis, MN) and activated as instructed upon purchase. MMPs were resuspended to 100 µM in TCNB buffer (50 mM Tris, 10 mM $CaCl_2$, 150 mM NaCl, 0.05% (v/v) Brij 35, pH 7.5) and activated in the presence of 1 µM APMA (4-aminophenylmercuronic acetate, Merck). MMP2 was incubated at 37 °C for 1 hour while MMP9 was incubated for 24 hours before both were diluted to a stock concentration (563 µM MMP2, 251 µM MMP9). Aliquots of 10 µL were prepared at this concentration to reduce the need for repeated freeze-thaw cycles. All aliquots were flash frozen in liquid nitrogen and stored at -80 °C until needed. When diluted to a final volume of 0.5 mL, the final MMP concentration was 10% that reported by Ladwig *et al.* at 800 nM MMP2 and 450 nM MMP9 respectively [164].

2.2.2 Zymography

To confirm MMP activity, both MMP2 and MMP9 were analysed by gelatin zymography. A protein concentration curve was produced at concentrations of 500, 1000, 2000, 5000, 10000 and 15000 ng/mL were produced by serial dilution in TNCB buffer used to activate the proteases.

Pre-made 10% gelatin zymography gels (Invitrogen™ Novex™, Cat #ZY00100BOX) were prepared and run for 90 min at 125 V in 1X Tris-Glycine SDS Running Buffer (Invitrogen™ Novex™, LC2675) as per kit instructions. Once run, gels were rinsed with dH_2O and transferred to 100 mL 1X renaturing buffer (Invitrogen™ Novex™, LC2670) for 60 min at room temperature with gentle agitation. The gels were then transferred into 100 mL 1X developing buffer (Invitrogen™ Novex™, LC2671) and incubated for 30 min at room temperature with further agitation before being transferred to a static 37 °C incubator for 24 hrs.

At this point, the buffer was removed, and the gel was stained for 72 hr in the presence of sufficient GelCode Blue Safe Protein Stain reagent. All gels were imaged using a UV transilluminator (G:Box, Syngene Geneflow).

2.3 Silk reeling of spiders for light microscopy

Dragline silk was directly reeled from adult female *Argiope trifasciata, Cyrtophora citricola, Dolomedes fimbriatus, Nephila madagascarensis* and *Pisaura mirabilis*. Spiders were encouraged to move along a corrugated cardboard 'walker' behind which the spiders would leave dragline silk. This silk was carefully wound directly onto the microscope slide. If spiders refused to walk along the apparatus, they were handled carefully, allowing them to descend from the handler and producing the dragline silk behind it. This silk was also wound directly onto the microscope slide before the spiders were returned to their tanks and webs. As no silk could be reeled from an adult female *Pholcus phalangioides*, dragline silk was collected directly from a freshly formed web.

2.4 Enzymatic degradation of natural silk fibres

To ensure protease solution remained on the silk fibres, rings of silicon grease were applied directly to the microscope slides. Slides were imaged with a white light gel transilluminator to produce a map of the individual ring locations as seen in **Appendix 8.1**. Protease solutions were diluted to assay concentrations (see **Table 4**) before 50 µL of each protease solution was placed in each grease ring. The microscope slides were then transferred carefully to a storage container that contained a wetted cloth to maintain humidity throughout the incubation period. The slides were then incubated at room temperature for one week before being analysed by bright field and birefringence microscopy.

2.5 Bright field and birefringence microscopy of natural silk

Natural fibres were imaged with both bright field and birefringence objectives at 100X magnification with oil immersion using a Zeiss Axioplan light microscope at 3200K light intensity with tungsten light source. Birefringence images were captured with samples at 45° to the light source to enable maximum visualisation. Images were captured and processed using the ImageJ to correct white balance and produce appropriate scale bars. As the natural fibres were observed at very high magnification, dark field microscopy images were not captured. The method used to capture microscopy images of recombinant silk fibres is described in **Methods 2.18**.

2.6 *In silico* mapping of MMP and protease target sites

The specific target sequences of all proteases determined by the literature before they were compared to the amino acid sequence of 4RepCT, specifically those of chymotrypsin, neutrophil elastase and MMPs 1, 2, 3, 7, 8, 9, 10, 11, 12 and 13. As with the natural spidroin analysis, target sequences that crossed the P1’ and P1 cleavage point were highlighted and scored accordingly. As described earlier, the scores were weighted to reflect the number of residues contained within a particular target sequence and subsequent expected proteolytic degradation.

2.7 Preparing electrocompetent *E. coli*

Under ultra-sterile conditions, overnight cultures of 'empty' *E. coli* (XL1-blue, DL41, Neb5α and BL21) were prepared in 5 mL LB. Tetracycline was added to the XL1-blue cultures to 10 µg/mL to take advantage of its natural resistance to the antibiotic. Overnight cultures first incubated at 37 °C for 15 hrs with agitation at 180 rpm before they were added to 500 mL sterile LB. Tetracycline was again added to a final concentration of 10 µg/mL and incubated at 37 °C with agitation at 200 rpm until the cell density reached an OD of 0.7. At this point cell growth was halted by incubation at 4 °C for 30 min. The volume was then divided into previously autoclaved and chilled 500 mL Oakridge bottles and centrifuged for 17 min at 3500 x *g* at 10°C. The resulting pellets were resuspended in 100 mL chilled dH_2O each and recombined before being centrifuged at 4500 x *g* for a further 12 min at 10 °C. This process was repeated six times before the pellet was twice resuspended in 100 mL dH_2O and centrifuged as before. After a total of 1400 mL dH_2O wash, the pellet was resuspended in 20 mL H_2O, centrifuged and finally resuspended in 5 mL 30% v/v glycerol, aliquoted into 80 µL and flash frozen in liquid nitrogen before being stored at -80 °C until use.

Electrocompetent DL41, Neb5α and BL21 *E. coli* were grown in the same manner without the addition of the antibiotic tetracycline. For all future antibiotic inoculations, kanamycin and ampicillin were introduced at final concentrations of 50 µg/mL and 100 µg/mL, respectively.

2.8 *E. coli* transformation by electroporation

Electrocompetent *E. coli* (XL1b, DL41) were transformed by electroporation with a pJExpress401 plasmid vector containing kanamycin selection marker, lac operon, T5 promoter and terminator and inserted 4RepCT sequence using a Micropulser, (BioRad) at 2500 V in 0.2 cm electroporation cuvettes (Flowgen Bioscience). T7 controlled cells (BL21 DE3, Rosetta 2011) were transformed with a pET22b (+) plasmid vector containing ampicillin selection marker. Newly transformed cells were then incubated in 1 mL LB broth at 37 °C with agitation at 180 rpm

for 1 hr before 50 µL were plated onto appropriately selective LB agar plates and incubated for 15 hrs at 37 °C in a static plate incubator (WTC binder, geprüfte Sicherheit) until single colony growth was seen. The plate was then sealed with parafilm and stored at 4 °C until future use.

Both pJExpress401 and pET22b(+) plasmids was isolated by plasmid preparation using a Monarch Plasmid Miniprep kit (NEB) and eluted in 30-40 µL of nuclease-free H_2O. Plasmid quantity was determined by nano-spectroscopy (ND-1000 Spectrophotometer, Labtech international). All plasmid constructs were extracted by this method and stored at -20 °C for future use.

2.9 Glycerol stocks of TRX_4RepCT

Appropriately selective LB agar plates were streaked with previously transformed *E. coli* (DL41, BL21, XL1b or Neb5α) and incubated at 37 °C overnight in a static plate incubator. An overnight culture containing 5 mL LB and antibiotic of choice was prepared under sterile conditions with a single colony of expression (DL41 and BL21) or storage (XL1b and Neb5α) strain *E. coli* and stored in 25% glycerol at -80 °C (MDF-DU700VH-PE Ultra-low temperature freezer, Panasonic).

2.10 Recombinant expression of TRX_4RepCT in LB media

Overnight cultures were grown as described and used to inoculate a sterile 1L solution of LB at 2% concentration. Prepared with dH_2O, the LB solution sterilised by autoclave (Ensign floor autoclave, Rodwell) at 120 °C for 20 min prior to inoculation.

1L broth was inoculated by an overnight culture supplemented with antibiotic under sterile conditions before being incubated at 37 °C until the optical density (OD600), analysed by spectrophotometry (UV1101, Biotech Photometer, WPA), reached log phase (0.7 – 1). Protein expression was induced by addition of IPTG to 1 mM and incubated with shaking at 180 rpm for 15 hrs at 20 °C. Once expressed, the cell suspension was centrifuged at 4,500 x *g* and supernatant

discarded. The pellet was re-suspended in 15 mL/L binding buffer ('Buffer A', 20 mM Tris, 300 mM NaCl, 15 mM imidazole, pH 7.5) and stored at -80 °C until further lysis and purification.

Cell suspensions were lysed by sonication (MSE Soniprep 150) at 15 µm amplitude for 30 second bursts, followed by 30 second rest intervals for a total of 10 minutes at 4 °C. Bacterial lysate was then centrifuged at 35000 x *g* for 30 min at 4 °C. The soluble fraction was collected and loaded onto a pre-equilibrated Ni^{2+} affinity column (Hi-Trap Chelating HP, GE) by peristaltic pump (Econo pump, BioRad) at room temperature at a speed of 3 mL/min. Once loaded, the affinity column was transferred to an ÄKTApure or ÄKTAstart for purification using Buffer A and Elution buffer ('Buffer B', 20 mM Tris, 300 mM NaCl, 700 mM imidazole, pH 7.5). The presence of protein was determined by UV absorption at 280 nm. During preliminary purifications all wash and elution steps were collected in 4 mL fractions. This is was altered to 10 mL and 5 mL fractions for the washes and elution, respectively. After preliminary purifications, the UV absorbance trace was used to identify fractions of high protein content and further analysed by 15% (w/v) SDS-PAGE. Purified 4RepCT was transferred to dialysis membrane (6 – 8 kDa MWCO, Molecularporous membrane tubing, Standar RC Tubing, Spectra/Por 1) and dialysed in 20 mM Tris pH 8.0 overnight at 4 °C. If required 4RepCT was purified further by gel filtration in the same buffer (Superdex S200-pg75, GE).

After dialysis, the concentration of the protein solution was determined by nanodrop spectroscopy (ND-1000 Spectrophotometer, Labtech international) before and after transferral to spin columns (10000 kDa MWCO, VivaSpin 20, Ultrafiltration products, Sartorius) for spin concentration.

In the 419 amino acid primary sequence, TRX_4RepCT contained only 12 tryptophan and tyrosine residues (protein parameters from http://web.expasy.org/protparam). The low number of aromatic residues subsequently reduced the protein's absorbance, underestimating the recorded protein concentration. As a result, the absorption readings were

adjusted with the protein's extinction coefficient of 26025 $M^{-1}cm^{-1}$ to ensure an accurate concentration was recorded. The effect of this calculation can be seen with the worked example (A = 0.5 and a volume of 20 ml):

$$A = \varepsilon c l$$

$$\frac{A}{\varepsilon l} = c$$

$$\left(\frac{A}{\varepsilon l} \times c\right) \times Mr = m$$

$$\left(\frac{0.5}{26025} \times \frac{20}{1000}\right) \times 39939.96 = 15.365\, mg$$

$$= \mathbf{0.77\ mg/ml}$$

$$0.77\, mg/ml > 0.5\, mg/ml\ as\ suggested\ by\ initial\ A$$

Samples were spun at 5000 x *g* at 4 °C until a final volume of 5 mL (approx.) was obtained. The concentrated protein was again assessed by nanodrop spectroscopy before being transferred to 1 mL Eppendorf tubes and flash frozen in liquid nitrogen and stored at -80 °C until future use.

2.11 Minimal media expression of TRX_4RepCT

Overnight colonies of auxotrophic DL41 *E. coli* were prepared and incubated as described above. 2L Erlenmeyer flasks were autoclaved containing 767 mL dH_2O before 5X M9 mineral media was added to make a 1X final concentration (50 mM $Na_2HPO_4.H_2O$, 22 mM KH_2PO_4, 8.5 mM NaCl, 9 mM NH_4Cl) in addition to 50 mg/mL kanamycin and trace elements as shown in **Table 2**. 100 mg methionine (dissolved in 5 mL 1X M9 salt solution) was added to allow methionine auxotrophic cell growth. Cells were incubated at 37 °C and agitated at 180 rpm until OD = 1.0 and protein expression was induced with IPTG to 1 mM and incubated at 20 °C with agitation at 180 rpm for 15 hrs. A further 100 mg/L methionine (dissolved as above) was also added to ensure protein expression was possible in minimal nutrient conditions. Unlike nutrient rich expression, no further purification was required after Ni^{2+} IMAC using

the same binding and elution buffers so TRX_4RepCT was dialysed against 20 mM Tris pH 8.0 and assessed by nano-spectrophotometry to give a corrected concentration.

Constituent	Concentration
Glucose	0.4 % (w/v)
$MgSO_4$	1 mM
$CaCl_2$	0.3 mM
Biotin/thiamine	1 mM
EDTA	134 µM
$FeCl_3$	3.1 µM
$ZnCl_2$	6.2 µM
$CuCl_2.H_2O$	0.76 µM
$CoCl_2.H_2O$	0.42 µM
H_3BO_3	1.62 µM
$MnCl_2.4H_2O$	81 nM

Table 2. Additional constituents of M9 media to provide a carbon energy source, nitrogen and minerals required for cell growth.

2.12 Chemical cell lysis for test expressions

At the point of protein expression induction, the OD was recorded. To ensure the same number of cells in all test samples, the cell density was standardised. In an OD sample volume of 1000 µL, the correction factor was calculated by dividing the volume by the optical density. For example, an OD = 2.4 produced a sample volume of 1000 µL / 2.4 = 417 µL final volume. The samples were then centrifuged at 18000 x *g* for 1 min, supernatant removed and stored at -20 °C overnight. For corrected volumes less than 25 µL, NaCl was added to a final concentration of 0.72% (w/v) at make removal of the supernatant possible.

Analysis of soluble and insoluble fraction of induced culture
Samples were thawed and resuspended in 200 µL CelLytic solution (Sigma Aldrich), 1 µL lysozyme (50 mg/mL, Sigma Aldrich), 0.5 µL Benzonase (250 units/µL, Sigma Aldrich), 3 µL 1M $MgCl_2$. Once resuspended, the samples were centrifuged at 18000 x *g* for 10 minutes at room temperature. The supernatant was then retained as the soluble fraction while the insoluble pellet was resuspended in 20 mM Tris pH 8.0. Both soluble and insoluble fractions were prepared with 6X reducing

loading dye to give a final volume of 300 µL. The samples were then prepared as described in **Methods 2.13**.

Total cell analysis for un-induced cultures
Samples were thawed and resuspended as described previously. Once resuspended, 6X reducing loading buffer was added to a final volume of 300 µL and treated as described in **Methods 2.13**.

2.13 SDS-PAGE analysis

SDS-PAGE resolving gels (pH 8.8) at 12% (w/v) SDS and 15% (w/v) SDS and stacking gels (pH 6.8) at 5% (w/v) SDS were prepared with 30% (w/v) bisacrylamide (37.5:1 acrylamide:bisacrylamide, Alfa Aesar), 1.5 M Tris, 10% (w/v) SDS and polymerised by 10% (w/v) ammonium persulfate and TEMED in a mini-PROTEAN Tetra cell gel kit (BioRad). When required, 1L running buffer (25 mM Tris-HCl, 200 mM glycine, 0.1% (w/v) SDS) was prepared and poured into SDS-PAGE tanks (BioRad). Protein samples were combined with 4X or 6X SDS loading buffer to obtain 1X concentration (100 mM dithiothreitol, 50 mM Tris-HCl, 2% (w/v) SDS, 10% glycerol, 0.1% (w/v) bromophenol blue) and denatured at 90 °C in a variable heat block (DB.2A Dri-Block, Techne). Molecular weight markers (MWM) were loaded to visualise approximate protein sizes of 10 kDa, 15 kDa, 25 kDa, 35 kDa, 55 kDa, 70 kDa, 100 kDa, 130 kDa and 250 kDa (Precision Plus Protein All Blue standards, BIORAD and PageRuler™ Plus Prestained Protein Ladder, Thermofisher) before the gel was electrophoresed using a Power Pac 200 (BIORAD) at 180 V for 10 minutes followed by 200 V for 45 minutes to allow full protein migration.

2.14 Protein stain and de-stain buffers

Once the dye front had migrated the full length of the gel, the gel was washed three times with H_2O to remove excess SDS before being stained with protein stain (GelCode Blue Safe Protein Stain, Thermo Scientific) for 5 min. Staining and washes were sped up by microwaving (800W NN-E28KBM, Panasonic) at 200 W for 150 seconds before being de-stained in H_2O overnight at room temperature. Gels were imaged by a UV transilluminator.

2.15 4RepCT mutagenesis

Site-directed mutagenesis of pJExpress401 was carried out using Q5 mutagenesis kit (New England Biolabs) as per protocol instructions. Polymerase chain reaction was carried out for each plasmid construct at annealing temperatures (T_a) suggested by NEB base changer (https://nebasechanger.neb.com/ [194]). Successful amplification of the PCR products was determined by 0.75% (w/v) agarose gel electrophoresis (10 cm x 10 cm x 1 cm) using a 2-log nucleotide ladder (NEB). Ethidium bromide was added to the gel at a final concentration of 125 ng/mL to allow visualisation of DNA products. Electrophoresis was run for 30 min at 100 V. All successful PCR constructs were cleaned by KLD reaction as per the kit instructions before electro-transformation was carried out on electrocompetent *E. coli* as described above.

2.15.1 Mutagenic primer design

Forward (5' CGCTCACAATTCCACAACG 3') and reverse (5' CTTTCGCCCGGGCTAATTA 3') primers were designed to read the T5 plasmid constructs while T7 forward (5' TAATACGACTCACTATAGGG 3') and reverse (5' GCTAGTTATTGCTCAGCGG 3') primers were supplied by the Source Bioscience sequencing company. Forward and reverse mutagenic primers were designed for Q5 mutagenesis and predicted by NEB Q5 mutagenesis base changer, as shown in **Table 3**. Apart from the company provided T7 forward and reverse primers, all primers were supplied at 100 µM as 'Pure and Simple' primers by Sigma Aldrich before being diluted to 10 µM with nuclease free water and stored at -20 °C until use.

Mutation name	Direction	Sequence (5' – 3')	Length (bp)	T_m (°C)	T_a (°C)
N156P	Forward	CGGTTCTGGTCCCTCGGGTATCC	23	62	63
N156P	Reverse	GATCCACGCGGAACAAGC	18	66	63
320P_S321R	Forward	GAACAGCGTTCCGCGCCGTCTGTCCAGCCCG	31	71	72
320P_S321R	Reverse	GCAACGGTGCTCGCCGCA	18	75	72
A336P_S338del	Forward	GTCAGCCTGGTGAGCAATGGC	21	68	69
A336P_S338del	Reverse	AGGCGAGCTAACGCGGCTCAC	21	69	69
S338P_339L	Forward	CTCGGCTGTCCCCCTGAGCCTGGTGAGCAATGGCC	35	68	69
S338P_339L	Reverse	CTAACGCGGCTCACGGCG	18	72	69
G344P	Forward	GGTGAGCAATCCCCAGGTCAATATGGCTG	29	67	68
G344P	Reverse	AGACTGCTGACAGCCGAG	18	62	68
S394P	Forward	CAGCTCTAGCCCCGTTGGTTACATTAAC	28	61	62
S394P	Reverse	ACAATCTGCACCAACGCC	18	66	62

Table 3. Mutagenic primers were designed using NEBase Changer for Q5 mutagenesis. Ta's were adjusted to give optimal PCR amplification.

2.16 Degradation of TRX_4RepCT

2.16.1 Casting TRX_4RepCT films

TRX_4RepCT stocks were concentrated to 5 mg/mL by dialysis (6 – 8 kDa MWCO, Molecularporous membrane tubing, Standar RC Tubing, Spectra/Por 1) against 20% (w/v) PEG20000 at 4 °C and confirmed by spectrophotometry at 280 nm. Meanwhile, empty 1.5 mL microfuge tubes were labelled and weighed with a high precision balance. 0.5 mL films were cast onto the side of 1.5 mL microfuge tubes and left to dry by $CaCl_2$ desiccation. A control tube filled with a higher volume of water (1 mL) was used to ensure full time had passed to allow complete evaporation. After the films had dried, the tubes were reweighed to calculate the mass of the resulting film (n=5).

2.16.2 Fibre formation

Fibre formation was induced by the cleavage of the thioredoxin solubility tag by thrombin protease cleavage in the presence of KPO_4 at 0.5 µL/mg protein, releasing the 15 kDa thioredoxin solubilisation tag, visualised by SDS-PAGE (see **Section 5.3.6.1, Figure 49**). During cleavage, the fibres were agitated at 95 rpm, 37 °C for 4 hr to allow insoluble fibres to form from solution spontaneously.

2.16.3 Soluble TRX_4RepCT and mutants

TRX_4RepCT was thawed and analysed by gradient SDS-PAGE between 5% and 15% (w/v) SDS. After the presence of 4RepCT was confirmed, each aliquot was analysed by nanospectroscopy to determine soluble protein concentration. Protein concentration was diluted to 1.0 mg/mL with 20 mM Tris pH 8.0. To ensure an assay volume of 500 µl different volumes of protein were added to protease solutions as shown in **Table 4.** To assess the effect of Tris on TRX_4RepCT degradation, 0.6 mL protein was dialysed against Milli-Q water over night at 4 °C. $CaCl_2$ was added to both MMP assay solutions to a final concentration of 2 µM to ensure MMP activity.

Protein samples were incubated at 37 °C and agitated at 180 rpm for 24 hr. At designated time points (0, 10, 30, 60, 120, 240, 1440 minutes), 20 µL samples were taken and combined with SDS-PAGE

loading dye to a final concentration of 1X and heated to 90 °C for 5 min to disrupt enzymatic activity before being stored at 4 °C until analysis by 15% (w/v) SDS-PAGE.

In subsequent protocols, TRX_4RepCT and its mutants were incubated at 25 °C and 37 °C without agitation to prevent the proteins from becoming insoluble during incubation.

Protease	Protease volume (µL)	Final protease concentration	4RepCT volume (µL)	Additions
MMP2	10	11.3 µM	489	2 µM $CaCl_2$
MMP9	10	5.84 µM	489	2 µM $CaCl_2$
ELNE	10	34 nM	490	-
α-chymotrypsin	25	120 mM	475	-
Tris	-	-	500	-
Water	-	-	500	

Table 4. Assay volumes and final protease concentrations during 4RepCT and N156P degradation.

2.16.4 Degrading TRX_4RepCT films

One aliquot of enzyme solution was transferred to each film and incubated at 37 °C for 24 hrs with agitation at 180 rpm. Every 24 hrs the enzyme solution was refreshed by sedimenting the film and removing the resulting supernatant before transferring a new 40 µL aliquot to the sample. This process was repeated five times for a total of 120 hrs total incubation time. After each 24 hr incubation period, a sacrificial sample was taken and sedimented by centrifugation at 18000 x *g* for 30 seconds. The supernatant was then denatured at 90 °C before being flash frozen in liquid nitrogen and stored at -20 °C until analysis. A dH_2O wash of 100 µL was applied to the films to remove any residual enzyme solution before being incubated at 37 °C with agitation. This wash was refreshed every 12 hrs with fresh 100 µL dH_2O. After a total wash incubation of 36 hrs, the micro Eppendorf lids were pierced and transferred to a calcium chloride desiccator to dry. The samples were left for a minimum of 3 days before being weighed.

Films were then subjected to 1 mL of protease solution and incubated at 37 °C for 72 hr, after which they were centrifuged at 18000 x *g* for 5 min. The supernatants were removed, and flash frozen in

liquid nitrogen and the films washed in Milli-Q water. The wash was incubated for a further 72 hrs at 37 °C before the centrifugation and supernatant removal was repeated. The degraded film was then dried by desiccation as before to ensure all moisture was removed before final weighing. Both protease and wash supernatants were analysed by 12% (w/v) SDS-PAGE to show any degradation that may have taken place.

2.16.5 4RepCT and mutant fibre degradation

Both 4RepCT and the mutant N156P fibres were formed in reaction tubes as described previously. The remaining solution was removed by pipette and 500 µL 20mM Tris pH 8.0 was added as an assay buffer in the presence of 2 µM $CaCl_2$. Protease was then added to a previously stated final assay concentration and incubated at 37 °C for up to 1 week. After time points of 30, 60, 120, 240, 1440, 10080 minutes, EDTA was added to the fibres at a final concentration of 40 mM to inhibit further protease activity. Samples of 50 µL were taken for SDS-PAGE analysis and the fibres were processed for imaging.

2.17 Densitometry of soluble degradation products

To estimate the degradation rate of TRX_4RepCT and its mutants, densitometry was used to analyse the thickness and size of SDS-PAGE protein bands. The protein concentration of the bands was also estimated using a bovine serum albumin (BSA) standard curve.

2.17.1 BSA standard curve and straight-line equation

BSA protein concentrations of 0.1 mg/mL, 0.2 mg/mL, 0.5 mg/mL, 1 mg/mL and 2 mg/mL was prepared by serial dilution from a 10 mg/mL stock solution (NEB) and run on 15% (w/v) SDS-PAGE. All concentrations were run in triplicate. The gels were then imaged with the gel imager using identical zoom, aperture and focus settings. The resulting images were cropped in ImageJ before the brightness and contrast values were adjusted with the ‘auto’ function.

Each individual protein lane was then selected to generate histogram of pixel density for each lane. The resulting peaks were manually integrated from the same point of each peak to ensure accurate

peak area readings. The average peak area for each concentration was recorded and plotted against protein concentration in GraphPad Prism 8 (GraphPad Prism version 8.0.0 for Windows, GraphPad Software, San Diego, California USA, www.graphpad.com). The linear regression of the standard curve was also calculated to produce a straight-line equation, enabling protein concentration to be approximated from gel band size.

2.17.2 TRX_4RepCT and mutant degradation kinetics

SDS-PAGE gels produced to analyse soluble TRX_4RepCT and mutant degradation were also analysed by protein band densitometry. To adjust brightness and contrast to the same level for each gel, the automatic adjust function on ImageJ was applied to each image before they were cropped and analysed. The minimum and maximum values given to each gel can be seen in **Table 5** to ensure reproducibility if required.

As with the standard curve, histograms of each lane were generated and peaks that corresponded to bands of interest were manually integrated to give the peak area under each curve. To ensure accuracy peaks were integrated at the same time and from the same points, reducing subjective bias. When the peak areas were plotted over time for a specific peak, the resulting graphs confirmed the formation and degradation of degradation products.

TRX_4RepCT			TRX_N156P		
Gel name	**Minimum**	**Maximum**	**Gel name**	**Minimum**	**Maximum**
MMP2 37°C	15	188	MMP2 37 °C	1	128
MMP2 25°C	10	151	MMP2 25 °C	2	135
MMP9 37 °C	2	154	MMP9 37 °C	1	106
MMP9 25 °C	2	151	MMP9 25 °C	1	104
ELNE 37 °C	3	147	ELNE 37 °C	9	169
ELNE 25 °C	2	149	ELNE 25 °C	16	154
Chymotrypsin 37 °C	5	147	Chymotrypsin 37 °C	2	159
Chymotrypsin 25 °C	4	160	Chymotrypsin 25 °C	2	168
Tris 37 °C	5	169	Tris 37 °C	7	146
Tris 25 °C	7	162	Tris 25 °C	7	120
Water 37 °C	4	141	Water 37 °C	10	130
Water 25 °C	3	154	Water 25 °C	11	151

Table 5. Brightness and contrast adjustments made using ImageJ to reduce background pixel density. Images were automatically corrected, and the values recorded for future replication.

2.18 4RepCT and N156P mutant fibre imaging

Once enzyme activity had been inhibited, fibres were transferred to gelatinised glass slides by careful inversion. Once inverted, the reaction tube was removed, and the remaining assay buffer was removed by pipette aspiration. The resulting fibre was then allowed to dry on a hot plate (IJES hotplate) before they were imaged using a Zeiss Axioplan light microscope as before at 3200K light intensity. Fibres were imaged at low (10x) and high (40x) magnification using bright field, dark field and birefringence microscopy.

At the lower magnification, bright field was used to identify locations on the fibre that showed 'flowing fibre', 'crossing fibres', and other areas of interest. At each image location, images were captured with bright field, dark field and birefringence lens filters. At high magnification, only bright field and polarised light microscopy were used at the previously identified points of interest. Exposure time and magnification for each microscopy technique was as shown in **Table 6**. As with the natural fibre microscopy, the generated images were captured and processed using the ImageJ to correct image white balance and to produce appropriate scale bars.

Filter	Magnification	Exposure (ms)
Bright field	10x	20
Bright field	40x	20
Dark field	10x	20
Birefringence	10x	300
Birefringence	40x	700

Table 6. Exposure times for different microscopy techniques were adjusted to allow sufficient light required for image capture.

3. Understanding the link between natural silk sequence and observed enzymatic degradation

3.1 Introduction

The investigation into natural polymer biodegradation has been of interest for many years. In this chapter, the degradation properties of natural spider silk have been investigated from both a bioinformatics and *in vitro* approach and compared to the recombinant spidroin 4RepCT.

3.1.1 Degradation of natural silk fibres

While natural silk aging has been investigated over a 4 year period by Agnarsson *et al.* [51], many studies have focussed on recombinant silk as it becomes increasingly popular for biomedical applications [195,196].

The degradation of spider silk can be compared to the similar silk of silkworms, a material whose abundance has provided material for multiple studies [197,198]. Silkworm silk degradation was investigated as a 3-dimensional scaffold by Zhang *et al.* demonstrating tuneable degradation rates by chemically influencing the pore size within the silk scaffold. During this experiment the scaffold degradation rate, measured by % weight loss over time in the presence of Protease VIX, was 5-fold higher with scaffolds produced with NaOH compared to LiBr or $CaCl_2$ [198]. In addition to this, *in vivo* studies by Liu *et al.* observed that both silk fibroin and sericin implanted into rats began to undergo degradation after 7 days once the silk had been degummed to reduce the host immune response. As some undegraded silk persisted after 146 days however, it is clear that silkworm fibres require long periods of time before significant degradation is seen *in vivo* [197,198]. As with spider silk, the morphology greatly influences the rate of degradation, with porous 3-dimensional scaffolds degrading at a faster rate than spun fibres .

With recombinant spider silk, it has been reported that the smaller the monomeric spidroin, the faster the resulting degradation [195]. Dinjaski *et al*. reported that less folding occurred within smaller fibres and allowed greater access to proteases. In addition to size, degradation rates can also be influenced by treating fibres with antioxidants to

suppress thermo-oxidation of fibres, reducing the formation of free radical species from oxidative degradation [196]. While attempts to tune synthetic fibre degradation by altering the spidroin size or fibre functionalisation have been promising, no investigations have approached it by changing the protein amino acid sequence.

3.1.2 Introduction to different spider genera

The spiders of interest in this chapter belonged to three different families, namely Araneidae (orb weavers), Pisauridae (nursery-web spiders) and Pholcidae (tangle web spiders), chosen to reflect a variety of silk types, web styles and bioavailability. By comparing the spidroin sequences and corresponding proteolytic degradation, predictions for future silk biomaterials may be possible.

Araneidae

The family Araneidae contain the orb-weaving spiders alongside the Tetragnathidae ('long-jawed orb weavers') and Uloboridae ('hackled orb weavers'), of which Araneidae is the largest [1]. With a total of 3122 species and 172 genera, this study focused of the genera of *Araneus, Argiope, Cyrtophora* and *Nephila* with physical silks from *C. citricola* and *N. madagascarensis* and protein sequences of *A. diadematus, A. argentata, A. bruennichi, A. trifasciata, C. moluccensis, N. clavipes, N. pilipes and N. senegalensis* being investigated. As many orb-weavers consume the old web in the process of rebuilding [52,53], the spidroins may contain proteolytic target sequences within the protein sequence that could be used to enable controlled enzymatic degradation.

Pisauridae

The common name for the Pisauridae family is 'nursery-web spiders' as female *Pisaura mirabilis* carry their egg sacs in their jaws, rather than with their spinnerets [16]. The genera of interest in this study are that of *Dolomedes* (fishing/raft spider), *Euprosthenops* (Australian nursery-web spider) and *Pisaura* to reflect bioavailability and online sequence information.

Pholcidae

Known colloquially as 'daddy long-legs' and 'cellar spiders', *Pholcus phalangioides* belongs to the family Pholcidae. Unlike orb-weavers, the

capture web of Pholcidae is that of a tangle web, utilising a complex network of silk strands to snap, break and ensnare its prey [199] making it an interesting comparison to orb-web silk. An abundance of Pholcidae webs also allowed easy collection for *in vitro* silk degradation.

3.1.3 Evolution of the ability of consuming silk

The presence of proteolytic target sequences within spidroin sequences may be explained by the arachnid phylogeny. Illustrated in **Figure 10** and **Figure 11**, the phylogenetic tree of the order Araneae [200] (**Figure 10**) and families of Araneidae [53] and Pisauridae [201] (**Figure 11**) have been highlighted to identify the relationship between genera within this study.

Using these diagrams, it is possible to better understand and predict phenotypic behaviours. For example, many spiders consume their own silk during repair or during times of famine [52,171,202,203]. As this behaviour is not always conserved within a genera, it suggests that it may have appeared many times during spider evolution but had not been retained in some species. These phylogenetic relationships can then be used to identify new silks from species that may be susceptible to greater proteolytic degradation for biomedical applications.

For spiders to consume their silk, the protein must be susceptible to digestive enzymatic degradation [204,205]. As digestive proteases such as protease K have been shown to degrade silk rapidly [72], it posed the question whether proteases with higher substrate specificity could also degrade silk, specifically those found in wound sites. For this to occur, the silk sequence would need to contain the enzymatic target sequences required for proteolytic cleavage [172,173,206]. If present, the proteinaceous could be expected to undergo proteolytic degradation if the target sequences are accessible by the relevant protease [72,172,173].

The ability to eat one's silk has been observed across a number of different species but rarely as direct neighbouring species [207–209]. While at some time an ancestor of these species must have consumed its silk for the ability to be retained, it appears that many silk-consuming species have since lost the ability or have not survived to present day [210]. It is

therefore possible that those observed to consume their silk today may at some point lose this behaviour. The presence of target sequences in the conserved regions of spidroins also suggests that they were not detrimental to the function of the silk fibre, to be lost by evolution.

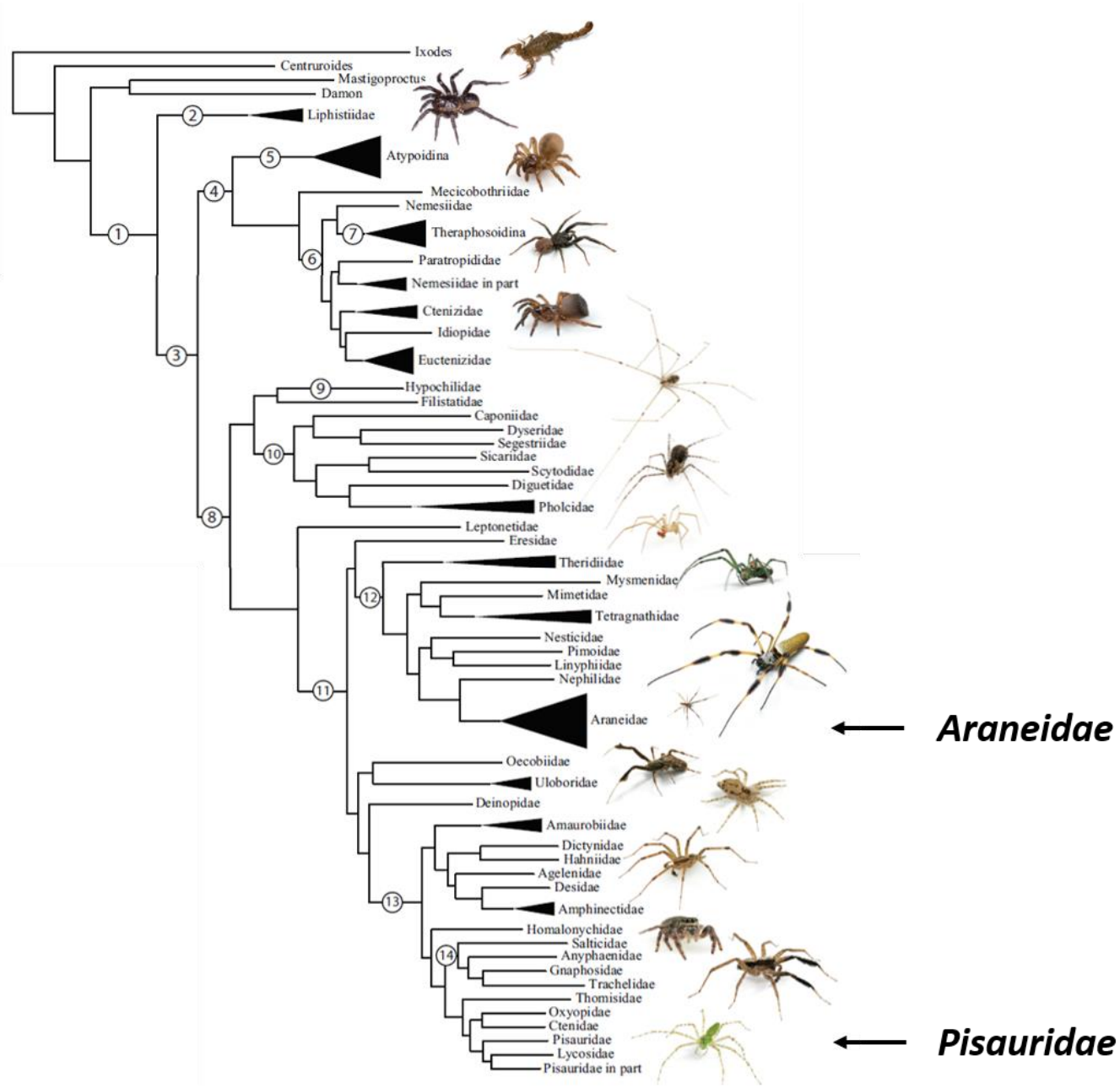

Figure 10. An overview of the phylogenetic tree of spiders with emphasis on the Araneidae and Pisauridae families. Figure adapted from 'Spider phylogenomics: untangling the Spider Tree of life', Garrison 2016.

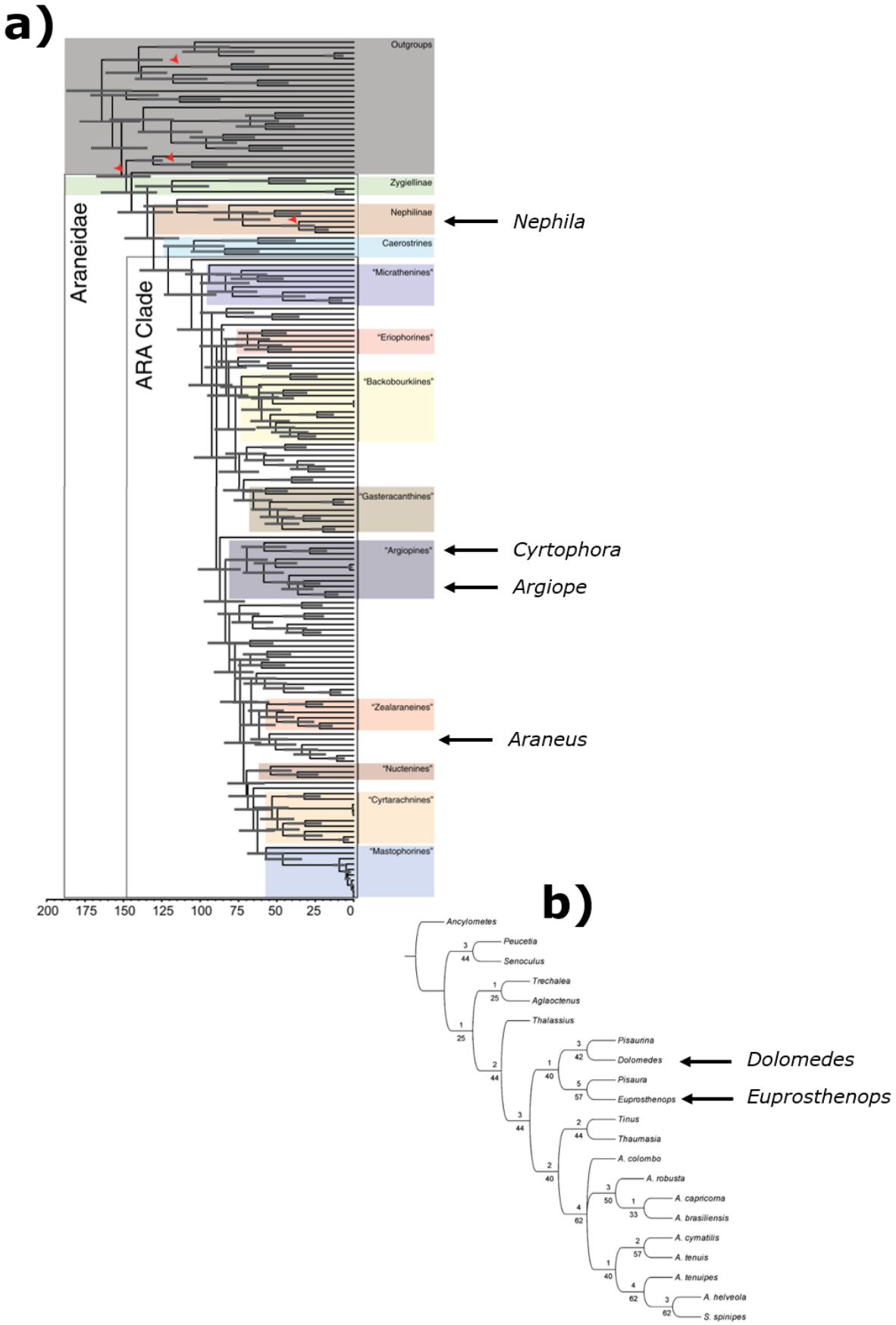

Figure 11. The genetic family trees of Araneidae (**a**) and Pisauridae (**b**). The genera *Araneus, Argiope, Cyrtophora, Dolomedes, Euprosthenops* and *Nephila* have been highlighted as relevant to this study. Figure adapted from 'Phylogeny of the orb-weaving spider family Araneidae (Araneae: Araneoidea)', Scharff 2019 and 'A phylogenetic analysis of the nursery-web spider family Pisauridae, with emphasis on the genera *Architis* and *Staberius* (Araneae: Lycosoidea)', Santos 2007.

3.2 Aims of the chapter

The aim of this chapter was to establish a link between MaSp1 termini sequence profiles and observed degradation of natural silk fibres. By compiling target sequences for MMP2 and MMP9 from the literature and online prediction software, profiles of each spidroin termini were produced and compared to the predicted *in vitro* degradation.

By establishing a reliable method of *in silico* analysis, this method could be applied to recombinant silk sequences and provide information on subsequent mutation locations. Classic *in silico* prediction software presents a limitation in the attempt to highlight locations for future cleavage sites. While these techniques enable present target sequences to be identified, the ability to identify future locations for mutation is essential. In this work, this novel *in silico* approach is trialled on natural spidroin sequences and the recombinant spidroin 4RepCT. Using the profiles generated the degradation behaviour of 4RepCT is significantly influenced with the introduction of identified potential target sequences.

An *in silico* approach can also be used for future spidroin prospecting, identifying spidroin sequences with high protease coverage, presenting them as a potential candidates for future recombinant biomaterials.

3.3 Results

3.3.1 Spidroin sequence alignment

Amino acid sequences of natural MASP1 gathered from Genbank® were aligned against sequences of the same species and termini. From this alignment, a consensus sequence was generated that could be compared between species and used to compare against MMP target sequences to generate enzymatic profiles. These profiles were then compared with *in vitro* degradation of natural silks.

3.3.1.1 Generating consensus sequences for natural MaSp1

Amino termini

When multiple sequences for a single species were collected from Genbank®, an alignment of sequences from a single species was carried out, as shown in **Figure 12**. For the amino terminus, only *E. australis* [37,211–213] **Figure 12a**) and *N. clavipes* [214] **Figure 12b**) were found to contain more than one sequence for MaSp1 N-termini. They were therefore aligned using an online MAFFT algorithm and viewed with JalView with Clustalx-assigned residue colours. Amino acid sequences for the amino termini of *A. diadematus* [214], *A. argentata* [214] and *C. moluccensis* [215] were also gathered, but only single entries were retrieved.

Seen in **Figure 12c**), the alignments were used to generate consensus sequences for each species. These were used to create enzymatic profiles and conservation studies between species.

Carboxyl termini

The same method was used to generate consensus sequences for the carboxyl termini, seen in **Figure 13**. Multiple sequences were available for **Figure 13a**) *A. diadematus* [214,216], **Figure 13b**) *C. moluccensis* [217], **Figure 13c**) *E. australis* [28,212,218,219], **Figure 13d**) *N. clavipes* [26,214,220,221] and **Figure 13e**) *N. pilipes* [217].

Figure 13f) Single sequences were also available for *A. argentata* [214], *A. trifasciata* [222], *A. bruennichi* [223], *D. tenebrosus* [222],

N. madagascarensis [222] and *N. senegalensis* [222] and were included in subsequent studies.

The greatest variation within a species was seen from *A. diadematus* with three unique sequences identified for the C-termini. Variation within species was seen in all sequences except *E. australis* (**c**) where sequences were identical.

Single sequences were retrieved for *A. argentata, A. bruennichi, A. trifasciata, D. tenebrosus, N. madagascarensis* and *N. senegalensis*, seen in **Figure 13f**), so no alignment was conducted.

N terminus

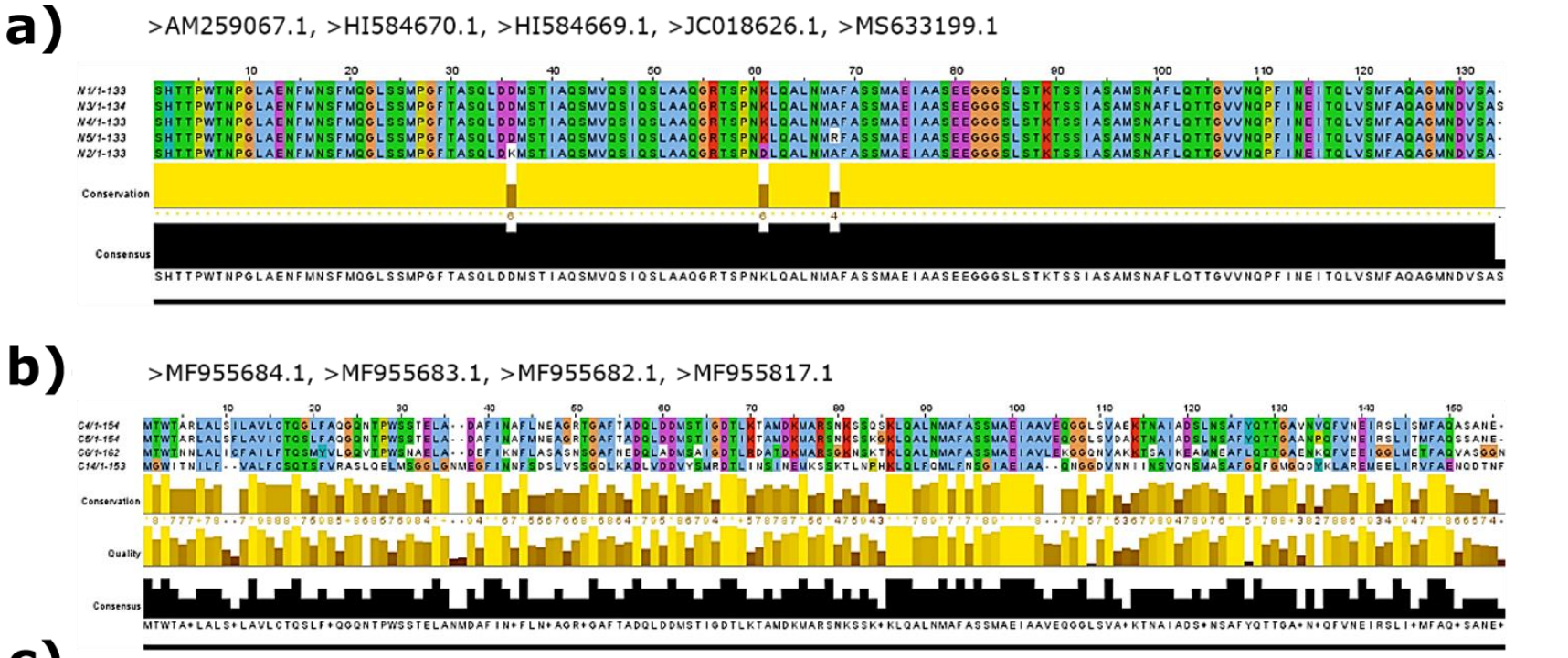

Figure 12. MAFFT alignments of (**a**) *E. australis* [37, 211 – 213] and (**b**) *N. clavipes* [214] MaSp1 amino terminal sequences with the resulting (**c**) N-termini consensus sequences. As single amino terminal sequences for *A. diadematus* [214], *A. argentata* [214] and *C. moluccensis* [215] were gathered, no alignments were possible. All sequences were gathered from Genbank®, aligned and viewed using Jalview. The resulting consensus sequences were seen in (**c**). The sequences were used for subsequent *in silico* analysis and for inter-species conservation studies.

C terminus

a) >MF955762.1, >DL189450.1, >DI166778.1, >DI166498.1, >DL189449.1

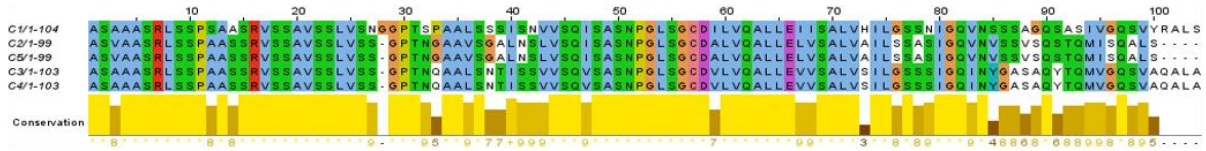

Consensus –
ASVAASRLSSPAASSRVSSAVSSLVSSGPTNGAAVSGALNSLVSQISASNPGLSGCDALVQALLELVSALVAILSSASIGQVNVSSVSQSTQMISQALS

b) >AY666063.1, >AY666061.1, >AY666062.1, >AY666081.1, >AY666080.1, >AY666078.1, >AY666079.1, >AY666060.1

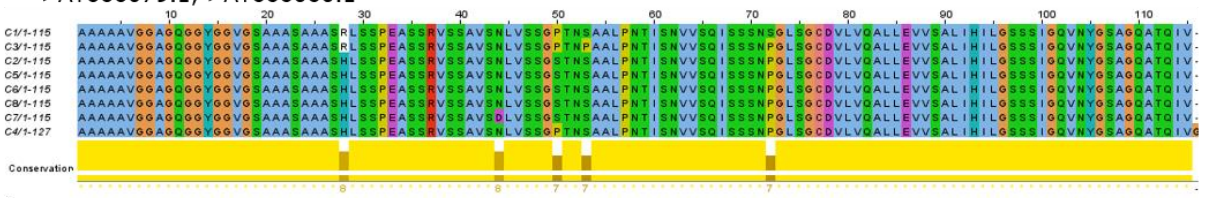

Consensus –
AAAAAVGGAGQGGYGGVGSAAASAAASHLSSPEASSRVSSAVSNLVSSGSTNSAALPNTISNVVSQISSSNPGLSGCDVLVQALLEVVSALIHILGSSSIGQVNYGSAGQATQIV

c) >AJ973155.1, >CS675201.1, >MS926196.1, >HI584670.1

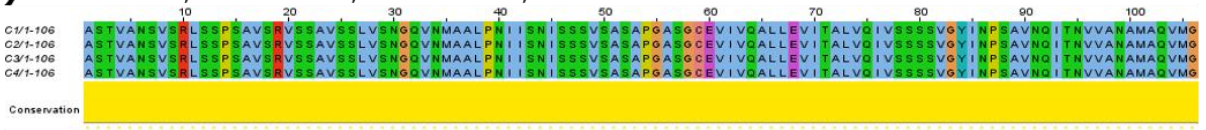

Consensus –
ASTVANSVSRLSSPSAVSRVSSAVSSLVSNGQVNMAALPNIISNISSSVSASAPGASGCEVIVQALLEVITALVQIVSSSSVGYINPSAVNQITNVVANAMAQVMG

d) >MF955766.1, >AY654292.1, >MF955765.1, >AY654291.1, >AY654290.1, >EU617338.1, >AY061814.1, >AY654289.1, >AY654288.1, >U20329.1

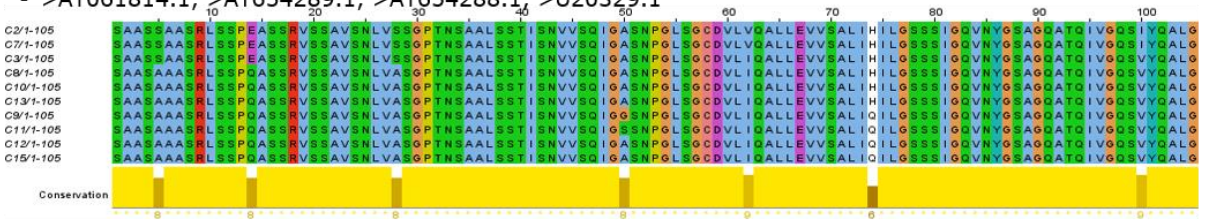

Consensus –
SAASAAARLSSPQASSRVSSAVSNLVASGPTNSAALSSTISNVVSQIGASNPGLSGCDVLIQALLEVVSALIHILGSSSIGQVNYGSAGQATQIVGQSVYQALG

e) >AY666074.1, >AY666073.1, >AY666072.1, >AY666054.1, >AY666051.1, >AY666050.1, >AY666048.1, >AY666056.1, >AY666053.1, >AY666052.1, >AY666049.1, >AY666055.1

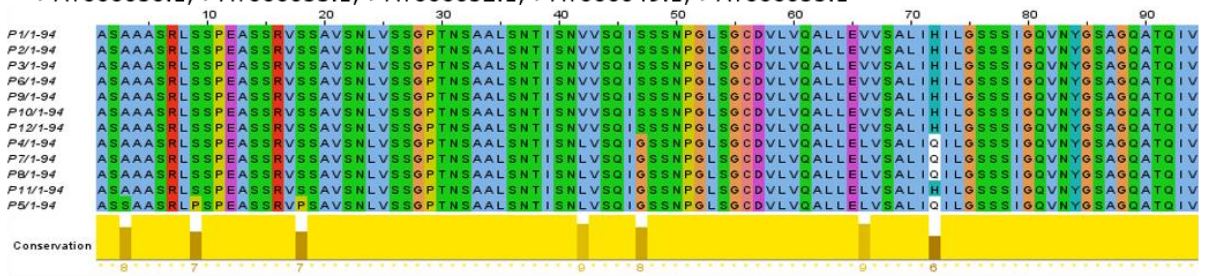

Consensus –
ASAAASRLSSPEASSRVSSAVSNLVSSGPTNSAALSNTISNVVSQISSSNPGLSGCDVLVQALLEVVSALIHILGSSSIGQVNYGSAGQATQIV

f) ***A. argentata:*** (>MF955761.1)
ASVAAASAAASRLSSPGAASRVSSAVTSLVSSGGPTNGAALSNTISNVVSQISASNPGLSGCDVLVQALLEIVSALVHILGSANIGQVNSNSAGRSASLVGQSVYQALS

A. trifasciata: (>AF350266.1)
ASVATASAAASRLSSPGAASRVSSAVTSLVSSGGPTNSAALSNTISNVVSQISSSNPGLSGCDVLVQALLEIVSALVHILGSANIGQVNSSGVGRSASIVGQSINQAFS

A. bruennichi: (>JX112871.1)
ASAAASRLSSPSAASRVSSAVTSLISGGGPTNPAALSNTFSNVVYQISVSSPGLSGCDVLIQALLELVSALVHILGSAIIGQVNSSAAGESASLVGQSVYQAFS

D. tenebrosus: (>AF350269.1)
AVSSLVSNGQVNVDALPSIISNLSSSISASATTASDCEVLVQVLLEVVSALVQIVCS

N. madagascarensis: (>AF350277.1)
ASAAASRLSSPQASSRVSSAVSNLVASGPTNSAALSSTISNAVSQIGASNPGLSGCDVLIQALLEVVSALIHILGSSSIGQVNYGSAGQATQ

N. senegalensis: (>AF350279.1)
ASAAASRLSSPEASSRVSSAVSNLVSSGPTNSAALSSTISNVVSQIGASNPGLSGCDVLIQALLEVVSALVHILGSSSIGQVNYGSAGQATQ

Figure 13. Multiple sequences were available for (**a**) *A. diadematus* [214, 216], (**b**) *C. moluccensis* [217], (**c**) *E. australis* [28, 212, 218, 219], (**d**) *N. clavipes* [26, 214, 220, 221] and (**e**) *N. pilipes* [217]. All sequences were gathered from Genbank®, aligned and viewed using JalView to generate the consensus sequence shown below each alignment. (**f**) The consensus sequence for the single *A. argentata* [214], *A. trifasciata* [222] *A. bruennichi* [223], *D. tenebrosus* [222], *N. madagascarensis* [222] and *N. senegalensis* [222] entries were also recorded.

3.3.1.2 Conservation of spidroin termini between species

The amino and carboxyl consensus sequences were aligned to identify regions of conservation within them, seen in **Figure 14**.

Figure 14a) The five sequences for the amino terminus contained the species *A. diadematus, A. argentata, C. moluccensis, E. australis* and *N. clavipes*. **Figure 14b**) The C-termini sequences contained amino acid sequences from the above species in addition to *A. bruennichi, A. trifasciata, D. tenebrosus*, *N. madagascarensis*, *N. pilipes* and *N. senegalensis*.

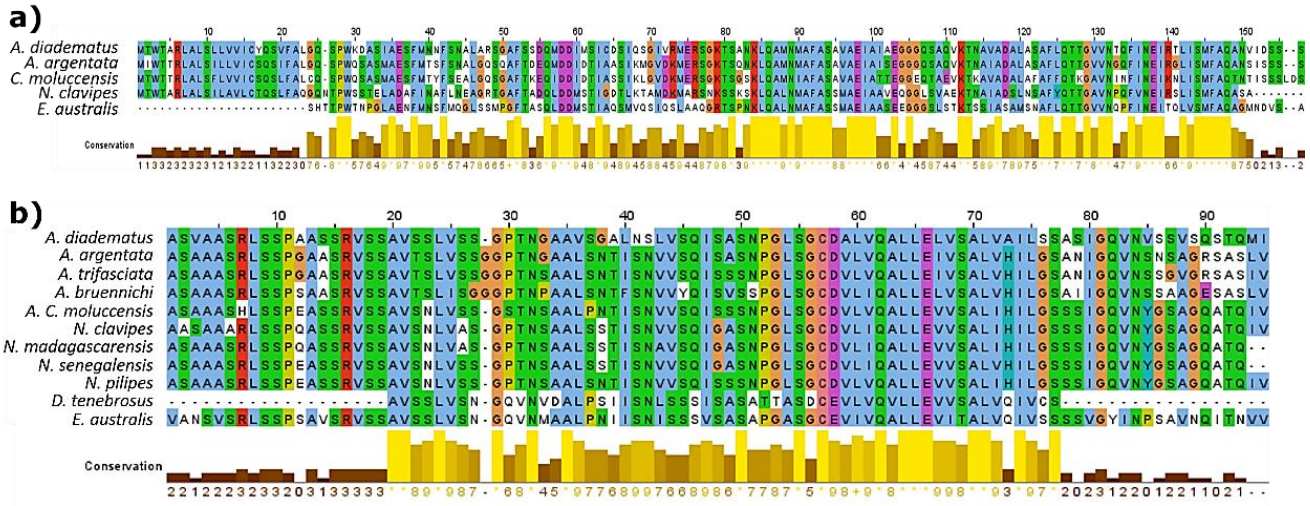

Figure 14. MAFFT alignments of natural MASP spidroin amino termini (**a**) and carboxyl termini (**b**). (**a**) Amino termini alignments included sequences from *A. diadematus, A. argentata, C. moluccensis, E. australis* and *N. clavipes.* (**b**) The carboxyl termini alignments displayed consensus sequences for *A. diadematus, A. argentata, A. bruennichi, A. trifasciata, C. moluccensis, D. tenebrosus, E. australis, N. clavipes, N. madagascarensis, N. pilipes and N. senegalensis.*

3.3.2 MMP profiles

The target sequences for MMP2 and MMP9 were gathered from the literature as summarised in **Tables 7 – 11** [172,173,192] with The position of each amino acid was denoted by 'P#' with residues after the cleavage point described as prime ('). If multiple amino acids appeared for a single position, each permutation was considered in the final profile. However, only sequences that crossed the cleavage point, between P1 and P1' were recorded. The largest variation was displayed in Chen's summary of MMP2 substrates, seen in **Table 9** [192]. The higher scores seen from the MMP2 profiles were attributed to this variation within substrate specificity.

Scissile bond

MMP2

P3	P2	P1	P1’	P2’	P3’	P4’
P	Q	G	I	A	G	Q
	A	A	L	V		A

Table 7. The specific position of amino acids that made up MMP2’s target motifs, as suggested by ‘Active site specificity profiling of the MMP family’ – U Eckhard, 2016

P4	P3	P2	P1	P1’	P2’	P3’
I	P	V	S	L	R	S
V	V	A	G	M	Y	A
	I		A	I	K	G
			E	Y	M	
				F	I	
					V	

Table 8. The specific position of amino acids that made up MMP2’s target motifs, as suggested by ‘Determination of protease cleavage site motifs using mixture-based oriented peptide libraries’ – Benjamin Turk, 2001

P3	P2	P1	P1’	P2’	P3’
P	Y	V	I	W	L
L	M	A	K	T	A
Y	V	W	Y	M	S
S	A	R	A		V
V	G	S	L		T
	S	D			

Table 9. The specific position of amino acids that made up MMP2’s target motifs, as suggested by ‘Substrate recognition by MMPs’ – Emily Chen, 2001

MMP9

P3	P2	P1	P1’	P2’	P3’
P	A	A	L	I	G
	S	G	I	V	A
	R	R		Q	S
				H	
				S/T	
				K/R	

Table 10. The specific position of amino acids that made up MMP9’s target motifs, as suggested From Active sites specificity profiling of the MMP family – U Eckhard, 2006

P4	P3	P2	P1	P1’	P2’	P3’
V	P	L	S	L	R	S
	V	Y		M	T	A
				I	Y	G
				Y	V	
				F	I	

Table 11. The specific position of amino acids that made up MMP9’s target motifs, as suggested by ‘Determination of protease cleavage site motifs using mixture-based oriented peptide libraries’ – Benjamin Turk, 2001

3.3.3 *In silico* analysis of spidroins

3.3.3.1 MMP2

Amino termini
The N-terminal consensus sequences were compared against the target sequences and matching residues that crossed the cleavage point (between P1 and P1') were highlighted to reflect the number of amino acids matched at a particular site, as seen in **Figure 15**. Scores were also assigned to reflect the overall coverage and weighted to prioritise longer matching sequences. For example, the sequence of *A. diadematus* displayed 18 accounts of two residues crossing the cleavage point, 5 of three residues, 7 of four and no five or higher. This gave a score of **79**.

Where identified sequences overlapped, the sequence with highest weighting or length was prioritised in the final score and profile. Amino acids were highlighted to show the highest score attributed to a single residue.

The score of each sequence were summarised in the table below. The highest score (90) was achieved by the 17.6 kDa sequence of *A. argentata* while the lowest (56) was scored by the 13.8 kDa sequence of *E. australis*.

Carboxyl termini
The C-terminal profiles *of A. diadematus, A. argentata, A. bruennichi, A. trifasciata, C. moluccensis* and *D. tenebrosus* are shown in **Figure 16** while the termini profiles of *E. australis, N. clavipes, N. madagascarensis, N. pilipes* and *N. senegalensis* are shown in **Figure 17**. As anticipated, the shorter termini lengths produced lower scores than the N-termini as the probability of encountering specific sequences was reduced. This was more pronounced in the MMP9 profiles as lower variability further limited acceptable amino acids. All profiles were scored by the same method, summarised in the table below. In this case, the highest score (74) was achieved by the 9.4 kDa protein of *A. diadematus*, while the lowest (46) was scored by the 5.7 kDa *D. tenebrosus* protein.

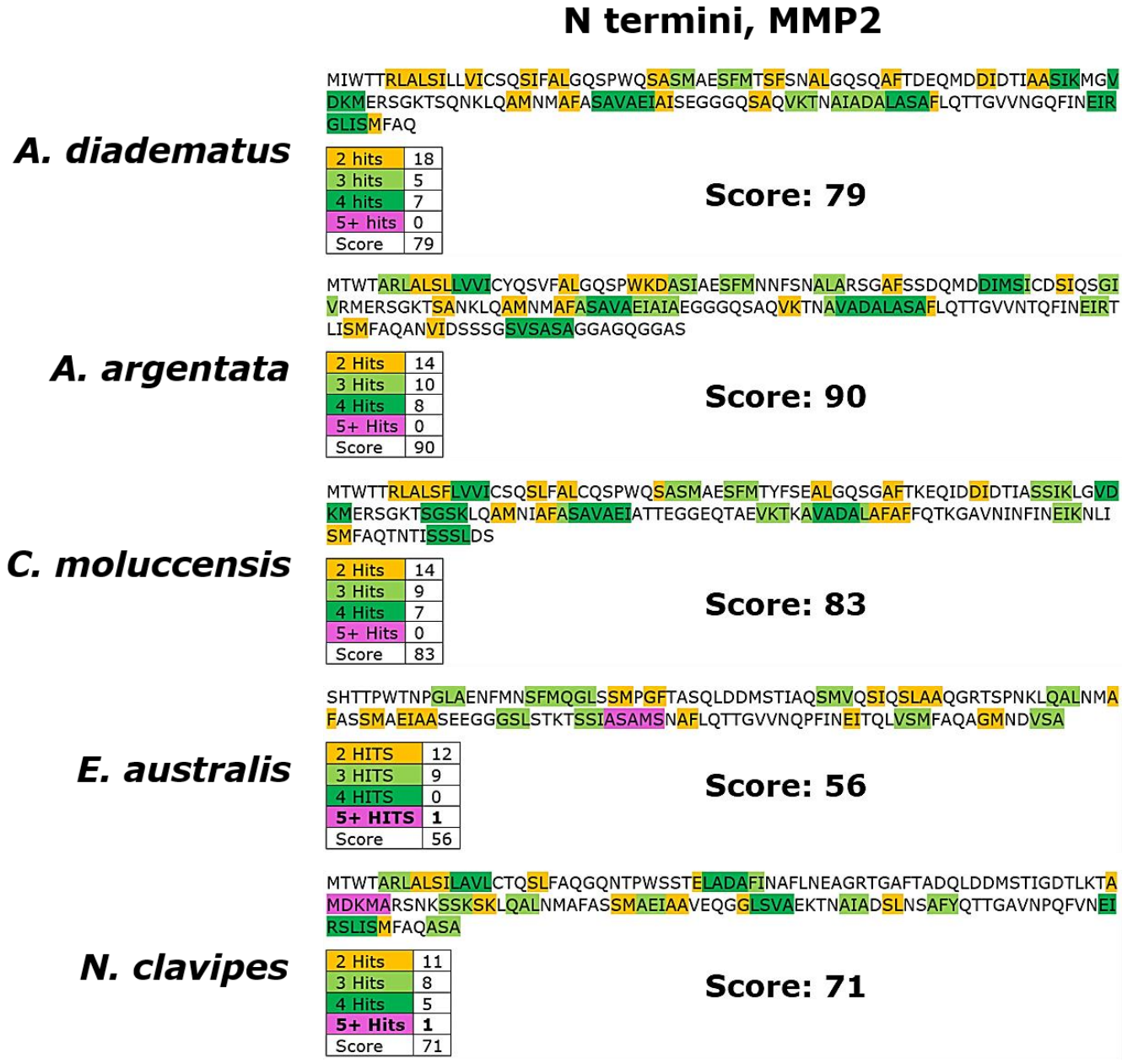

Genus	Species	Spidroin size (kDa)	2 Hits	3 Hits	4 Hits	5+ Hits	Score
Araneus	*diadematus*	17.6	14	10	8	0	**79**
Argiope	*argentata*	15.6	18	5	7	0	**90**
Cyrtophora	*moluccensis*	16.8	14	9	7	0	**83**
Euprosthenops	*australis*	13.8	12	9	0	**1**	**56**
Nephila	*clavipes*	16.0	11	8	5	**1**	**71**

Figure 15. The enzymatic degradation profile of MMP2 of MaSp1 N-termini. The frequency of matching sequence lengths is summarised in the table in addition to the final score for each termini. The scores demonstrate the overall coverage and length of matching sequences by MMP2 with the highest scores attributed to greatest likelihood of cleavage.

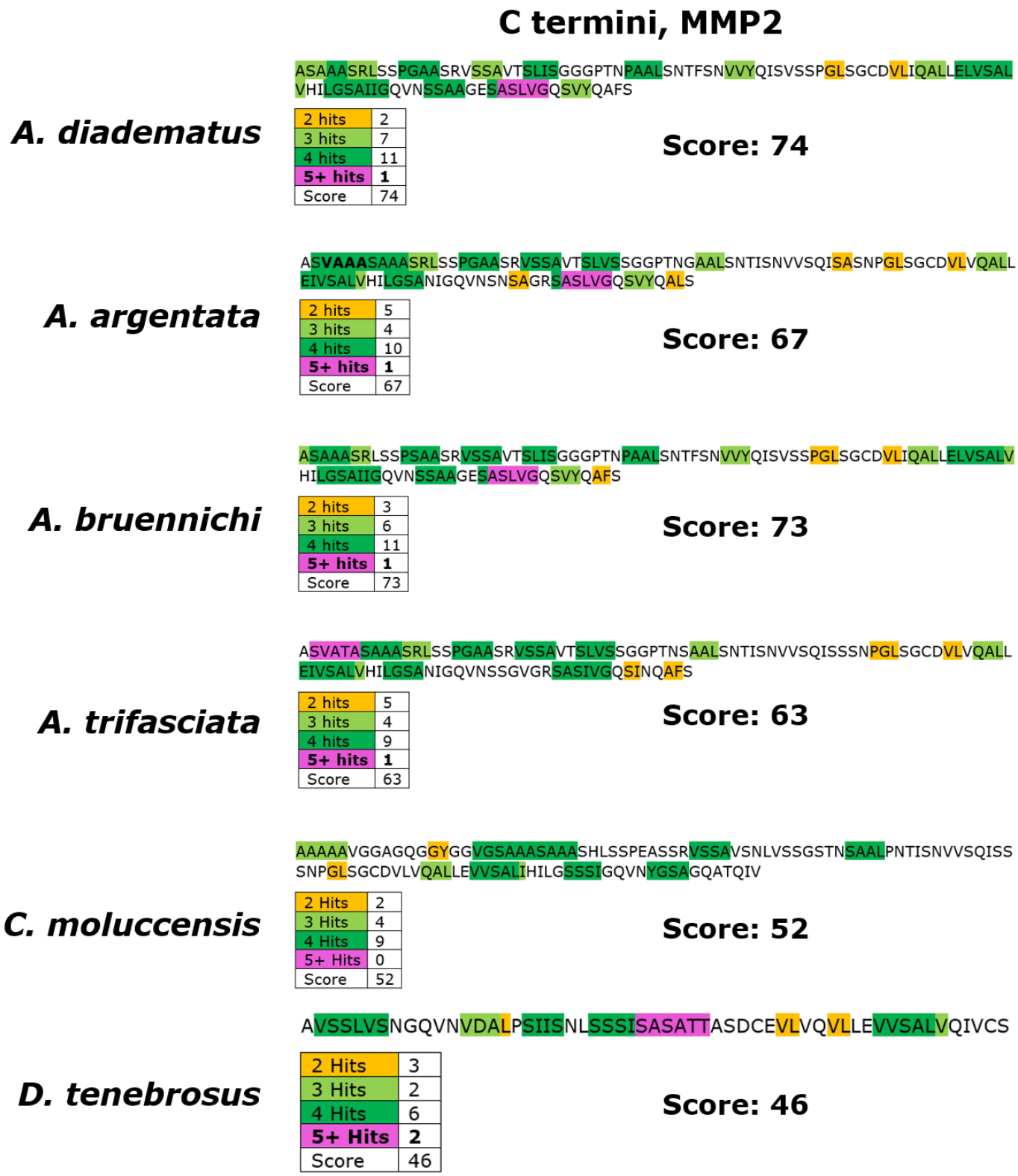

Figure 16. The enzymatic profiles of *A. diadematus*, *A. argentata*, *A. bruennichi*, *A. trifasciata*, *C. moluccensis* and *D. tenebrosus* MaSp1 C-termini when compared to MMP2. The scores are were generated to reflect the coverage of each sequence and the length of the matching sequences.

E. australis

ASTVANSVSRLSSPSAVSRVSSAVSSLVSNGQVNMAALPNIISNISSSVSASAPGASGCEVIVQALLEVIT
ALVQIVSSSSVGYINPSAVNQITNVVANAMAQVL

2 HITS	3
3 HITS	8
4 HITS	7
5+ HITS	0
SCORE	58

Score: 58

N. clavipes

SAASAAASRLSSPQASSRVSSAVSNLVASGPTNSAALSSTISNVVSQIGASNPGLSGCDVLIQALLEVVSA
LIHILGSSSIGQVNYGSAGQATQIVGQSVYQALG

2 Hits	4
3 Hits	6
4 Hits	7
5+ Hits	0
Score	54

Score: 54

N. madagascarensis

ASAAASRLSSPQASSRVSSAVSNLVASGPTNSAALSSTISNAVSQIGASNPGLSGCDVLIQALLEVVSALI
HILGSSSIGQVNYGSAGQATQ

2 Hits	4
3 Hits	6
4 Hits	6
5+ Hits	0
Score	50

Score: 50

N. pilipes

ASAAASRLSSPEASSRVSSAVSNLVSSGPTNSAALSNTISNVVSQISSSNPGLSGCDVLVQALLEVVSALI
HILGSSSIGQVNYGSAGQATQIV

2 hits	3
3 hits	6
4 hits	6
5+ hits	0
Score	48

Score: 48

N. senegalensis

ASAAASRLSSPEASSRVSSAVSNLVSSGPTNSAALSSTISNVVSQIGASNPGLSGCDVLIQALLEVVSALV
HILGSSSIGQVNYGSAGQATQ

2 hits	3
3 hits	6
4 hits	6
5+ hits	0
Score	48

Score: 48

Genus	Species	Spidroin size (kDa)	2 Hits	3 Hits	4 Hits	5+ Hits	Score
Araneus	*diadematus*	9.4	2	7	11	**1**	**74**
Argiope	*argentata*	10.4	5	4	10	**1**	**67**
	bruennichi	10.1	3	6	11	**1**	**73**
	trifasciata	10.4	5	4	9	**1**	**63**
Cyrtophora	*moluccensis*	10.7	2	4	9	0	**52**
Dolomedes	*tenebrosus*	5.7	3	2	6	**2**	**46**
Euprosthenops	*australis*	10.3	3	8	7	0	**58**
Nephila	*clavipes*	10.1	4	6	7	0	**54**
	madagascarensis	8.8	4	6	6	0	**50**
	pilipes	9.1	3	6	6	0	**48**
	senegalensis	8.9	3	6	6	0	**48**

Figure 17. The enzymatic profiles of *E. australis*, *N. clavipes*, *N. madagascarensis*, *N. pilipes* and *N. senegalensis* MaSp1 C-termini when compared to MMP2. A 'hit' was classified as matching amino acid residues that crossed the cleavage point within the target sequence with the number of reflecting the length of the matching sequence. The frequency of matching sequence lengths for all profiles are summarised in the table in addition to the final score for each termini.

3.3.3.2 MMP9

Amino termini
The N-terminal consensus sequences were then compared against the target sequences for MMP9 shown in **Figure 18**. Only one 5-residue sequence was identified across all amino termini, found in *A. argentata*. All profiles were scored by the same method and summarised in the table below. The highest score (31) was achieved by both the 17.6 kDa protein of *A. diadematus* and the 15.6 kDa protein of *A. argentata*, while the lowest (18) was scored by both the 16.8 kDa *C. moluccensis* protein and the 16.0 kDa termini of *N. clavipes*.

Carboxyl termini
As with the MMP2 results, the termini profiles were separated into two figures for clarity. The termini profiles of *A. diadematus, A. argentata, A. bruennichi, A. trifasciata, C. moluccensis* and *D. tenebrosus* were shown in **Figure 19** while the termini profiles of *E. australis, N. clavipes, N. madagascarensis, N. pilipes* and *N. senegalensis* were shown in **Figure 20**.

The lowest scores of all the *in silico* analysis were seen from these results, in correlation with termini size and the increased specificity exhibited by MMP9. Despite this, seven 5-residue sequences were identified across all C-termini, highlighted in pink. All profiles were scored in the same way and summarised in the table found in **Figure 20**. The highest score (37) was achieved by the 10.4 kDa termini of *A. trifasciata* while the lowest (14) was scored by the 5.7 kDa *D. tenebrosus* protein.

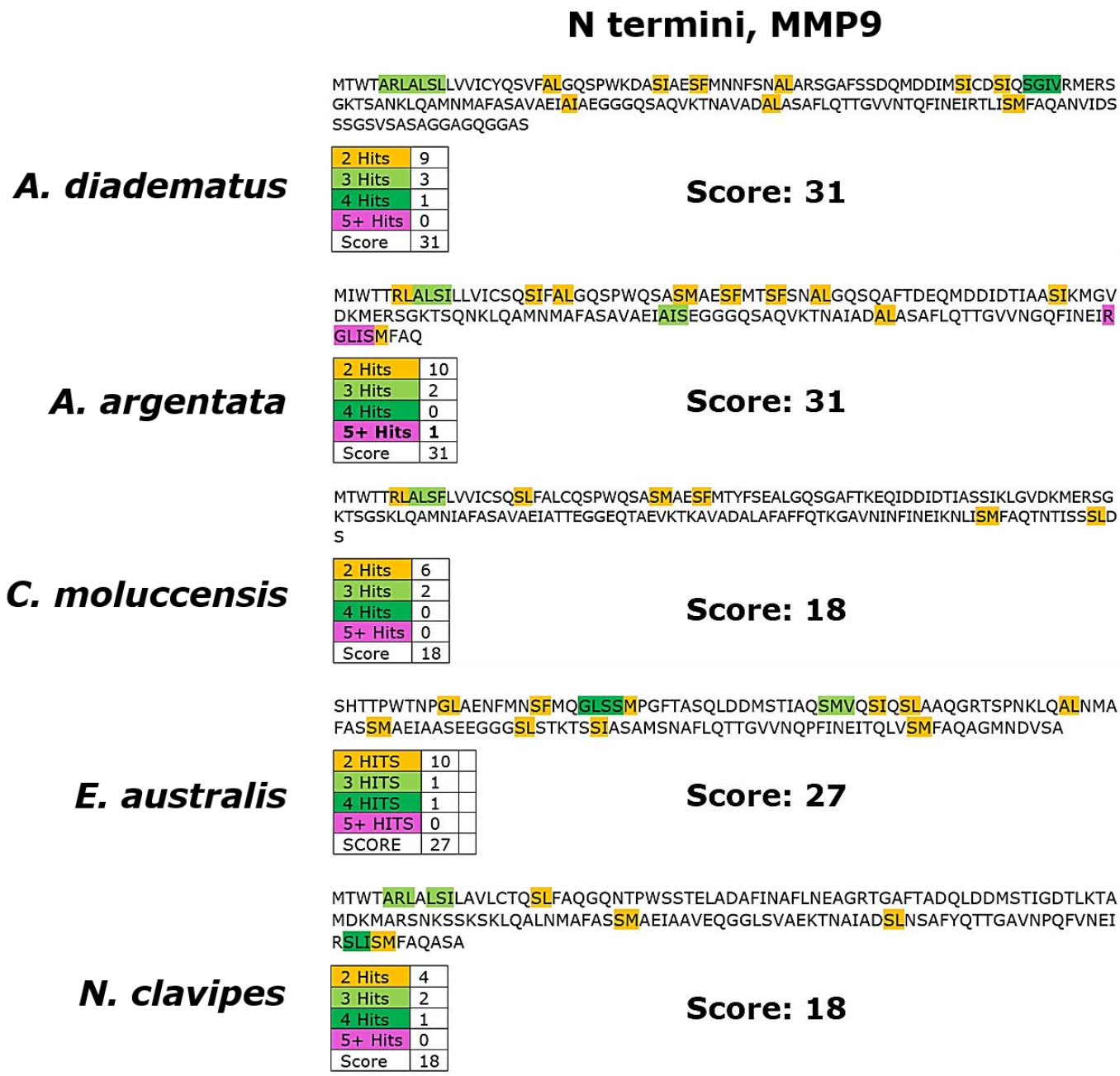

Genus	Species	Spidroin size (kDa)	2 Hits	3 Hits	4 Hits	5+ Hits	Score
Araneus	*diadematus*	17.6	9	3	1	0	**31**
Argiope	*argentata*	15.6	10	2	0	**1**	**31**
Cyrtophora	*moluccensis*	16.8	6	2	0	0	**18**
Euprosthenops	*australis*	13.8	10	1	1	0	**27**
Nephila	*clavipes*	16.0	4	2	1	0	**18**

Figure 18. The enzymatic profiles of MaSp1 N-termini when compared to MMP9. The frequency of matching sequence lengths is summarised in the table in addition to the final score for each termini. As with MMP2 profiles, the scores demonstrate the overall coverage and length of matching sequences by MMP9 with the highest scores attributed to greatest likelihood of cleavage.

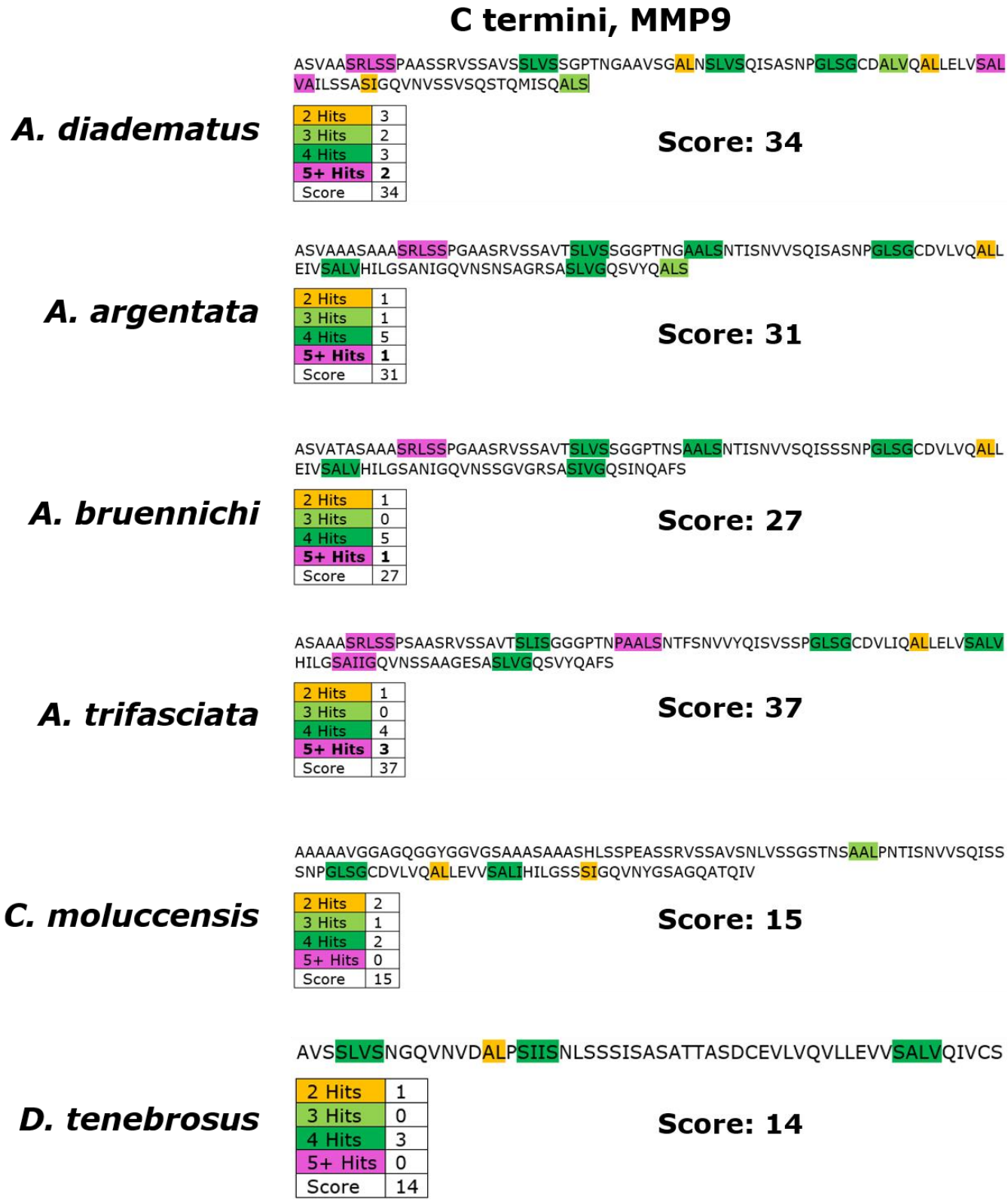

Figure 19. The enzymatic profiles of *A. diadematus*, *A. argentata*, *A. bruennichi*, *A. trifasciata*, *C. moluccensis* and *D. tenebrosus* MaSp1 C-termini when compared to MMP9. The scores are were generated to reflect the coverage of each sequence and the length of the matching sequences.

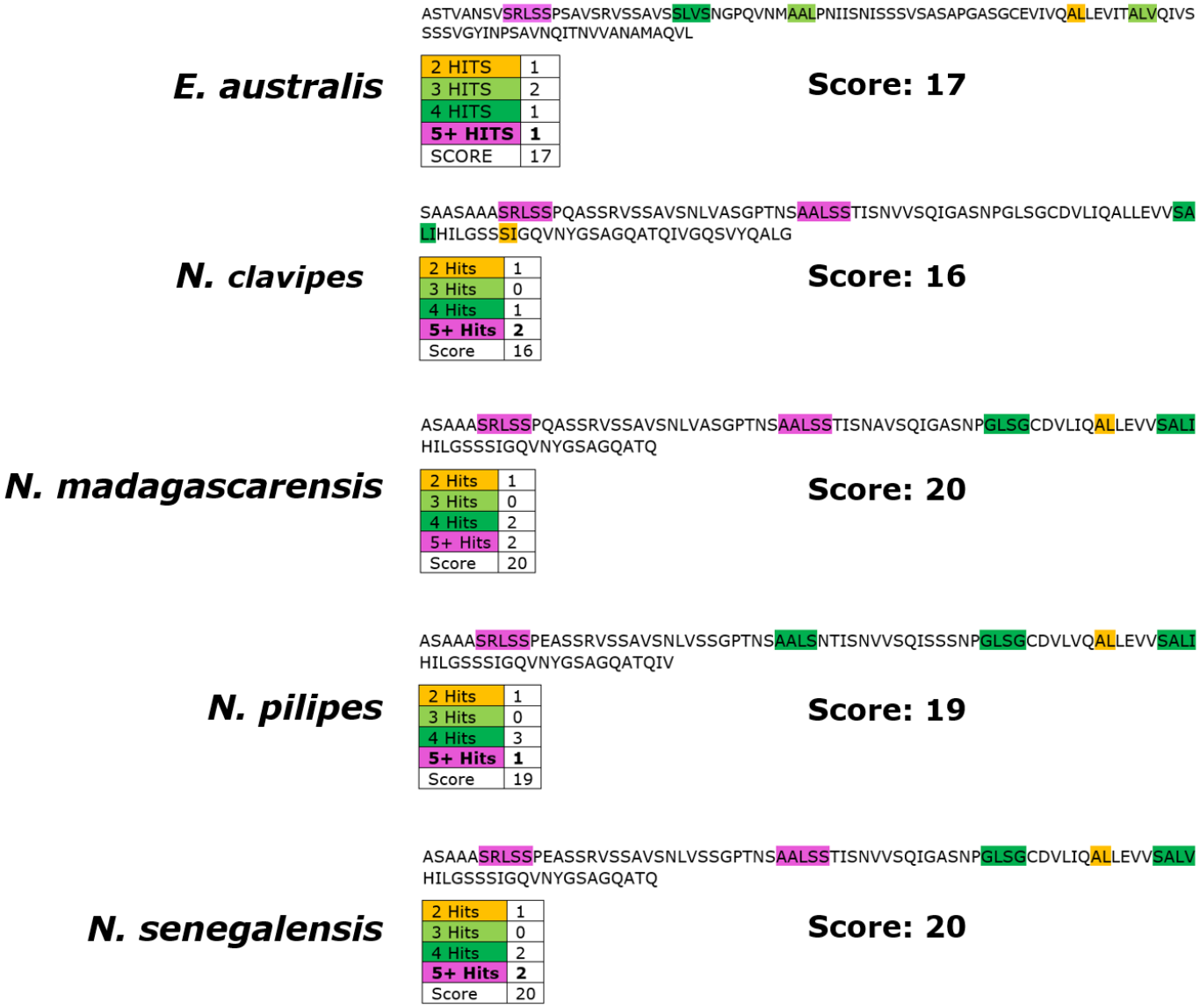

Genus	Species	Spidroin size (kDa)	2 Hits	3 Hits	4 Hits	5+ Hits	Score
Araneus	*diadematus*	9.4	3	2	3	**2**	**34**
Argiope	*argentata*	10.4	1	1	5	**1**	**31**
	bruennichi	10.1	1	0	5	**1**	**27**
	trifasciata	10.4	1	0	4	**3**	**37**
Cyrtophora	*moluccensis*	10.7	2	1	2	0	**15**
Dolomedes	*tenebrosus*	5.7	1	0	3	0	**14**
Euprosthenops	*australis*	10.3	1	2	1	**1**	**17**
Nephila	*clavipes*	10.1	1	0	1	**2**	**16**
	madagascarensis	8.8	1	0	2	**2**	**20**
	pilipes	9.1	1	0	3	**1**	**19**
	senegalensis	8.9	1	0	2	**2**	**20**

Figure 20. The enzymatic profiles of *E. australis, N. clavipes, N. madagascarensis, N. pilipes* and *N. senegalensis* MaSp1 C-termini when compared to MMP9. As with MMP2 profiles, a 'hit' was classified as matching amino acid residues that crossed the cleavage point within the target sequence with the number reflecting the length of the matching sequence. The frequency of matching sequence lengths for all profiles are summarised in the table in addition to the final score for each termini.

3.3.4 PROSPER analysis of natural spidroins

The spidroin sequences were submitted to the online PROSPER analysis tool to identify pre-determined MMP cleavage sites that existed within the sequences [224]. The likelihood of cleavage from MMP2 or MMP9 was identified (final column), shown in **Table 12 – 15**.

MMP2

The total number of cuts for MMP2 was lower than that seen from MMP9, with no cleavage expected from some N-terminal sequences (**Table 12,** *C. moluccensis* and *N. clavipes*). However, the C-terminus of *C. moluccensis* contained 4 cuts, the highest alongside *A. diadematus*, seen in **Table 13**.

MMP9

The PROSPER predictions suggested that both termini contained multiple cleavage sites in all species as seen in **Table 14** and **Table 15**. The highest number of predicted cleavage events was identified in both termini of *E. australis*, with 9 and 13 cuts being predicted, respectively. Conservation between spidroins meant that many of the same sequences were identified across different sequences. For example, the sequence 'AASH/R¦LSSP' (where ¦ denotes the cleavage point) is seen in the C-terminus of five species, while 'AVSN/S¦LVSS' was seen eight termini in **Table 15.**

MMP2, N termini PROSPER results								
Genus	**Species**	**Termini size (kDa)**	**Number of cuts**	**Position**	**Segment**	**N fragment size (kDa)**	**C fragment size (kDa)**	**Score**
Araneus	*diadematus*	17.6	1	149	AQAN¦VIDS	15.8	1.8	1.07
Argiope	*argentata*	15.6	1	140	EIRG¦LISM	14.8	0.8	1.01
Cyrtophora	*moluccensis*	16.8	0	-	-	-	-	-
Euprosthenops	*australis*	14.87	1	47	MVQS¦IQSL	5.40	9.47	1.02
Nephila	*clavipes*	16.79	0	-	-	-	-	-

Table 12. The amino terminal sequences of the natural spidroins were submitted to a PROSPER database to identify MMP2 target sequences.

MMP2, C termini PROSPER results								
Genus	**Species**	**Termini size (kDa)**	**Number of cuts**	**Position**	**Segment**	**N fragment size (kDa)**	**C fragment size (kDa)**	**Score**
Araneus	*diadematus*	9.4	4	69	LVSA¦LVAI	6.5	2.9	1.11
				23	AVSS¦LVSS	2.1	5.7	1.01
				45	LVSQ¦ISAS	4.1	5.3	1.00
				41	ALNS¦LVSQ	3.7	5.7	0.98
Argiope	*argentata*	10.4	2	47	TISN¦VVSQ	4.2	6.2	1.17
				75	IVSA¦LVHI	7.0	3.4	1.13
	bruennichi	10.1	3	35	NPAA¦LSNT	3.2	6.9	1.12
				70	LVSA¦LVHI	6.8	3.3	1.11
				23	AVTS¦LISG	2.1	8.0	1.03
	trifasciata	10.4	2	47	TISN¦VVSQ	4.3	6.1	1.17
				75	IVSA¦LVHI	7.1	3.3	1.13
Cyrtophora	*moluccensis*	10.7	4	90	VVSA¦LIHI	8.2	2.5	1.28
				62	TISN¦VVSQ	5.5	5.2	1.17
				44	AVSN¦LVSS	3.8	6.9	1.10
				28	AASH¦LSSP	2.2	8.5	0.97
Dolomedes	*tenebrosus*	5.7	3	22	IISN¦LSSS	2.2	3.5	1.05
				50	VVSA¦LVQI	4.9	0.8	1.03
				4	AVSS¦LVSN	0.3	5.4	1.01
Euprosthenops	*australis*	10.3	2	16	SPSA¦VSRV	1.5	8.8	1.10
				26	AVSS¦LVSN	2.5	7.8	1.01
Nephila	*clavipes*	10.1	3	71	VVSA¦LIHI	6.4	3.7	1.28
				43	TISN¦VVSQ	4	6.1	1.17
				25	AVSN¦LVAS	2.3	7.8	1.10
	madagascarensis	8.8	2	69	VVSA¦LIHI	6.6	2.2	1.28
				23	AVSN¦LVAS	2.2	6.6	1.10
	pilipes	9.1	3	69	VVSA¦LIHI	6.7	2.4	1.28
				41	TISN¦VVSQ	3.9	5.2	1.17
				23	AVSN¦LVSS	2.2	6.9	1.10
	senegalensis	8.9	3	41	TISN¦VVSQ	3.9	5.0	1.17
				23	AVSN¦LVSS	2.2	6.7	1.10
				69	VVSA¦LVHI	6.6	2.3	1.03

Table 13. The carboxyl terminal sequences of the natural spidroins were submitted to a PROSPER database to identify MMP2 target sequences.

MMP9, N termini PROSPER results								
Genus	**Species**	**Termini size (kDa)**	**Number of cuts**	**Position**	**Segment**	**N fragment size (kDa)**	**C fragment size (kDa**	**Score**
Araneus	*diadematus*	17.6	7	88	QAMN¦MAFA	9.6	8.0	1.34
				83	SANK¦LQAM	9.1	8.5	1.25
				72	GIVR¦MERS	7.9	9.7	1.07
				37	AESF¦MNNF	4.1	13.5	1.07
				150	QANV¦IDSS	15.9	1.7	1.03
				140	EIRT¦LISM	14.8	2.8	1.01
				118	VADA¦LASA	12.4	5.2	0.94
Argiope	*argentata*	15.6	4	88	QAMN¦MAFA	9.6	6.0	1.34
				140	EIRG¦LISM	14.8	0.8	1.14
				37	AESF¦MTSF	4.1	11.5	1.05
				22	SIFA¦LGQS	2.5	13.1	0.94
Cyrtophora	*moluccensis*	16.8	7	131	GAVN¦INFI	14.0	2.8	1.17
				88	QAMN¦IAFA	9.6	7.2	1.14
				140	EIKN¦LISM	15.0	1.8	1.14
				83	SGSK¦LQAM	9.0	7.8	1.12
				37	AESF¦MTYF	4.1	12.7	1.05
				122	LAFA¦FFQT	12.9	3.9	1.05
				118	VADA¦LAFA	12.5	4.3	0.94
Euprosthenops	*australis*	13.8	9	66	QALN¦MAFA	7.1	6.7	1.28
				14	LAEN¦FMNS	1.5	12.3	1.27
				61	SPNK¦LQAL	6.5	7.3	1.26
				33	TASQ¦LDDM	3.6	10.2	1.20
				19	MNSF¦MQGL	2.2	11.6	1.12
				43	IAQS¦MVQS	4.6	9.2	1.12
				72	FASS¦MAEI	7.7	6.1	1.08
				96	IASA¦MSNA	9.9	3.9	1.03
				121	QLVS¦MFAQ	12.6	1.2	1.01
Nephila	*clavipes*	16.0	8	89	QALV¦MAFA	9.6	6.4	1.28
				135	NPQF¦VNEI	14.3	1.7	1.20
				84	SKSK¦LQAL	9.1	6.9	1.15
				95	FASS¦MAEI	10.2	5.8	1.08
				70	LKTA¦MDKM	7.5	8.5	0.98
				72	TAMD¦KMAR	7.7	8.3	0.97
				124	NSAF¦YQTT	13.1	2.9	0.96
				73	AMDK¦MARS	7.9	8.1	0.96

Table 14. The amino terminal sequences of the natural spidroins were submitted to a PROSPER database to identify MMP9 target sequences.

MMP9, C termini PROSPER results								
Genus	**Species**	**Termini size (kDa)**	**Number of cuts**	**Position**	**Segment**	**N fragment size (kDa)**	**C fragment size (kDa**	**Score**
Araneus	*diadematus*	9.4	4	7	AASR¦LSSP	0.7	8.7	1.17
				23	AVSS¦LVSS	2.1	7.3	1.12
				69	LVSA¦LVAI	6.5	2.9	1.11
				92	QSTQ¦MISQ	8.7	0.7	1.09
Argiope	*argentata*	10.4	4	12	AASR¦LSSP	1.0	9.4	1.17
				74	IVSA¦LVHI	7.0	3.4	1.11
				50	NVVS¦QISA	4.5	5.9	1.06
				47	TISN¦VVSQ	4.2	6.2	1.01
	bruennichi	10.1	4	35	NPAA¦LSNT	3.2	6.9	1.36
				7	AASR¦LSSP	0.6	9.5	1.17
				70	LVSA¦LVHI	6.8	3.3	1.11
				43	FSNV¦VYQI	4.0	6.1	0.96
	trifasciata	10.4	5	12	AASR¦LSSP	1.0	9.4	1.12
				75	IVSA¦LVHI	7.1	3.3	1.11
				50	NVVS¦QISS	4.6	5.8	1.06
				40	NSAA¦LSNT	3.6	6.8	1.04
				47	TISN¦VVSQ	4.3	6.1	1.01
Cyrtophora	*moluccensis*	10.7	6	44	AVSN¦LVSS	3.8	6.9	1.35
				28	AASH¦LSSP	2.2	8.5	1.26
				90	VVSA¦LIHI	8.2	2.5	1.22
				65	NVVS¦QISS	5.8	4.9	1.06
				62	TISN¦VVSQ	5.5	5.2	1.01
				113	QATQ¦IV	10.5	0.2	1.01
Dolomedes	*tenebrosus*	5.7	4	50	VVSA¦LVQI	4.9	0.8	1.24
				22	IISN¦LSSS	2.2	3.5	1.22
				4	AVSS¦LVSN	0.3	5.4	1.12
				52	SALV¦QIVC	5.2	0.5	1.02
Euprosthenops	*australis*	10.3	13	89	NPSA¦VNQI	8.7	1.6	1.22
				102	NAMA¦QVL	10.0	0.3	1.19
				95	QITN¦VVAN	9.3	1.0	1.12
				26	AVSS¦LVSN	2.5	7.8	1.12
				91	SAVN¦QITN	8.9	1.4	1.12
				72	VITA¦LVQI	7.0	3.3	1.11
				74	TALV¦QIVS	7.2	3.1	1.11
				100	VANA¦MAQV	9.8	0.5	1.10
				104	MAQV¦L	10.2	0.1	1.10
				99	VVAN¦AMAQ	9.7	0.6	1.06
				10	SVSR¦LSSP	1.0	9.3	1.02
				34	GQVN¦MAAL	3.3	7.0	1.01
				37	NMAA¦LPNI	3.6	6.7	0.98
Nephila	*clavipes*	10.1	7	25	AVSN¦LVAS	2.3	7.8	1.35
				71	VVSA¦LIHI	6.7	3.4	1.22
				9	AASR¦LSSP	0.8	9.3	1.17
				46	NVVS¦QIGA	4.3	5.8	1.06
				36	NSAA¦LSST	3.3	6.8	1.04
				43	TISN¦VVSQ	4.0	6.1	1.01
				94	QATQ¦IVGQ	9.0	1.1	1.01
	madagascarensis	8.8	5	23	AVSN¦LVAS	2.2	6.6	1.35
				69	VVSA¦LIHI	6.6	2.2	1.22
				7	AASR¦LSSP	0.6	8.2	1.17
				44	NAVS¦QIGA	4.1	4.7	1.12
				34	NSAA¦LSST	3.2	5.6	1.04
	pilipes	9.1	7	23	AVSN¦LVSS	2.2	6.9	1.35
				69	VVSA¦LIHI	6.7	2.4	1.22
				7	AASR¦LSSP	0.6	8.5	1.17
				44	NVVS¦QISS	4.2	4.9	1.06
				34	NSAA¦LSNT	3.2	5.9	1.04
				41	TISN¦VVSQ	3.9	5.2	1.01
				92	QATQ¦IV	8.9	0.2	1.01
	senegalensis	8.9	6	23	AVSN¦LVSS	2.2	6.7	1.35
				69	VVSA¦LVHI	6.6	2.3	1.24
				7	AASR¦LSSP	0.6	8.3	1.17
				44	NVVS¦QIGA	4.2	4.7	1.06
				34	NSAA¦LSST	3.2	5.7	1.04
				41	TISN¦VVSQ	3.9	5.0	1.01

Table 15. The carboxyl terminal sequences of the natural spidroins were submitted to a PROSPER database to identify MMP9 target sequences.

3.3.5 The effect of sequence variance on *in silico* profiling

The sequence alignments conducted in **Section 3.3.5** identified different amino acid sequences for the termini of *N. clavipes* (N-terminal) and *A. diadematus* (C-terminal). The variation within these sequences was therefore investigated to identify the effect these differences had on predicted protein cleavage.

N-termini

The four sequences of *N. clavipes* were compared against target motifs and submitted to the PROSPER prediction software and seen in **Figure 21**. As before, an *in silico* approach was taken for MMP2 and MMP9, seen in **Figure 21a**) and **Figure 21b**) respectively. The sequences were also submitted to a PROSPER prediction software to identify cleavage sites for the same enzymes, seen in **Figure 21c**) and **Figure 21d**) for MMP2 and MMP9 respectively.

Figure 21a) The *in silico* profiles scored between 70 (Sequence 4) and 83 (Sequence 2) between the four sequences suggesting substantial coverage by MMP2. A five-length matching sequence was identified in all sequences except Sequence 3. **Figure 21b)** When compared to MMP9 target sequences, the scores ranged from 17 - 24. Only one 5-length matching sequence was identified, located in Sequence 4.

When submitted to the PROSPER prediction software for MMP2 predictions, seen in **Figure 21c)**, cleavage sites were only identified in Sequences 1, 3, and 4. Of these 3 results, Sequence 4 was predicted to undergo cleavage in 3 distinct locations.

PROSPER prediction for MMP9, seen in **Figure 21d)**, identified 40 cleavage sites with 16 sites identified within Sequence 4. As with MMP2 (**Figure 21c**), the highest number of sequences were identified in Sequence 4 while the lowest number was produced by Sequence 2 with six. Although many of the cleavage locations were similar between the proteins, the variation within Sequence 4 produced many unique cleavage sites.

a)

MMP2 N termini *N. clavipes*						
Sequence number	**Termini size (kDa)**	**2 Hits**	**3 Hits**	**4 Hits**	**5+ Hits**	**Final score**
1	16.2	16	7	6	**1**	**82**
2	16.2	14	10	5	**1**	**83**
3	16.4	9	15	3	0	**75**
4	16.7	10	7	6	**1**	**70**

b)

MMP9 N termini *N. clavipes*						
Sequence number	**Termini size (kDa)**	**2 Hits**	**3 Hits**	**4 Hits**	**5+ Hits**	**Final score**
1	16.2	6	4	0	0	**24**
2	16.2	7	3	0	0	**23**
3	16.4	3	2	1	0	**17**
4	16.7	4	2	1	**1**	**23**

c)

MMP2, N termini PROSPER results of *Nephila clavipes*							
Sequence number	**Termini size (kDa)**	**Number of cuts**	**Position**	**Segment**	**N fragment size (kDa)**	**C fragment size (kDa)**	**Score**
1	16.2	1	132	GAVN¦VQFV	13.9	2.3	1.05
2	16.2	0	-	-	-	-	-
3	16.4	1	141	EIGG¦LMET	15.1	1.3	1.05
4	16.7	3	109	DVNN¦IINS	11.9	4.8	1.20
			11	LFVA¦LFCS	1.3	15.4	0.98
			55	LKAD¦LVDD	5.9	10.8	0.97

d)

MMP9, N termini PROSPER results of *Nephila clavipes*							
Sequence number	**Termini size (kDa)**	**Number of cuts**	**Position**	**Segment**	**N fragment size (kDa)**	**C fragment size (kDa)**	**Score**
1	16.2	8	132	GAVN¦VQFV	13.9	2.3	1.30
			89	QALN¦MAFA	9.6	6.6	1.28
			95	FASS¦MAEI	10.2	6,0	1.08
			84	SQSK¦LQAL	9.0	7.2	1.05
			70	LKTA¦MDKM	7.5	8.7	.098
			72	TAMD¦KMAR	7.7	8.5	0.97
			124	NSAF¦YQTT	13.1	3.1	0.96
			73	AMDK¦MARS	7.8	8.4	0.96
2	16.2	6	89	QALN¦MAFA	9.6	6.6	1.28
			135	NPQF¦VNEI	14.3	1.9	1.20
			95	FASS¦MAEI	10.2	6.0	1.08
			72	TAMD¦KMAR	7.8	8.4	0.97
			124	NSAF¦YQTT	13.1	3.1	0.96
			73	AMDK¦MARS	7.9	8.3	0.96
3	16.4	10	89	QALN¦MAFA	9.7	6.7	1.28
			101	EIAV¦LEKG	10.9	5.5	1.15
			141	EIGG¦LMET	15.1	1.3	1.14
			22	SMYV¦LGQV	2.6	13.8	1.11
			19	FTQS¦MYVL	2.2	14.2	1.09
			132	GAEN¦KQFV	14.2	2.2	1.08
			95	FASS¦MAEI	10.3	6.1	1.08
			124	NEAF¦LQTT	13.3	3.1	1.07
			41	FIKN¦FLAS	4.6	11.8	1.03
			73	ATDK¦MARS	8.0	8.4	0.98
4	16.7	16	84	NPHK¦LQLF	9.3	7.4	1.45
			136	LARE¦MEEL	14.9	1.8	1.31
			62	DVYS¦MRDT	6.7	10.0	1.30
			132	QDYK¦LARE	14.4	2.3	1.17
			23	VRAS¦LQEL	2.6	14.1	1.16
			109	DVNN¦IINS	11.9	4.8	1.09
			34	GLGN¦MEGF	3.7	13.0	1.08
			73	SINE¦MKSS	8.0	8.7	1.05
			89	QLFQ¦MLFN	9.9	6.8	1.04
			147	FAEN¦QDTN	16.2	0.5	1.01
			37	NMEG¦FINN	4.0	12.7	1.01
			15	LFCS¦QTSF	1.7	15.0	1.00
			26	SLQE¦LMSG	3.0	13.7	0.98
			19	QTSF¦VRAS	2.2	14.5	0.98
			121	MASA¦FGQF	13.1	3.6	0.97
			143	LIRV¦FAEN	15.7	1.0	0.95

Figure 21. The different N-terminal sequences of *N. clavipes* were compared against the *in silico* profiles of MMP2 (**a**) and MMP9 (**b**). They were also submitted to the PROSPER prediction software to identify locations within the peptides that cleavage was expected to take place for each enzyme respectively (**c** and **d**).

C-termini

As before, an *in silico* approach was taken for MMP2 and MMP9, seen in **Figure 22a**) and **Figure 22b**) respectively. The sequences were also submitted to the PROSPER prediction software for MMP2 and MMP9 respectively, seen in **Figure 22c**) and **Figure 22d**).

Figure 22a) The *in silico* profiles scored between 58 (Sequence 3) and 67 (Sequence 2) between the three sequences. A single five-length matching sequence was identified in Sequence 1. **Figure 22b**) MMP9 profiles scored between 29 (Sequence 1) and 35 (Sequence 2). A total of four 5-length matching sequences were identified between the three sequences, with a single 6-residue motif identified in Sequence 1, highlighted in blue.

MMP2 cleavage sites were identified by PROSPER prediction in all sequences, seen in **Figure 22c**). With a total of nine cleavage sites from MMP2 predictions, all sequences were expected to facilitate multiple cleavage events with four identified in Sequence 2, three in Sequence 1 and two sites located in Sequence 3.

As with the N-terminal predictions, MMP9 predictions identified a greater number of cleavage sites than from MMP2. Seen in **Figure 22d**), 14 sites were identified in total, with Sequence 1 presenting six locations for potential cleavage. Sequences 2 and 3 both produced 4 sites each, many of which were the same sequence within the two peptides.

a)

MMP2 C termini *A. diadematus*						
Sequence number	**Termini size (kDa)**	**2 Hits**	**3 Hits**	**4 Hits**	**5 Hits**	**Final score**
1	9.4	3	4	10	**1**	**63**
2	9.4	4	5	11	0	**67**
3	9.5	4	6	8	0	**58**

b)

MMP9 C termini *A. diadematus*							
Sequence number	**Termini size (kDa)**	**2 Hits**	**3 Hits**	**4 Hits**	**5 Hits**	**6 Hits**	**Final score**
1	9.4	1	0	4	**1**	**1**	**29**
2	9.4	5	1	3	**2**	0	**35**
3	9.5	3	1	4	**1**	0	**30**

c)

MMP2, C termini PROSPER results of *Araneus diadematus*							
Sequence number	**Termini size (kDa)**	**Number of cuts**	**Position**	**Segment**	**N fragment size (kDa)**	**C fragment size (kDa)**	**Score**
1	9.4	3	70	IISA¦LVHI	6.6	2.8	1.11
			35	SPAA¦LSSS	3.2	6.2	1.10
			23	AVSS¦LVSN	2.1	7.3	1.01
2	9.4	4	69	LVSA¦LVAI	6.5	2.9	1.11
			23	AVSS¦LVSS	2.1	7.3	1.01
			45	LVSQ¦ISAS	4.1	5.3	1.00
			41	ALNS¦LVSQ	3.7	5.7	0.98
3	9.5	2	69	VVSA¦LVSI	6.5	3.0	1.03
			23	AVSS¦LVSS	2.1	7.4	1.01

d)

MMP9, C termini PROSPER results of *Araneus diadematus*							
Sequence number	**Termini size (kDa)**	**Number of cuts**	**Position**	**Segment**	**N fragment size (kDa)**	**C fragment size (kDa)**	**Score**
1	9.4	6	35	SPAA¦LSSS	3.2	6.2	1.24
			7	AASR¦LSSP	0.6	8.8	1.17
			23	AVSS¦LVSN	2.1	7.3	1.12
			70	IISA¦LVHI	6.6	2.8	1.11
			45	NVVS¦QISA	4.1	5.3	1.06
			42	SISN¦VVSQ	3.8	5.6	1.00
2	9.4	4	7	AASR¦LSSP	0.7	8.7	1.17
			23	AVSS¦LVSS	2.1	7.3	1.12
			69	LVSA¦LVAI	6.5	2.9	1.11
			92	QSTQ¦MISQ	8.7	0.7	1.09
3	9.5	4	69	VVSA¦LVSI	6.5	3.0	1.24
			7	AASR¦LSSP	0.6	8.9	1.17
			23	AVSS¦LVSS	2.1	7.4	1.12
			92	QYTQ¦MVGQ	8.9	0.6	1.03

Figure 22. The different C-terminal sequences of *A. diadematus* were compared against the *in silico* profiles of MMP2 (**a**) and MMP9 (**b**). They were also submitted to the PROSPER prediction software to identify locations within the peptides that cleavage was expected to take place for each enzyme respectively (**c** and **d**).

3.3.6 *In vitro* enzymatic degradation of natural silks

Dragline silk was successfully reeled from *C. citricola*, *D. fimbriatus, N. madagascarensis* and *P. mirabilis* while silk from the *P. phalangioides* was removed from freshly formed web. Silk was incubated for 1 week at room temperature before it was observed with bright field and birefringence microscopy at 100X magnification. Image white balance corrections and scaling was carried out on ImageJ.

3.3.6.1 Degradation of C. citricola silk

Degradation of *C. citricola* silk occurred in the presence of all proteases. Degradation was defined as observable regions of blemish, such as pitting and fraying, compared to the smooth unblemished control fibres (H_2O negative control) as seen from the **red** arrows in **Figure 23**. Although not quantifiable, the greatest frequency of degradation was seen from MMP2, although degradation was observed from all proteases.

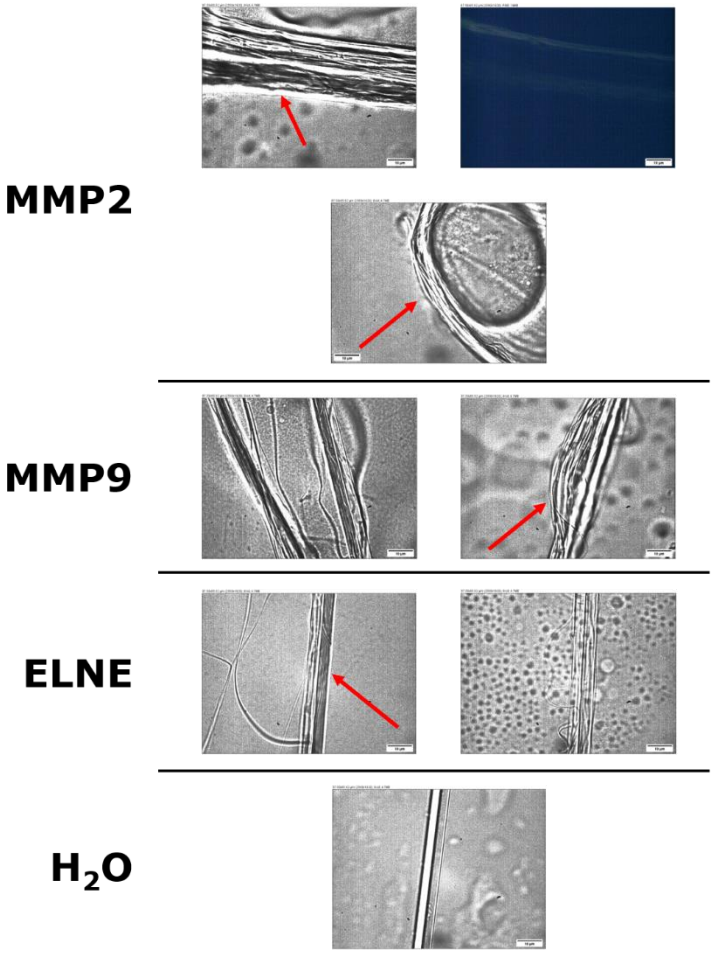

Figure 23. Silk from *C. citricola* was incubated in MMP2, MMP9, ELNE and H_2O for one week before it was analysed by bright field and birefringence microscopy at 100X magnification. Degradation was seen in fibres of all protease solutions while no degradation could be found in fibres that had been incubated in H_2O.

3.3.6.2 Degradation of *N. madagascarensis* silk

Degradation of *N. madagascarensis* dragline silk occurred when incubated in MMP2, MMP9 and α-chymotrypsin. Compared to the negative control, pitting, fraying and breaks could be seen in all fibres, indicated by **red** arrows in **Figure 24**.

The greatest deterioration was observed from MMP2 incubation in the form of fibre breaks. An increase in birefringence was also seen from MMP2 and α-chymotrypsin, compared to the little birefringence seen from the smooth negative control fibres.

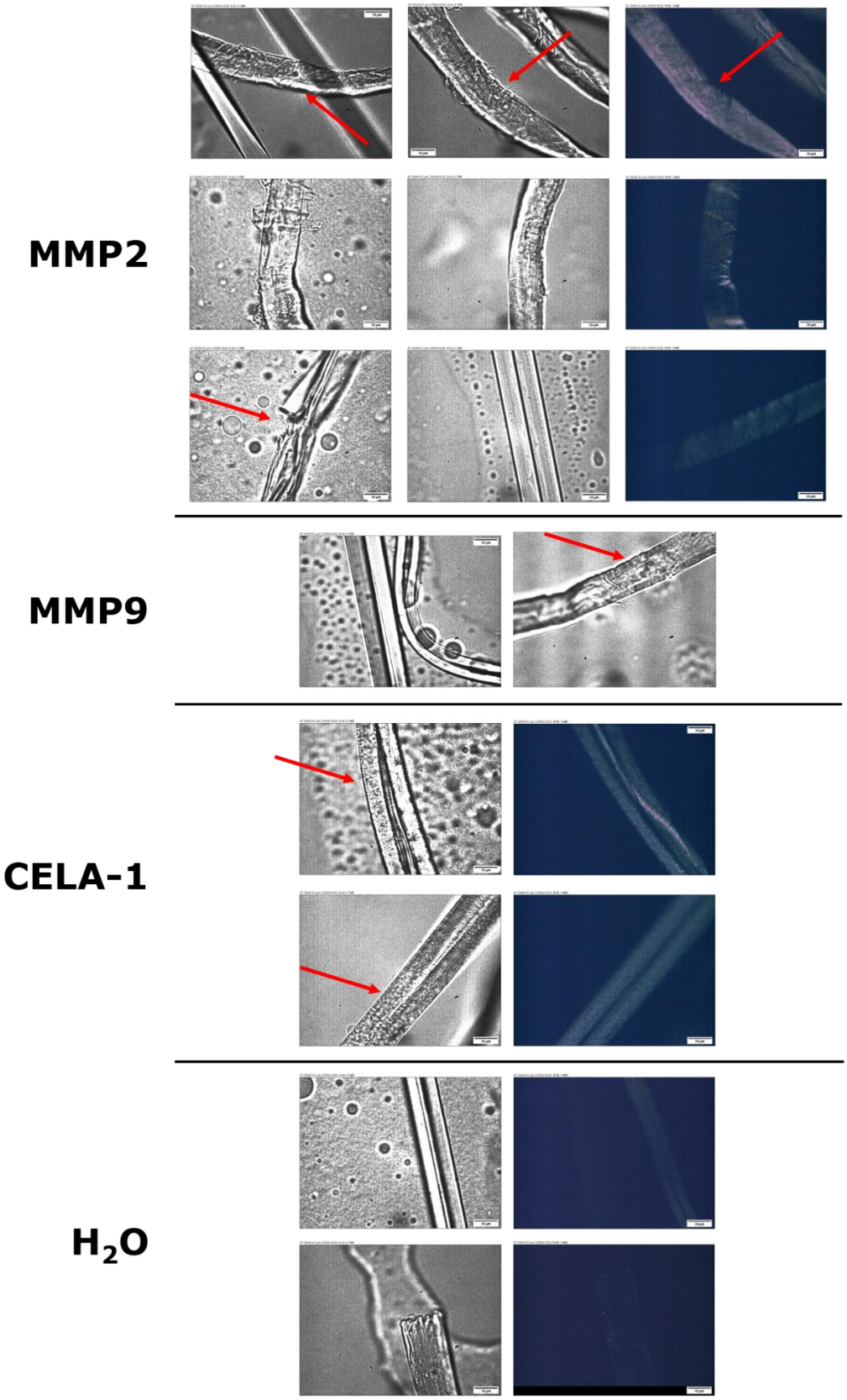

Figure 24. Dragline silk from *N. madagascarensis* was incubated in the presence of MMP2, MMP9 and α-chymotrypsin before they were imaged with bright field and birefringence microscopy. When compared to the negative control (H_2O), degradation was seen on the surface of fibres incubated with all proteases. Birefringence images also indicated that the fibres had undergone degrdation compared to the negative controls.

3.3.6.3 Degradation of *D. fimbriatus* silk

The dragline silk of *D. fimbriatus* underwent small levels of degradation in the presence of MMP2, indicated by the **red** arrows in **Figure 25**. However, in the presence of MMP9 and ELNE no degradation was seen compared to the negative control fibre (H_2O) with bright field or birefringence objectives.

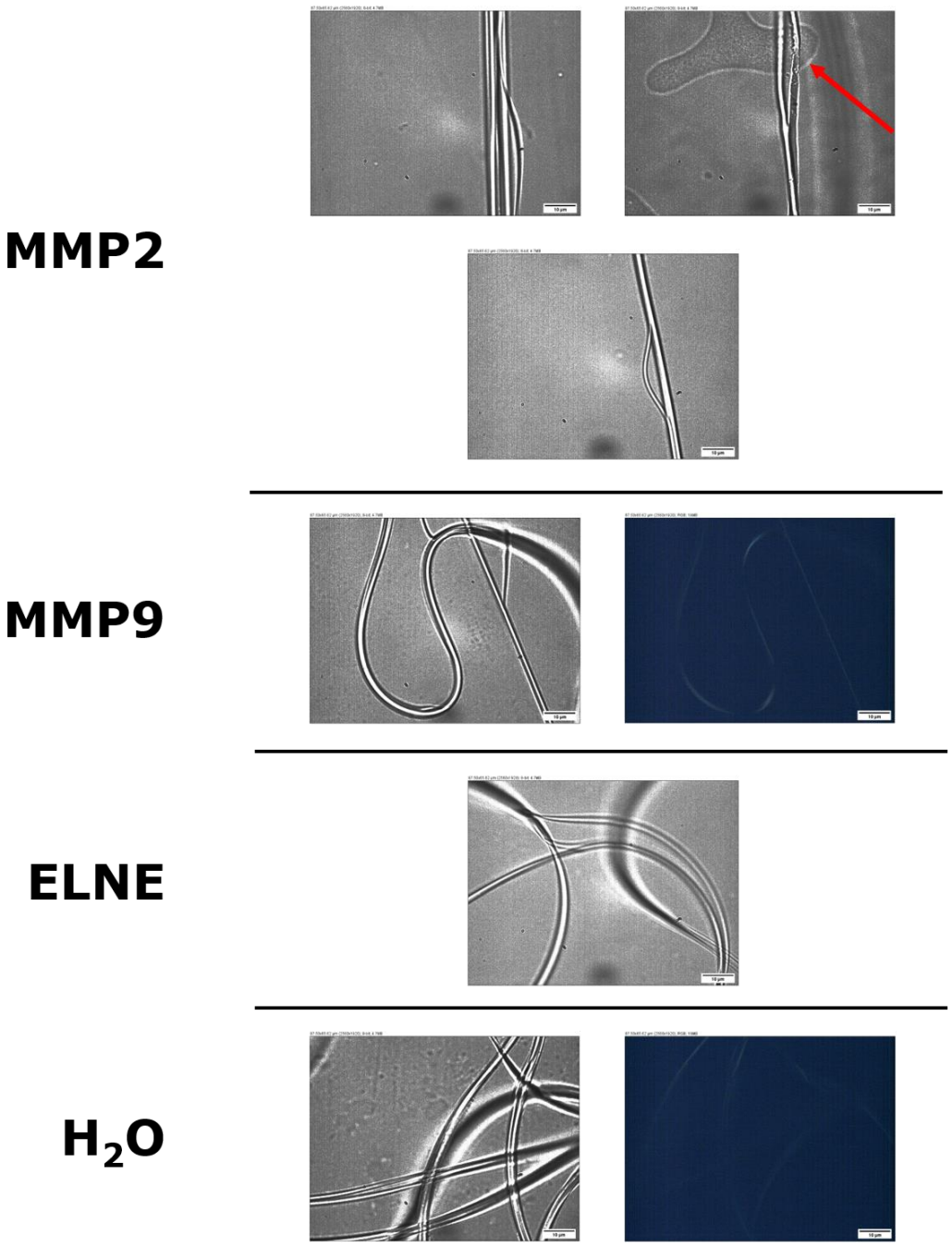

Figure 25. Silk from *D. fimbriatus* was incubated in MMP2, MMP9, ELNE and H_2O for 1 week before it was analysed by bright field and birefringence microscopy at 100X magnification. Only MMP2 was seen to produce observable degradation when compared to the H_2O negative control. Although some birefringence was visible, no significant difference could be seen between the negative control and MMP9.

3.3.6.4 Degradation of *P. mirabilis* silk

In the presence of MMP2, the *P. mirabilis* silk underwent small levels of degradation when viewed with bright field objectives, indicated by the **red** arrow in **Figure 26**. Under birefringence objectives however, no increase of fibre polarisation was seen. When compared to the control fibre, no degradation was seen in the presence of MMP9 and the fibre remained smooth along its length.

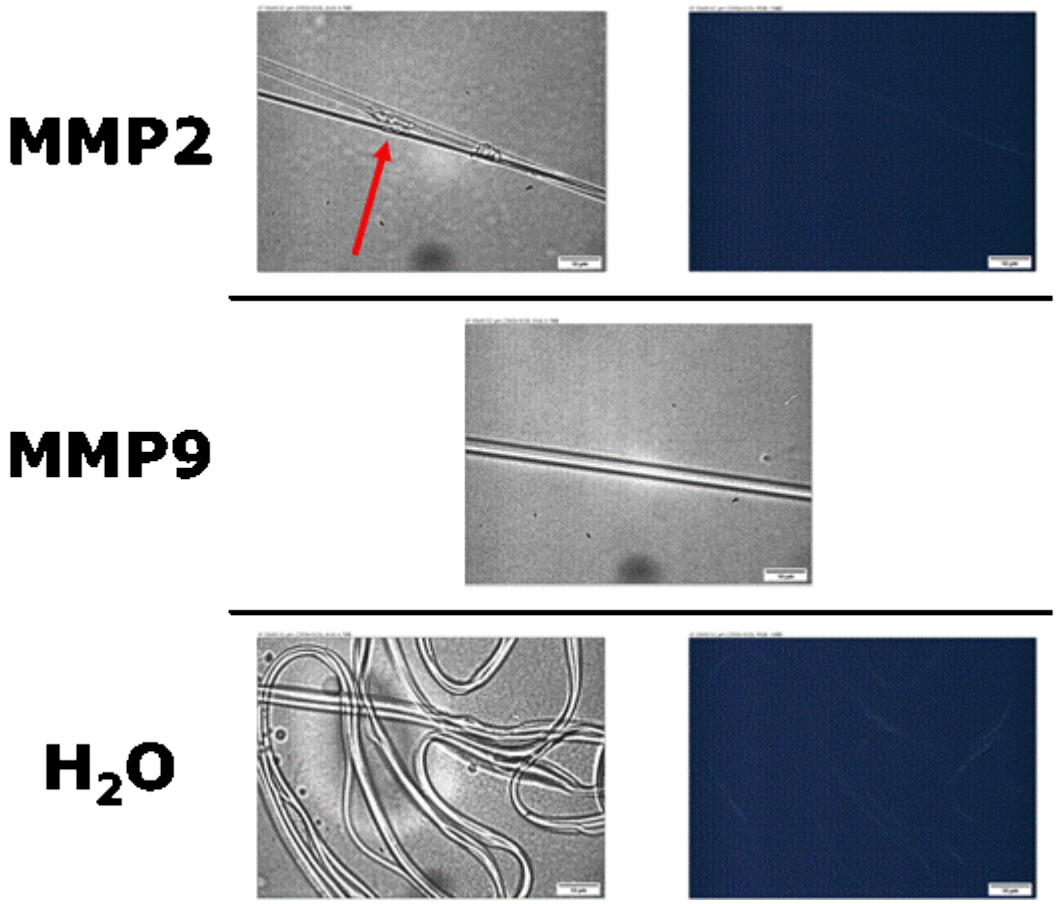

Figure 26. Silks from *P. mirabilis* were incubated in MMP2, MMP9 and H_2O for 1 week before they were analysed by bright field and birefringence microscopy at 100X magnification. Only MMP2 was seen to produce observable degradation when compared to the H_2O negative control. When viewed with polarised light microscopy, no significant difference could be seen between the negative control and after protease incubation suggesting that little degradation had occurred.

3.3.6.5 Degradation of *P. phalangioides* silk

The silk of *P. phalangioides* was collected directly from a web as forced-reeling was found to be ineffective.

Degradation was seen in the presence of MMP2 and MMP9 with greater levels of proteolytic activity observed by MMP2, indicated by the **red** arrow in **Figure 27**. Compared to the smooth control fibres, fibres in the presence of both proteases appeared rough at sites of proteolysis.

Unlike the force-reeled silks, the web silk displayed supercontraction behaviour in the presence of water. When viewed under the microscope, tightly packed coils could be seen, shown in **Figure 27 H_2O (arrowed)**.

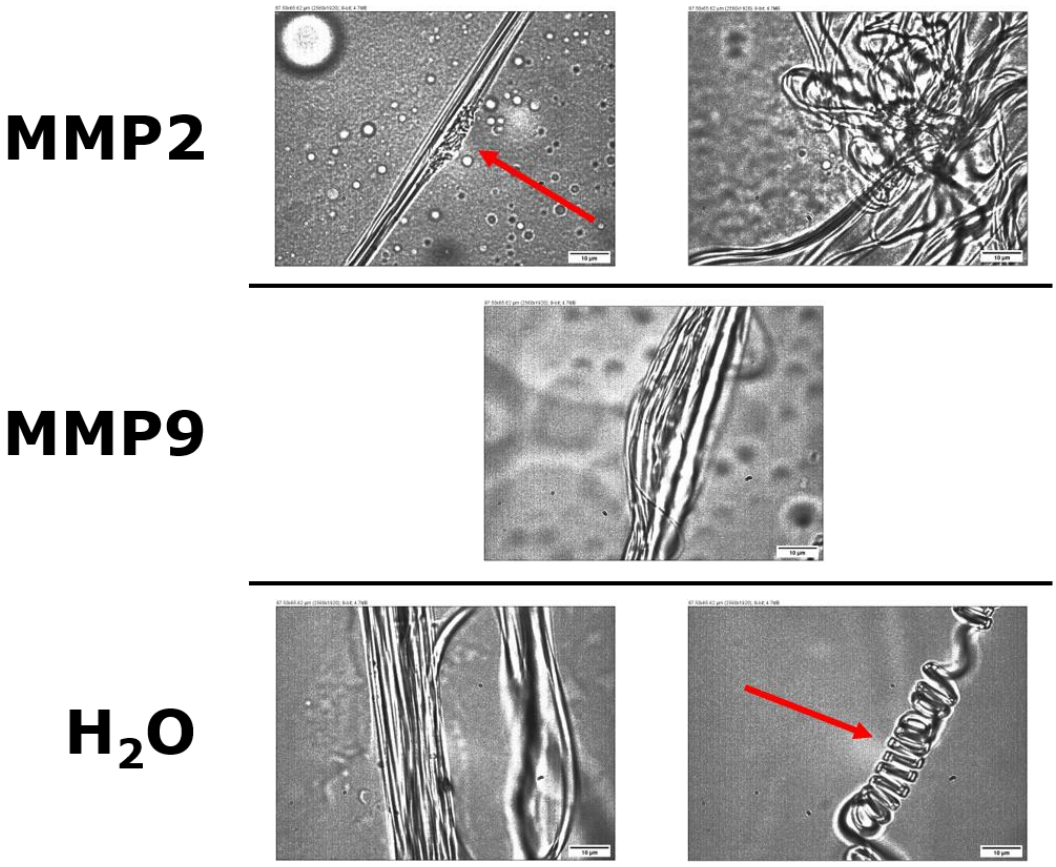

Figure 27. Silks from the web of *P. phalangioides* were incubated in MMP2, MMP9 and H_2O as a negative control for one week. After this time, the silk fibres were imaged using bright field microscopy at 100X magnification. Degradation was seen as a result of both MMP protease degradation, seen as pitting across the fibre. Although degradation was not observed from the negative control, supercontraction was observed in the form of tightly packed coils.

3.4 Discussion

The ability to accurately predict the degradation behaviour of (poly)peptides is a powerful tool in the development of future biomaterials [225,226]. However, the nature of biologically expressed biomaterials introduces the risk of genetic variation within proteins of the same material, further supporting the argument for recombinantly produced biomaterials such as 4RepCT.

As many proteases recognise substrate proteins through specific target sequences, variation within protein sequences can greatly alter the rate of substrate degradation. In the design of medically-active biomaterials, this variation in protein sequence could complicate patient recovery.

3.4.1 Differences between spidroin sequence

To accurately produce consensus sequences representative of each species, sequences of the same species and termini were aligned using a MAFFT algorithm (version 7) to enable multiple simultaneous alignments with an online webserver [190]. Seen in **Figure 12** and **Figure 13** consensus sequences were produced for all termini sequences. As a combined average of actual sequences, consensus sequences can fail to accurately represent spidroins that exists in nature [227]. However, the low variation within termini sequences of a single species ensured that the resulting consensus sequences were accurate.

To identify regions of termini conservation between species, the consensus sequences from the respective species were aligned against each other, seen in **Figure 14**. The N-termini, seen in **Figure 14a**, displayed greater variation throughout the peptide sequence, but homology was observed in the 'K-L-Q-A-L/M-N-M/I-A-F-A' motif. This motif was situated in the second α-helix of the MaSp N-termini and matched sequences found by Jiang *et al.* who recently modelled both termini of *E. australis* [43].

The greatest level of conservation was seen in the C-terminus as seen in **Figure 14b,** with a 35 amino acid domain conserved throughout all termini sequences. As expected, this region contained the conserved

QALLEVITAL motif, thought to contribute to spidroin dimerisation and polymerisation [36] and supporting a report by Strickland *et al.* that identified regions of conservation within spidroin C-termini [45]. However, as some variation was seen in this motif, in the form of 'QALLEVVSAL', it suggests that the overall shape of the α-helix has a greater role than the identity of the exact amino acids that it consists of [46].

3.4.2 *In silico* profiles of MaSp1 termini

Having compiled target sequences for MMP2 and MMP9, seen in **Tables 7 - 11**, the consensus sequences of each MaSp1 termini were compared against them, identifying matching target sequences within the peptide sequence. As gelatinases, the enzymes displayed similar substrate specificity, preferentially cleaving three residues downstream of proline. In addition to this, the carboxyl side of the cleavage point was often flanked by a leucine or isoleucine [172,173,192]. As a result, it was expected that similar target sequences would be identified for both enzymes. However, the greater variation accepted by MMP2 (**Table 9**), suggested by Chen *et al.* resulted in greater coverage by the protease compared to MMP9 [192]. This was explained by the increase in probability that results when the limiting factor, in this case the number of acceptable residues, is increased for a given sequence.

The *in silico* profiles shown in **Figure 15**, **Figure 16** and **Figure 17** were used to give an idea of protease coverage by MMP2. It also became apparent that the size of termini affected the coverage of the protease as larger peptides provided a higher number of residues to match the enzymatic profiles. Despite this, the highest N-terminal score was achieved by the second smallest terminus (90 scored by the 15.6 kDa terminus of *A. argentata*, seen in **Figure 15**). A difference in scores between termini was also seen with the larger amino termini (13.8 kDa - 17.6 kDa) ranging from 56 – 90 while the smaller carboxyl termini (5.7 kDa – 10.7 kDa) scored between 48 – 74, seen in **Figure 16** and **Figure 17**. Crucially, 5-residue matches (seen in pink) were identified in two of the N-termini (*E. australis* and *N. clavipes*) and five of the C-termini, namely *A. diadematus, A. argentata, A. bruennichi, A. trifasciata* and *D. tenebrosus*. Interestingly, the smallest termini

(5.7 kDa, *D. tenebrosus*) produced two 5-residue matches, making it highly likely that cleavage of the natural spidroin would occur in the presence of MMP2.

The same approach was also taken for MMP9 profiles, seen in **Figure 18**, **Figure 19** and **Figure 20**. In this case, the highest score across both termini was 37, scored by the 10.4 kDa carboxyl terminus of *A. trifasciata*. Only one 5-residue match was identified within the N-termini (*A. argentata*, see **Figure 18**) while 15 matches were found in the C-termini. Of these 15, two were identified in the sequences of *A. diadematus, N. clavipes, N. madagascarensis* and *N. senegalensis* (**Figure 20**) while three were located in the sequence of *A. trifasciata* (**Figure 19**). It was therefore likely that degradation would be observed in the presence of MMP9.

The manual *in silico* analyses were also supported by online prediction results, seen in **Tables 12 - 15**. Submitted to the PROSPER prediction service, cleavage sites in both termini were identified. Interestingly, two N-terminal sequences (*C. moluccensis* and *N. clavipes*) returned no cleavage predictions for MMP2, seen in **Table 12** despite *in silico* scores of 83 and 71, respectively. As a 5-residue match was identified in the sequence of *N. clavipes*, it was thought that a cleavage site would be identified in the same region of the peptide. Seen in **Table 13**, the C-terminal predictions identified at least two sites of cleavage in every peptide sequence with the highest number (4) being identified in *A. diadematus* and *C. moluccensis*. Unlike the *in silico* profiles, the correlation between spidroin size and the number of identified cleavage sites was reduced. While the *in silico* profiles highlighted any combination of residues that crossed the cleavage point (P1-P1'), only full 6-residue sequences were identified by the prediction software. As a result, it is likely that the size of peptide sequence would impact the average number of sequences identified but the termini were too small for this effect to be noticeable.

A higher number of cleavage sites were identified for MMP9 as seen in **Table 14** and **Table 15**, compared to MMP2. A total of 35

cleavage sites were located across the five N-terminal sequences, seen in **Table 14**. Of these, nine were identified within the consensus sequence of *E. australis*.

Although the sequence of *A. argentata* contained the lowest number of cleavage sites (4), the 5-residue motif (seen as pink highlight in **Figure 18**, ***A. argentata***) identified in the *in silico* screens was also confirmed in the prediction results, namely 'EIRG¦LISM' at position 140 (where '¦' denotes the point of cleavage). This therefore supports the use of the manual *in silico* screen approach to estimate the likelihood of peptide cleavage.

As with MMP2, the number of MMP9 target sites identified in the C-terminal sequences was higher than that identified from the N-termini with a total of 65 sequences located, seen in **Table 15**. The highest number of target sites (13) was again located within the peptide of *E. australis*. Crucially the 'AASR¦LSSP' sequence, located at the beginning of nine of the C-termini, was identified by both the *in silico* profile (seen in **Figure 19** and **Figure 20**) and prediction software (**Table 15**). However, only one other 5-residue sequence was discovered, located in the sequence of *A. diadematus* at position 69 with the sequence 'LVSA¦LVAI'.

3.4.3 Relevance to biomaterial applications

The difference between the two approaches enabled identification of existing and potential cleavage sites within the protein sequences. When combined with recombinant expression techniques, this method to identify regions of proteolytic susceptibility enables the development of tuneable degradation as new target sequences are introduced by point mutations.

The two approaches also highlighted the impact of protein sequence variation on potential substrate proteolysis. This was further investigated with a bioinformatics approach in **Figure 21** and **Figure 22**. By applying the same *in silico* screening and prediction software to the different sequences, the effect that natural mutations on subsequent degradation was evaluated.

The four unique sequences of *N. clavipes* N-termini as seen in **Figure 21**, produced similar results as the corresponding consensus sequence. However, although the *in silico* scores were similar, ranging from 70 – 83 for MMP2 (**Figure 21a**) and 17 – 24 for MMP9 (**Figure 21b**), the prediction results, seen in **Figure 21c**, suggested that no cleavage would take place in Sequence 2 in the presence of MMP2. Compared to the three locations within Sequence 4, this could have a significant effect of the degradation rates of the two spidroins. When analysed for MMP9 cleavage sites, seen in **Figure 21d**, multiple locations were identified for each sequence.

To investigate the effect on predicted C-terminal degradation, the three unique sequences of *A. diadematus* were investigated in the same manner, seen in **Figure 22**. The scores produced from *in silico* analysis ranged from 58 – 67 with MMP2 (**Figure 22a**) and 29 – 35 with MMP9 (**Figure 22b**), similar to those generated from the *A. diadematus* consensus sequence generated in **Figure 15**. However, variation within the sequences resulted in different 5-residue locations, seen in **Figure 22b,** with two 5-match sequences identified in Sequence 2 alone. In addition to this, a single 6-residue target sequence was located in Sequence 1 suggesting that the spidroin would likely undergo cleavage in the presence of MMP9.

When submitted to the prediction software, similar results were produced. While the number and coverage of MMP2 target sites **Figure 22c** was similar to those identified from the consensus sequences, a difference was seen when compared against MMP9 proteolysis. With MMP9, the same four sites were identified in both Sequence 2 and Sequence 3 while in Sequence 1 only two of these sequences were identified ('AASR¦LSSP' and 'AVSS¦LVSN'). However, another four unique cleavage locations were identified within Sequence 1.

Both **Figure 21** and **Figure 22** clearly demonstrate the need for recombinantly expressed spidroin-based biomaterials. Taking advantage of the monoclonal genetic approach, recombinant expression reduces

natural genetic variation and ensures that subsequent proteolytic degradation occurs at a predictable rate [25,28,72].

3.4.4 *In vitro* degradation of natural spider silks

As dragline silk consist of two spidroins, namely MaSp1 and MaSp2, it was unclear how the presence of MMP sites within a single spidroin would affect fibre degradation [228]. It is thought however, that cleavage of one of the spidroins would have considerable effects on the resulting fibre [229].

3.4.4.1 Visualising *in vitro* degradation

While silk from all species except *P. phalangioides* was collected by force-reeling, the quantity of silk reflected the ease of handling of each spider. As *N. madagascarensis* and *D. fimbriatus* were the easiest to handle during harvesting, the greatest quantity of silk was collected from these species. As a result, not all proteases could be investigated with every silk sample. However, sufficient silk was collected for each species to enable controls and MMP degradation. A summary of the *in vitro* results can be seen in **Table 16**, from which the increased degradation activity of MMP2 predicted from the *in silico* results was seen.

	MMP2	MMP9	ELNE	CELA - 1	Figure number
C. citricola	+ +	+	+	n/a	**Figure 23**
N. madagascarensis	+ +	+	n/a	+ +	**Figure 24**
D. fimbriatus	+	-	-	n/a	**Figure 25**
P. mirabilis	+	-	n/a	n/a	**Figure 26**
P. phalangioides	+ +	+	n/a	n/a	**Figure 27**

Table 16. *In vitro* degradation by respective proteases of dragline fibres from respective silks compared to incubation in H_2O are summarised above. The highest degree of degradation was seen after incubation with MMP2. The highest levels of degradation was represented by '+ +' while no degradation was represented by '-'. The corresponding images are referenced in the final column.

Birefringence microscopy

As silk fibres have been shown to undergo internal structural changes during aging and degradation [51], birefringence microscopy was utilised to observe this. Birefringence microscopy utilises differences in light polarity after passing through a sample [230,231]. In addition to the transmittance and wavelength of the observed light, the perceived brightness is also dependent on the thickness of sample and angle of polarisation [6,230]. Polarisation was expected to occur as light passed through regions of

crystallinity aligned in parallel to the fibre axis [232]. Spider silk fibres have been shown to become stiffer and crystalline as they age, improving their yield strength up to one year [51]. Attributed to a release of ammonia gas and breakdown of amino acids from gradual UV radiation deterioration, the internal β-sheets rearrange within the spidroin, increasing the fibre crystallinity [51]. As the fibre became increasingly crystalline the polarisation increased, enabling a method by which the fibres could be aged and deterioration measured [51,232]. However as polarisation is also effected by the hydration state, temperature and bends within the fibre, it is difficult to quantify the exact increase in polarisation observed [233]. If the loss of amino acids during aging contributed to a rearranging of β-sheets, it is plausible that the cleavage of single of multiple amino acids by enzymatic degradation would have a similar effect [234–236]. During *in vitro* degradation, the observed polarised brightness of the fibres was expected to increase with fibre crystallinity, providing a semi-quantifiable indication that degradation had occurred [235].

3.4.4.2 Orb web silk degradation (*Cyrtophora* and *Nephila*)

The silks of both *C. citricola* and *N. madagascarensis* underwent degradation in the presence of MMP2, MMP9, ELNE and α-chymotrypsin as seen in **Figure 23** and **Figure 24**. When compared to the smooth silk of the negative control fibres, roughing could be seen after incubation in each protease.

In the case of *N. madagascarensis*, seen in **Figure 24**, the fibre was seen to undergo pitting and breakages at the points of degradation, compared to the control fibre. As the same technique was used for harvesting of all fibres, breaks within the fibre was not introduced artificially. In addition to this, the control images were taken from the same fibre and showed no sign of physical deterioration.

Significant pitting was also seen in the presence of 120 mM α-chymotrypsin. These results are similar to that observed with silkworm silk film degradation in the presence of α-chymotrypsin [84] as reported by Brown *et al.* Brown found that α-helical content was reduced while β-sheet content increased during enzymatic proteolysis, attributed to

α-chymotrypsin's preference for α-helical motifs. Most prevalent in hydrogel degradation, it was suggested that the protease had greater access to the 3D architecture of the hydrogel compared to the 2D films.

The high protease concentrations are likely to have contributed to the results seen in **Table 16**. Without further investigation, it is difficult to assess fibre sensitivity to α-chymotrypsin. With lower concentrations it might be possible to establish fibre susceptibility to incremental increases of protease concentration. This information could also be compared to silkworm silk to determine the effect of the fibre morphology on protein degradation. As further laboratory investigation was preventing during the COVID pandemic, this line of enquiry was not investigated further.

Although birefringence microscopy images were taken for all fibres, the greatest difference in birefringence was observed by *N. madagascarensis* fibres in MMP2 and α-chymotrypsin, seen in **Figure 24**, compared to the faint negative control fibres. Polarised light was seen throughout the fibre which, coupled with bright field images, suggested that degradation had occurred through the fibre [84]. This further supports the hypothesis that degradation of silk fibres resulted in an increase of fibre crystallinity and light polarisation [51,235].

From the *in silico* analysis the C-terminus of *N. madagascarensis* consisted of two MMP2 cleavage sites (**Table 15**) identified by the prediction software and scored 50 from the target screens (**Figure 17**) within a range of 48 – 74. Placing it in the lower half of results, the *in silico* analysis suggested that degradation could take place but to a lesser extent than other silks that had been analysed. A similar result was predicted from MMP9 screens, identifying four cleavage sites (**Table 15**) and generating an overall score of 20 within a 14 – 37 range (**Figure 19**) although degradation was observed with half the concentration of MMP9 compared to MMP2. As the MaSp1 C-terminus only makes up a fraction of the silk fibre however, it is likely that further degradation occurred in other regions of the spidroin, explaining the greater physical degradation observed.

3.4.4.3 Nursery-web silk degradation (*Dolomedes* and *Pisaura*)

Unlike orb web silk, the silk of the nursery-web family (Pisauridae) did not undergo noticeable degradation, seen in **Figure 25** and **Figure 26**. Although small regions of fibre deterioration were observed with MMP2, the majority of the silk fibre was unaffected. When compared to the negative control, fibres that had been incubated with MMP9 and ELNE remained smooth and unmarked by the proteases. As C-terminal sequence of *D. tenebrosus* had been analysed for possible protease cleavage sites, it was possible to evaluate this conclusion.

The C-terminus of *D. tenebrosus* MaSp1 was the smallest of the analysed sequences at 5.7 kDa and produced *in silico* scores of 46 and 14 for MMP2 (**Figure15**) and MMP9 (**Figure 18**) respectively, the lowest of all the scores produced. The prediction software identified three sites with the peptide for MMP2 and four sites for MMP9, seen in **Table 13** and **Table 15,** respectively. While the small size of the peptide effected the scores, the results from both *in silico* and *in vitro* experiments support each other. Apart from MMP2, which generated some *in silico* results and observable degradation, the silk was not expected to be cleaved by MMP9.

As the same physical degradation was observed for the silk of *P. mirabilis*, it suggested that similar results would be found if the sequence were analysed for protease cleavage sites. At this time, no sequences are currently available to confirm this hypothesis.

The silk of *E. australis* would also be important to investigate as an alternative approach. Residing in the same family (Pisauridae) as *Dolomedes* and *Pisaura*, it is unknown if its silk would display similar physical degradation behaviour. From the *in silico* studies, they suggest that degradation could occur with both MMPs with greater degradation occurring when incubated with MMP9, see **Table 14** and **Table 15**. Although the recombinant protein 4RepCT consists of the *E. australis* C-terminus, the fibres produced have very different morphology and prevent accurate comparisons [28].

3.4.4.4 Tangle-web degradation (*Pholcus*)

Unlike the other silks that were reeled directly onto the microscope slides, the silk of *P. phalangioides* was collected from a freshly formed web and wrapped around the slide. As a result, they behaved differently to those that had been force-reeled. In particular, the silk was seen to undergo supercontraction as it formed tightly packed coils in the presence of H_2O, see **Figure 27**. This difference in silk behaviour is likely due to the tensions that the silks were produced under [237,238]. The force-reeled samples consisted only of dragline silk as they were collected directly from the spinnerets of the spiders. Silk harvesting under these conditions will have resulted in greater tension than if spun at the leisure of the spider. It is also possible that, although effort was taken to ensure dragline silk was removed from the web by selecting the 'spokes' of the complex tangle web, the fibres were a mixture of different silk types. As explained in **Section 1.1.1**, each silk has unique properties to allow it to carry out its function [22,23]. If the silk sample contained a mixture of silk types, it is possible that the unique coiling observed was not dragline silk [237,239].

3.4.5 Consolidating physical degradation to *in silico* predictions

As expected from the *in silico* predictions, many silks underwent proteolytic degradation. Although the degradation of *D. fimbriatus*, *P. mirabilis* and *P. phalangioides* silk was less apparent, some degradation was seen from MMP2 in all samples. The specificity of both MMPs suggested that the target sequences recognised by both enzymes were present in each silk fibre. Without further investigation however, it was not possible to determine the location of the enzymatic cleavage within each spidroin.

3.4.6 MMP target sites in nature

While MMP homologues have been found in the genomes of animals spanning *Chordata* and *Arthropoda* phylum, it is very unlikely that spider silk would come into contact with these enzymes in the wild [240,241]. Moreover, the ability of some spiders to eat their own silk for food or repair suggests that the silk would be susceptible to host digestive

proteases, rather than those involved in ECM remodelling [72,171]. Compared to ECM proteases, digestive proteases have broader substrate specificity, explaining the degradation by digestive enzymes such as α-chymotrypsin and Protease XIV seen in the literature [72,84,175]. With this in mind, it is unlikely that ECM target sequences were retained by selective pressure [53]. From this, it should be considered that the presence of specific sequences within the silk fibres was not part of advantageous evolution during divergence [52,171].

3.5 Conclusions

Using the literature on MMP specificity, it was possible to construct a range of target sequences recognised by MMP2 and MMP9. These sequences were successfully compared against the terminal sequences of natural MaSp1 from a range of different spider species. By identifying naturally occurring MMP substrate sequences, it was possible to identify potential future fibres for further investigation as biomaterials. In doing so, it allows greater understanding of expected silk properties when new-silk inspired biomaterials are investigated. By utilising silk that may be expected to contain enzymatic target sites within their sequences, it could allow the development of biodegradable materials with tune-able degradation rates.

Online prediction software was also utilised to identify target sequences within the spidroins, estimating each fibre's susceptibility to proteolytic degradation. The presence of the target sequences was confirmed by *in vitro* degradation studies. The degree of degradation also supported the coverage and number of sites proposed the *in silico* studies.

This work also serves to highlight the difference between both *in silico* approaches. Proteolytic cleavage was accurately predicted by the identification of exact cleavage sites within the spidroin sequences using online prediction software. However, this technique fails to identify areas within a sequence that could be utilised for further degradation studies. In the development of spidroins with tuneable degradation properties,

the ability to identify sequence motifs that could be mutated to introduce enzymatic target sequences is essential. Using the profile technique described in the chapter, the artificial spidroin 4RepCT was mutated to significantly alter its potential degradation rate.

This chapter highlights the need for recombinant spidroin production in the development of future biomaterials. Although natural spidroins contain regions of high conservation, variation within spidroin sequences risks affecting the degradation behaviour of the resulting biomaterial. To prevent this, it is important that spidroins are produced genetically identical, a feature of the recombinant approach. However, these points of variation also identify residues within areas of sequence conservation that may be confidently mutated without significantly altering the spidroin or protein termini. Using these as a guide to the number of amino acids supported in a single location, *in silico* prediction studies can be used alongside these mutants to introduce complete target sequences throughout the spidroin sequence. By influencing the number of complete target sequences, the degradation behaviour of the spidroin will be significantly altered, enabling tuned degradation.

4. Proteolytic degradation of 4RepCT

4.1 Introduction

4.1.1 Biomedical material breakdown

Since the introduction of biomaterials to artificially recreate environments within the body, the understanding and prediction of interactions between host and implant have been vital for improving patient safety and wound recovery [242]. One part of this complex procedure is understanding a material's degradation during and after it has finished as a scaffold [243]. To ensure accurate predictions, materials must be studied in conditions that closest resemble that of the host environment at the scene of the activity. For materials involved in sub-cutaneous wound healing such as ECM scaffolds, these conditions include behaviour in the presence of proteolytic enzymes that are released by the host in response to trauma to prevent infection.

As a result, artificial scaffolds destined for wound conditions should be studied *in vitro* with exposure to these proteases. The incorporation of biopolymers into wound scaffolds also presents a danger in the form of unexpected thrombosis seeded from the release of macroscopic degradation products as a direct result of proteolytic cleavage as shown in **Figure 28** [244–246]. If released into the bloodstream, the accumulation of these degradation products could cause life-threatening complications such as blood clots, ischaemia or stroke. In an attempt to prevent this, biomaterial behaviour is usually studied in the presence of various chemical and biological degrading environments [247–249]. For this reason, the degradation behaviour of silk-based biomaterials have previously been studied both *in vitro* and *in vivo* to better improve understanding and to improve the final biomedical product [66,72,88,90,250]. Compiling information gathered from these experiments will allow researchers to efficiently develop 4RepCT as a biomaterial, improving the safety of the final products derived from it.

Of the 23 MMPs expressed in humans, particular interest is given to those expressed during the course of wound healing and recovery [251,252]. Of these, many studies have focused on MMP2 and MMP9,

providing a high quality of proteomic data including expressed protein concentrations in normal, acute and chronic wound conditions [253–256]. Much work has also been conducted on accurately identifying substrate motifs for both MMPs, allowing enzymatic profiles of 4RepCT to be compiled with confidence [172,173]. As gelatinases, both enzymes are easily quantified by gelatin zymography, providing visual confirmation of activation and level of activity therein.

Although both MMPs are overexpressed during wound recovery, it is the sustained overexpression of MMP9 that is thought to contribute to the development of chronic wounds, preventing the wound from closing and allowing the entry of invading bacteria [257,258].

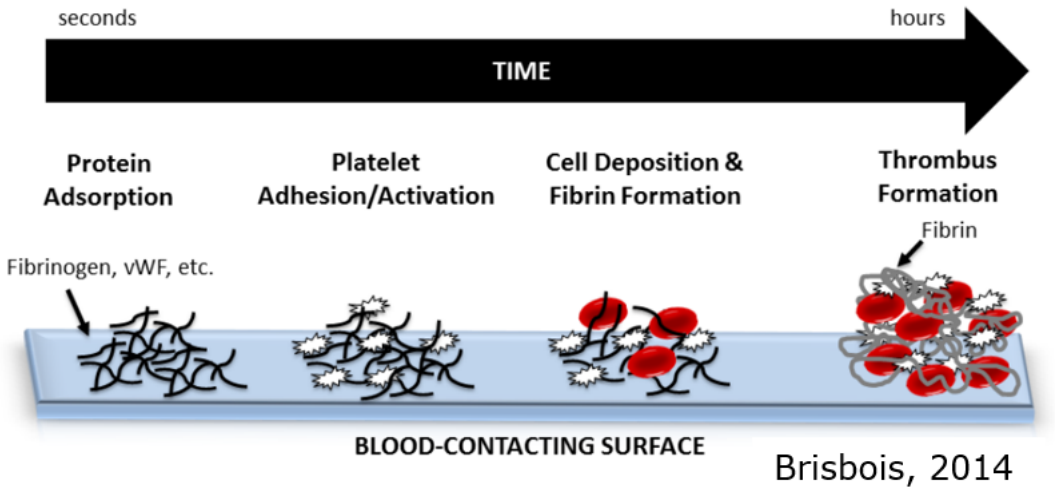

Figure 28. Sequence of events leading to thrombus formation on blood-contacting surfaces (e.g. implanted medical devices).

Using Proteomic Identification of protease Cleavage Sites (PICS), the cleavage sites of many human MMPs have been determined by Eckhard *et al.* Within the study, over 4300 cleavages were performed to produce a detailed 'heat map' of the six amino acid target sequence for each MMP [172]. Within a wound environment, a single MMP may have multiple different substrate proteins, each containing the specific motif for that respective protease. Utilising PICS, it allowed variation within the sequences to be identified while also revealing the overall sequence that

all substrate proteins must contain. As gelatinases, MMP2 and MMP9 have similar target sequences, although some variation does occur.

4.1.2 Development of 4RepCT as a biomaterial

In addition to investigating insoluble 4RepCT fibre degradation, its behaviour in alternative forms should also be examined to develop a thorough understanding of the material's properties. However, the difference between these material conformations usually result from differences in protein sequence. For example, soluble 4RepCT and insoluble fibres are facilitated by the loss of the thioredoxin solubility fusion protein. This 15 kDa protein is significant in size and is highly structured, a combination of alpha helices and beta sheet folds. Unlike fibres however, 4RepCT films are formed from soluble protein which becomes insoluble as the solvent is removed by evaporation. Despite the presence of the thioredoxin solubility tag, the process of becoming insoluble is irreversible.

The secondary structure of 4RepCT is divided into two sections, an amorphous repetitive domain and a highly conserved and structured alpha helical C-terminus shown in **Figure 29**. The model of 4RepCT's C-terminus was determined using I-TASSER sequence [259] and structure homology database at infinite dilution and pure water and produced by the Thomas lab (unpublished) [260].

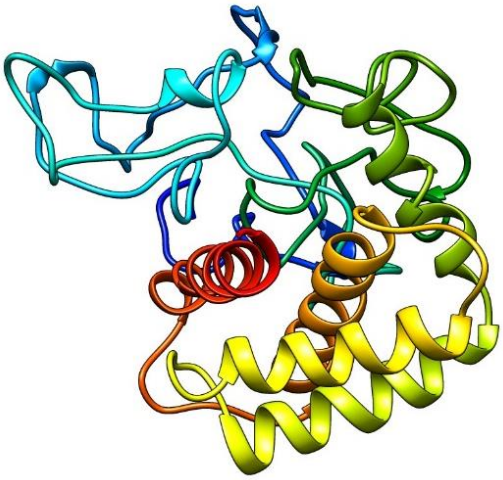

Figure 29. The repetitive and C terminal domains of 4RepCT. The ordered C terminal contains five α helices while the amorphous repetitive region does not display inherent structure. The thioredoxin solubility tag has been removed in this model. This model was constructed using I-TASSER, an online homology modelling program at infinite dilution and in pure water by Thomas research group (unpublished).

The amorphous nature of this domain, generated by the flexible poly-glycine motifs [20] allows access to any protein that may be interacting with the spidroin, specifically proteolytic enzymes. The flexible nature of the repetitive region prevents it from being imaged accurately by NMR or X-ray crystallography as the variability of position produced in this region is too great to determine [261]. In comparison, the C-terminus contains five α-helices that are thought to be important for dimer interactions and subsequent polymerisation [36,262]. These alpha helices are highly conserved within naturally occurring MaSp C-termini, including the QALLEVITAL motif as seen in **Figure 30** [31,45].

The thrombin cleavage site is situated at the 'neck' of the protein, immediately after the thioredoxin solubility tag, releasing the 4RepCT protein once cleaved. If the protein underwent MMP degradation at or near this point before thrombin cleavage, it is likely that the resulting cleavage product could also form fibres. If MMP degradation occurred within the C-terminus however, it is unlikely that the resulting

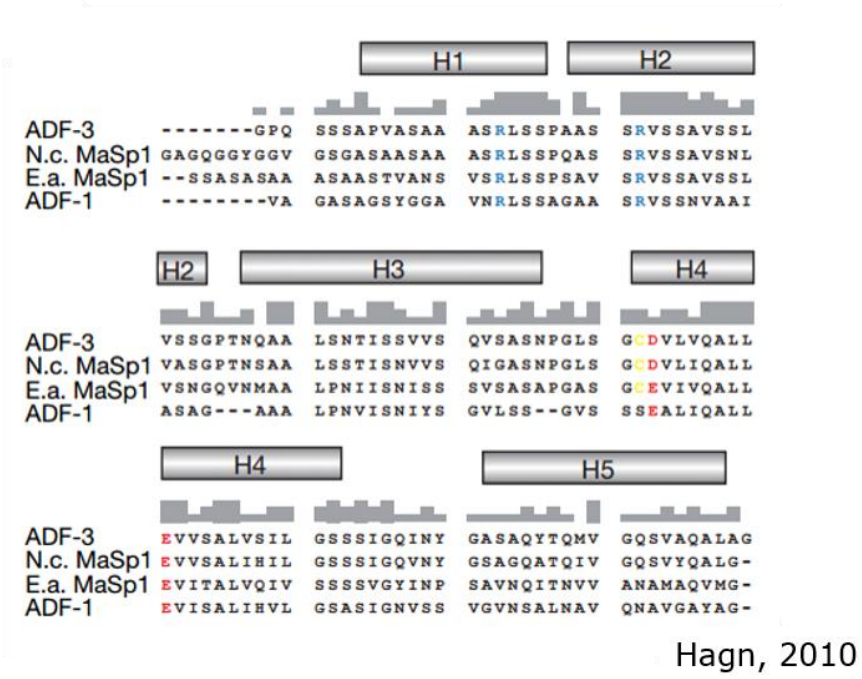

Figure 30. Sequence alignment of the C-terminal NR domains of the major ampullate silk proteins (MaSp) of *A. diadematus*, *N. clavipes*, and *E. australis*, and minor ampullate silk fibroin (ADF-1) of A. *diadematus* (top to bottom). Grey bars indicate the degree of conservation between these sequences. The conserved charged residues are coloured.

degradation products would remain soluble if the conserved structure were disrupted or cleaved from the solubility tag.

It is well documented that the temperature of a wound and surrounding tissue increases in the presence of inflammation, as high as 42 °C [263]. However, tissue temperature of chronic wounds has been found to drop as low as 31 °C – 35 °C, some 7 °C lower than acute inflammation as blood flow is restricted during the formation of the chronic wound [264]. In light of this, the temperature at which the degradation protocols are conducted must be considered. Investigations *in vitro* should therefore be conducted at a range of temperatures to reflect the range of conditions encountered within the host environment. The temperatures investigated in this chapter ranged from 25 °C – 37 °C to reflect the variation observed in chronic wound environments.

4.2 Aims of the chapter

4RepCT has been established as miniaturised recombinant spidroin that spontaneously forms macroscopic fibres at the removal of its thioredoxin solubility tag. This investigation sought to investigate the effects of potential protein degradation as a result of exposure to MMP2 and MMP9 at concentrations 10-fold lower than that observed at chronic wound conditions.

At these concentrations, the degradation behaviour of 4RepCT could be observed in biological environments below that seen at the extremes of chronic wounds without the need for excess costly enzyme use. 4RepCT was investigated in a number of different morphologies including soluble protein, fibres and films for time periods of up to one week at physiological and laboratory temperatures. From this investigation further studies are proposed in an attempt to influence the rate of observed degradation.

4.3 Results

4.3.1 *In silico* screening of TRX_4RepCT

The primary amino acid sequence of TRX_4RepCT was analysed for pre-existing target sequences for ELNE, α-chymotrypsin and wound-related MMPs (MMPs 1 – 3 and 7 – 13) as seen in **Figure 31**. The target sites for elastase and MMPs were determined from the literature and compared against the TRX_4RepCT sequence [172,173,192,206] and supported by online cleavage prediction sites [224]. While α-chymotrypsin and ELNE cleaved after a single amino acid (hydrophobic and alanine/valine respectively), the six-residue target sequences of MMPs required annotation that identified the degree of sequence coverage. As a result, the number of residues flanking the cleavage motif were coloured accordingly: 2 residues = yellow/orange, 3 residues = light green, 4 residues = dark green, 5+ residues = pink. To recognise the difference in ELNE's preference specificity for valine over alanine, valine residues were coloured green while alanine residues were highlighted in yellow.

As with the *in silico* investigations of natural silk, seen in **Section 3.3.3,** each profile was also scored to reflect the coverage of each enzyme. The highest scoring MMPs (MMP1, MMP2 and MMP9) are shown in the figure with scores of 42, 180 and 44, respectively. The elastase and chymotrypsin scores were also recorded to reflect the enzyme's potential to cleave the protein, at 119 and 30, respectively.

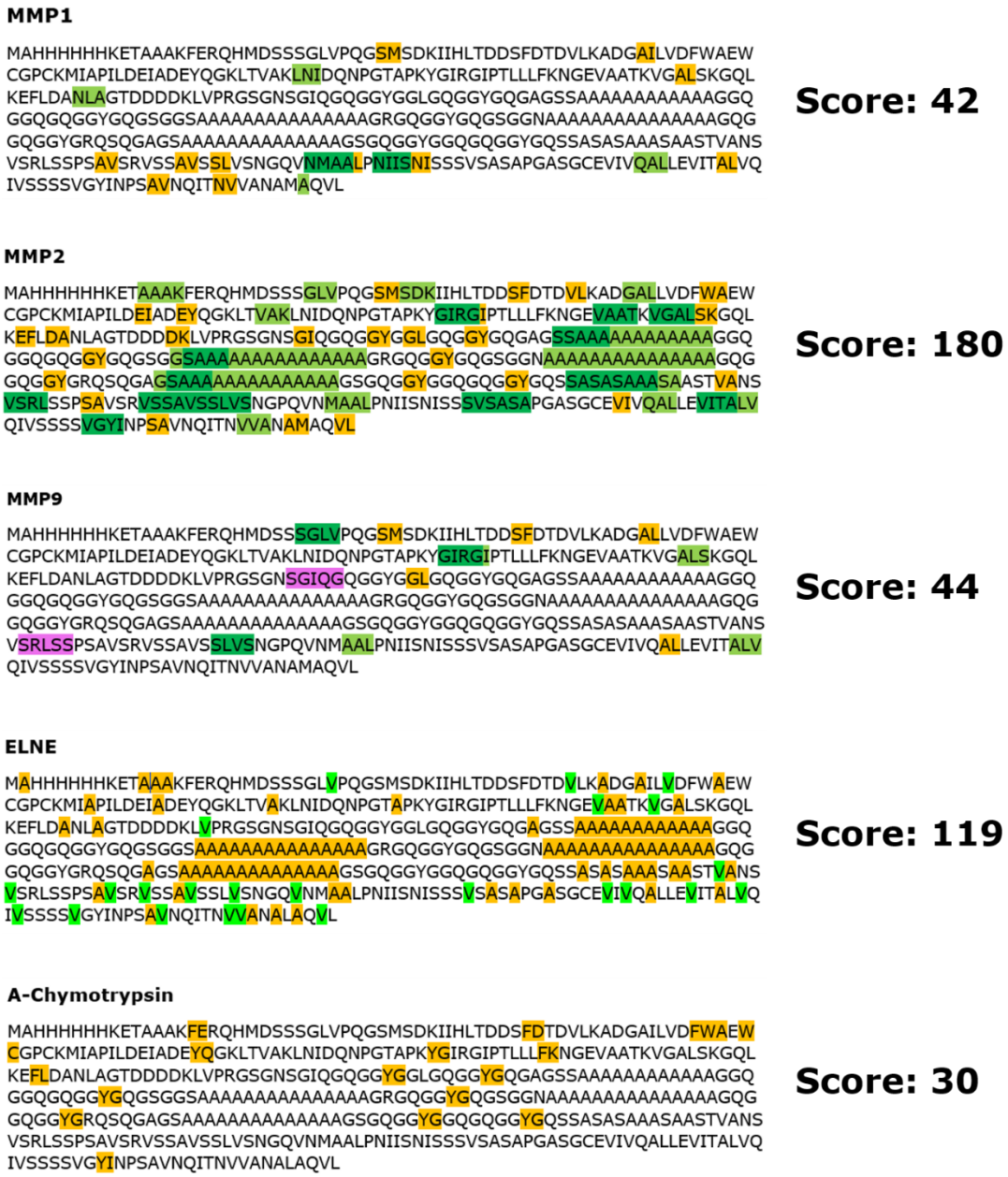

Figure 31. The amino acid sequence of TRX_4RepCT was compared to target sequences of MMPs, neutrophil elastase and chymotrypsin to generate *in silico* profiles. Matching residues over the cleavage point were highlighted according to the number of consecutive amino acids (2 residues over the cleavage point were highlighted yellow, 3 highlighted in light green, 4 in dark green and 5 or more in pink). The profiles were also scored to reflect both the coverage of the protein and the nature of the identified cleavage sequences.

4.3.2 Gelatinase zymography

To confirm protease activity, MMP2 and MMP9 were analysed by gelatin zymography electrophoresis. Utilising the same techniques and concepts as SDS-PAGE, protease samples were prepared to final concentrations of 500, 1000, 2000, 5000, 10000 and 15000 pg/ml by serial dilutions of the activated stock aliquots. In the presence of MMP, the gelatin was cleaved and prevented staining to produce a white band as seen in **Figure 32**.

As expected, zymogenic pro-form MMP was also seen at the higher molecular weight bands with subsequent active protease in the bands below. Although not inherently able to cleave the gelatin substrate, the renaturing process is thought to expose the active site of the enzyme to the substrate, allowing subsequent cleavage despite existing in its inactive form.

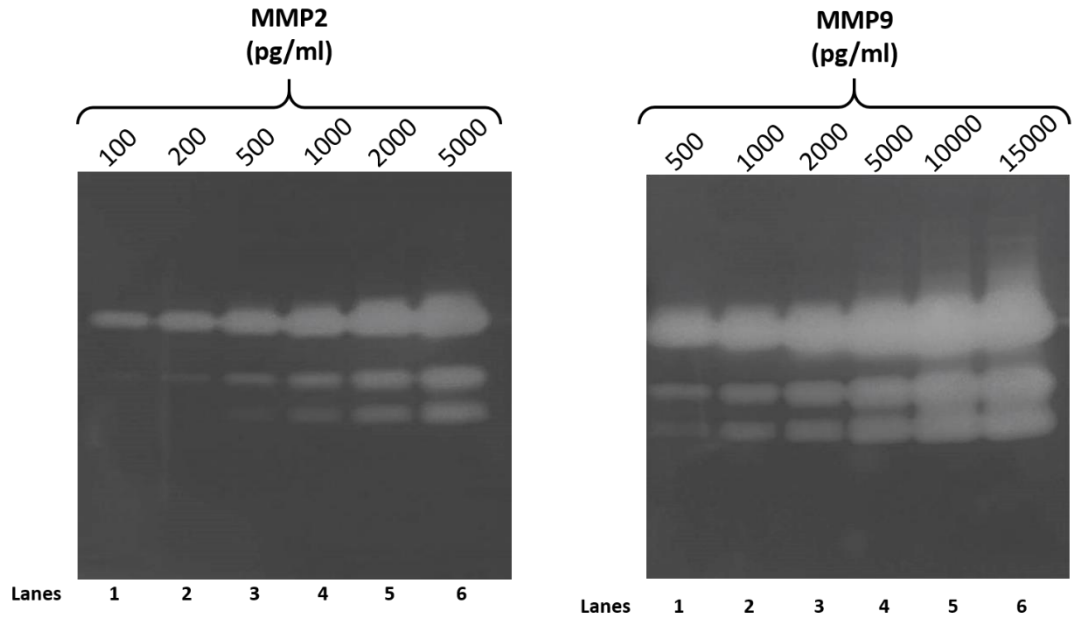

Figure 32. Active MMP2 and MMP9 were analysed by gelatin zymography and stained using GelCode Blue Protein Stain over 72 hrs at room temperature with agitation. A standard protein curve was established at 500, 1000, 2000, 5000, 10000 and 15000 pg/ml.

4.3.3 Proteolytic degradation of TRX_4RepCT

After storage at -80 °C, TRX_4RepCT protein aliquots were thawed slowly on ice to avoid protein aggregation. Protein concentration was checked and recorded as 1.53 mg/ml suggesting that no protein had been lost before being diluted to 1 mg/ml with 20 mM Tris pH 8.0.

Analysis by 15% (w/v) SDS-PAGE before the degradation protocol confirmed the presence of the full length 39 kDa band as seen in **Figure 33**. In addition to the monomeric protein, the 80 kDa dimeric protein could also be seen. Additional proteins could also be seen and were attributed to products of expression. Despite attempts to further purify 4RpeCT by gel filtration, these proteins could not be removed, similar to previous expression from the literature [28].

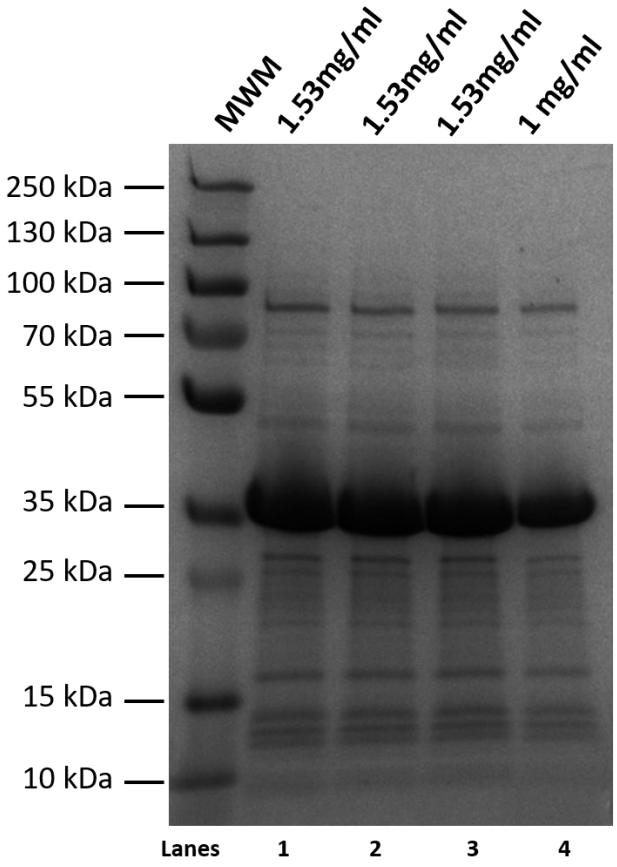

Figure 33. Before degradation, thawed TRX_4RepCT was analysed by 15% (w/v) SDS-PAGE to ensure protein solubility and to give reference for potential degradation. TRX_4RepCT is seen as a 39 kDa band in all lanes. The higher molecular weight band of 80 kDa indicated the presence of dimeric TRX_4RepCT. Lower molecular weight bands present in the gel were a result of recombinant expression.

4.3.3.1 Stability of TRX_4RepCT in 20 mM Tris pH 8.0

To investigate the stability of soluble TRX_4RepCT in 20 mM Tris pH 8.0, TRX_4RepCT was incubated in assay buffer for 24 hrs at 25 °C and 37 °C as seen in **Figure 34**.

At 25 °C TRX_4RepCT remained soluble throughout the experiment, although a small amount was seen in the insoluble fraction (**lane 9**), seen as a 39 kDa band in all lanes. A second band (20 kDa) could also be seen in the insoluble fraction, although the protein was not identified.

At 37 °C 4RepCT remained soluble for 2 hrs (**lane 5**), before the band was lost. The same band was then observed faintly in the insoluble band after the incubation period, shown in **lane 9**. Lower molecular weight bands were also lost after 2 hrs. Unlike in the presence of proteolytic enzymes (**Figure 36**, **Figure 37**, **Figure 38**, **Figure 39**), no low molecular weight bands became visible during the protocol.

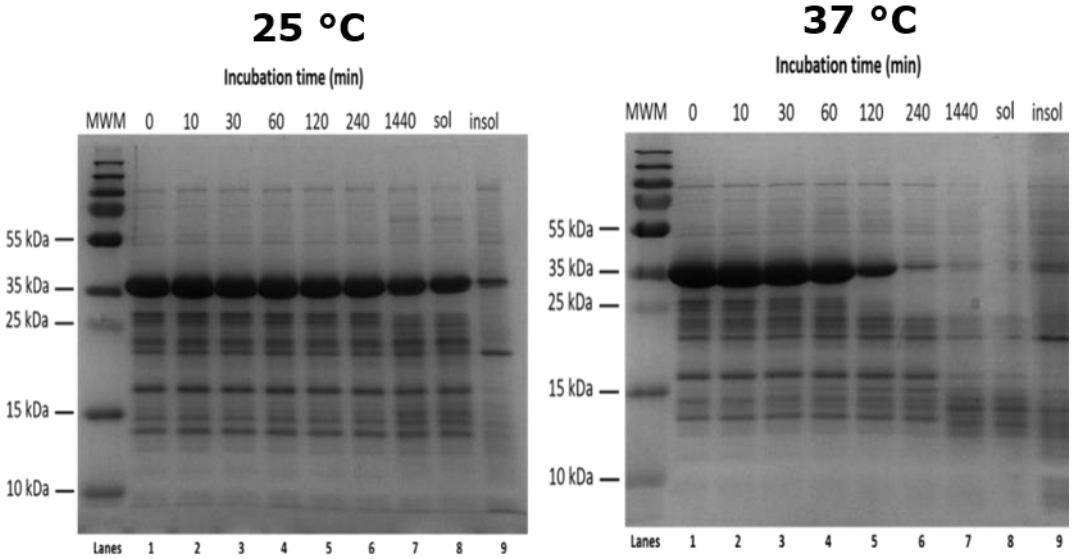

Figure 34. To determine the activity of the proteases, a negative control containing only TRX_4RepCT and 20 mM Tris pH 8.0 was incubated at 25 °C and 37 °C for 24 hrs. At 25 °C the protein remained soluble and no degradation was observed. At 37 °C, the 39 kDa band was lost after 2 hrs, seen in lane 5. Although the protein band was lost, no degradation products were observed at later time points.

4.3.3.2 Stability of TRX_4RepCT in dH_2O

To investigate the effect of H_2O on the solubility of TRX_4RepCT, soluble TRX_4RepCT was incubated in dH_2O for 24 hrs as seen in **Figure 35**.

At 25 °C TRX_4RepCT remained soluble throughout the experiment, although a small amount was seen in the insoluble fraction (**lane 9**) after it was lost after 4 hrs (**lane 6**), seen as a 39 kDa band in **all lanes**.

At 37 °C, protein solubility was lost after 2 hrs (**lane 5**) instead of 4 hrs. As with incubation in assay buffer (**Figure 34**), lower molecular weight bands remained constant throughout the protocol.

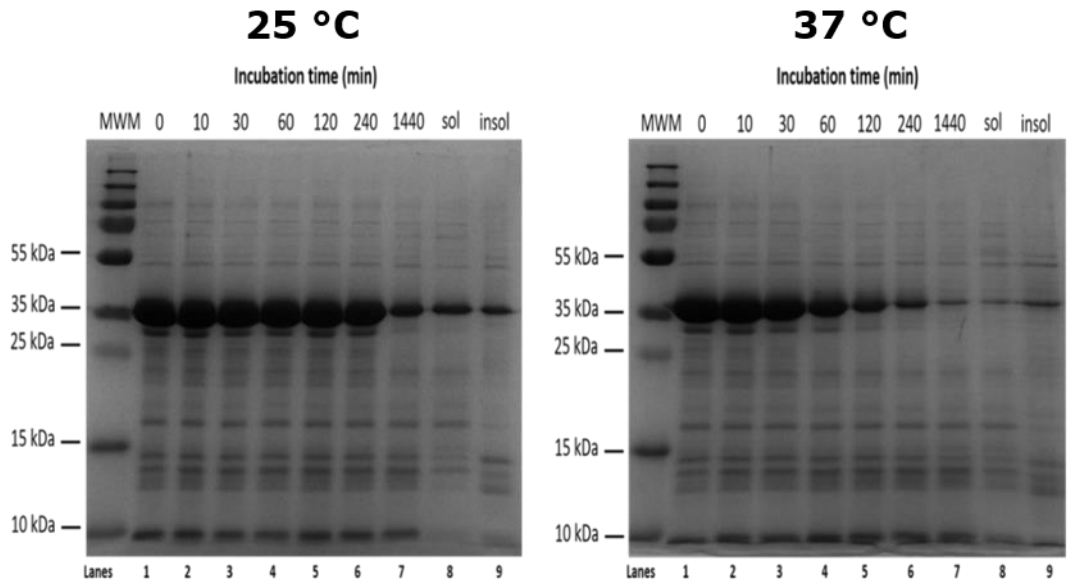

Figure 35. To determine any effect of 20 mM Tris storage buffer on TRX_4RepCT stability, the protein was incubated in dH_2O at 25 °C and 37°C for 24 hrs and analysed by 15% (w/v) SDS-PAGE. At 25 °C TRX_4RepCT remained soluble, shown by the 39 kDa band in all lanes, although some soluble protein was lost up to 24 hrs. At 37 °C TRX_4RepCT was lost after 4 hrs, seen in lane 6, becoming insoluble after this time, shown by a 39 kDa band in lane 9.

4.3.3.3 Degradation of TRX_4RepCT by MMP2

TRX_4RepCT was incubated in 20 mM Tris pH 8.0 in the presence of 11.3 µM MMP2 (>1000 pmol/min/µg protein) for 24 hrs at 25 °C and 37 °C at a final protein concentration of 1 mg/ml, as seen in **Figure 36**.

Samples were collected at time points of 0, 10, 30, 60, 120, 240 and 1440 minutes and denatured in the presence of SDS by heat before being analysed by 15% (w/v) SDS-PAGE. After 24 hrs, samples were centrifuged to pellet any insoluble protein that had been produced over the course of the experiment, seen in **lane 9** in both gels.

Soluble TRX_4RepCT (39 kDa) was seen at 4 hrs (**lane 6**) and 2 hrs (**lane 5**) at 25°C and 37°C respectively before being lost from subsequent time points, as seen in **Figure 36**. At this point, low molecular weight (<15 kDa) bands became visible (**lanes 7 and 6**). These degradation products were insoluble after 24 hr, seen as dark bands in **lane 9** between 10 – 25 kDa.

Lanes containing just MMP2 (**lane 10** in both gels) appeared blank to reflect the low concentration of protease used.

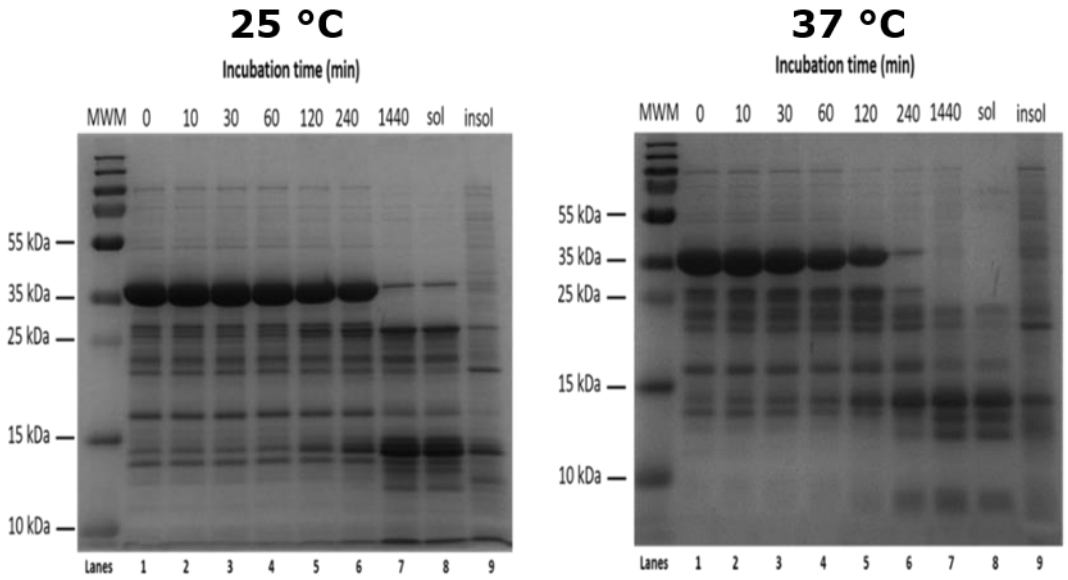

Figure 36. TRX_4RepCT was subjected to MMP2 protease for up to 24 hrs at 25 °C and 37°C respectively and analysed by 15% (w/v) SDS-PAGE. After 24 hrs, soluble 39 kDa TRX_4RepCT was degraded at 37 °C, seen in lane 6. At 25 °C the protein remained for 4 hrs until it was degraded by the protease. Low molecular weight degradation products were seen from 4 hours at 37 °C. Other bands were attributed to products of expression and were dismissed from this experiment.

4.3.3.4 Degradation of TRX_4RepCT by MMP9

TRX_4RepCT at a 1 mg/ml concentration was incubated in assay buffer in the presence of 5.84 µM MMP9 (>1300 pmol/min/µg protein) at 25 °C and 37 °C. As with MMP2 incubation, samples were taken after 0, 10, 30, 60, 120, 240 and 1440 minutes and analysed by 15% (w/v) SDS-PAGE.

While soluble TRX_4RepCT (39 kDa) remained present throughout the experiment at 25 °C, the 39 kDa protein was lost after 4 hrs at 37 °C, seen in **Figure 37**. Similar to MMP2 (**Figure 36**), low molecular weight (<10 kDa) degradation products could be seen after 24 hrs at both temperatures (**lanes 7 and 8**). The total insoluble fraction was pelleted and analysed after resolubilisation by 6X SDS-PAGE loading dye. At both temperatures two bands (>10 kDa and 20 kDa) were observed in the insoluble fraction (**lane 9**) and attributed to degradation products, becoming insoluble once cleaved from the full length protein. Some full-length protein (39 kDa) was also observed in the insoluble fraction (**lane 9**).

As with MMP2, the enzyme-only lane appeared blank to reflect the low concentrations of protease present within the samples.

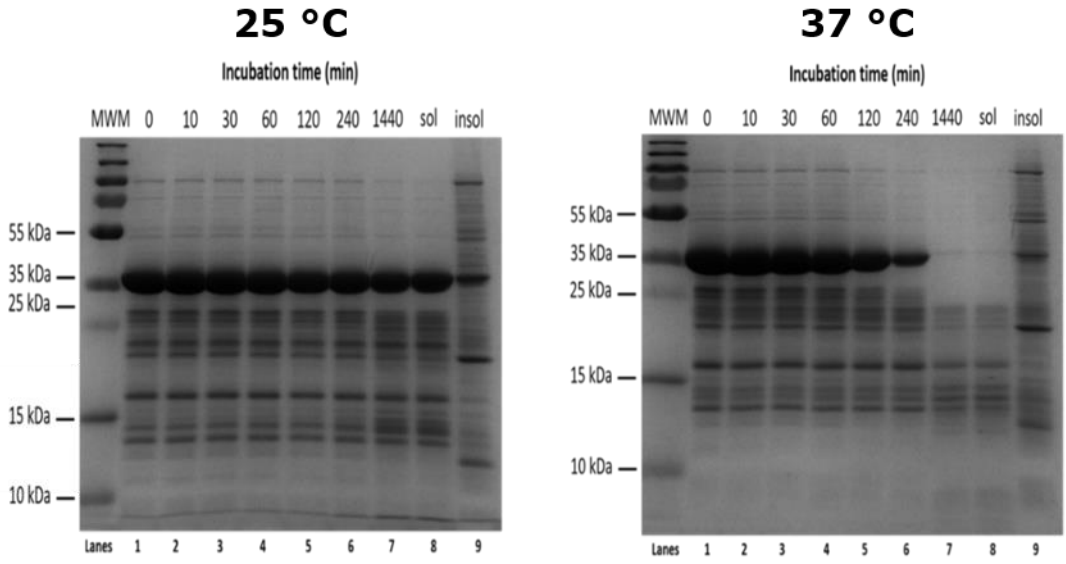

Figure 37. TRX_4RepCT was subjected to MMP9 protease for up to 24 hrs at 25 °C and 37 °C respectively and analysed by 15% (w/v) SDS-PAGE. After 4 hrs, soluble 39 kDa TRX_4RepCT was degraded at 37 °C, seen in lane 6. At 25 °C the protein remained soluble past 24 hrs. Unlike MMP2 degradation, low molecular weight degradation products were not observed during the course of the experiment.

4.3.3.5 Degradation of TRX_4RepCT by ELNE

A positive control of ELNE was used to confirm TRX_4RepCT degradation as a result of the elastin-like poly-alanine tracts it contains [28,265]. Incubated at 25 °C and 37 °C, TRX_4RepCT was degraded in the presence of 34 nM ELNE (20 µmol/min/mg protein) for 24 hrs as seen in **Figure 38**.

After 1 hr at 37°C, soluble TRX_4RepCT (39 kDa) was lost, seen in **lane 4**, while the same band remained throughout the experiment at 25 °C. At both temperatures, 23 kDa bands could be seen and became more prominent as the experiment proceeded seen in **lanes 3 – 8**.

At 37 °C low molecular weight degradation products were observed after 30 minutes (**lane 3**). Similar sized insoluble bands were observed at both temperatures after 24 hrs (**lane 9**). The low protease concentration resulted in no visible band in the enzyme only lane (**lane 10**).

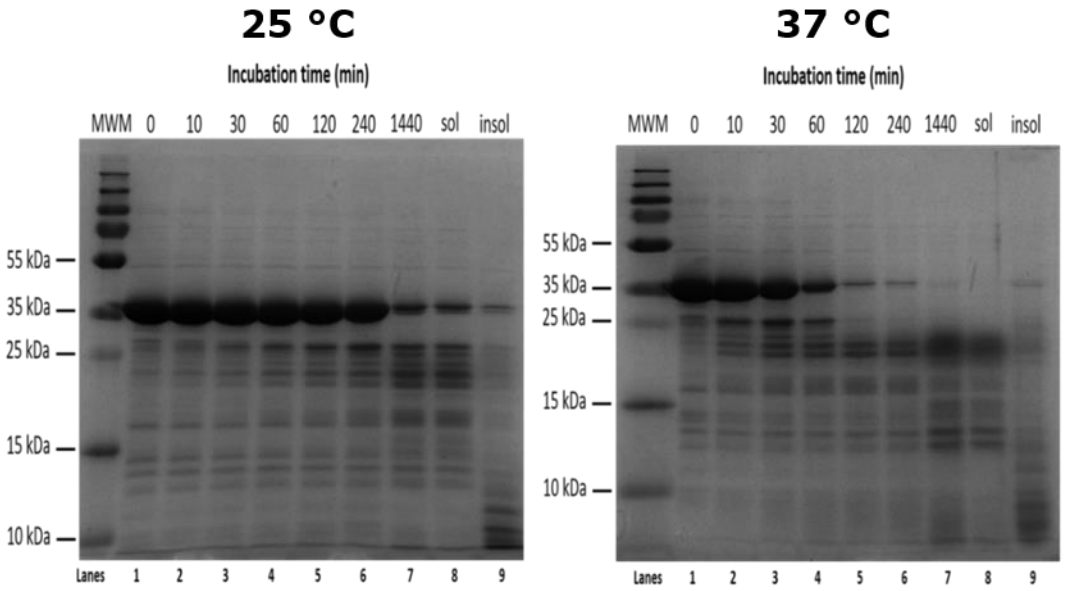

Figure 38. 4RepCT was subjected to human neutrophil elastase for up to 24 hrs at 25 °C and 37 °C respectively before being analysed by 15% (w/v) SDS-PAGE. After 1 hr, soluble 39 kDa 4RepCT was degraded at 37 °C, seen in lane 4. At 25 °C the protein remained soluble up to 24 hrs. Lower molecular weight degradation products were observed from 60 minutes.

4.3.3.6 Degradation of TRX_4RepCT by α-chymotrypsin

The high concentration of α-chymotrypsin was chosen to directly compare degradation of silkworm silks as investigated by Brown et *al* [84].

In the presence of 120 mM α-chymotrypsin (40 units/mg protein), TRX_4RepCT was found to degrade almost immediately as seen in **Figure 39**. Although samples were taken immediately, the full length 39 kDa protein was not observed at any point in the assay. Although it was not observed during the assay, TRX_4RepCT was prepared to 1 mg/ml before α-chymotrypsin was added at T=0 (**lane 1**).

Instead, the 25 kDa protease band was seen in all lanes, becoming insoluble after 24 hrs, seen in **Figure 39 lane 9**. Bands approximately 15 kDa also appeared to undergo degradation after 2 hrs (**lane 5**) before two bands of similar weight were observed after 24 hrs at both temperatures. As a result, no conclusions could be drawn from the experiment.

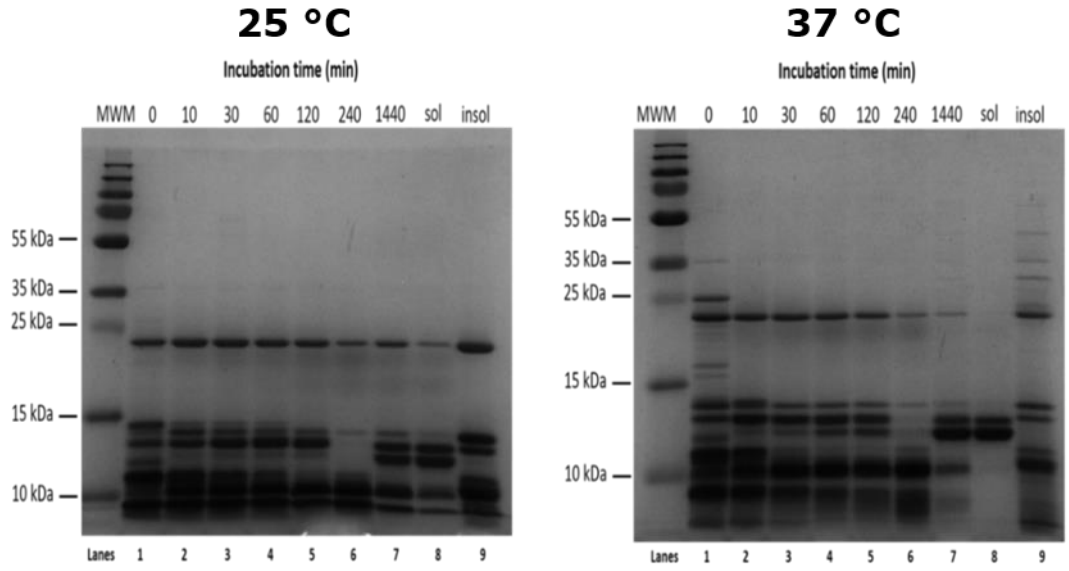

Figure 39. Cleavage of TRX_4RepCT by α-chymotrypsin over 24 hrs at 25 °C and 37 °C was analysed by 15% (w/v) SDS-PAGE. Although the 39 kDa band of 4RepCT was not seen, the 25 kDa protease band was seen at both temperatures throughout the experiment. In addition to the protease band, many smaller bands were visible throughout the experiment, but it was unclear if these had resulted from cleaved TRX_4RepCT.

4.3.4 Proteolytic degradation of insoluble TRX_4RepCT films

TRX_4RepCT films were subjected to control solutions of 0.8 mM ELNE (20 µmol/min/mg protein) (+ve) and H_2O (-ve) over 72 hrs at 37 °C with agitation. At this point, the supernatants were analysed by SDS-PAGE (lanes 2, 4, 6 and 8) while the films were washed with H_2O for a further 72 hrs as seen in **Figure 40a**. The resulting 'washed supernatants' were also analysed by SDS-PAGE (**Figure 40a**, **lanes 3, 5, 7** and **9**). The 5 mg/ml stock solution of TRX_4RepCT used to prepare the films was analysed in **lane 1** to allow protein size comparison.

The soluble protein could be seen in the stock lane (**lane 1**), but this was not observed in any other lane, suggesting that the soluble protein was no longer present. Bands between 10 – 15 kDa could be seen in the supernatant lanes (**lanes 2, 4, 6** and **8**) in both controls, although they were more prominent after ELNE proteolysis seen in **lane 2** and **lane 4**. No bands were observed in the washed supernatants, suggesting the washing had been effective at removing protein from the films. The films were then dried and analysed by weight loss.

Shown in **Figure 40b**, all films (n = 5) incubated in enzyme solution showed weight loss between 15% - 26% of their original mass, while water-incubated films underwent weight loss of 10% as non-film protein was lost from the assay container, reducing the final weight.

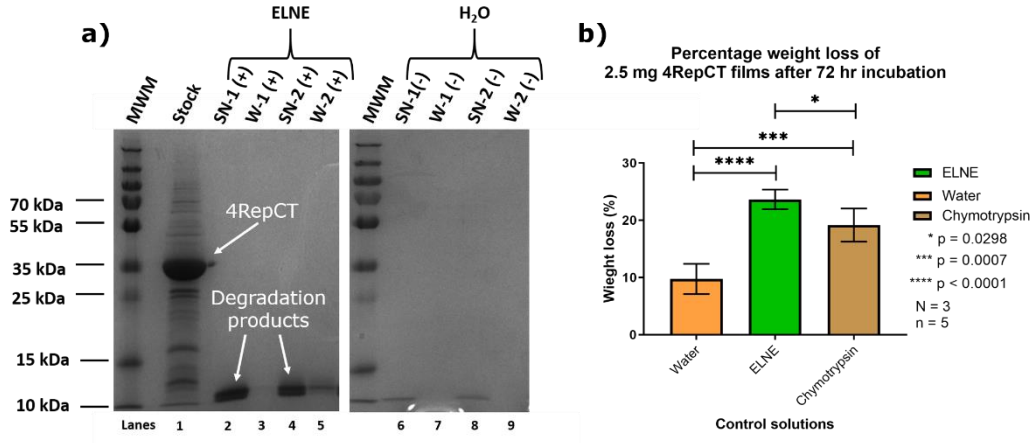

Figure 40. Degradation of TRX_4RepCT films seen by SDS-PAGE (**a**) and dry weight loss (**b**). **a**) TRX_4RepCT films were incubated in ELNE and H_2O over 72 hrs. After this time, bands 10 – 15 kDa could be seen in lanes 2 and 4. Faint bands were also seen in lanes 6 and 8, although these were less prominent than those produced by incubation with ELNE. **b**) Weight loss of TRX_4RepCT films was analysed after films had been thoroughly dried after washing. Weight loss of 15% – 26% was observed from films incubated in enzyme solution while 10% weight loss was observed from water-incubated films as non-film protein was removed from the reaction mixture.

4.3.5 Proteolytic degradation of insoluble 4RepCT fibres

Upon thrombin cleavage, 4RepCT remained soluble until agitation and macroscopic fibres were able to form spontaneously. The critical protein concentration for this was recorded as approximately 1.5 mg/mL in a reaction volume of 1 mL. At lower concentrations, insufficient protein was available in the surrounding solution to polymerise and form fibres.

4.3.5.1 Short term

Short term degradation was defined by incubation of 4RepCT fibres in MMP2 for up to 4 hrs. During this time, fibres were removed from the experiment after 30 minutes and 1hr (shown in **Figure 41**) in addition to 2 hr and 4 hrs.

Fibres were analysed using bright field microscopy at 10x and 40x magnification. Although some aggregate protein could be seen, indicated by the **red** arrow, macroscopic fibres were observed at all points throughout the experiment. The higher magnification images displayed the intrinsic disordered folding expected from spontaneous fibre formation, but no degradation of the fibres was observed.

4.3.5.2 Long term

Long term degradation was defined by incubation for up to 1 week. During this time, fibres were removed at defined time points of 24 hr and 1 week to be analysed by bright field microscopy at the same magnifications, as seen in **Figure 42**. When compared to the original fibres, shown at 0 min, more aggregation could be seen along the length of the fibres.

At the higher magnifications, fraying of the fibres could be observed after 24 hrs, shown by the **red** arrows, suggesting deterioration may have taken place.

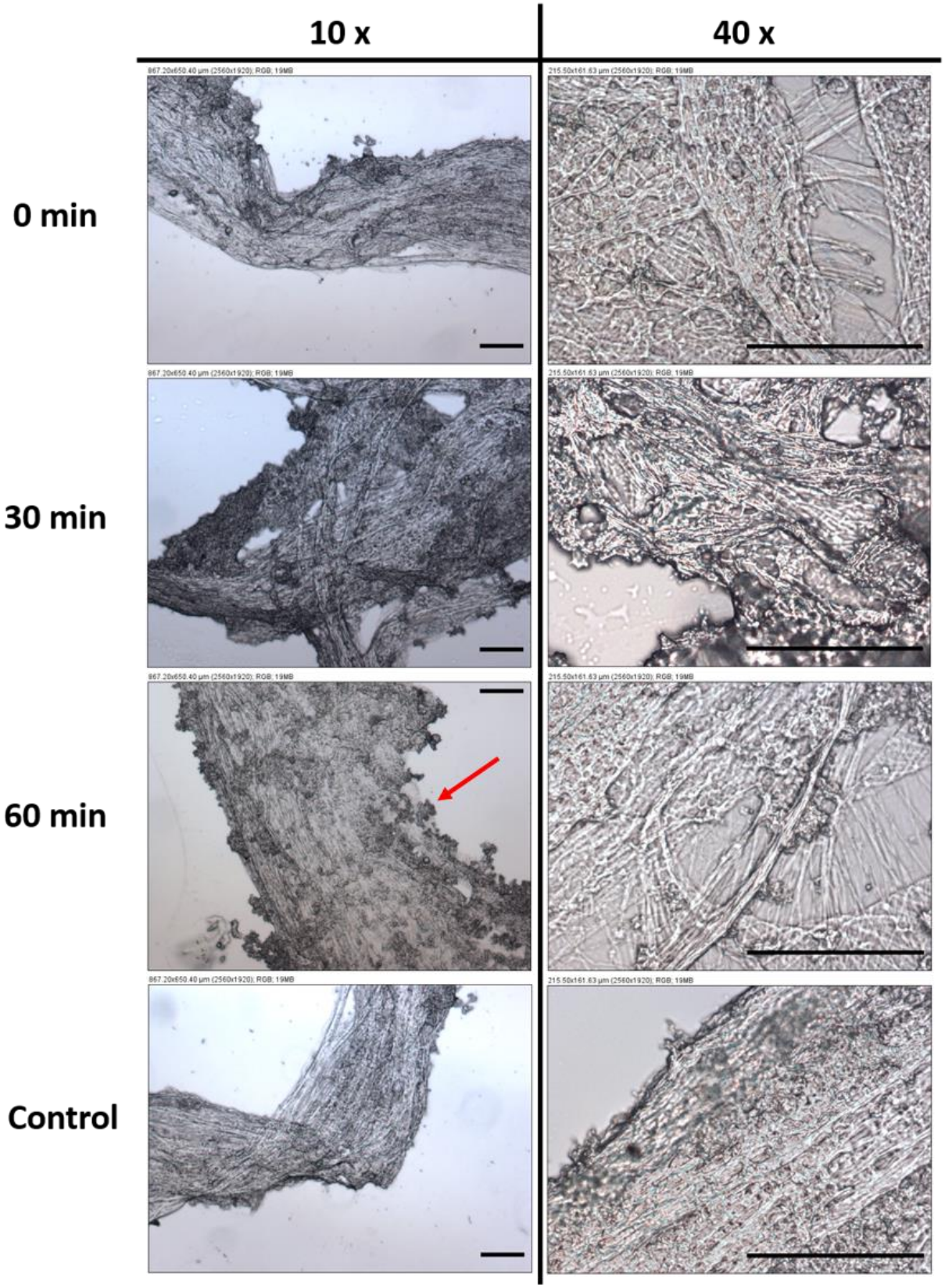

Figure 41. The effect of MMP2 incubation on 4RepCT fibres was investigated using bright field light microscopy at 10X and 40x magnification. Fibres were imaged over the course of 1 week to allow degradation to take place. Aggregated protein was observed after 60 min as indicated by the **red** arrow. Short term degradation was observed up to 4 hrs before further incubation up to 1 week. Images are representative of full image collection, shown in **Appendix 8.6.1** Scale bar = 100 µm.

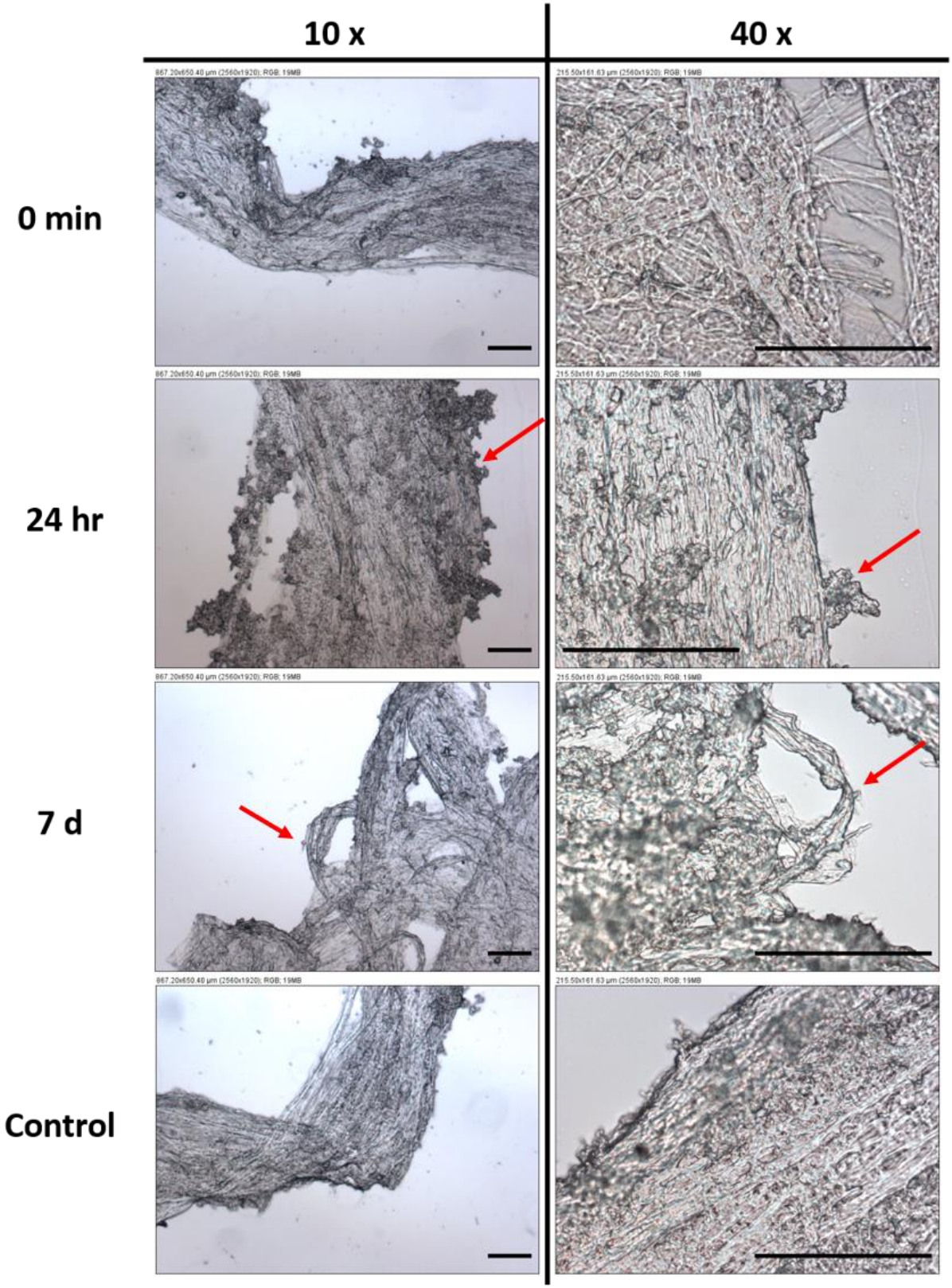

Figure 42. Degradation of 4RepCT fibres was observed by bright field light microscopy at 10x and 40x magnification. Fibres were imaged over the course of 1 week to allow degradation to take place. Degradation was seen in the form of fraying and accumulation of aggregated protein after 24 hrs, as shown by the **red** arrows. Long term degradation was observed up to 1 week during incubation at 37 °C. Images are representative of full image collection, shown in **Appendix 8.6.1.** Scale bar = 100 µm.

4.3.5.3 Effect of fibre degradation on dark field and birefringence microscopy

As with the natural fibres, *in vitro* degradation was also evaluated using dark field and birefringence microscopy as seen in **Figure 43** [6,9]. As described in **Methods 2.5**, samples were imaged at 45° to the light source for maximum visualisation [230,231]. Imaged at 10x (dark field and birefringence) and 40x (birefringence) magnifications, care was taken to ensure images were captured in the same fibre location for comparison. The presence of protein aggregation along the fibres could easily be seen using these filters, increasing as the fibres aged.

As described in **Section 3.4.4.1**, birefringence microscopy allowed the degree of polarisation within the fibres to be observed. An increase in light polarisation was seen after 24 hrs suggesting that fibre crystallinity had increased [51,235].

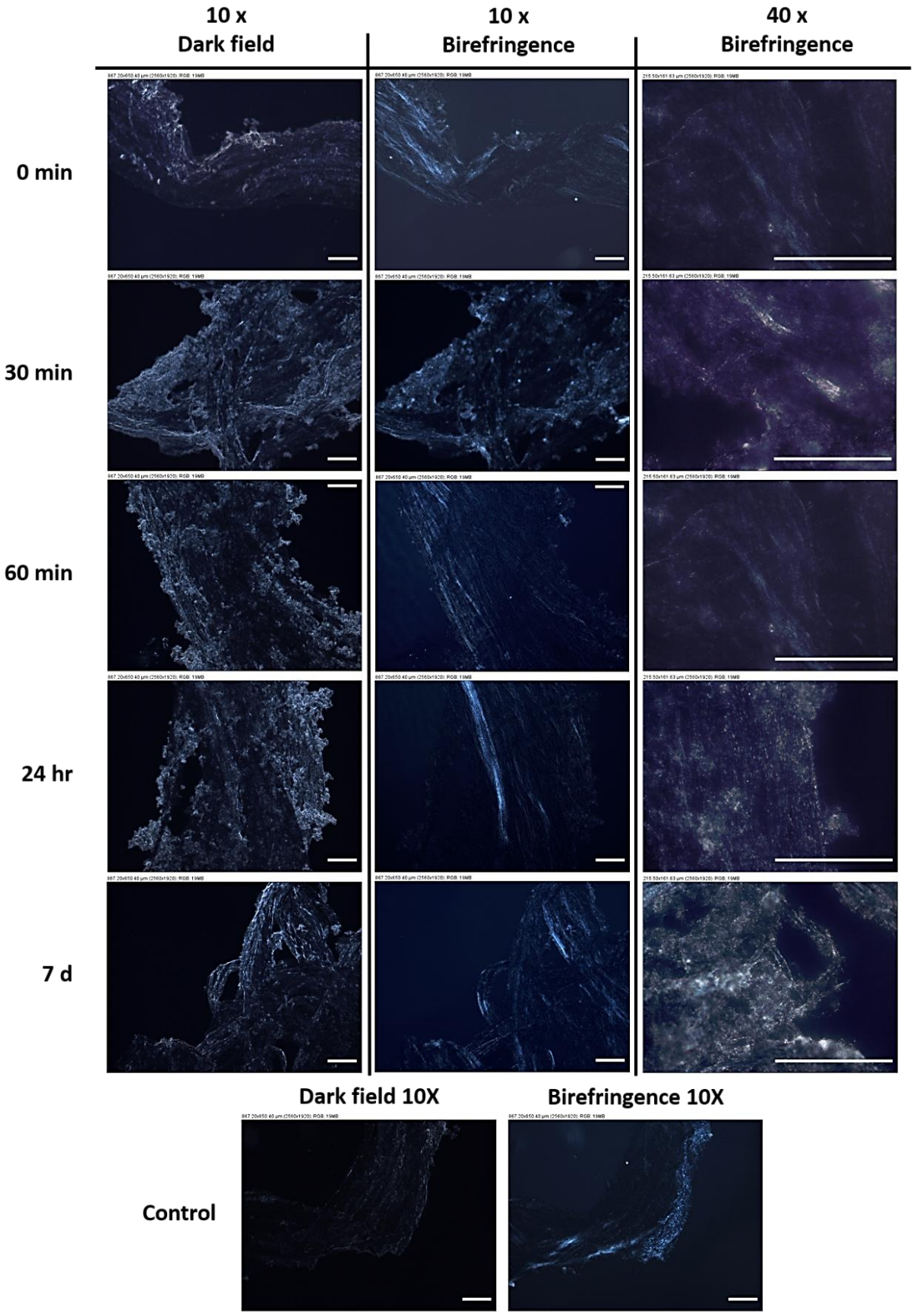

Figure 43. Fibres were also examined by dark field and birefringence microscopy at the same magnification. As degradation occurred, images captured by birefringence became brighter as the fibres became more crystalline, increasing the proportion of polarised light. Images are representative of full image collection, shown in **Appendix 8.6.1.** Scale bar = 100 μm.

4.4 Discussion

4.4.1 Recombinant expression of TRX_4RepCT

Expression of TRX_4RepCT was based on the previously established recombinant expression protocol developed by Stark *et al* [28]. While expression in minimal media enabled future non-natural amino acid incorporation, it prevented the use of the more proficient T7 phage controlled *E. coli* [83]. As a result, the pJ401 plasmid (see **Appendix 8.2**) was utilised with T5 phage polymerase containing DL41 *E*.coli, a methionine auxotroph of BL21 *E.coli*. However, recent studies have demonstrated that non-natural amino acid incorporation could also be possible in T7 systems, enabling greater expression as a result [266]. As the successful incorporation of azidohomoalanine into T7 systems has not yet been reported however, T5 expression remains the optimal route for this desired recombinant expression.

4.4.2 Presence of MMP target sequences within TRX_4RepCT

Before TRX_4RepCT was subjected to MMPs *in vitro*, its sequence was first analysed to predict whether proteolytic cleavage would occur.

4.4.2.1 Choice of proteases

As with the natural silk profiles generated in **Section 3.3.3**, the full TRX_4RepCT sequence was compared against target sequences of MMP1, MMP2, MMP3, MMP7, MMP8, MMP9, MMP10, MMP11, MMP12 and MMP13 as seen in **Figure 31**.

ELNE and α-chymotrypsin were also studied as positive controls. α-Chymotrypsin was originally investigated to provide a direct comparison to enzymatic degradation of silkworm silk fibres and films by Brown *et al* [84]. A second control was also chosen to provide information on TRX_4RepCT in the presence of wound-relevant enzymes.

An elastase by substrate specification, ELNE demonstrated selectivity for multiple alanine residues and valine residues making it a suitable positive control for the multiple alanine tracts within 4RepCT. As

expected, the profile of ELNE showed the greatest coverage of the substrate protein compared to the highly selective MMPs, supporting its use as an appropriate positive control.

4.4.2.2 Proteolytic coverage location

As expected the majority of protease coverage was located within the N- and C-termini of TRX_4RepCT protein, with very little coverage seen within the repetitive region of the fusion protein. The low variability within the repetitive region reduced the likelihood of finding target sequences within this area. As highly structured functional domains, the N-terminus (thioredoxin) and C-terminus (MaSp1 of *Euprosthenops australis*) contained a greater variety of amino acid residues to enable dimerisation or increased solubility.

However, this further raised questions about the potential for fibre production. As previously described in the literature, 4RepCT spontaneously forms macroscopic fibres upon the removal of the thioredoxin solubility tag [28]. When removed, a large proportion of the proteolytic coverage was lost, although it was unclear how this would affect subsequent fibre degradation.

4.4.3 Processing of proteases

MMP2 and MMP9 were activated in the presence of APMA using an industry standard protocol. The protease solutions were then diluted to a final assay concentration of 11.3 µM (>1000 pmol/min/µg protein) and 5.84 µM (>1300 pmol/min/µg protein) respectively, 10-fold lower than the concentrations observed in the literature from chronic wound fluid [164]. Although significantly lower concentrations seen in chronic conditions, the concentration of both MMPs was higher than that seen during acute wound by 20-fold. The low concentration provided a more cost-effective approach to replicate wound conditions, at which protease concentrations could reach as high as 8000 ng/ml in the case of active MMP2 [167].

The concentration of ELNE was first proposed by Brown *et al.* at a standardised concentration achieved with a FRET excitation/emission (490/525 nm) of 160 RFU^{-1} (0.8 mM) to enable comparison of enzymatic rates of degradation between silkworm and TRX_4RepCT films. However,

a report by Vasilyeva *et al.* suggested concentrations of ELNE between 0.031 μM and 0.31 μM would still produce observable results [193,267] and were therefore used for subsequent soluble protein degradation protocols.

The activation of MMP2 and MMP9 was confirmed using gelatin zymography electrophoresis as seen in **Figure 32**. Using a gelatin infused acrylamide gel, the MMPs were denatured, migrated and renatured to enable enzymatic cleavage of the surrounding gelatin within the gel matrix. Incubation in resuspending and developing buffers allowed the activity of the proteases to be visualised when stained with a standard protein stain. Where the protease had migrated however, the gelatin was cleaved and no staining had occurred, leaving a blank band.

Interestingly, the 'pro' form of the proteases was also seen as bands of greater molecular weight as shown in **Figure 32**. Although not inherently capable of cleaving the surrounding gelatin, the renaturing process was thought to have exposed the catalytic site of the enzymes to the gelatin, resulting in the pro form becoming visible. The gel was therefore able to confirm the proportion of active to zymogenic enzyme. As the active bands were clear for both MMPs, it gave good confidence that subsequent proteolytic degradation in the presence of both MMPs was as a result of their activity. The concentration of the MMPs was also assessed. As shown, activity was confirmed with as little as 100 pg/ml, some four times lower than the assay concentrations used (450 pg/ml and 800 pg/ml for MMP2 and MMP9 respectively).

4.4.4 TRX_4RepCT and 4RepCT degradation

Although protein expression and purification had been shown to produce soluble TRX_4RepCT, precipitated protein was observed in thawed aliquots containing 20 mM Tris pH 8.0. Removed by filtration, the remaining soluble fractions were analysed using a Nano-drop (ND-1000 Spectrophotometer, Labtech international) with absorption at 280 nm to calculate the correct concentration of the protein, as seen in **Methods 2.10**. As a further precaution, protein samples were analysed by SDS-PAGE, shown in **Figure 33**, at the concentrations used during

the degradation assays. As full size protein bands were clearly seen in all fractions, it was evident that TRX_4RepCT had remained soluble during the freeze thaw process. As a result, it was likely that the precipitation seen was from contaminating proteins present from recombinant expression. **Figure 33** was also used for comparison for TRX_4RepCT before proteolytic degradation. Despite the presence of the reducing agent SDS in the loading dye, dimeric TRX_4RepCT (80kDa) was seen when expressed in nutrient rich LB media as a result of a single disulphide bridge in the spidroin C-terminus [41]. It is thought that when dimerised, the disulphide bridge found in naturally MASP C-termini is shielded from the reducing agents in solution, allowing the dimer to persist in reducing conditions [31].

4.4.4.1 Soluble TRX_4RepCT degradation

Effect of temperature on TRX_4RepCT stability
TRX_4RepCT stability in both assay buffer (20 mM Tris pH 8.0, **Figure 34**) and H_2O (**Figure 35**) was evaluated at both 25 °C and 37 °C. As shown in **Figure 34**, TRX_4RepCT remained soluble at 25 °C throughout the experiment while solubility appeared to be lost after approximately 2 hours at 37 °C.

This was a common theme throughout the experiments, suggesting that spidroin stability was reduced at the higher temperatures given that natural environment inhabited by many spiders is less than 37 °C. As cold-blooded organisms, the internal temperature for the majority of spiders is unlikely to reach higher than 30 °C. This is further supported by the stability retained when TRX_4RepCT was incubated at 25 °C with the same proteases. If biological properties are vastly affected by the difference in temperature, it will be important for mechanical strength to be investigated under similar conditions. Although acute wound sites are often warmer than the remainder of the body as a result of increased inflammation and blood flow, chronic wounds have been observed to reduce in temperature as a result of low blood flow [263,264]. If introduced to chronic wounds as a scaffold, the raised temperature may have significant effects on performance. However, it should also be noted that *in vivo* uses will likely utilise the already insoluble form of the

protein to avoid any immune response from the biologically active thioredoxin solubility tag [65,268].

The similarity of band position between the negative controls (**Figure 34** and **Figure 35**) and those seen in MMP2 and MMP9 protease degradation results (**Figure 36** and **Figure 37** respectively) suggests that little proteolytic degradation had taken place in the case of MMP2. However, the presence of small molecular weight degradation products suggested that low levels of degradation may have taken place.

The assay time points were chosen to provide information on the early degradation behaviour of TRX_4RepCT, with focus given to the first 2 hours of the experiment. As the protein was not seen to undergo cleavage within this time, further investigation is required to investigate when proteolysis actually occurred. The loss of the soluble protein occurred between 4 – 24 hr, a larger time range than the rest of the time points. As degradation was not seen to occur within the first 2 hrs, the time points should have been shifted to investigate the second half of the assay to provide clarity in this time frame. However as degradation products had been observed after 4 hrs, this was not undertaken.

MMP2 and MMP9

In the presence of MMP2, TRX_4RepCT was shown to undergo proteolysis after 4 hrs at 25 °C and 2 hrs at 37 °C, as shown in **Figure 36** (**lane 6** and **lane 5** respectively). At these times, the soluble protein (39 kDa) was no longer visible by SDS-PAGE while smaller proteins (<10 kDa) became visible. The difference observed between temperatures was also noted, suggesting that at higher temperatures the solubility of TRX_4RepCT was lost for the reasons suggested previously. The loss of stability may also have had an effect of proteolytic degradation, resulting in the formation of insoluble cleavage products. At 25 kDa, a band can be seen becoming more prominent, suggesting it had been reduced by 10 kDa, corresponding to the degradation products seen after 24 hrs.

When incubated with MMP9, TRX_4RepCT did not undergo significant degradation, although soluble protein was lost after 4 hrs at 37 °C, as seen in **Figure 37**, **lane 6**. As discussed previously, the loss of

protein seen at 37 °C was likely due to protein instability at higher temperatures. As soluble protein was observed after 24 hrs at 25 °C, it confirmed that no degradation had occurred, and the protein had remained soluble. This was also supported by the absence of smaller degradation product formation later in the assay.

ELNE and α-chymotrypsin

ELNE was selected as a positive control on account of its presence during wound repair and its preference for alanine residues, of which TRX_4RepCT contained 95. Although some of soluble full-length protein was present throughout at 25 °C, the protein band was lost at 37 °C, as seen in **Figure 38**.

The low concentrations of protease may also have contributed to the low levels of degradation seen. At 37 °C the soluble protein was reduced after 60 minutes (**lane 4**) at which point soluble proteins of approximately 25 kDa were produced for the remainder of the experiment. At the lower temperature, TRX_4RepCT was not seen to undergo degradation, although some lower molecular weight bands became more prominent throughout the course of the experiment. Neither temperatures produced insoluble degradation products although some full-length protein as visible at 25 °C in the insoluble fraction.

Shown in **Figure 39**, incubation of TRX_4RepCT with α-chymotrypsin produced a number of degradation products almost immediately. As the full-length protein (39 kDa), was not observed at any point during the assay, it suggested that proteolysis had occurred before the initial sample could be taken, denatured and imaged.

During the preparation of the experiment, it could have been possible for the reaction to have occurred before the first samples had been taken, resulting in a loss of the original protein band when analysed by SDS-PAGE. As all reactions were run from the same sample of protein stock (**Figure 33**), it had previously been confirmed that the protein had been present at the beginning of the experiment. At 37 °C, TRX_4RepCT was seen as a faint 39 kDa band at 0 hr (**Figure 39**, **lane 1**), although the majority had already been degraded. Instead, a <25 kDa band was

seen at all time points and remained present for the majority of the reactions, becoming insoluble after 24 hrs. However, when compared to the enzyme only lane, it was revealed that this band corresponded to the 25 kDa α-chymotrypsin enzyme that eventually became insoluble over the duration of the experiment. The smaller bands between 10 kDa and 15 kDa were present in all gels. One band in particular (11 kDa, **lane 7**) was of interest as it became visible after 1440 minutes incubation, suggesting that it may be the result of further degradation. Interestingly, this band was not later seen in the insoluble fraction suggesting that it had remained soluble despite the degradation.

α-Chymotrypsin purity and concentration

The high number of contaminating bands seen in all lanes in **Figure 39** suggests that the α-chymotrypsin was impure or at an excess concentration. As the protease was purchased and resuspended as instructed, any contaminating proteins from production would be retained and seen in the final assay results. Full length α-chymotrypsin is usually observed at 25 kDa, clearly seen in the figure. Attempts to further purify the protease solution by gel filtration were unsuccessful due to excessive dilution of the original sample. As a result, the experiment was not repeated with α-chymotrypsin at a higher purity. The concentration of α-chymotrypsin (120 mM, 40 units/mg protein) reflected concentrations described by Brown *et al.* who investigated enzymatic degradation of silkworm films [84]. However, as no substrate protein band was seen at any time during the assay, no further information could be gathered about TRX_4RepCT degradation compared to that of silkworm degradation.

4.4.4.2 4RepCT film and fibre degradation

The topography of TRX_4RepCT films was assumed to be that of 2D material, with little exposure of protein under the initial surface to the surrounding protease. Although unlikely to be utilised as a film biomaterial, this would provide information on 4RepCT's surface degradation behaviour. Instead, 3D matrices or hydrogels of 4RepCT were more likely to be utilised for use in the ECM. However, as molecules

of 4RepCT would likely be exposed at the film surface, suggesting that some degradation might be possible.

Film degradation products

TRX_4RepCT has previously been shown to produce protein films when cast onto plastic and glass surfaces [269]. At 5 mg/ml the resulting 2.5 mg films could be weighed accurately without the need for excessive protein use. To avoid loss of protein during film transfer, the films were cast *in situ* to the side of assay micro-centrifuge tubes. After incubation with ELNE, H_2O and α-chymotrypsin, the supernatants were analysed by SDS-PAGE, as seen in **Figure 40a**. Degradation by ELNE appeared to produce protein bands between 10 kDa and 15 kDa (**lane 2** and **lane 4**). Bands of similar size were also seen after incubation in H_2O (**lane 6** and **lane 8**) although they were much fainter.

The films were resolubilised after incubation at 90°C in SDS-containing protein loading buffer for 5 minutes. As insoluble films, it was unlikely that cleavage products would remain soluble, preventing them from being observed by SDS-PAGE. As a result, the observed bands were considered to be the 12 kDa thioredoxin tag. However, preliminary matrix-assisted laser desorption ionisation time of flight (MALDI-TOF) investigations failed to confirm the exact identity of the protein bands.

Film mass loss

Film mass was shown to decrease in all controls, including the negative H_2O control as shown in **Figure 40b**, supporting the use of 5 mg/mL stock solutions. Films containing less protein, whilst cheaper and easier to produce, would likely increase the percentage error during measuring, reducing the confidence in the results. Although some mass loss (9.7%) was observed from the negative control, a significant increase in mass loss of 23.6% and 19.2% was observed when incubated with ELNE and α-chymotrypsin respectively, suggesting that degradation had occurred. The mass lost from the negative control is likely down to removal of contaminating proteins that had accumulated during the concentrating steps. Upon washing, the contaminating proteins were removed, and the resulting films appeared to lose mass. Despite this, the films had

undergone degradation in the presence of ELNE and α-chymotrypsin, as predicted by the *in silico* studies seen in **Figure 31**.

4.4.4.3 Fibre formation

Insoluble protein aggregation was seen throughout the fibre incubation, likely caused as a direct result of spontaneous fibre formation. Unlike the synthetic silk eADF4, which produces predictable fibres when the reel distance and electric charge is altered during electrospinning, the fibre production of 4RepCT is spontaneous and outside of human influence [72]. At protein concentrations between 1 – 1.5 mg/ml following the cleavage of the solubility tag, 4RepCT is in sufficient proximity to itself that dimerisation and polymerisation can occur, with only gentle agitation required to allow macroscopic fibres to form within the reaction vessel. However, this approach inherently causes a large quantity of waste material, namely insoluble 4RepCT that has not managed to polymerise, subsequently precipitating and aggregating with other insoluble protein within the solution.

Short term fibre degradation

4RepCT fibres were analysed using bright field, dark field and birefringence microscopy over the course of 7 days. Any degradation that occurred during this time was categorised as short term (0 min – 60 min) shown in **Figure 41**, or long term (120 min – 7 days), shown in **Figure 42**.

After 60 min, 4RepCT fibres were not degraded sufficiently, as seen in **Figure 41**. Fibres removed from protease solution at these time points did not show significant fraying or deterioration at either 10x or 40x magnification. When dried, 4RepCT fibres adhered to the glass slides, preventing them from being returned to the protease solution and allowing comparisons of the same fibre. As a result, individual fibres were removed at the designated time points and compared.

Long term fibre degradation

Long term incubation (120 min – 7 days) resulted in fraying edges of some fibres as disordered protein accumulated in the surrounding solution, as seen in **Figure 42**. It was possible that as the fibre was degraded, cleavage products from proteolytic activity aggregated in

clumps, contributing to the levels of precipitated protein observed in samples undergoing extended incubation times although this was not quantified.

Birefringence and dark field microscopy
Dark field microscopy was used to produce images with better contrast although samples were still observed using transmitted light, as with bright field. Unfortunately, images were often saturated with aggregated protein, so little further information was gathered from this technique.

Birefringence microscopy, seen in **Figure 43**, confirmed that polarisation within fibres increased after 24 hrs as the fibres were subjected to protease solution. As with the natural silk fibres, crystallinity was increased in the presence of MMPs, thought to signify enzymatic proteolysis within the fibres [51]. However, the aggregated protein observed in the surrounding solution also polarised the transmitted light, making it unclear if the fibres had undergone significant proteolytic degradation [235,270,271]. As low levels of degradation had been observed with soluble 4RepCT as seen in **Figure 36**, it was likely that similar levels of cleavage had occurred.

4.5 Conclusions

4RepCT was successfully expressed and purified by both LB and minimal media as described. Utilising techniques described in the last chapter, the amino acid sequence of 4RepCT was analysed for MMP target sites and identified a number of potential sequences that could facilitate protease recognition and subsequent cleavage. This work serves to support the confidence of the *in silico* proposed in the last chapter. The degradation behaviour of 4RepCT the *in silico* profile, confirming that it could be used to propose future mutations to introduce target sequences into the recombinant sequence.

Both soluble and insoluble 4RepCT was slightly degraded in the presence of MMP2 but little degradation was seen as a result of MMP9 incubation. Although further investigation would be required to better

determine the time frame by which Trx_4RepCT undergoes cleavage, all results indicated that TRX_4RepCT was not readily degraded.

The results seen in this chapter also provide information on the protein stability in solution. In all assays, the soluble form of TRX_4RepCT lost solubility after 4 hrs, appearing in the insoluble fraction after 24 hrs. As the recombinant spidroin would likely be used in its insoluble fibre form, this instability is unlikely to cause issue in its role as a biomaterial.

4RepCT was also degraded by ELNE as expected, owing to the elastin-like regions of repetitive alanine tracts seen within the protein [265]. Incubation with α-chymotrypsin was inconclusive at such extreme protease concentrations preventing effective analysis or conclusions. With further investigation, the degradation of 4RepCT by α-chymotrypsin would be studied at lower concentrations in time frames that reflected the loss of solubility seen with MMP2, MMP9 and ELNE. With a greater insight into the time frame of spidroin degradation, derived biomaterials can be designed with the potential for tuneable degradation properties.

5. Introducing MMP target sites into TRX_4RepCT to influence spidroin degradation

5.1 Introduction

5.1.1 Complications faced by implantation procedures

The implantation of medical scaffolds is usually restricted by three potential complications; namely the initial host response, the persistent life span of the implant and thirdly its eventual removal [272]. Current biodegradable medical devices, such as sutures, often have short life spans as the devices are degraded promptly with the recovery of the wound, or are removed with little trauma to the affected area [272,273]. However, it should also be noted that biodegradable sutures are often inserted at sites of acute wound repair, such as surgery boundaries, rather than the highly complex environment of a chronic wound.

5.1.2 Evidence of targeted MMP degradation

Many tissue implants and scaffolds are being developed to increase MMP susceptibility, encouraging their breakdown if they persist in the wound. In particular, polyethylene glycol (PEG) has been used in conjunction with MMP-sensitive peptides to produce hydrogels and implants that undergo proteolysis [274]. A report by Vigen *et al.* functionalised the PEG polymer with two different peptides shown to facilitate MMP cleavage at two distinct rates. Coupled with an RGD motif, the resulting hydrogels were found to encourage angiogenesis and vascularisation as the migrating cells degraded the scaffold as they migrated.

This was developed further by Jiang *et al.* by coating a poly(ε-caprolactone) (PCL) scaffold with hydrophobin (HFBI), an amphiphilic protein that forms self-assembled layers to facilitate protein-protein interactions, as seen in **Figure 44**. In this case, collagenase was associated with the hydrophobin to investigate the role of collagenase ECM in tissue engineering [275]. It was observed that utilising collagenase encouraged the migration and infiltration of smooth muscle cells.

Incorporating specific target sequences of MMPs into synthetic biomaterials is similar to the approach taken with TRX_4RepCT in this chapter. Incorporating the target sites proposed in the last chapter, it was thought that material breakdown would be significantly altered. The sequences used by Vigen consisted of a slower 'collagen-derived' sequence (GPQG¦IWGQ) where '¦' denoted the point of cleavage, and a faster cleaving sequence (VPMS¦MRGG) [276–279]. The derived collagen structure of the target peptides ensured they could be cleaved by several MMPs.

Utilising target sequences specific to enzymes of interest can also be considered, as was the approach with TRX_4RepCT. Here, target sequences for MMP2 and MMP9 were introduced to the spidroin sequence based on previous *in silico* investigations. This increased specificity was intended to provide greater control of material degradation but also reflected typical overexpression of MMP2 and MMP9 observed in chronic wounds [164].

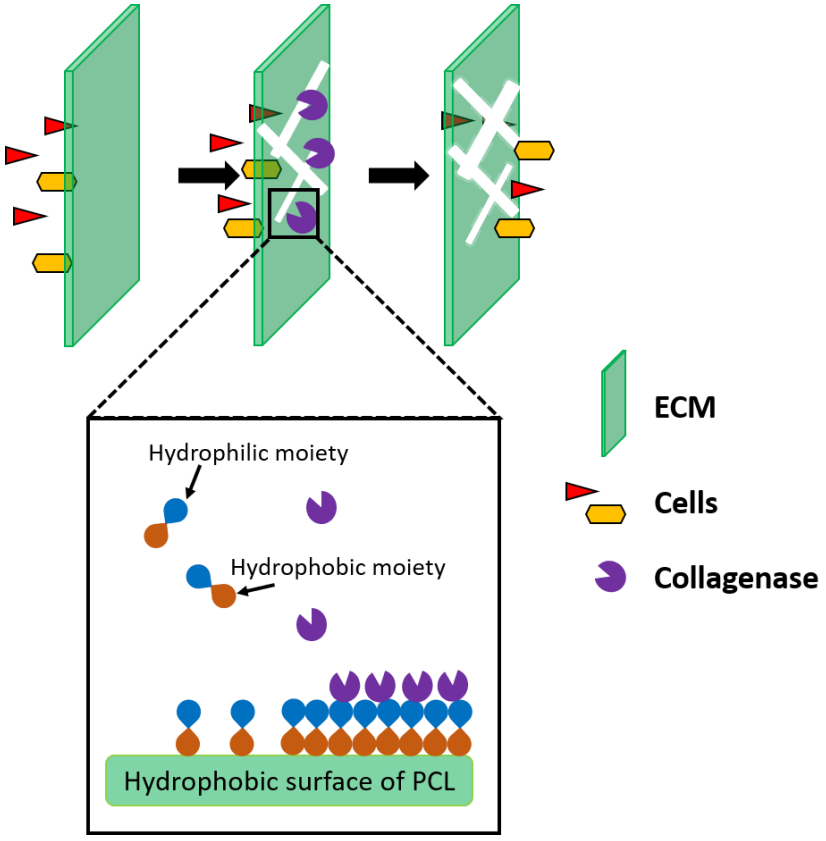

Figure 44. HFBI-coated PCL scaffold modified with collagenase to promote cell migration through ECM degradation. Image adapted from 'An electrospun poly(ε-caprolactone) scaffold modified with matrix metalloproteinase for cellularisation and vascularization', Jiang et al. 2018.

5.1.3 MMP sensitive TRX_4RepCT

As mentioned in **Section 1.4.2**, protease concentrations within chronic wounds reach in excess of 40 times higher than that seen during acute repair [167]. As a result, protein biodegradation occurs much faster, preventing the sustained formation of host structural proteins such as collagen and laminin [153,280,281].

In an attempt to rebalance this equilibrium, it has been suggested that reducing the active concentration of MMPs would allow surrounding protein architecture to recover. While increasing the TIMP concentrations to the relevant proteases has been considered, this approach risks preventing the sufficient wound environment remodelling if the enzymatic concentration were reduced too far or for sustained periods of time [282].

A second approach could be to reduce the effective concentration of the active proteases, reducing the effect of their presence, acting as a competitive substrate inhibitor. By introducing a biomaterial that is readily degraded by specific MMPs, it could provide sufficient time to allow the natural expression of TIMPs to better control the elevated MMP concentration.

In the previous chapter TRX_4RepCT was shown undergo low levels of degradation in the presence of MMP2. If this degradation could be increased in a controlled manner, TRX_4RepCT presents itself as an ideal material in regenerative medicine. The *in silico* studies seen in **Section 4.3.1** identified a number of sites that could be utilised by possible point mutations. If readily degraded, by introduction of the identified mutants, TRX_4RepCT would have the effect of diluting the active protease concentration at the wound. This would remove active MMP from surrounding structural and regulatory proteins, allowing the balance of acute repair to be recovered over time.

5.1.3.1 Possible effects of mutating TRX_4RepCT

The structured C-terminus of TRX_4RepCT is thought to allow spidroin dimerisation and polymerisation to a fibre. The conserved nature of spidroin termini suggests that mutating residues within structural regions

could disrupt the correct folding of TRX_4RepCT. It was therefore important to select mutations outside of the five α-helices, especially as MMP target sequences often displayed a helix-breaking proline at P3 of their six residue sequences [172].

The overall location of each mutation should also be considered to ensure the access of the protease to the target sequence. Considering that the thioredoxin solubility tag was removed for fibre formation, mutations within this N-terminus would have little effect on subsequent fibre degradation rates. If buried within the structured C-terminus, the protease may not have access to the target sequence, resulting in no effect on rate of proteolysis. However, if a mutation were placed within the more easily accessible amorphous region, it is likely that the sequence would have greater influence on the rate of proteolysis.

5.2 Aims of the chapter

The aim of this chapter was to influence the rate of proteolytic degradation of the recombinant protein TRX_4RepCT in the presence of MMP2 and MMP9. This was achieved by introducing target sequences specific to each protease into the primary sequence of the recombinant spidroin.

Once introduced, the resulting mutants were characterised and optimised for recombinant expression. The effect of the mutations on degradation rate was evaluated as soluble protein and insoluble fibres in the presence of wound-relevant proteases and quantified by SDS-PAGE protein band densitometry. As with 4RepCT, macroscopic fibres were analysed by light microscopy using both bright field and polarisation.

As a result of this work, two TRX_4RepCT mutants were recombinantly expressed that exhibited unique degradation rates in the presence of MMP2 and MMP9. This serves to provide confidence in the *in silico* technique detailed earlier in this thesis. This proof-of-concept study highlights the potential for prediction techniques that identify sequences close to exact cleavage sites.

5.3 Results

5.3.1 Selecting TRX_4RepCT mutants

From the *in silico* screen displayed in **Section 4.3.1**, the majority of suggested mutations resided within the highly conserved C-terminus of the spidroin as shown in **Figure 45a**. The repetitive nature of the amorphous region of TRX_4RepCT prevented many target sequences from being introduced at this region. Fibre formation from TRX_4RepCT required the removal of the thioredoxin solubility tag, so mutations present within this region were unlikely to have great effect on fibre formation or degradation.

Apart from TRX MASP15_N156P, all selected mutations (**ringed**) were selected within the C-terminus, avoiding ordered α-helices and highly conserved regions such as the dimeric interface and conserved motifs. As seen in **Figure 45b,** seven mutations were identified with interest in MMP1, MMP2 and MMP9 activity as these were prominent at chronic wound sites.

a)

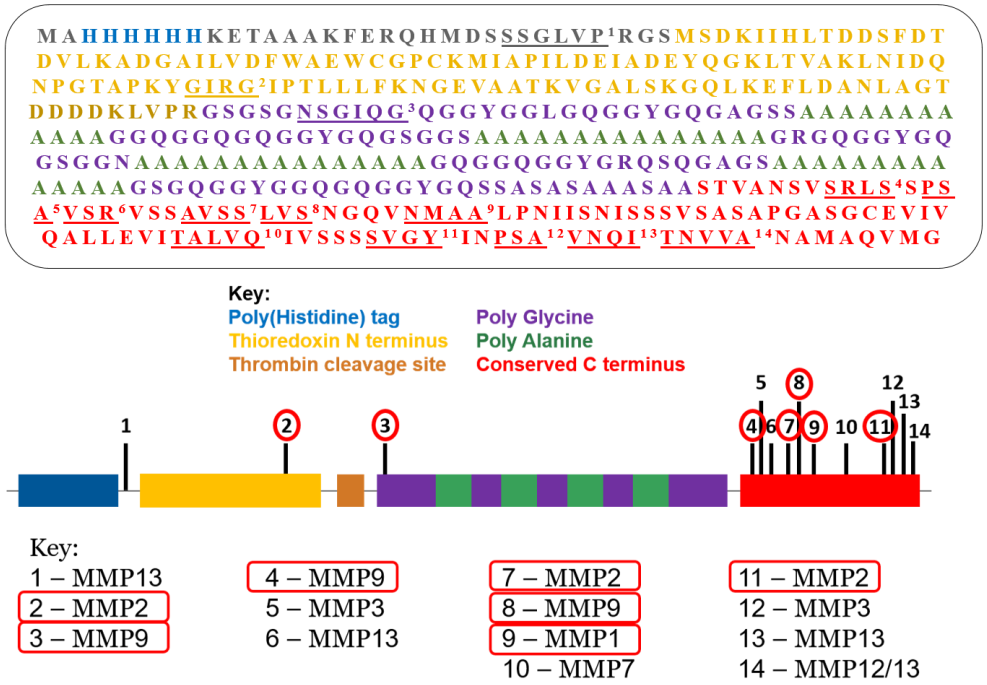

b)

Mutation number	Name of mutation (TRX MASP15_)	Target sequence	Targeted MMP
2	102P_Y103V	P-V-G¦I-R-G	MMP2
3	N156P	P-S-G¦I-Q-G	MMP9
4	320P_S321R	P-R-R¦L-S-S	MMP9
7	A336P_S338del	P-V-S¦L-V-S	MMP2
8	S338P_339L	P-L-S¦L-V-S	MMP9
10	G344P	P-Q-V¦N-M-A	MMP1
14	S394P	P-V-G¦Y-I	MMP2

Figure 45. The location of the mutations (**a**) and summarising table (**b**) were proposed from the *in silico* studies. **a**) From these profiles, 14 possible target sites were identified although only seven (ringed in red) were processed to avoid critical structural elements within the protein. **b**) Each mutation was named to reflect its location and amino acid substitution. The selected sequences were targeted predominantly for MMP2 and MMP9's respective target sequences to reflect their overexpression at chronic wound sites.

5.3.2 Mutating TRX_4RepCT

pJ401Express plasmid vector

Having identified the mutations of interest, mutagenic primers were designed using the NEBase changer for the pJ401Express plasmid vector as seen in **Appendix 8.2**. Site-directed mutagenesis was performed using the parameters determined from the primer design, as described in **Methods 2.15** and confirmed by 1% (w/v) agarose gel electrophoresis. When run on a 10 cm^2 1% (w/v) agarose gel, all 5 kb mutated plasmids were visible, seen in **all lanes** of **Figure 46a**. A smaller 2 kb construct was also seen for TRX MASP15_S321R suggesting that shorter section of the plasmid had been amplified as well.

After XL1b *E. coli* electro-transformation, colony growth of TRX_N156P, A336P_S338del, S338P_339L, G344P and S394P was seen after overnight incubation at 37 °C as seen in **Appendix 8.3**. After repeated attempts, TRX MASP15_102P_Y103V and 320P_S321R constructs failed to be taken up by the XL1b *E. coli* despite successful amplification by PCR.

pET22b plasmid vector

Site directed mutagenesis was also attempted with a pET22b(+) plasmid vector as seen in **Appendix 8.4**, to utilise the increase expression yield of the T7 polymerase controlled system. As before, NEBase changer was used to design new mutagenic primers against the alternate template plasmid. Successful plasmid amplification was seen for all constructs, seen in **Figure 46b, lanes 1 – 7** at approximately 6 kb. A second band between 0.5 - 1 kb was also amplified for the TRX_N156P construct. However, as the N156P mutation had previously been successfully expressed using pJ401Express, no further investigation was undertaken with regards to this construct. TRX_102P_Y103V, A336P_S338del, S338P_339L, G344P and S394P was all successfully transformed into NEB5α *E. coli*.

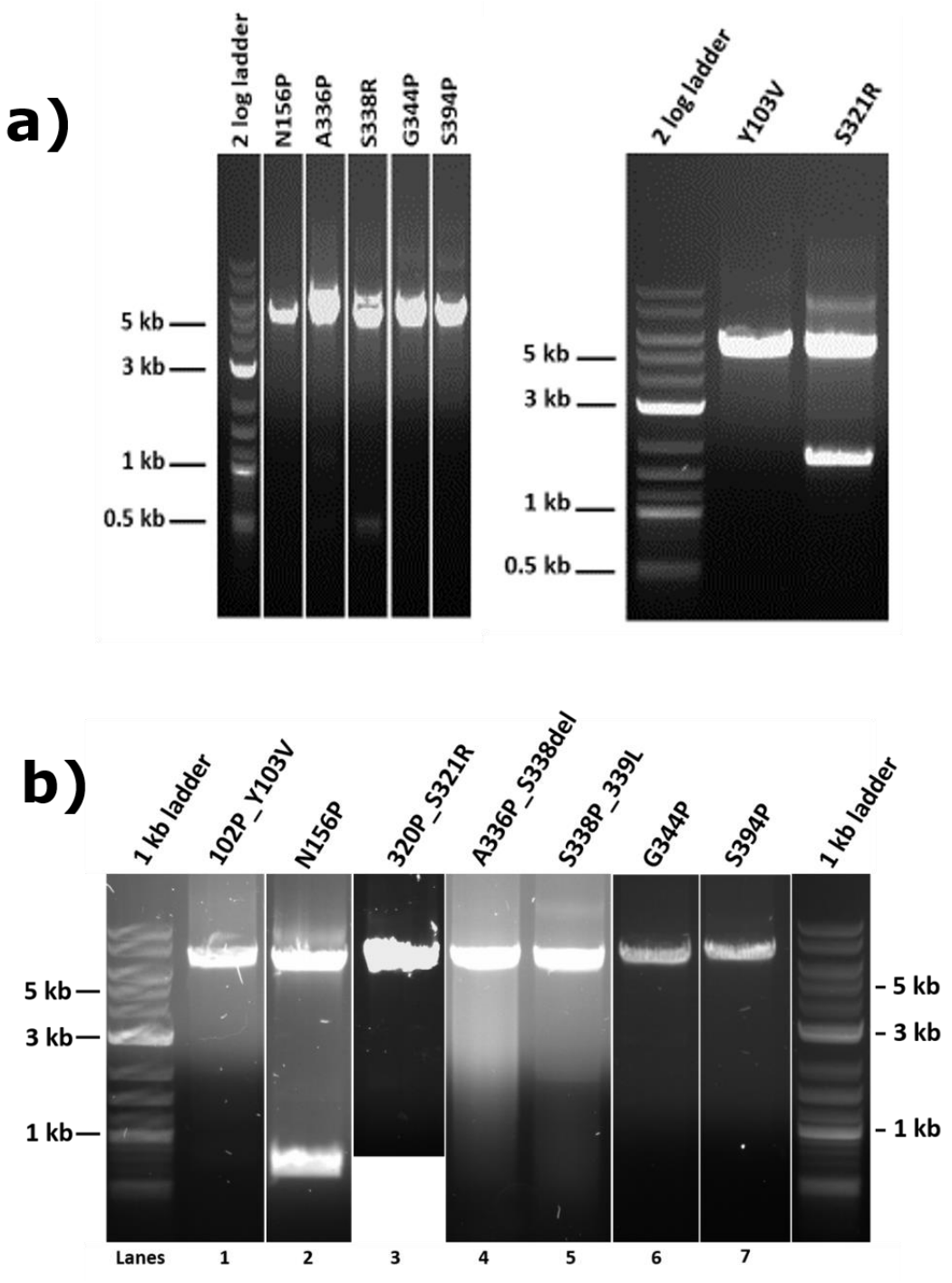

Figure 46. Mutant PCR amplification products were viewed by 1% (w/v) agarose (10 cm^2) gels after Q5 mutagenesis of pJ401Express (**a**) and pET22b (**b**) plasmids. All gels were run for 30 minutes with a constant voltage of 100 V. **a**) Although template amplification was observed with all plasmid constructs, the left hand samples were successfully transformed into DL41 *E. coli* while the right hand constructs were unsuccesful. **b**) 4RepCT mutations were also introduced into a pET22b expression vector. Template amplification was seen from all constructs and were subsequently transformed into Neb5α *E. coli*.

5.3.3 Expression and purification of TRX_4RepCT mutants in LB and M9 minimal media

TRX_N156P

TRX_N156P was successfully expressed by DL41 *E. coli* in both LB and supplemented minimal M9 media as seen in **Figure 47a**. TRX_N156P was successfully purified as a 39.6 kDa fusion protein after Ni^{2+} IMAC step interval, seen in **lane 8** of **Figure 47a** in both gels. TRX_N156P expression produced approximately 25 mg protein/L of growth media. As with TRX_4RepCT, the N156P mutant was also dialysed against 20 mM Tris pH 8.0 and flash frozen before it was stored at -80 °C until use. In minimal media, the 80 kDa dimeric form of TRX_N156P was not seen in the eluted fraction, in contrast to the protein elution fraction (**Figure 47a, lane 8**) from LB media expression.

TRX_A336P_S338del

As TRX_A336P_S338del was expressed in BL21 *E. coli*, expression was only possible in LB media as seen in **Figure 47b**. A336P_S338del was purified using a 10 mM – 70 mM imidazole gradient (0% – 10% elution buffer) as a 40 kDa fusion protein (seen in **Figure 47b, lanes 5 – 8**) before the imidazole concentration was increased in steps of 105 mM, 280 mM and 700 mM respectively. Unlike TRX_N156P and TRX_4RepCT which expressed readily, TRX_A336P_S338del only produced 7 mg protein/L of growth media. Although the protein yield was low, sufficient protein was produced to allow further investigations so subsequent optimisation was not continued.

Unsuccessful Mutations

The remaining mutations were not successfully recombinantly expressed despite numerous attempts to increase protein yield. The investigations carried out included time point expression tests, insoluble pellet purification and purification with denaturing and non-denaturing elution buffers. As no recombinant mutants were able to be expressed or purified, these results can be seen in **Appendix 8.5**.

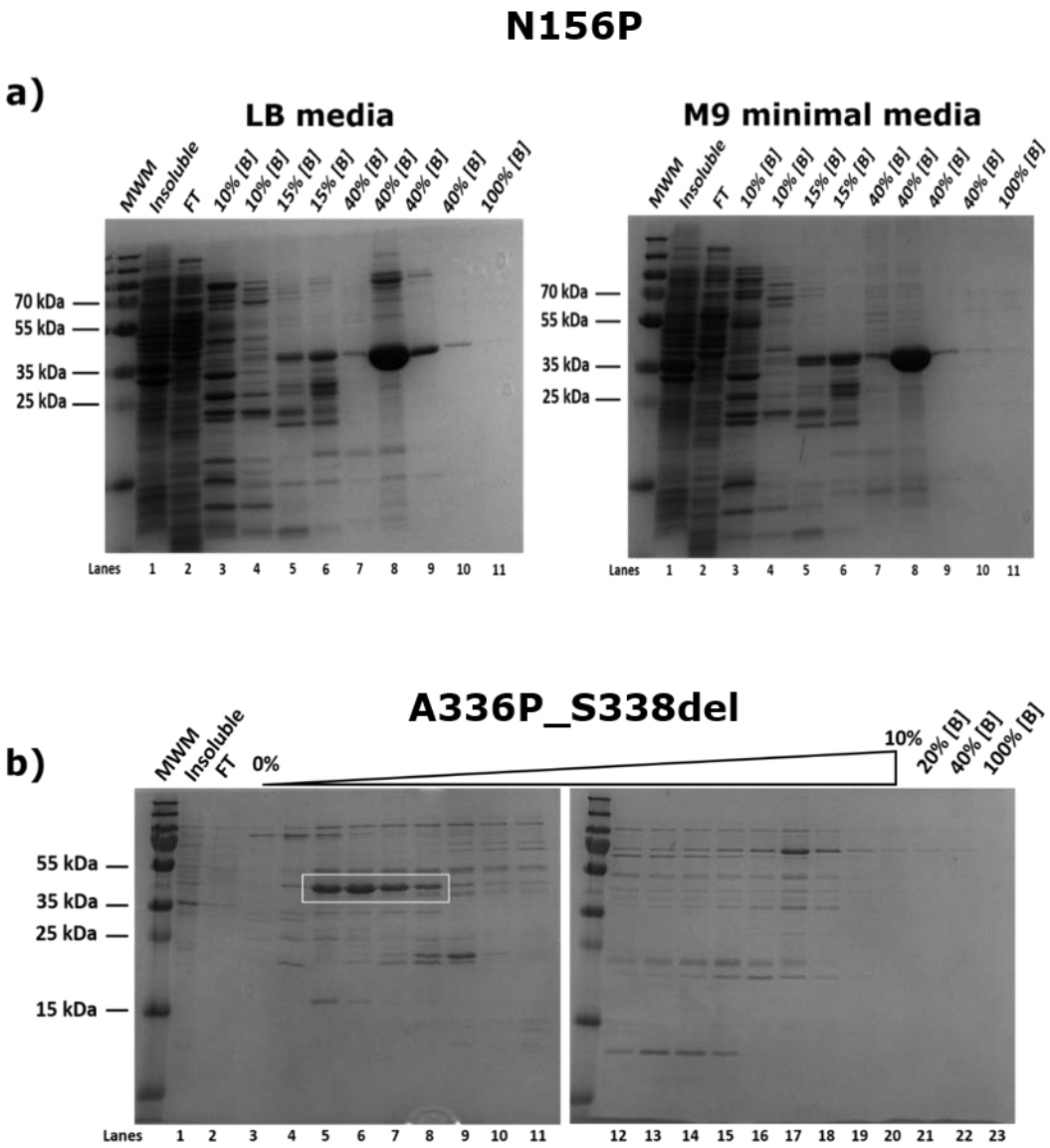

Figure 47. Ni^{2+} IMAC purification of the N156P mutant from 1L LB and M9 minimal media expression (**a**) and gradient IMAC purification of A336P_S338del (**b**) analysed by 15% (w/v) SDS-PAGE. **a**) TRX_N156P was eluted at 272 mM imidazole (40% elution buffer) shown in lane 8. Expression in both media produced a large, relatively pure yeild of TRX_N156P, although the dimeric form could not be seen when expressed in minimal media. **b**) Expression and purificaiton of TRX_A336P_S338del mutant was only possible after expression in BL21 E.coli with an imidazole concentration gradient of 10-70 mM (0% - 10% elution buffer), seen in lanes 5 - 8. Once purified, both mutants were dialysed against 20 mM Tris pH 8.0 overnight at 4 °C before being stored at -80 °C until needed.

5.3.4 Screening inserted mutations for unintended proteolytic target sites

Difficulties in protein expression could have been caused by proteolytic degradation within *E. coli* before it was purified. To check this, the protein sequences were entered into the PROSPER proteolytic database to determine whether protein cleavage could be expected [224]. However, the generated results, seen in **Table 17**, only identified target sequences for MMP3 and ELNE in addition to the expected targeted MMP target sequences. It was also realised that the target sequences that had been introduced would enable both MMP2 and MMP9 cleavage thanks to the substrate similarity between the two gelatinases. However, no cleavage was proposed that explained the lack of expression from the *E. coli* expression hosts.

Mutation name	A336P_S338del	S338P_339L	G344P	S394P
Target MMP	MMP2	MMP9	MMP1	MMP2
Target Sequence	SPVS¦LVSN	SLPA¦VSRV	NPQV¦NMAA	SPVG¦YINP
Gain (compared to 4RepCT)	SPVS¦LVSN (MMP9)	SLPA¦VSRV (MMP2, MMP9) MMP3 (1.00)	NPQV¦NMAA (MMP9) ELNE (1.28)	SPVG¦YINP (MMP9) MMP3 (1.05)
Loss (compared to 4RepCT)	AVSS¦LVSN (MMP2, MMP9)	-	-	-

Table 17. After poor recombinant expression of the mutants was observed, the target sequences were submitted to online PROSPER database to check if additional protease target sequences had been introduced by accident. When compared to 4RepCT, the target sequences for all mutations were picked up in the screen in addition to sequences for MMP3 in the case of S338P_339L and S394P and ELNE with G344P. The only lost target sequence was AVSS¦LVSN which is cleaved by both MMP2 and MMP9. However, this sequence was lost as a direct result of the proline insertion.

5.3.5 BSA standard curve

A protein concentration standard curve was produced with BSA to estimate degradation product concentrations as seen in **Figure 48**. Seen in **Figure 48a**), the 66 kDa protein band could be seen at 0.1 mg/mL, 0.2 mg/mL, 0.5 mg/mL, 1 mg/mL and 2 mg/mL. Pixel density histograms were produced for each lane using ImageJ and the relevant peaks were manually integrated to give an area under curve value for each peak. The average value of each concentration was then plotted protein concentration to produce a standard curve, seen in **Figure 48b**). A straight line equation was produced from a line of linear regression, with the equation: y = 3395x + 3609 and an R^2 of 0.9162, as calculated with Prism 8.

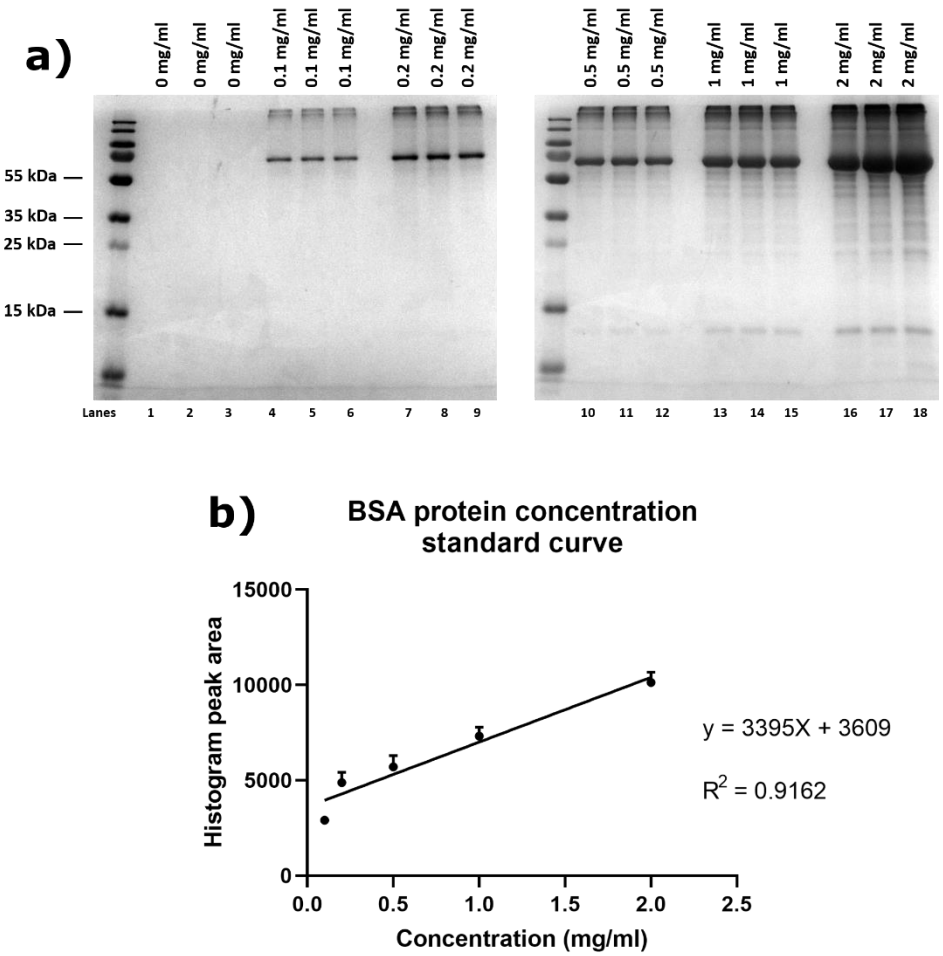

Figure 48. A protein concentration standard curve was produced with BSA **a**) which was then used to calculate a straight line equation **b**). **a**) BSA was analysed by 15% (w/v) SDS-PAGE at protein concentrations of 0 mg/mL – 2 mg/mL. Once stained with Coomassie blue and imaged, the gels were used to generate a standard curve and straight line equation from the area under the curve of pixel density histograms. **b**) The resulting straight line equation was used to estimate protein concentrations after proteolytic cleavage.

5.3.6 Degradation of soluble TRX_4RepCT mutants

5.3.6.1 Identifying TRX_4RepCT mutants by thrombin cleavage

The specific thrombin target sequence enabled identification of TRX_4RepCT and any derived proteins by predictable cleavage as seen in **Figure 49**. As the C-terminal mutant A336P_S338del was eluted in low concentrations of imidazole, the final stock solutions contained many contaminating proteins. As a result, the identity of the mutant was confirmed by thrombin cleavage. Incubation with the human protease thrombin released the 16 kDa thioredoxin solubility tag of TRX_4RepCT and subsequent mutants over the course of 4 hrs at 30 °C.

TRX_4RepCT, seen in **Figure 49a**) as a full length 39 kDa band in **lane 1** (**red** box) underwent proteolysis into shorter 16 kDa and 23 kDa bands representing the thioredoxin (**blue** box) and silk protein (**green** box) respectively. Although the silk protein lost solubility after 120 min (**Figure 49a, lane 5**), the thioredoxin solubility tag remained soluble for the remainder of the experiment.

A similar result was seen with TRX_N156P **Figure 49b**), as the full length 39 kDa protein band (**red** box) was cleaved to the 16 kDa thioredoxin tag (**blue** box) and 23 kDa silk protein (**green** box) after 10 min (**Figure 49b, lane 2**), thus confirming its identity as a 4RepCT mutant.

For A336P_S338del **Figure 49c**) the 40 kDa band of A336P_S339del (**red** box) was cleaved over the course of the experiment to produce two fragments of 16.5 kDa and 23.4 kDa seen by SDS-PAGE (**blue** and **green** box respectively). As with 4RepCT, the cleaved mutant spidroin became insoluble in the absence of the thioredoxin solubility tag. As a result, the cleavage band at 23.4 kDa disappeared after 2 hrs as seen in **Figure 49c, lanes 3 – 7**, and was later observed in the insoluble band (**Figure 49c lane 9**).

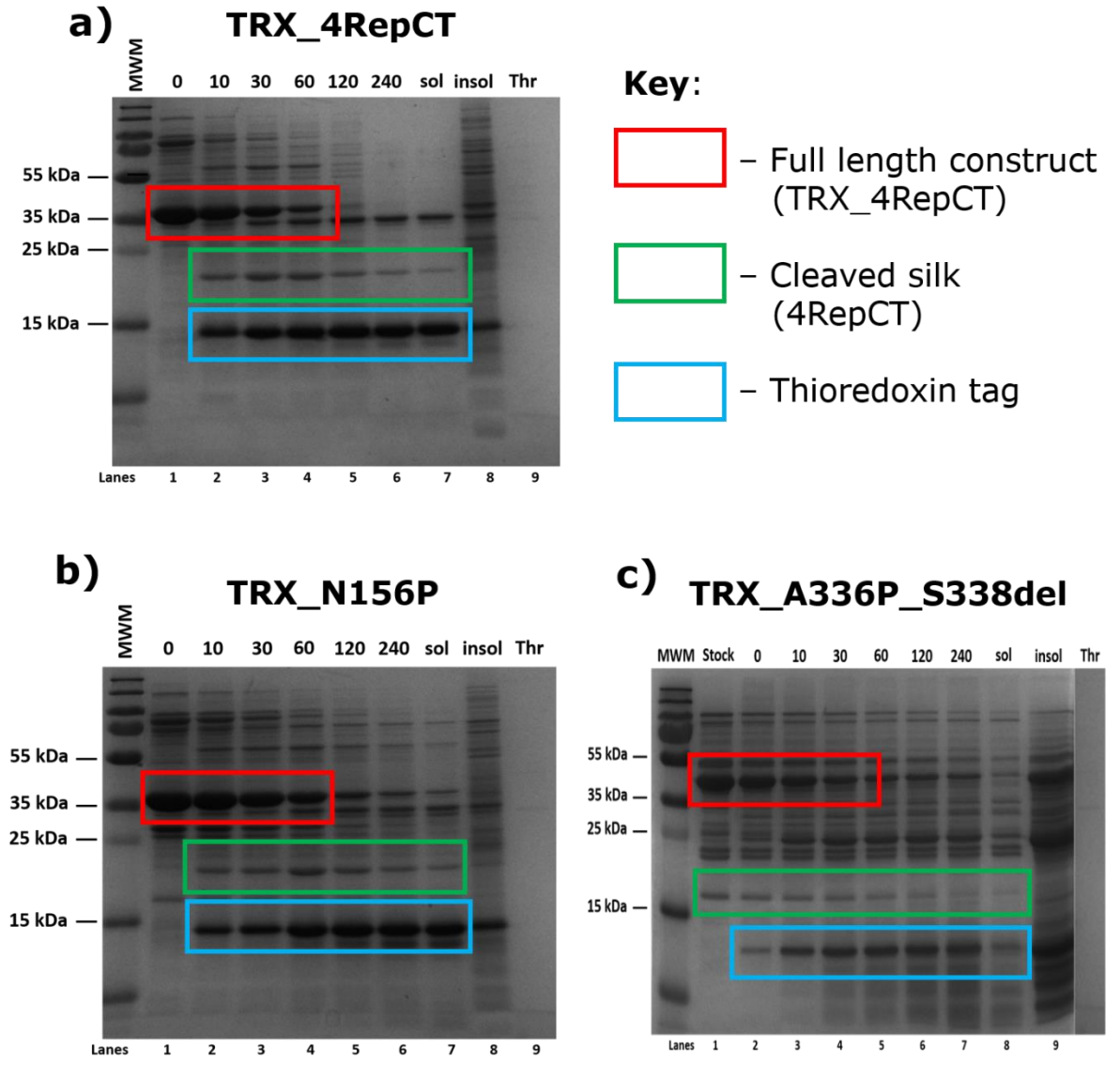

Figure 49. The identity of TRX_4RepCT (**a**) and the mutants TRX_N156P (**b**) and TRX_A336P_S338del (**c**) were confirmed by proteolytic cleavage by the human thrombin protease. Analysed by 15% (w/v) SDS-PAGE, all gels displayed the full length protein (39 - 40 kDa, **red** box) in lane 1 before the 16 kDa (**blue** box) and 23.4 kDa (**green** box) protein bands became visible, representing the thioredoxin solubility tag and the cleaved silk protein respectively. Both cleavage products became insoluble by the end of the experiment, seen in lane 8. The thrombin protease was also run at assay concentrations, seen as a faint band at approximately 30 kDa in lane 9.

5.3.6.2 Stability of TRX_N156P in assay buffer

To see if the introduction of the N156P mutant had affected protein stability at 25 °C or 37 °C, the mutant was incubated in 20 mM Tris pH 8.0 for 24 hrs both temperatures, as seen in **Figure 50**.

At 25 °C, seen in **Figure 50a**), TRX_N156P (40 kDa) remained soluble for 4 hrs (**Figure 50a, lane 6**) before the protein lost solubility and the band was greatly reduced in size. The dimeric form of TRX_N156P could also be seen as an 80 kDa band for the same length of time as the full length protein.

At 37 °C, soluble TRX_N156P (**b**) was present for more than 2 hrs (**Figure 50b, lane 5**) before it became insoluble, shown by the band in **Figure 50b, lane 9**. As with TRX_4RepCT, no bands of low molecular weight became visible suggesting that no degradation of TRX_N156P had occurred to cause a loss of the full length 40 kDa protein band.

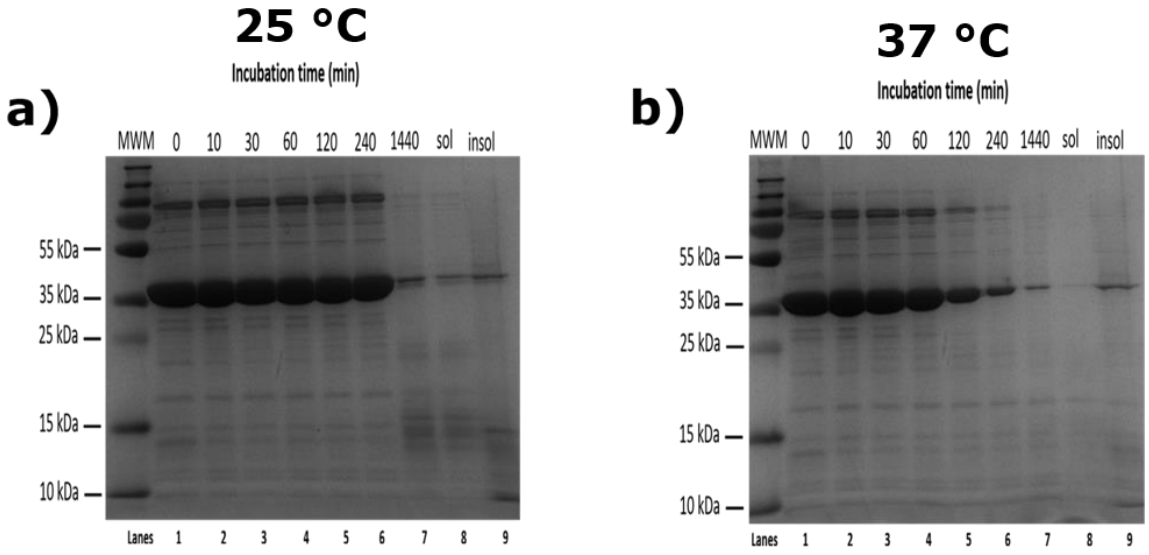

Figure 50. To confirm that loss of protein was caused by proteolysis, a negative control containing only TRX_N156P and 20 mM Tris pH 8.0 was incubated at 25 °C **a**) and 37 °C **b**) for 24 hrs. **a**) At 25 °C the mutant TRX_N156P remained soluble for over 4 hrs before the 40 kDa band was lost. **b**) At 37 °C, the 40 kDa band began to reduce from 2 hrs until the end of the experiment (24 hrs). A 40 kDa band could be seen in the insoluble fraction after 24 hr suggesting the protein had become insoluble over the course of the experiment at 37 °C although no degradation was thought to have occurred.

5.3.6.3 Stability of TRX_N156P in dH_2O

To investigate the effect of 20 mM Tris pH 8.0 on the solubility of the N156P mutant, the protein was incubated at 25 °C and 37 °C in dH_2O with a final protein concentration of 1 mg/mL as seen in **Figure 51**.

At 25 °C, seen in **Figure 51a**), TRX_N156P remained soluble throughout the experiment, although a small amount was seen in the insoluble fraction, seen as a 40 kDa band in **all lanes**. As with tris incubation, the dimeric TRX_N156P could also be seen at both temperatures for the same length of time as the full length protein.

The same was also seen for 37 °C, seen in **Figure 51b**), although protein solubility was lost after 4hr, seen in **Figure 51b, lane 6**. No degradation of TRX_N156P was shown to occur.

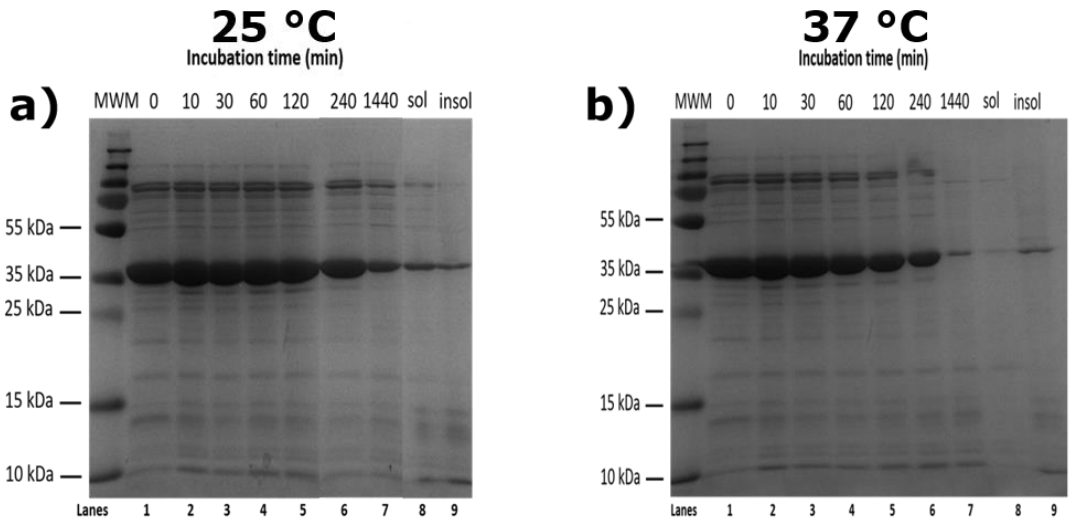

Figure 51. To determine any effect of 20 mM Tris storage buffer on TRX_N156P stability, TRX_N156P was incubated in dH_2O at 25 °C and 37°C for 24 hrs and analysed by 15% (w/v) SDS-PAGE. At 25 °C TRX_N156P remained soluble, shown by the 40 kDa band in all lanes, although some soluble protein was lost after 24 hrs. Similar to TRX_4RepCT, at 37 °C TRX_N156P was also lost after 4 hrs, seen in lane 6, becoming insoluble after this time shown in lane 9.

5.3.6.4 Stability of TRX_N156P by densitometry

In an attempt to quantify any change in protein band size seen over the course of the experiments, protein band densitometry was investigated for protein bands of interest seen by 15% (w/v) SDS-PAGE as shown in **Figure 52**.

At 25 °C, TRX_4RepCT (**Figure 52a**, **full line**) remained constant throughout the experiment, although a sharp drop in size was seen when incubated in water after 60 minutes. TRX_N156P (**dotted line**) was seen to remain constant for 240 minutes before gradually reducing for the remainder of the experiment.

At 37 °C, **Figure 52b**), both proteins lost band intensity rapidly before becoming more gradual after 240 minutes.

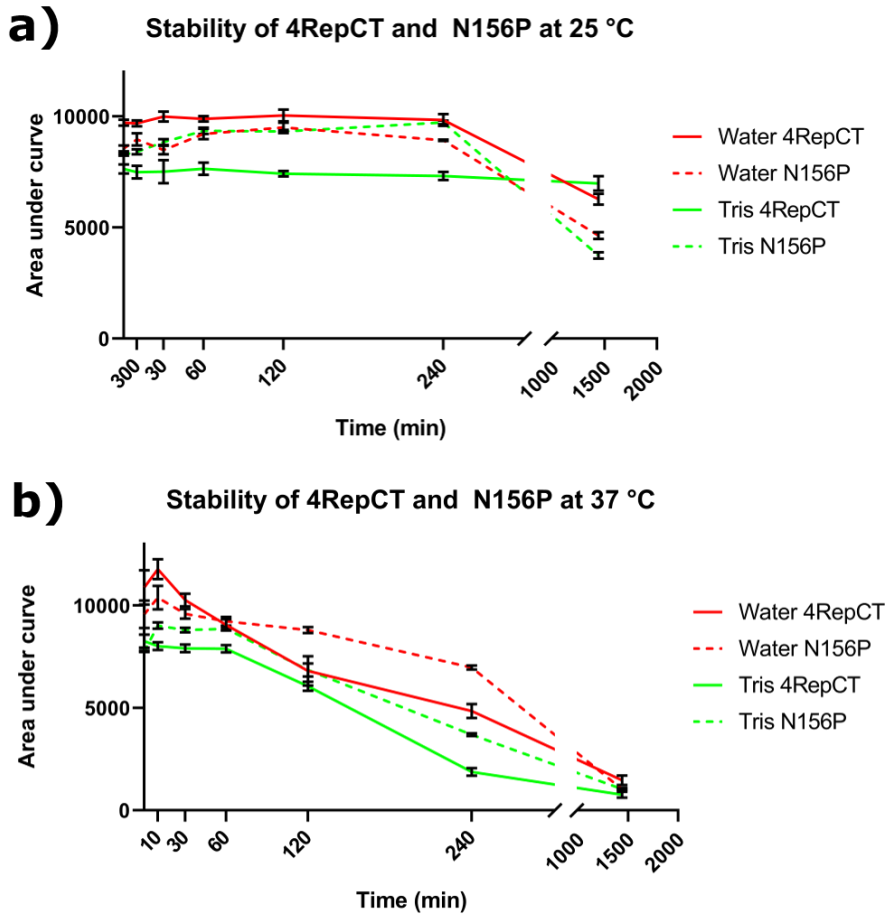

Figure 52. The band density of the full length TRX_N156P protein was plotted against time to visualise the stability of the protein over time at both 25 °C **a**) and 37 °C **b**). **a**) At 25 °C, TRX_4RepCT (full line) remained constant throughout the experiment, although a sharp drop in size was seen when incubated in water after 60 minutes. TRX_N156P (dotted line) was seen to remain constant for 240 minutes before gradually reducing for the remainder of the experiment. **b**) At 37 °C, both proteins lost band intensity rapidly before becoming more gradual after 240 minutes.

5.3.6.5 Degradation of soluble TRX_N156P by MMP2

The degradation behaviour of the mutant N156P was determined by the same protocol as TRX_4RepCT (see **Section 4.3.3.3**). With MMP2 assay concentrations of 11.3 μM (>1000 pmol/min/μg protein), TRX_N156P was shown to degrade after 10 minutes at both temperatures, as seen in **Figure 53**. The soluble 40 kDa band (**all gels, lane 1**) was greatly reduced after 10 minutes, at which point 3 distinct bands at 15 kDa, 20 kDa and 35 kDa became visible.

At 25 °C, **Figure 53a**), the 20 kDa and 35 kDa band remained for a further 4 hrs (**gel a, lane 6**) before whilst the 15 kDa remained throughout the experiment at both temperatures. This was confirmed by gel band densitometry as the 20 kDa band (**red**) became visible and later disappeared after 4 hrs meanwhile the 15 kDa band (**green**) remained visible throughout the experiment. A 10 kDa band (**blue**) became visible, confirmed by densitometry, after 2 hrs (**gel a, lane 5**) and remained until the end of the experiment.

At 37 °C, **Figure 53b**), although the same products could be seen, the 20 kDa band was lost after 30 minutes while the 35 kDa band remained for a further 4 hrs. Similar to that seen at 25 °C, two bands (<10 kDa and 15 kDa) were also seen in the insoluble fraction (**gel b, lane 9**) suggesting that after 24 hrs, the degradation products had become insoluble.

Densitometry of the full length protein bands **Figure 53c**) clearly showed an increase in the rate of degradation over the course of the experiment. At both temperatures, band representing TRX_4RepCT (**full line**) was not greatly reduced in size suggesting little degradation had taken place. The band representing TRX_N156P (**dotted**) displayed a change of density of 320 area min^{-1} and 336.6 area min^{-1} respectively over the first 10 minutes.

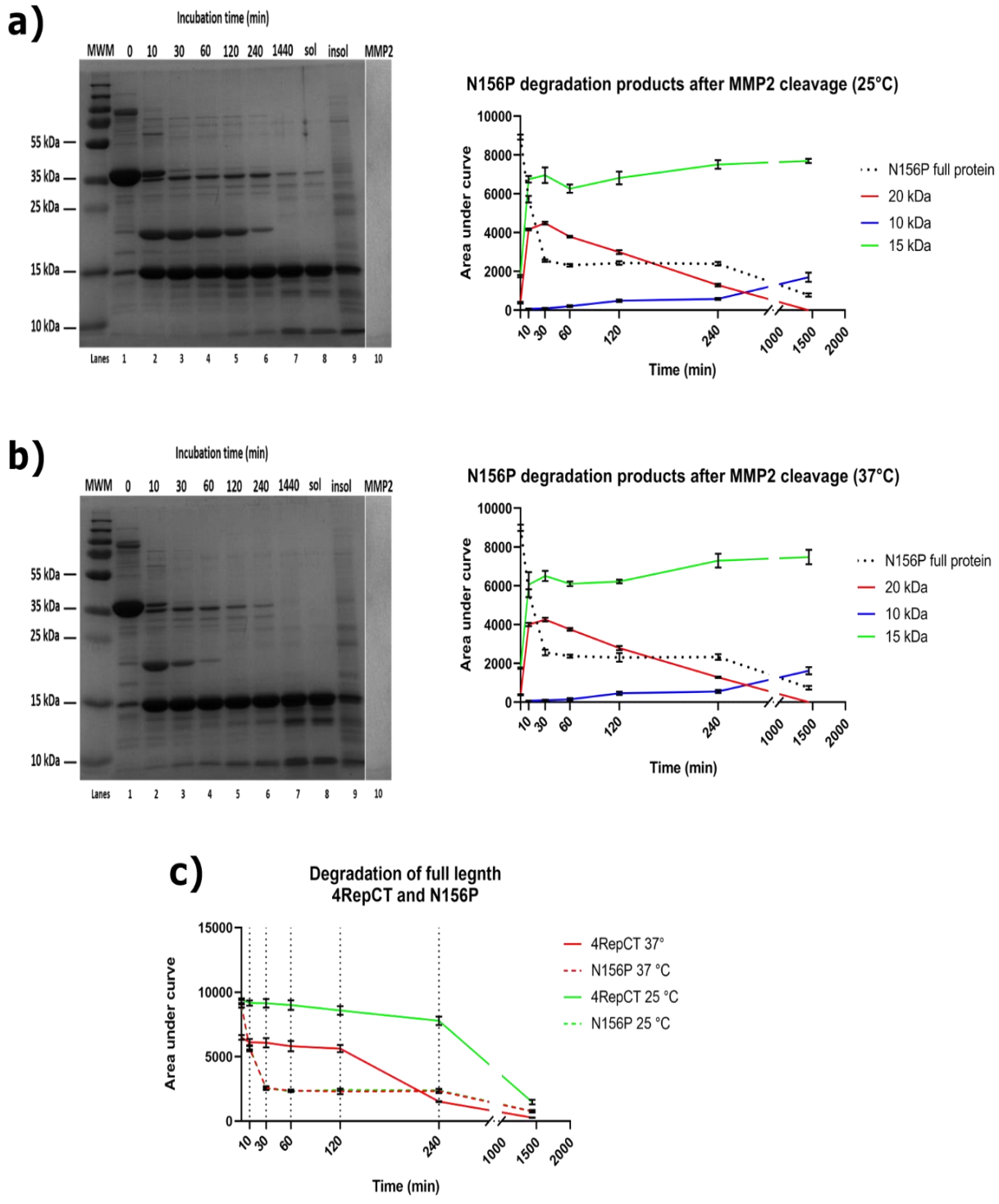

Figure 53. MMP2 cleavage of TRX_N156P was analysed by 15% (w/v) SDS-PAGE and densitometry at 25 °C **a**) and 37 °C **b**) in addition to band densitometry of the full length mutant protein compared to 4RepCT **c**). At both temperatures, the 40 kDa band was degraded within 10 minutes to produce four distinct degradation products (<10 kDa, 15 kDa, 20 kDa and 35 kDa respectively). **a**) At 25 °C these degradation products persisted for 4 hrs at which point lower molecular weight bands become visible from lane 5 onwards. **b**) The same band is present for an hour at 37 °C before it is further degraded and the <10 kDa band is seen from 10 minutes into the experiment. The peak area pixel density was plotted over time for the protein bands representing the full length protein (dotted), 20 kDa (red), 15 kDa (green) and 10 kDa (blue). **c**) The full length protein (dotted line) band was also compared to the full length band of 4RepCT (full line) over the same time period at both temperatures (25 °C and 37 °C, green and red respectively) and clearly displayed the increased rate of degradation.

5.3.6.6 Degradation of soluble TRX_N156P by MMP9

Incubated in 5.84 μM MMP9 (>1300 pmol/min/μg protein), TRX_N156P was seen to undergo degradation after 10 minutes at both temperatures as shown in **Figure 54**. The 40 kDa band was cleaved to produce four cleavage products at 35 kDa, 20 kDa (**red**), 15 kDa (**green**) and 10 kDa (**blue**).

At 25 °C, **Figure 54a**), the 15 kDa and 20 kDa bands were observed after 10 minutes. While the 15 kDa band remained soluble throughout the experiment, confirmed by densitometry, the 20 kDa band was further degraded after 4 hrs to produce the 10 kDa band (blue) seen in **lane 7** (**gel a**). After the experiment, the 10 kDa, 15 kDa and 35 kDa products could all be seen in the insoluble fraction, seen in **lane 9**.

At 37 °C, **Figure 54b**), the 20 kDa band was lost after 1 hr (**gel b**, **lane 4**) before it was further degraded to produce the 10 kDa band which remained until the end of the experiment. A 35 kDa band was also seen after 1hr (**lane 4**) incubation before it was later lost after 4 hrs in **lane 6**. Similar to 25 °C, the 10 kDa and 15 kDa bands could be seen in the insoluble fraction (**lane 9**) in addition to the 25 kDa band.

Densitometry of the full length protein bands **Figure 54c**) clearly showed an increase in the rate of degradation over the course of the experiment although slower than that seen from MMP2 cleavage. As seen, the TRX_4RepCT band (**full line**) was not greatly reduced in size suggesting little degradation had taken place. The band representing TRX_N156P (**dotted**) showed a change in band density of 60 area min^{-1} and 82 area min^{-1} respectively.

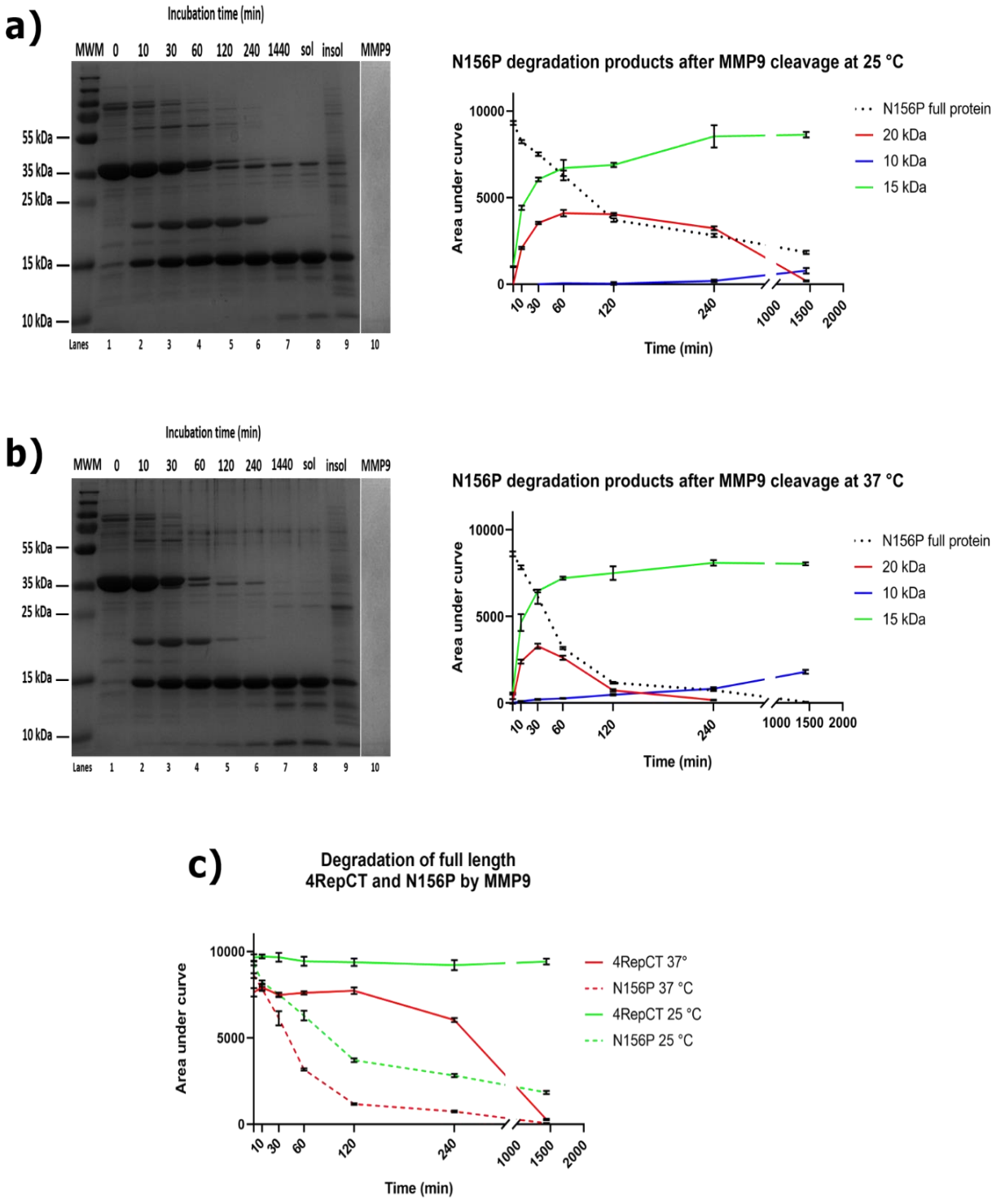

Figure 54. MMP9 cleavage of TRX_N156P was analysed by 15% (w/v) SDS-PAGE and densitometry at 25 °C **a**) and 37 °C **b**) and compared to 4RepCT **c**). Similar to MMP2, degradation products could be seen from 10 minutes, although the 40 kDa band remained present for 4hrs and 1 hr at 25 °C and 37°C respectively. **a**) At 25 °C the 40 kDa was visible for up to 1 hr, confirmed by densitometry (dotted). The 20 kDa degradation product (red) persisted for 4 hrs, seen in lane 7, at which point lower molecular weight bands (10 kDa, blue) became visible. **b**) At 37 °C, the full length protein (40 kDa) disappeared after 30 minutes before degradation products became visible. After 2 hrs, the 20 kDa band (red) was degraded and the 10 kDa band (blue) became visible, shown in lane 5. The thioredoxin protein band (15 kDa) remained soluble at both temperatures, shown in green. As with MMP2, the peak area pixel density was plotted over time for the protein bands representing the full length protein (dotted), 20 kDa (red), 15 kDa (green) and 10 kDa (blue). **c**) The full length protein (dotted line) band was also compared to the full length band of 4RepCT (full line) over the same time period at both temperatures (25 °C and 37 °C, green and red respectively) and clearly displayed the increased rate of degradation, although slower than seen from MMP2.

5.3.6.7 Degradation of TRX_N156P by ELNE

The same positive control was used for TRX_N156P as for TRX_4RepCT. As before (**Section 4.3.3.5**), TRX_N156P at 1.17 mg/mL was incubated in the presence of 34 nM ELNE (20 µmol/min/mg protein) as seen in **Figure 55**.

At 25 °C, **Figure 55a**), TRX_N156P (40 kDa) remained present for 24 hrs, although its solubility was lost.

At 37**°**C, **Figure 55b**), the same band was lost after 4 hrs, seen in **gel b**, **lane 6**. At both temperatures, multiple bands between 10 – 30 kDa became visible after 10 minutes as a result of enzymatic degradation, seen in **Figure 55b**, **lane 2**. At both temperatures two prominent bands could be seen in the insoluble fraction (**Figure 55b, lane 9**) at 10 kDa and 40 kDa.

Although densitometry of the full length protein bands **Figure 55c**) did not show a difference in degradation between proteins (**full** and **dotted**), they did show a difference between temperatures (**red** and **green**). Both TRX_4RepCT and TRX_N156P became insoluble at a slower rate at 25 °C than at 37 °C.

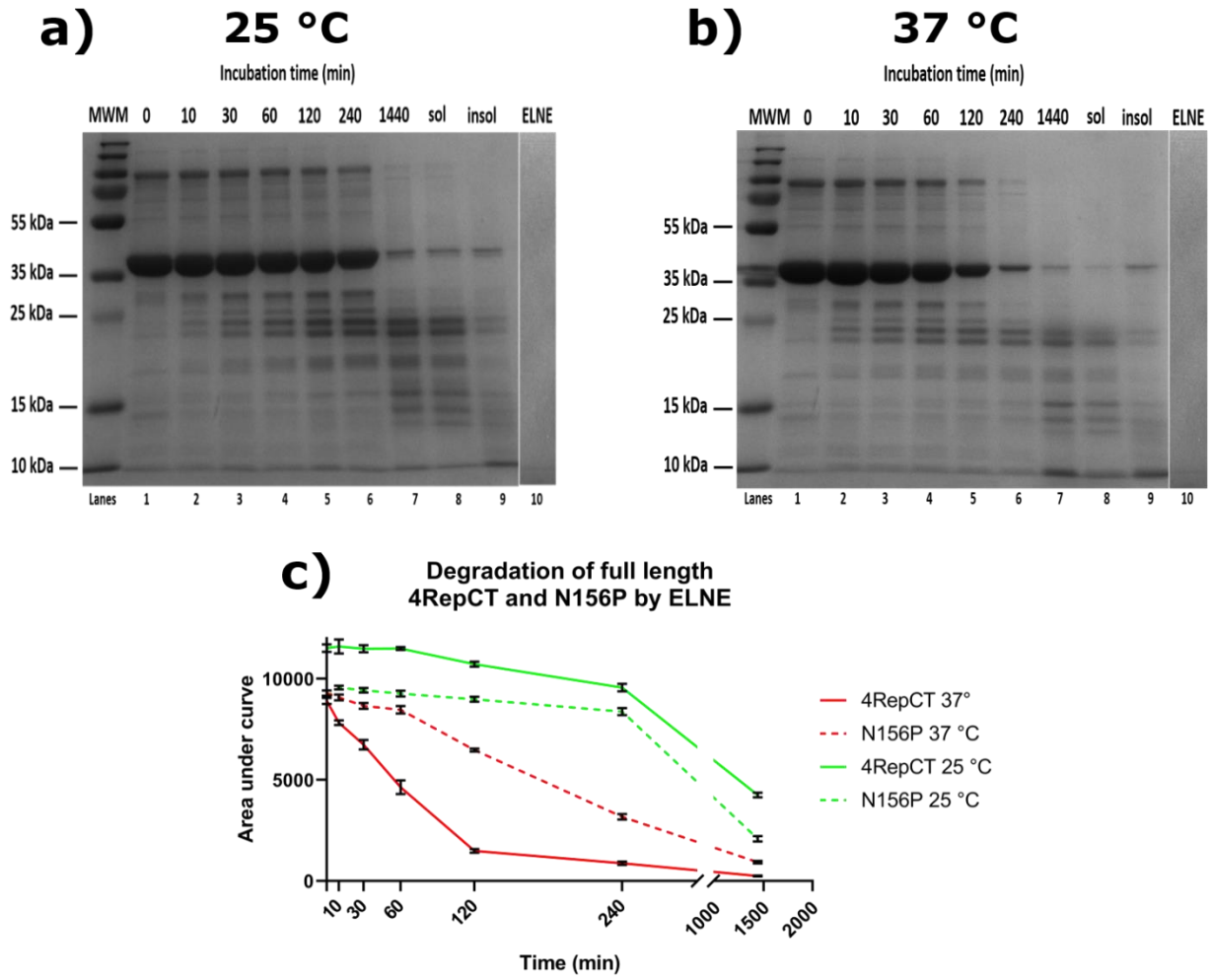

Figure 55. TRX_N156P was incubated with human neutrophil elastase for 24 hrs at 25 °C **a**) and 37 °C **b**) respectively and compared to full length TRX_4RepCT by peak densitometry **c**). **a**) At 25 °C, the soluble 40 kDa band of was degraded after 4 hrs. **b**) At 37 °C, the same band was lost after 2 hrs. At both temperatures, degradation products between 10 – 25 kDa could be seen from 10 minutes into the experiment, shown in lane 2. **c**) Peak densitometry of the full length protein did not show a significant difference in peak area change between proteins. However, the higher temperature (red), the band density was decreased faster over 2 hrs.

5.3.6.8 Degradation of TRX_N156P by α-chymotrypsin

As with TRX_4RepCT, the high concentration of α-chymotrypsin was chosen to directly compare degradation of silkworm silks as investigated by Brown et *al* [84].

The high α-chymotrypsin concentration meant that the full length 40 kDa protein was not observed at any point in the assay as seen in **Figure 56**. Instead, a <25 kDa protease band was seen in all lanes at 25 °C, becoming insoluble after 24 hrs (**lane 9**) while this band was lost after 4 hrs at 37 °C.

At 37 °C, bands <15 kDa also appeared to undergo degradation after 2 hrs (**lane 5**) and remained present for the remainder of the experiment. The same bands were seen at 25 °C after 24 hrs.

As no starting protein band was observed, peak area densitometry was not possible, and no conclusions could be drawn from the experiment.

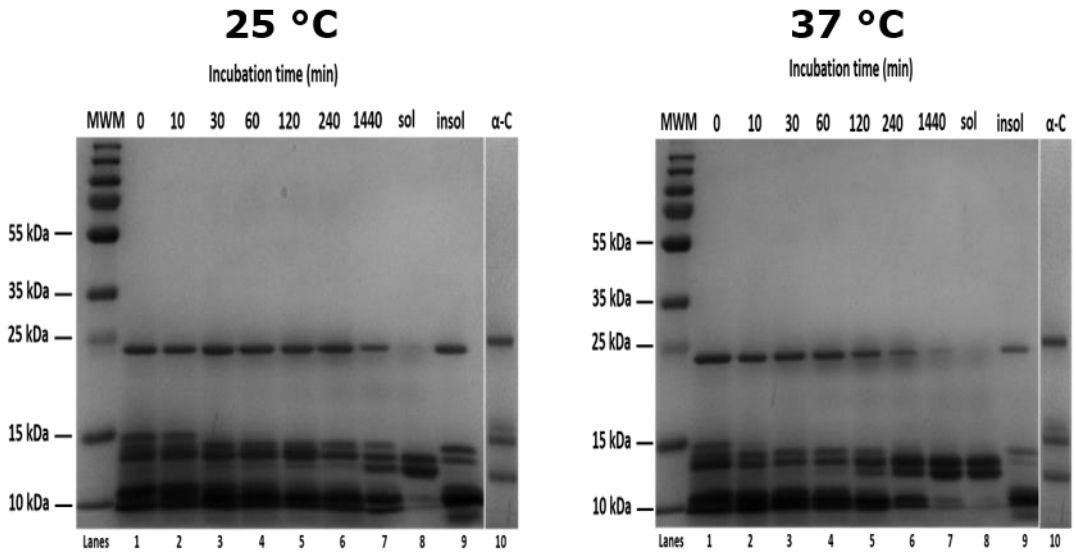

Figure 56. TRX_N156P was incubated with α-chymotrypsin for 24 hrs at 25 °C and 37 °C respectively and analysed by 15% (w/v) SDS-PAGE. Although the 40 kDa band of TRX_N156P was not seen, a protease band <25 kDa was seen for 4 hrs at 37 °C (lane 5) and 24 hrs at 25 °C (lane 7) before it disappeared. At both temperatures, smaller <15 kDa bands could be seen (lane 7 and 8 at 25 °C and lanes 5 – 8 at 37 °C) throughout the experiment but it was unclear if these had resulted from cleaved TRX_N156P.

5.3.6.9 TRX_A336P_S338del cleavage by MMP2 and MMP9

As with TRX_4RepCT and the N156P mutant, TRX_A336P_S338del was also subjected to proteolytic degradation by MMP2 (**Figure 57a**) and MMP9 (**Figure 57b**) at assay concentrations of 11.3 μM (>1000 pmol/min/μg protein) and 5.84 μM (>1300 pmol/min/μg protein) respectively at 30 °C. The low imidazole concentration used to purify the mutant resulted in numerous contaminating protein bands but the 4RepCT mutant was confirmed by thrombin cleavage as seen in **Section 5.3.6.1**.

When incubated with MMP2 (**Figure 57a**), the full length protein remained visible throughout the experiment, seen as the 40 kDa band in **Figure 57a, lanes 1 – 7**. Although the mutation position expected to produce cleavage products of 8 kDa and 31 kDa, no distinct bands were seen at these sizes, suggesting that cleavage had not taken place. After 10 minutes, seen in **Figure 57a lane 3**, a 15 kDa band was seen and remained for the duration of the experiment.

The full length protein (40 kDa) was also seen throughout the experiment when incubated with MMP9 **Figure 57b**). Unlike incubation with MMP2, no 15 kDa band was seen at any point.

The insoluble fraction of both experiments (**lane 9**) showed that the majority of the protein had become insoluble by the end of the experiment.

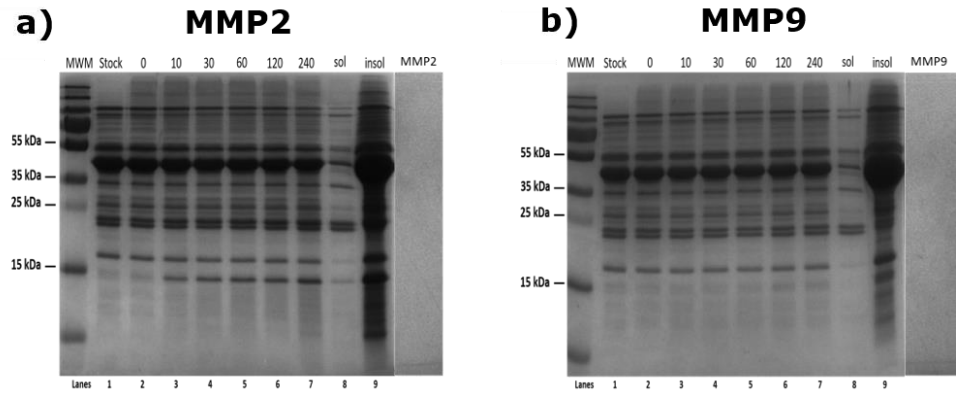

Figure 57. The C-terminal mutant A336P_S338del was incubated with MMP2 **a**) and MMP9 **b**) as described previously and analysed by 15% (w/v) SDS-PAGE. **a**) After MMP2 incubation, the full length 40 kDa protein was seen throughout the experiment while a 15 kDa band appeared after 10 minutes, seen in lane 3. No further proteolysis was seen to have occurred. **b**) MMP9 incubation also failed to produce cleavage products as the 40 kDa band remained throughout the experiment. The full length protein was seen in the insoluble fraction in both experiments as well as the 15 kDa band seen after MMP2 proteolysis.

5.3.6.10 Position of A336P_S338del mutation prevents access by protease to allow proteolysis

To expose the target cleavage sequence to the proteases, TRX_A336P_S338del was denatured by heating to 90 °C for 10 minutes before it was incubated with MMP2 and MMP9 at 30 °C, shown in **Figure 58**.

When incubated with MMP2 (**Figure 58a**), for the same length of time, the full length 40 kDa protein band remained throughout the experiment. By the end of the incubation, the band had become insoluble, appearing in **Figure 58a**, **lane 6**. As before, a 15 kDa band became visible after 60 minutes (**Figure 58a**, **lane 3**) and was still seen after 4 hrs (**Figure 58a, lane 4**).

MMP9 incubation (**Figure 58b**) also failed to produce cleavage products after denaturation. With the 40 kDa band remaining throughout the experiment, the same protein bands were seen as in **Figure 57b**.

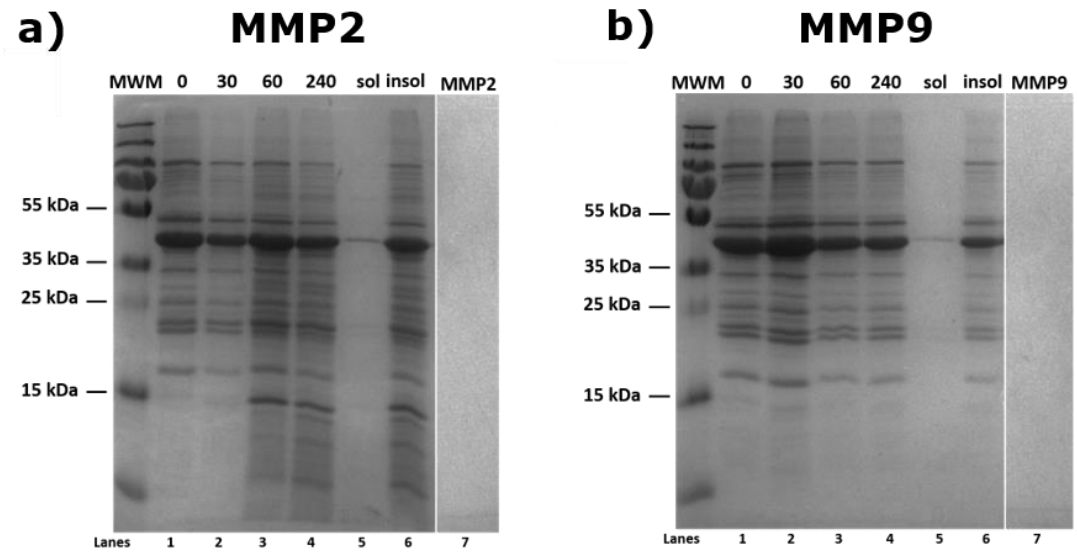

Figure 58. The terminal mutant was denatured by heating to 90 °C and again incubated with MMP2 (**a**) and MMP9 (**b**) before being analysed by 15% (w/v) SDS-PAGE. **a**) The full length (40 kDa) protein was seen for the duration of the experiment, becoming insoluble after 4 hrs, seen in lane 6. As before, a 15 kDa band was seen after MMP2 incubation which remained for the rest of the experiment. **b**) Apart from the full length protein, which remained for the full experiment, no other degradation products were seen as a result of MMP9 proteolysis, despite attempts to denature the mutant protein with high temperatures.

5.3.7 Mutant fibre formation

To investigate the possible spontaneous formation of fibres from MMP cleavage near the thrombin site, the N156P mutant at 1.5 mg/mL was cleaved in the presence of both MMPs and incubated as described for fibre formation (**Methods 2.16.2**).

Seen in **Figure 59**, spontaneous fibre formation was observed in all tubes except the negative control (TRX_N156P + 20 mM Tris pH 8.0). The positive control (TRX_4RepCT + thrombin) produced a single shorter fibre while the remaining solution contained precipitated protein. This was a similar observation for TRX_N156P with thrombin and when incubated with MMP2, although fibres were formed. The largest and most numerous fibres were produced by MMP9 cleavage of TRX_N156P. All fibres were still present after storage at 4 °C for 72 hrs although MMP2-induced fibres had visibly reduced in size.

As no MMP cleavage was observed with the A336P_S338del mutation, seen in **Figure 57** and **Figure 58**, subsequent no fibre formation was investigated. The low imidazole purification required to purify A336P_S338del also prevented sufficient protein expression for fibre formation. As the mutation was not situated near the thrombin cleavage site, it was not likely that MMP cleavage would result in spontaneous fibre formation like the N156P mutation.

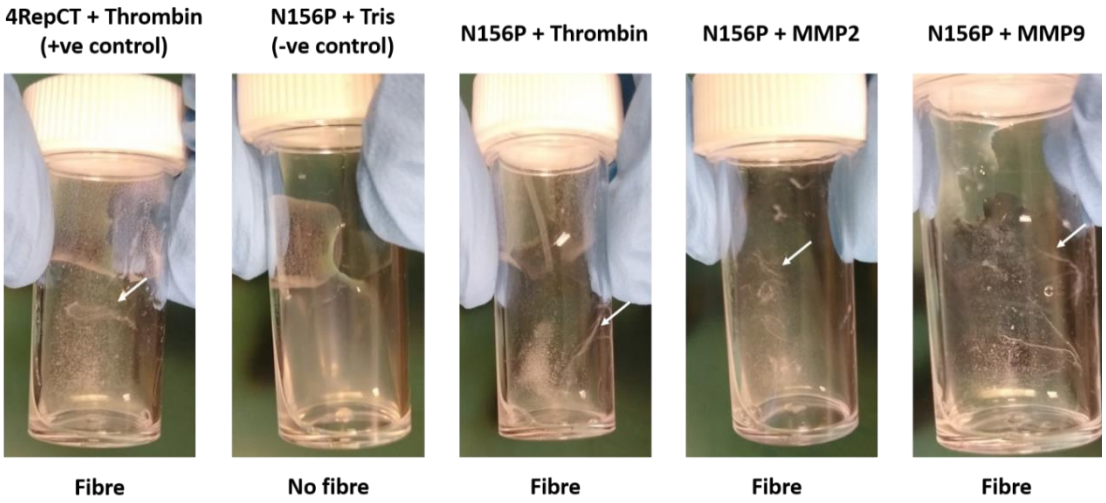

Figure 59. After standard fibre formation agitation as described in (**Methods 2.16.2**), mutant N156P fibres were formed in the presence of both MMPs and thrombin protease, the largest being observed after MMP9 cleavage. After storage at 4 °C for 72 hrs, MMP9-cleaved fibres persisted while MMP2-cleaved fibres decreased in size. After this time, thrombin-induced fibres were still present but not as large as those formed from MMP9. TRX_N156P was also incubated in 20 mM Tris pH 8.0 as a negative control. After 4hrs incubation, most of the protein had been lost from solution and no fibres had been formed.

5.3.8 Proteolytic degradation of mutant fibres

5.3.8.1 Short term

As with 4RepCT fibres, N156P mutant fibres were also degraded in MMP2 for the same time as described in **Section 4.3.5.1**. During this time, fibres were removed from the experiment after 30 minutes and 1hr (shown in **Figure 60**) in addition to 2 hr and 4 hrs. As before, fibres were analysed using bright field microscopy at 10x and 40x magnification. Although more aggregated protein, shown by **red** arrows, could be seen throughout the experiment, macroscopic fibres were observed at all points throughout the experiment. As with 4RepCT fibres, while the spontaneous formation of fibres resulted in random folding seen by the higher magnification images, no degradation of the fibres was observed.

5.3.8.2 Long term

After longer incubation with MMP2, N156P fibres were observed to undergo deterioration after 24 hrs when viewed at 10X magnification as seen in **Figure 61** and highlighted with **red** arrows. When compared to the fibre 0 min and the control fibres, fraying and splintering were seen. In addition to this, greater levels of protein aggregation were also seen in all samples.

5.3.8.3 Effect of fibre degradation on dark field and birefringence microscopy

When viewed with dark field and birefringence objectives, greater detail on the fibre degradation could be seen. The presence of protein aggregation along the fibres was seen to increase as the fibres aged.

Throughout the experiment, seen in **Figure 62**, visible polarised light increased within fibres suggesting that the fibre crystallinity had increased compared to the control fibres.

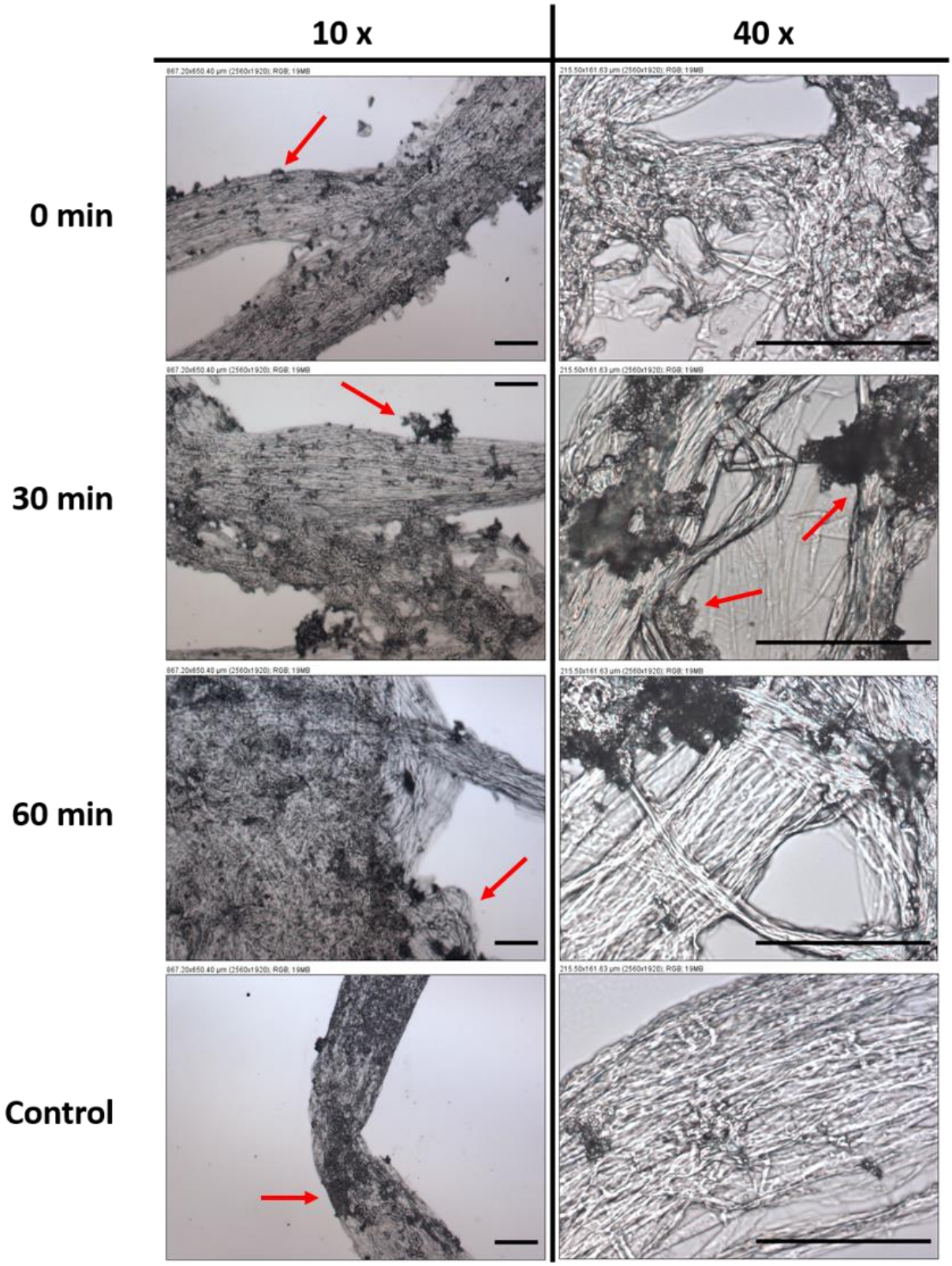

Figure 60. The effect of MMP2 incubation on N156P mutant fibres was investigated in the same way as 4RepCT in **Section 4.3.5.1**. Fibres were imaged over the course of 1 week to allow degradation to take place. Short term degradation was observed up to 4 hrs before further incubation up to 1 week. Higher levels of insoluble protein aggregation could be seen than with 4RepCT and are indicated by a **red** arrow. Images are representative of full image collection shown in **Appendix 8.6.2.** Scale bar = 100 µm.

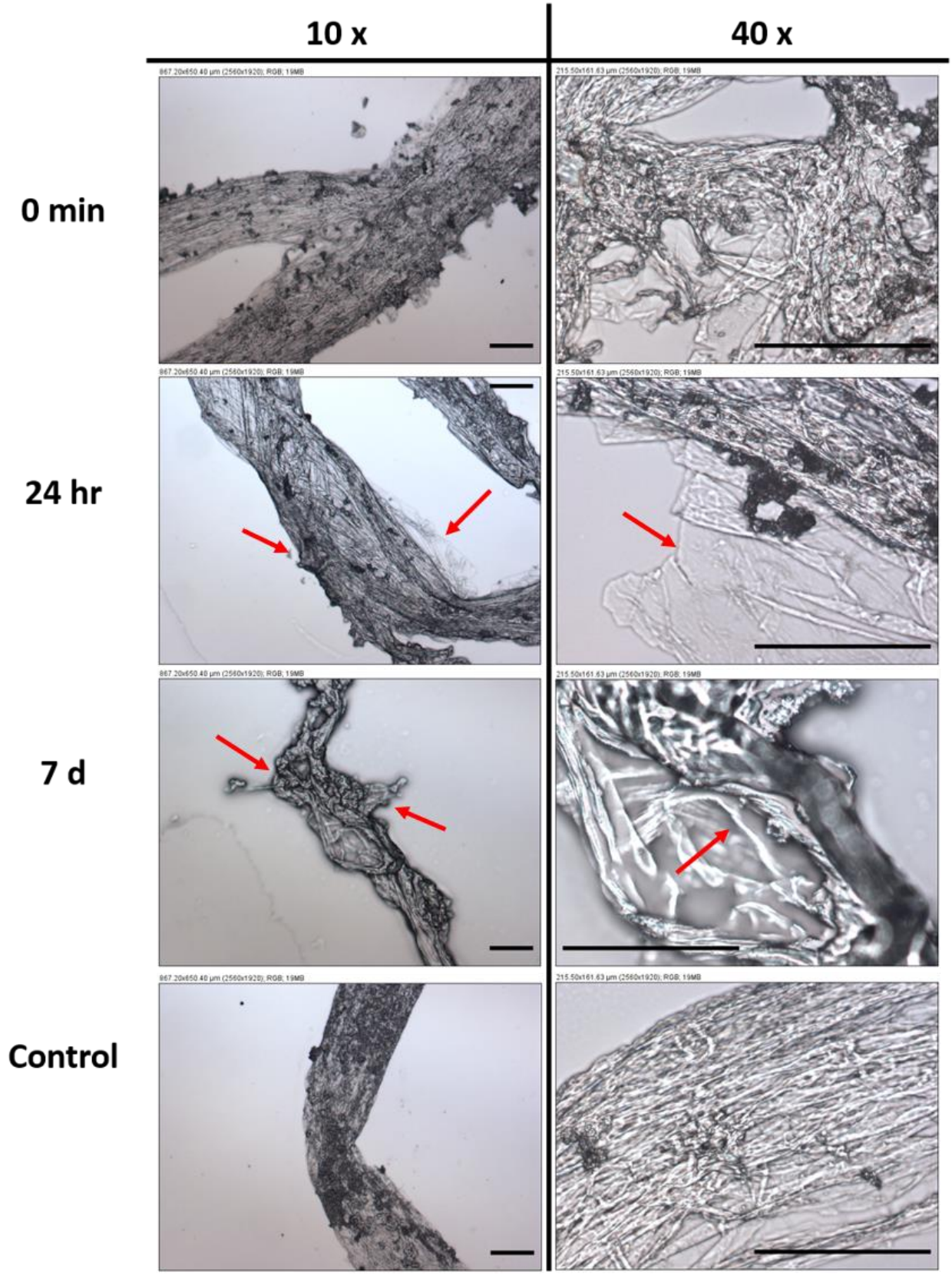

Figure 61. Greater degradation of N156P fibres was observed over the course of 1 week however compared to 4RepCT fibres. After 24 hrs, fibre fraying and splintering could be seen, suggesting that the fibres had undergone greater levels of deterioration. The locations of degradation are indicated by **red** arrows. Images are representative of full image capture, shown in **Appendix 8.6.2.** Scale bar = 100 μm.

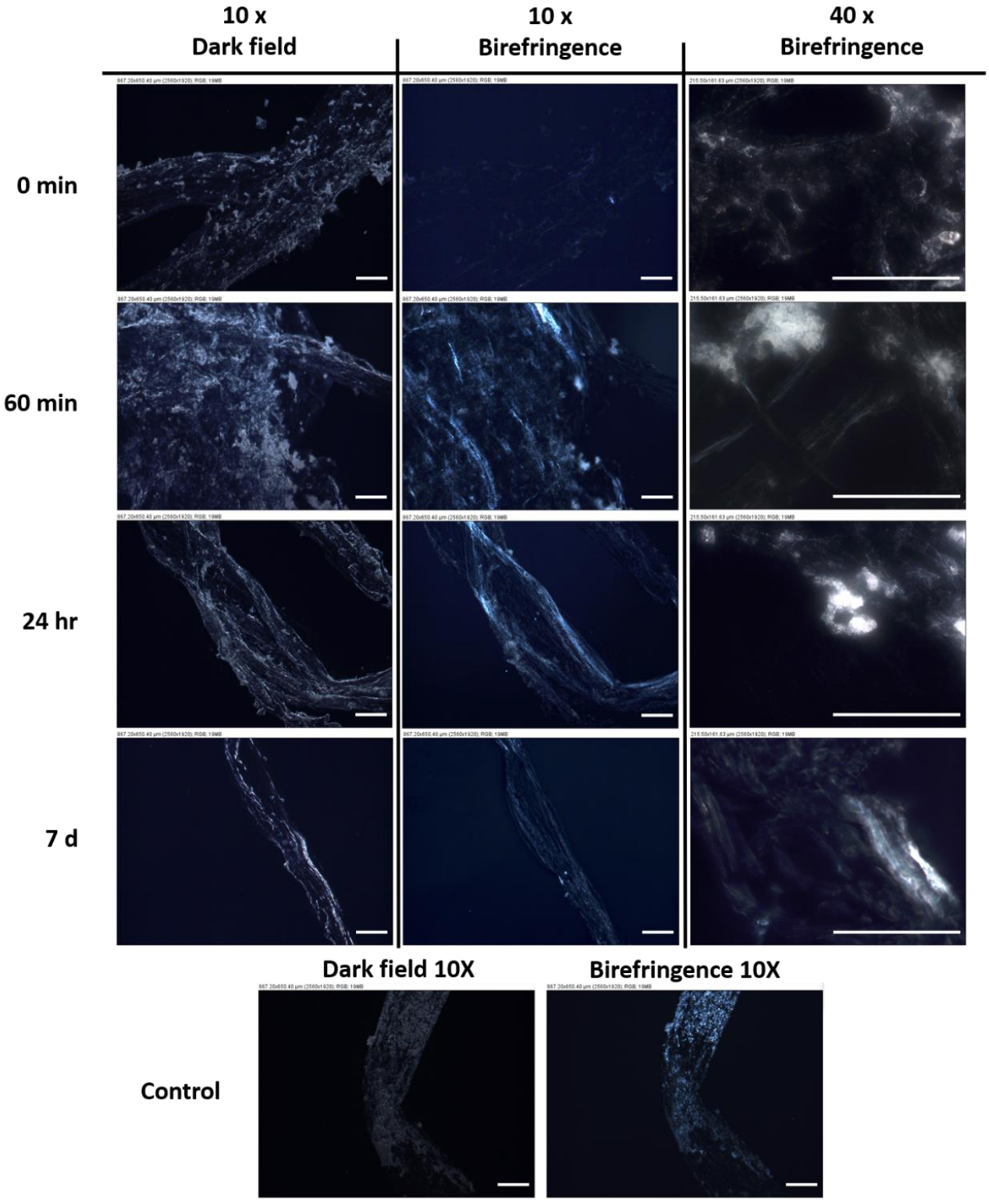

Figure 62. When viewed under dark field and birefringence however fibres showed changes in visible polarised light suggesting that a change in crystallinity had occurred on a nano-scale. Although some birefringence could be seen from the control fibre, this was caused by high levels of aggregated protein and not the fibre itself. Images are representative of full image capture, shown in **Appendix 8.6.2.** Scale bar = 100 µm.

5.4 Discussion

To enable proteolytic degradation in the ECM wound environment, wound-relevant MMP target sequences were introduced into the primary sequence of TRX_4RepCT [164,283]. By introducing a potential enzyme substrate into an environment containing elevated protease concentrations, it is thought that competitive substrate inhibition will occur to reduce the concentration of active MMPs. In turn this would allow wound repair mechanisms and active MMP inhibitors to be re-expressed to return the ECM to the process of controlled wound repair [149].

5.4.1 Selecting targets sequence mutations

From the enzymatic profiles that were generated of TRX_4RepCT against MMP2 and MMP9 seen in **Section 4.3.1**, a number of potential mutation sites were identified. Seen in **Figure 45a**, the location of these sites was spread across the full length of the protein, including two in the solubility tag. A further 12 were identified within the spidroin sequence, 11 of which resided within the conserved C-terminus. Although the mutations attributed to multiple different MMPs (MMP1, MMP2, MMP3, MMP9, MMP7, MMP12 and MMP13), mutations for MMP2 and MMP9 were prioritised due to their activity throughout wound repair, summarised in **Figure 45b**.

The location of each suggested sequence was also considered to avoid areas of high conservation within natural spidroins. These regions included the QALLEVITAL motif, thought to be important in spidroin dimerisation [36] and polymerisation [45], in addition to α-helices that formed 3-dimensional structure of the C-terminus as shown in **Figure 29**.

As disruption of α-helix folding would likely prevent dimer formation and fibre formation only seven of the suggested 14 mutations were taken forward to investigate; 102P_Y103V, N156P, 320P_S321R, A336P_S338del, S338P_339L, G344P and S394P shown by the **ringed** mutations in **Figure 45**. These seven mutations contained three sequences for MMP2 (102P_Y103V, A336P_S338del and S394P), three sequences for MMP9 (N156P, 320P_S321R and S338P_339L) and one sequence for MMP1 (G344P).

5.4.2 Mutagenesis complications and plasmid sequencing

pJ401Express plasmid

One difficulty faced when mutating regions of MaSp's is their inherently repetitive nature, causing problems for both protein expression and genetic editing [57,59]. While recombinant protein expression is limited by the natural pool of tRNA present within the cells for highly repetitive amino acid sequences, mutagenic manipulation is hindered by multiple regions of identical base pairs. The presence of similar codons prevents the use of site-specific primers in this regions or risk introducing multiple mutation events at once [284]. This was particularly prevalent for TRX_N156P which was situated within the 'neck' of the protein, within the first polyglycine region.

For this reason, mutagenic primers were designed for the pJ401Express plasmid vector using the NEBase changer software [194] and then compared to the full gene sequence to ensure that the resulting primer would only bind to mutation location and not elsewhere within the plasmid. PCR results using 25 repeat cycles produced results for all seven mutations, shown in **Figure 46a**. Successful amplification was seen for all constructs with an additional band approximately 2000bp produced by the 320P_S321R mutation, shown in **lane 7**.

However, when bacterial transformation was attempted, neither 102P_Y103V nor 320P_S321R mutations could be successfully transformed into NEB5α *E. coli*. The remaining constructs were successfully transformed into NEB5α *E. coli* and plated on kanamycin selective plates to ensure that the plasmid had been successfully taken up. The presence of antibiotics also ensured that the plasmid was retained within the cells to maintain antibiotic resistance. Once grown, the plasmid was purified from the NEB5α *E. coli* storage strain and submitted for Sanger DNA sequencing to determine the presence of the mutations using sequencing primers that flanked the TRX MASP15 protein sequence.

pET22b(+) plasmid

After recombinant expression failed to produce any of the mutations except N156P, it was suggested that the mutations should be

incorporated into a pET22b construct of the protein. Controlled with the more proficient T7 phage polymerase, pET22b protein expression is higher than that seen from T5 controlled systems such as pJ401Express plasmids.

As before, mutagenic primers were redesigned with NEBase changer before site directed mutagenesis was carried out. PCR products, seen in **Figure 46b**, showed amplification of the full plasmid, suggesting that mutagenesis had been successful. A second band between 500 and 1000 bases was also seen for TRX_N156P, seen in **lane 2**. However, as expression of TRX_N156P was already possible in the DL41 *E. coli* T5 system, no further optimisation was conducted to improve this further.

5.4.2.1 Confirming successful mutagenesis

To confirm the presence of the mutations in the pJ401Express plasmid, primers were designed to locate the T5 promoter and terminator sequence to allow forward and reverse sequencing of the gene sequence. The raw chromatographic data was assessed and translated before it was submitted to Nucleotide Blast reference tool to identify any differences with 4RepCT [285,286].

5.4.3 Expression of mutated TRX_4RepCT

Of the seven mutations taken forward for mutagenesis, five were successfully mutated and produced plasmids NEB5α *E. coli*. As with 4RepCT (**Methods 2.8**), the plasmids were transformed into XL1b and DL41 *E. coli* for storage and expression.

However, upon growth in both LB and minimal nutrient media, Ni^{2+} IMAC failed to produce recombinant protein for any C-terminal mutants as seen in **Appendix 8.5.1**. If recombinant protein had been expressed, it was expected to be eluted at 272 mM imidazole (40% elution buffer) but no 40 kDa band was observed. As the growth of the cells had not appeared to be affected, growing to exponential phase within 4 hrs, further investigation was undertaken to increase the expression of the C-terminal mutants.

5.4.3.1 Increase expression of C-terminal mutants

Insoluble pellet purification
If the C-terminal mutants had been expressed, it was possible that the folding of the conserved C-terminus had been disrupted, preventing soluble protein expression and subsequent purification. Shown in **Appendix 8.5.2 Figure 70**, expression was encouraged by resolubilising the insoluble pellet (**Figure 70a**), further time point expression tests (**Figure 70b**) and introducing additives to the purification buffers (**Figure 70c** and **Figure 70d**).

Time point expression tests
To investigate this, time point expression tests were conducted for all insoluble mutants and with TRX_4RepCT as a comparison in LB media. The expression test for A336P_S338del is shown in **Figure 70b**. By investigating the soluble and insoluble fractions at time points after protein expression had been induced, it was hoped that protein expression could be observed before it was subsequently removed. Over the course of 4 hrs, no definitive protein expression was seen to have occurred.

Supplemented elution buffers
Before recombinant expression was attempted in a different expression host, IMAC purification was also attempted with supplemented buffers, specifically non-denaturing (5% (v/v) glycerol) and denaturing (8M urea) additions, seen in **Figure 70c** and **Figure 70d** respectively. As no C-terminal mutants were expressed or purified, it was suggested that they were introduced into expression systems that encouraged 'difficult-to-express' proteins such as BL21 Rosetta and BL21 DE3 C41 *E. coli*.

5.4.3.2 Screening for unexpected target sequences

One theory to explain the low expression observed was that the mutations may have introduced unexpected protease cleavage sites, in addition to those for the targeted enzymes, resulting in proteolysis of the fusion protein before purification. To evaluate this, the protein sequences were submitted to an online PROSPER [224] screen and scanned for potential protease cleavage, seen in **Table 17.** The sequence was screened against different classes of proteases including aspartic,

cysteine, serine and metalloproteinases. In addition to the MMP target sequences, two mutations (S338P_339L and S394P) also introduced the target sequence for MMP3 while the G344P mutation had introduced a cleavage site for ELNE. However, as these proteases were not naturally present in *E. coli* this was not considered a problem and did not explain the lack of expressed protein. To increase recombinant expression, BL21-derived strains such as DL41 *E. coli* lack the bacterial proteases Lon and OmpT [57,287].

The PROSPER screen also highlighted the similarity between MMP2 and MMP9 target specificity. Although the target sequences had been introduced to encourage a single MMP, the screen suggested that many of the target sequences could be recognised by both MMPs. However, in a chronic wound environment, this shared substrate specificity was unlikely to cause issue as both proteases are known to be overexpressed, increasing the effectiveness of 4RepCT's potential for substrate inhibition [164,165,167].

5.4.3.3 Soluble TRX_4RepCT mutants

TRX_N156P

Unlike the C-terminal mutants, TRX_N156P was successfully expressed in both LB and minimal media from DL41 *E. coli*. To prevent protein misfolding, expression was conducted at a reduced temperature of 20 °C.

As with TRX_4RepCT, purification by Ni^{2+} IMAC produced >95% pure mutant protein in the presence of 272 mM imidazole (40% elution buffer), seen in the elution fraction, **Figure 47a**, **lane 8**. The resulting purification produced a yield of up to 25 mg protein/L of starting culture, higher than that produced by TRX_4RepCT (20 mg protein/L starting culture). The dimeric form, seen as an 80kDa band in **lane 8**, was also observed after nutrient rich LB media expression. The absence of this band from the minimal media expression suggests that the cells were restricted to only express protein under the control of the T5 promoter but no further expression. As with TRX_4RepCT, the purified protein was stable in 20 mM Tris pH 8.0 once dialysed overnight at 4 °C and able to be stored at -80 °C.

TRX_A336P_S338del

After poor expression from T5 controlled DL41 *E. coli* was observed for the C-terminal mutants, expression was attempted in T7 phage controlled BL21 *E. coli* and derived strains. Despite their increased protein expression, T7 expression systems had previously been avoided as a result of their limitations with use in minimal media and unnatural amino acid incorporation. However, a lack of protein expression from T5 systems suggested that a change in *E. coli* strain could be an option.

Utilising ampicillin resistance provided by the pET22b expression plasmid, TRX_A336P_S338del was expressed in BL21 *E. coli* in nutrient rich LB media. As seen in **Figure 47b**, the 40 kDa fusion protein was expressed and purified by an imidazole gradient of 10 – 70 mM (0% - 10% elution buffer), seen in **lanes 5 – 8**. The low concentration of imidazole also eluted a number of contaminating proteins, but this was not a concern for subsequent investigations.

It is unclear why the mutant was eluted at significantly lower concentrations of imidazole than TRX_4RepCT or the N156P mutant. As a C-terminal mutant, the mutation was far from the N-terminal poly(histidine) tag and was not thought to affect its association with the Ni^{2+} beads in the affinity column. Although not optimised, this method of recombinant expression and purification produced a yield of approximately 7 mg protein/L expression media. Like TRX_RepCT and the N156P mutant, the A336P_S338del mutant was dialysed in 20 mM Tris pH 8.0 and stored at -80 °C.

5.4.4 Quantifying TRX_4RepCT degradation

In an attempt to quantify the degradation of soluble TRX_4RepCT and its mutants, protein band densitometry was investigated. By manually integrating the area under the histogram curve generated from the change in pixel density between dark bands and light background, the size and concentration of protein could be estimated. However, the accuracy of this technique was limited by subjective elements such as post-capture image adjustment, the reliability of repeated manual integration, and the accuracy of the pixel histograms. As care was taken

to minimise these inaccuracies, the confidence in the densitometry was sufficient to support the conclusions produced by the physical gel results.

The accuracy of this technique was first investigated with the use of BSA, to produce a protein standard curve, as seen in **Figure 48**. The small range in densitometry values for each protein band provides good confidence that this technique would be effective when evaluating TRX_4RepCT cleavage products. However, it is important to note that Coomassie staining is sequence specific, binding to the positively charged residues within the denatured peptide [288,289]. As a result, gel bands of different proteins of the same concentration appear differently when stained with Coomassie stain depending on the number of positively charged residues within them [290].

Although a standard curve was produced, seen in **Figure 48b**, and a line of linear regression was plotted with an R^2 value of 0.9162, the protein concentrations calculated from the straight line equation could not be reconciled with the known assay protein concentrations that had been used. While protein concentrations of 0.8 mg/mL – 1.2 mg/mL could be accurately estimated, concentrations outside of this range were inaccurate. For example, the 20 kDa band produced by MMP2 cleavage of the N156P mutant, seen in **Figure 53a, lane 2,** produced an AUC value of 3491 (data not shown) which produced an estimated protein concentration of -0.03 mg/mL. Attempts to reconcile the straight line equation to better reflect assay concentrations was unsuccessful. To avoid this, the BSA standard curve was not used to estimate TRX_4RepCT protein concentrations. As a result, only the raw AUC values for bands were used to visualise degradation product kinetics instead of protein concentration estimations.

5.4.5 Identifying TRX_4RepCT mutants

Utilising the specific cleavage motif of the protease thrombin, the identity of TRX_4RepCT and its mutants could be confirmed by proteolysis. While not essential for TRX_4RepCT and the N156P mutant identification because recombinant overexpression was sufficient for identification, expression of the C-terminal mutant A336P_S338del was unclear within

the impure elution that resulted from elution with low imidazole concentrations.

Shown in **Figure 49**, undisturbed cleavage of TRX_4RepCT was expected to produce two cleavage products of 16 kDa (thioredoxin) and 23 kDa (4RepCT) in size. As shown in **Figure 49**, this occurred as expected with the normal TRX_4RepCT (**Figure 49a**) and N156P (**Figure 49b**) mutant protein with cleavage products seen after 10 minutes (**lane 2**) and remaining for the full experiment, while the full length 39 kDa protein (**lane 1**) was degraded.

After attempts to improve the purity with additional IMAC purifications were unsuccessful and risked the loss of the mutant protein, TRX_A336P_S338del was stored as impure fractions at -80 °C. However, the full length protein was still seen to degrade in the presence of thrombin over 4 hrs as seen in **Figure 49c.** Although not in line with the appropriate protein markers, two cleavage products could still be perceived at <15 kDa and <25 kDa, becoming visible after 10 minutes in **lane 2**. These products were clearer to identify from the insoluble lane (**lane 9**) as the individual proteins had become insoluble over the course of the assay.

All three proteins were incubated without agitation to avoid the loss of cleaved spidroin solubility. Released from its solubility tag, 4RepCT and its derivatives become insoluble with gentle agitation. This explains the difference in band intensity of the two cleavage products. While ideally both bands would display with equal intensity as both are released from a single cleavage event, the spidroin protein immediately became insoluble, reducing the band intensity. In an attempt to visualise the insoluble fraction, the assays were centrifuged to pellet precipitated protein before they were resuspended in SDS-PAGE loading dye in the presence of DTT. When compared to A336P_S338del insoluble lane (**lane 9**), very little cleaved spidroin can be seen from 4RepCT or N156P (**Figure 49a** and **Figure 49b** respectively).

5.4.6 Effect of the N156P mutation on protein degradation

Effect of temperature on mutant solubility and stability
To determine the effect of the mutant , on protein stability and solubility, TRX_N156P incubated in 20 mM Tris pH 8.0 and water over 24 hrs at 25 °C and 37 °C, seen in **Figure 50** and **Figure 51** respectively. When compared to TRX_4RepCT, the N156P mutation appeared to reduce its stability in assay buffer, as the protein band was lost after 4 hrs (**Figure 50a, lane 6**) at 25 °C. Although the same rate of decrease was seen from both proteins at 37 °C, becoming insoluble after 2 hrs (**Figure 50b, lane 2**).

The asparagine to proline substitution was located at the 'neck' of the protein, immediately after the thioredoxin solubility tag as seen in **Figure 45a**. When compared to the protein's behaviour in pure water, a similar solubility time was observed. In water, the protein remained visible for 4 hrs at both temperatures, seen in **Figure 51 lane 6**. The similarity in solubility between the two assay conditions confirmed that the tris buffer had no effect on protein stability.

In an attempt to quantify the rate of degradation that may have occurred, band densitometry was performed for each gel. When investigating the overall stability of the protein, the presence of the full length protein was analysed, seen in **Figure 52**. The resulting graphs clearly displayed a difference in behaviour between TRX_4RepCT and its mutant when incubated at 25 °C (**Figure 52a)**.

Although the initial protein bands remained constant over 120 minutes, the mutant then proceeded to lose band intensity and size over 24 hrs, compared to TRX_4RepCT which remained constant after an initial decrease. At 37 °C however, seen in **Figure 52b**, the protein band sizes and intensities decreased from the start of the experiment in both water and tris buffer. As discussed in **Section 4.4.4.1**, it was likely that the spidroin fusion proteins had lost their solubility in the higher temperature, considerably greater than that experienced by spiders and the habitats which natural spidroins would be expressed.

MMP2 and MMP9

The N156P mutation had a significant effect on the degradation rate of TRX_4RepCT in the presence of both MMP2 and MMP9, confirmed by both SDS-PAGE and densitometric analysis.

Cleaved by MMP2 after 10 minutes at both temperatures, seen in **Figure 53 lane 2**, the 40 kDa protein produced two distinct cleavage products at 15 kDa and 20 kDa. As the mutation was situated close to the already present thrombin cleavage site, the resulting products were similar in size, as seen in **Figure 49b**. While the 15 kDa band persisted for the remainder of the experiment, the 20 kDa band was later lost after 4 hrs (**Figure 53a, lane 6**) and 1 hr (**Figure 53b, lane 4**) into the experiment at 25 °C and 37 °C respectively. At this point a smaller band at 10 kDa became visible, thought to be a product of subsequent degradation that had taken place.

This theory was supported by densitometry of both gels, clearly displaying the peak size of all three degradation products. Interestingly, the 20 kDa band (**red**) is produced at the same rate as the smaller 15 kDa band (**green**) before it is later degraded and replaced by the 10 kDa (**blue**) degradation product. As expected the rate of proteolysis of the full length TRX_N156P was fastest at 37 °C at 336.6 area min^{-1} (n=5) compared to 320 area min^{-1} at 25 °C. When compared to the original TRX_4RepCT protein, seen in **Figure 53c**, it was clear that the introducing the N156P mutation had greatly increased the rate of proteolysis when in the presence of MMP2.

When incubated with MMP9, seen in **Figure 54**, a similar result was seen. At both temperatures, the full length protein (seen in **lane 1**) was degraded to produce two cleavage products at 15 kDa and 20 kDa. As with MMP2, the 20 kDa band underwent further degradation to produce a 10 kDa although the rate of cleavage was slower (60 area min^{-1} and 82 area min^{-1} for 25 °C and 37 °C respectively). As expected the formation and loss of bands was quicker at the higher temperature (**Figure 54b**) but overall proteolysis was slower compared to that by MMP2.

This was also supported by densitometry of the full length protein degradation, seen in **Figure 54c**. Despite this difference in cleavage rate, it was evident that the introduction of the N156P mutation had clearly influenced the rate of spidroin degradation by both MMPs.

ELNE and α-chymotrypsin

As anticipated, the N156P mutation did not have a dramatic effect on the degradation rate of TRX_4RepCT in the presence of either human neutrophil elastase or α-chymotrypsin, seen in **Figure 55** and **Figure 56**.

At 25 °C, full length TRX_N156P remained soluble for 4 hrs before it became insoluble after that time, seen in **Figure 55a, lane 6**. However, smaller sized bands were seen suggesting that low levels of proteolysis may have occurred, similar to that seen with TRX_4RepCT, becoming visible after 10 minutes.

At 37 °C however, TRX_N156P remained soluble for 120 minutes (**Figure 55b, lane 5**) compared to TRX_4RepCT which was lost after half that time. As with TRX_4RepCT, bands of approximately 25 kDa were also seen and became more prominent as the experiment continued. Seen in **Figure 55c**, densitometry suggested that temperature had affected the loss of solubility rather than the mutation. Although stable for longer, both band intensities were reduced faster at 37 °C compared to 25 °C.

Incubation of both TRX_4RepCT and its mutant with α-chymotrypsin produced a number of degradation products almost immediately, seen in **Figure 56**. As the full length protein (39 kDa TRX_4RepCT and 40 kDa TRX_N156P respectively), was not seen at any point for either protein, it suggested that proteolysis had occurred before the initial sample was taken. Similar to TRX_4RepCT, a 25 kDa band was seen for TRX_N156P cleavage at both temperatures from the beginning of the experiment (**lane 1**), remaining present for 24 hrs before it became insoluble. Although first thought to be a cleavage product, it is likely that this band represented the α-chymotrypsin enzyme that eventually became insoluble. The smaller bands between 10 kDa and 15

kDa were present in all gels at all time points. However, as the same bands were seen in both gels it is difficult to determine whether the mutation affected the degradation rate. For greater clarity, the first 10 minutes should be investigated closer, with a lower enzyme concentration to investigate protein sensitivity.

5.4.6.1 Effect of A336P_S338del mutation on soluble degradation

When incubated with either MMP2 or MMP9, the C-terminal mutant TRX_A336P_S338del was not seen to undergo degradation. Analysed by SDS-PAGE, the full 40 length kDa protein band remained for the full 4 hrs, seen in **Figure 57**. Despite contaminating proteins as a result of low imidazole purification, the recombinant protein was easily identifiable at assay concentrations of 1 mg/mL.

When incubated with MMP2, shown in **Figure 57a**, a band approximately 15 kDa was seen to appear after 10 minutes, shown in **lane 3**. However, the position of the mutation was expected to yield degradation products of 8 kDa and 32 kDa, neither of which were observed. As a result, it was concluded that cleavage of the spidroin had not taken place.

A similar result was seen after MMP9 incubation, seen in **Figure 57b**. As no change in band intensity was observed, it was concluded that no degradation had taken place although the insoluble lanes for both figures (**lane 9**) were overloaded with contamination. Within this lane however, the 40 kDa band was also seen suggesting that the protein had eventually become insoluble over the course of the experiment. The observed concentration increase within the insoluble fraction was an artefact from the preparation of the insoluble fraction. To renature the insoluble protein, they were first pelleted at 18000 x *g* to sediment precipitated protein. As the resulting pellet was resuspended in a smaller volume of DTT-containing loading dye than the 500 µl assay volume, a higher concentration of protein was produced.

Located at the beginning of one of the five α-helices within TRX_4RepCT's C-terminus, it was possible that the target sequence was

not accessible by either protease, buried within the terminal domain. Despite this, introducing the mutation did not prevent subsequent dimer formation as the 80 kDa band was visible in **Figure 57** and **Figure 58**.

In an attempt to increase protease accessibility, the mutant was denatured with heat before being subjected to the same degradation protocol as before. While chemical denaturants would have allowed continuous denaturation, they would have likely interfered with protease folding and activity, inhibiting them as a result. As seen from **Figure 58** however, attempts to denature the spidroin did not result in greater proteolysis. While the sequence may have still be hidden from the respective proteases, it was possible that the denatured protein retained their structure before the enzymes could cleave the protein.

Another consideration is that fusion spidroins have previously been purified by heat precipitation as a result of their extreme stability at high temperatures [68]. However, this procedure was carried out on the recombinant proteins ADF3 and ADF4. As these proteins only consist of the repetitive regions of *Araneus diadematus* MaSp1 absent of any spidroin N-termini, it is unclear if the structured TRX_4RepCT could be treated with extreme heat given the loss of solubility observed from sustained 37 °C incubation.

A third consideration is that the mutated sequence was never incorporated into the spidroin sequence. While this could explain the lack of degradation seen from MMP2 and MMP9, it is unlikely because the sequences were confirmed before transformation and expression. In addition to this, the low concentration of imidazole required to elute the protein during purification would have given rise to concern for wildtype TRX_4RepCT.

It is also possible that the contaminating *E. coli* proteins may have been degraded by the proteases, acting as unexpected substrate inhibitors. While this issue would also affect the results of TRX_4RepCT and TRX_N156P, the increased contamination observed for TRX_A336P_S338del may have been sufficient to prevent observable cleavage of the protein. If this is indeed the case, it also acts as a proof

of concept for substrate inhibition and the application of 4RepCT as a biomaterial. When introduced into wounds, 4RepCT would be expected to fulfil the opposite role, inhibiting the MMPs expressed at wound sites to reduce the degradation of the ECM and allow the recovery of the balanced wound repair process.

5.4.7 Effect of the N156P mutation on fibre formation

The proximity of the N156P mutation to the thrombin cleavage site suggested that fibre formation could also be possible after MMP cleavage. Situated six amino acids downstream of the original cleavage site, the MMP cleavage would produce products of similar size and function. Indeed, when cleaved by either MMPs with gentle agitation, macroscopic fibres were seen in both assays, seen in **Figure 59**.

Figure 59 also demonstrated that thrombin-cleaved fibres were still able to be formed with the mutant spidroin, remaining present in solution after a week at 4 °C. While the formation of fibre-inducing degradation products could lead to uncontrolled thrombosis during wound healing, the degradation results seen from MMP2 and MMP9 as seen in **Figure 53** and **Figure 54** showed that these products underwent further degradation to soluble 10 kDa products. It is also unclear if these fibres would be formed at wound sites, given the constant and gentle agitation required for their formation. Although this should be investigated *in vivo*, it is likely that if initial polymerisation occurred, the resulting fibrils would be disrupted by further degradation or by the comparatively high agitation seen in physical injury.

This method of fibre formation also presents itself as a potential new approach in fibre formation. Although the cost of recombinant human MMPs was greater than that of human thrombin, the MMP concentrations required for fibre formation was far lower. If readily expressed and activated, MMPs could be utilised for future fibre formation. The traditional thrombin approach introduced the protease to substrate ratio of 1:600 and a total protease mass of 2.5 µg per mL of reaction [28]. As shown from the degradation protocols, MMP2 (>1000 pmol/min/µg protein) and MMP9 (>1300 pmol/min/µg protein) were

capable of cleaving TRX_N156P at concentrations as low as 11.3 μM and 5.84 μM, respectively. At these concentrations, only 0.81 μg for MMP2 and 0.54 μg for MMP9 would be required to effectively cleave the same volume of TRX_N156P, 3x and 4.3x less than that needed by thrombin to cleave TRX_4RepCT.

5.4.8 N156P fibre degradation

As with 4RepCT, insoluble protein aggregation was also seen during fibre formation but at greater quantities than seen before. The macroscopic fibres were also larger and more diffuse than those formed with 4RepCT although this is difficult to attribute as a direct effect of the mutation.

Short term fibre degradation

As with RepCT fibres, the N156P mutant fibres were analysed using bright field, dark field and birefringence microscopy over the course of 7 days. Any degradation that occurred during this time was categorised as short term (0 min – 60 min) shown in **Figure 60**, and long term (120 min – 7 days) as shown in **Figure 61**.

After 60 min, the mutant fibres were not degraded at either magnification, although greater levels of aggregated protein were observed as seen in **Figure 60**. Although not confirmed, it was possible that the reduced stability of the mutant, observed in **Figure 52** lead to the accumulation of aggregated protein during the fibre formation. A real-time study investigating fibre formation would help to better understand the process of fibre formation.

Long term fibre degradation

Longer term incubation (120 min – 7 days) resulted in the fraying and deterioration of fibres, greater than that seen from 4RepCT. Seen in **Figure 61** at both magnifications, deterioration of the fibres was observed after 24 hrs up to one week. Although the results generated were subjective, it was clear that the mutant fibres had undergone greater degradation than the normal 4RepCT fibres. A method of re-submersion would also allow the same fibres to be re-evaluated over time to see the progression of degradation. Throughout the incubation, aggregated protein levels continued to increase, suggesting that the

precipitated protein originated from the fibres, potentially accumulating as the fibre degraded.

Birefringence and dark field microscopy
Dark field microscopy was again used to produce images with better contrast, but the high levels of protein aggregation images prevented much information from being gathered.

As mentioned previously, it was anticipated that deteriorating fibres underwent a rearrangement of their crystalline regions, increasing the fibres overall crystallinity [51]. Seen in **Figure 62**, it was clear that an increase in polarisation had occurred, particularly after **24 hrs**. However, high levels of polarisation could also be seen from the **control fibre**. Upon closer inspection it became apparent that the polarisation seen from the **control fibre** originated from the aggregated protein, seen from the same fibre in bright field (**Figure 60** and **Figure 61**). It is likely that the aggregated protein was also highly structured and contributed to the high levels of polarised light seen by birefringence microscopy. The light seen from the **24 hr** fibre was along the length of the fibres, rather than the point light seen from aggregated protein.

5.4.9 Future investigations

Despite attempts to quantify the degradation of soluble TRX_4RepCT and its mutants, the resulting standard curve was not able to accurately predict protein concentrations for peaks with an area of 3609 or less. This could be addressed by producing a standard curve from pure TRX_4RepCT or relevant mutant protein. In doing so, the most accurate staining of TRX_4RepCT would be ensured, reducing the impact of sequence-specific staining like Coomassie blue. At the same concentrations as previously attempted with BSA, it would be possible to improve the standard curve and the accuracy of the protein concentration calculations.

Having successfully introduced two mutations into distinct regions of TRX_4RepCT, the continued investigation into new C-terminal mutations would be carried out. Investigations into expression of the four mutations 320P_S321R, S338P_339L, G344P and S394P should be

continued in T7 controlled systems such as BL21 Rosetta *E. coli*. If successful, these mutations would allow insight into the effects of different mutation locations within the C-terminus and their facilitated proteolytic degradation.

The successful introduction of a second C-terminal mutant would also provide a comparison to A336P_S338del. Incorporating two target sequences within the same spidroin also presents a basis for tuneable degradation. From these investigations, the order and possible hierarchy of target sequences could be established, an important factor for designing biodegradable material.

5.5 Conclusions

This work serves as a proof-of-concept for the novel *in silico* approach proposed earlier in this thesis. This chapter successfully presents results that show that the introduced mutations suggested by the *in silico* tool increased the rate of degradation.

The results of this chapter also confirm that the position of the mutations was critical in facilitating degradation. Of the two mutations that were introduced into the recombinant spidroin, only one clearly influenced the degradation rate. As suggested from the model of 4RepCT, the accessibly of the N156P target sequence to the proteases enabled rapid and processive cleavage of the peptide sequence in both soluble and insoluble forms. Although the A336P_S338del mutant was introduced into the C-terminal, its location prevented cleavage by the protease, leaving the spidroin whole.

The N156P mutation greatly increased the degradation rate, both as a soluble protein and as insoluble fibres. Although full fibre proteolysis was not seen, the mutant fibres displayed greater deterioration than the original 4RepCT fibres. The soluble degradation results also revealed that the cleavage products underwent secondary degradation, a result that was predicted from the *in silico* studies. The *in silico* approach can therefore be regarded with confidence as it supported observations from natural silk termini and 4RepCT.

6. Final conclusions

It was the aim of this project to control the degradation rate of the recombinant spidroin 4RepCT by introducing MMP target sequences into its primary amino acid sequence. By predictably influencing the rate of proteolysis, 4RepCT can be further developed into a biodegradable protein scaffold for tissue regeneration. The approach of introducing specific proteolytic sequences into the spidroin protein backbone has not been attempted previously.

In 2015 the concept of tuneable degradation through the introduction of specific target sequences was proposed by Müller-Hermann and Scheibel [72]. Since then, a number of approaches have sought to influence the degradation behaviour of recombinant spider silks [25,195]. The degradation of silk and silk-based materials have also been investigated using physical and chemical means such as thermo-oxidation and freeze-drying [291,292]. Although these approaches have been shown to yield tuneable degradation, the nuanced approach of targeting specific wound-relevant proteases in this study is novel [104].

While prior investigations into controlled degradation have highlighted the effect of spidroin size and the use of MMP-specific sequences to encourage proteolysis, this project takes the unique approach of introducing the sequences directly into the spidroin protein sequence [195,293]. The results presented in final chapter of this work demonstrate that this aim was achieved, showing the effect of mutation location on subsequent MMP proteolysis. This contributes to the rich knowledge surrounding the structure and function of the non-repetitive C-terminal domain [45]. In particular this work confirms that the location of the A336P_S338del mutation site is buried within the tertiary structure of the domain, as predicted by Ittah *et al* [44]. This result was achieved using *in silico* profile techniques that were designed and evaluated in Chapter 3.

Chapter 3 further reinforces the need for recombinant spidroin-based scaffolds for biomedical applications. Using protein sequences of natural spidroin termini, proteolytic cleavage by wound

relevant MMPs was accurately predicted. Supported by *in vitro* degradation by MMP2, MMP9, ELNE and α-chymotrypsin, the *in silico* approach enabled mutations within 4RepCT to be identified and introduced. As discussed in the chapter, the use of sequence prediction software to detect already present target sequences is not a new development [259]. However, the method outlined in Chapter 3 provides researchers with the ability to identify potential and future target sequences as well. Using this approach, natural silk sequences can be prospected for attractive sequences.

This chapter also confirms the presence of naturally occurring target sequences within natural spidroin sequences. While the ability to consume silk has been well established, little was known about the presence of proteolytic target sequences. Although it is unlikely that the occurrence of these sites has resulted from any evolutionary pressure, their presence further presents spidroins as suitable degradable biomaterials. The *in silico* results also suggested that these sites were common within spidroins, suggesting that many silks could be utilised in biodegradable applications.

This project also served to further characterise the recombinant spidroin TRX_4RepCT, as discussed in Chapter 4. Building on the protocols reported by Stark *et al.,* TRX_4RepCT was successfully expressed, purified and stored as a soluble fusion protein [28,60]. This allowed 4RepCT to be investigated as a soluble protein and insoluble films or fibres after spontaneous polymerisation after cleavage of the solubility tag [28,65]. In these morphologies it was observed that little *in vitro* degradation occurred in the presence of MMP2, MMP9 or ELNE despite the presence of target sites within the protein sequence. This is similar to degradation observed by Müller-Hermann *et al.* with the similar recombinant spidroin eADF4 [72]. As with eADF4, degradation of 4RepCT was minimal until the targeted cleavage sites were introduced.

The effect of introducing specific target sequences into 4RepCT was assessed in Chapter 5. Located in the flexible amorphous region of 4RepCT, the N156P mutation significantly increased the degradation of

the spidroin in the presence of MMP2 and MMP9, supported by protein band densitometry and polarised light microscopy. The mutation location was not observed to affect protein folding and allowed TRX_N156P was stored as a soluble fusion protein. Furthermore, the solubility tag could be removed to allow the spontaneous formation of recombinant fibres, similar to 4RepCT [60]. Without genetic manipulation, the enzymatic degradation of silk fibres has been shown to be a slow and gradual process [25,84,294]. Through the introduction of protease sequences, the degradation behaviour of silk-based biomaterials has been shown to increase [188]. In addition to soluble protein degradation, the N156P mutation also increased the degradation of 4RepCT fibres, supported by birefringence microscopy as fibre crystallinity increased during degradation. Fibre formation was also observed from MMP cleavage products suggesting an alternative method for future fibre formation.

A recent review by Las Heras *et al.* compared the therapeutic approaches available for the treatment of chronic wound [151]. In this review, Las Heras comments on the use of decellularised scaffolds to encourage the migration of host cells while preventing further microbial infection. Although a number of scaffold treatments are currently in use, including collagen-based (Pelnac®) [295], polysaccharide-based (Talymed® and Hyalomatrix®) [168,296] and purely synthetic scaffolds (Suprathel®) [297], none of the reviewed scaffolds sought to act as a competitive inhibitor to ECM proteases [151,162,297]. As described in Chapter 5, the novel use of 4RepCT-based scaffolds as a competitive inhibitor has exciting potential.

The structure of 4RepCT's C-terminal domain was also explored further in this study. Although the A336P_S338del mutation was successfully introduced and expressed by BL21 Rosetta *E. coli*, targeted proteolysis by MMP2 or MMP9 was not observed. As discussed in the chapter, it was thought that cleavage was prevented by substrate inhibition by contaminating proteins or an inability to access the target sequences within the structured C-terminus of the protein.

Overall this project highlights the potential of tuneable spidroin degradation in silk-based scaffolds. By reducing the prevalent MMP

concentrations in chronic wounds, silk-based scaffolds will encourage the migration of new fibroblasts into the healing wound [90,149,151]. 4RepCT implants have already been shown to facilitate wound healing *in vivo* [90,110]. By incorporating techniques demonstrated in this project silk-based tissue scaffolds can be developed with targeted, tuneable degradation properties, improving the recovery pathway of chronic wounds.

7. References

1. Natural History Museum, B. World Spider Catalog. *World Spider Catalog.* (2019). doi:10.24436/2

2. Araneidae (Orb-weavers) - Spider Identification & Pictures. *Spider ID* Available at: https://spiderid.com/spider/araneidae/. (Accessed: 11th September 2020)

3. Araneus (Angulate & Round-shouldered Orb-weavers) - Spider Identification & Pictures. *Spider ID* Available at: https://spiderid.com/spider/araneidae/araneus/. (Accessed: 11th September 2020)

4. Argiope (Garden Orb-weavers) - Spider Identification & Pictures. *Spider ID* Available at: https://spiderid.com/spider/araneidae/argiope/. (Accessed: 11th September 2020)

5. Hudecki, A., Kiryczyński, G. & Łos, M. J. Biomaterials, definition, overview. *Stem Cells Biomater. Regen. Med.* 85–98 (2019). doi:10.1016/B978-0-12-812258-7.00007-1

6. Abramowitz, M. & Davidson, M. W. Light and Color - Optical Birefringence | Olympus Life Science. *Olympus America Inc* Available at: https://www.olympus-lifescience.com/en/microscope-resource/primer/lightandcolor/birefringence/. (Accessed: 11th September 2020)

7. Microscopy Resource Center | Olympus Life Science. *Olympus America Inc* Available at: https://www.olympus-lifescience.com/en/microscope-resource/. (Accessed: 11th September 2020)

8. Cyrtophora (Tent-web Spiders) - Spider Identification & Pictures. *Spider ID* Available at: https://spiderid.com/spider/araneidae/cyrtophora/. (Accessed: 11th September 2020)

9. Abramowitz, M., Tchourioukanov, K. I. & Davidson, M. W. Specialized Microscopy Techniques - Darkfield Illumination | Olympus Life Science. *Olympus America Inc* Available at: https://www.olympus-lifescience.com/en/microscope-resource/primer/techniques/darkfieldindex/. (Accessed: 11th September 2020)

10. Dolomedes (Fishing Spiders) - Spider Identification & Pictures. *Spider ID* Available at: https://spiderid.com/spider/pisauridae/dolomedes/. (Accessed: 11th September 2020)

11. Euprosthenops - Spider Identification & Pictures. *Spider ID* Available at: https://spiderid.com/spider/pisauridae/euprosthenops/. (Accessed: 11th September 2020)

12. Nephila (Golden Silk Orb-weavers) - Spider Identification & Pictures. *Spider ID* Available at: https://spiderid.com/spider/araneidae/nephila/. (Accessed: 11th September 2020)

13. Pholcidae (Cellar Spiders) - Spider Identification & Pictures. *Spider ID* Available at: https://spiderid.com/spider/pholcidae/. (Accessed: 11th September 2020)

14. Pholcus - Spider Identification & Pictures. *Spider ID* Available at: https://spiderid.com/spider/pholcidae/pholcus/. (Accessed: 11th September 2020)

15. Pisaura - Spider Identification & Pictures. *Spider ID* Available at: https://spiderid.com/spider/pisauridae/pisaura/. (Accessed: 11th September 2020)

16. Sierwald, P. Phylogenetic analysis of Pisaurine nursery web spiders, with revisions of Tetragonophthalma and Perenethis (Araneae, Lycosoidea, Pisauridae). *J. Arachnol.* **25**, 361–407 (1997).

17. Pisauridae (Nursery Web Spiders) - Spider Identification & Pictures. *Spider ID* Available at: https://spiderid.com/spider/pisauridae/. (Accessed: 11th September 2020)

18. Vainker, S. J. *Chinese silk : a cultural history*. (British Museum Press, 2004).

19. MarketsandMarketResearchLtd. Silk Market Analysis | Recent Market Developments | Industry Forecast to 2016-2021. *Market Research Report* 1–11 (2017). Available at: https://www.marketsandmarkets.com/Market-Reports/silk-market-110379892.html. (Accessed: 22nd January 2021)

20. Eisoldt, L., Smith, A. & Scheibel, T. Decoding the secrets of spider silk. *Mater. Today* **14**, 80–86 (2011).

21. Bott, R. A., Baumgartner, W., Bräunig, P., Menzel, F. & Joel, A. C. Adhesion enhancement of cribellate capture threads by epicuticular waxes of the insect prey sheds new light on spider web evolution. *Proc. R. Soc. B Biol. Sci.* **284**, (2017).

22. Vollrath, F. Strength and structure of spiders' silks. *Rev. Mol. Biotechnol.* **74**, 67–83 (2000).

23. Doblhofer, E., Heidebrecht, A. & Scheibel, T. To spin or not to spin: spider silk fibers and more. *Appl. Microbiol. Biotechnol.* **99**, 9361–9380 (2015).

24. Yarger, J. L., Cherry, B. R. & Van Der Vaart, A. Uncovering the structure-function relationship in spider silk. *Nat. Rev. Mater.* **3**, 1–11 (2018).

25. Holland, C., Numata, K., Rnjak-Kovacina, J. & Seib, F. P. The Biomedical Use of Silk: Past, Present, Future. *Adv. Healthc. Mater.* **8**, (2019).

26. Xu, M. & Lewis, R. V. Structure of a protein superfiber: spider dragline silk. *Proc. Natl. Acad. Sci. U. S. A.* **87**, 7120–7124 (1990).

27. Heim, M., Keerl, D. & Scheibel, T. Spider silk: From soluble protein to extraordinary fiber. *Angew. Chemie - Int. Ed.* **48**, 3584–3596 (2009).

28. Stark, M. *et al.* Macroscopic Fibers Self-Assembled from Recombinant Miniature Spider Silk Proteins. *Biomacromolecules* **8**, 1695–1701 (2007).

29. Humenik, M., Smith, A. M. & Scheibel, T. Recombinant Spider Silks—Biopolymers with Potential for Future Applications. *Polymers (Basel).* **3**, 640–661 (2011).

30. Schacht, K. & Scheibel, T. Processing of recombinant spider silk proteins into tailor-made materials for biomaterials applications. *Curr. Opin. Biotechnol.* **29**, 62–69 (2014).

31. Hagn, F. *et al.* A conserved spider silk domain acts as a molecular switch that controls fibre assembly. *Nature* **465**, 239–242 (2011).

32. Guinea, G. V., Elices, M., Pérez-Rigueiro, J. & Plaza, G. Self-tightening of spider silk fibers induced by moisture. *Polymer (Guildf).* **44**, 5785–5788 (2003).

33. Guinea, G. V, Elices, M., Pérez-Rigueiro, J. & Plaza, G. R. Stretching of supercontracted fibers: a link between spinning and the variability of spider silk. *J. Exp. Biol.* **208**, 25–30 (2005).

34. Savage, K. N. & Gosline, J. M. The role of proline in the elastic mechanism of hydrated spider silks. *J. Exp. Biol.* **211**, 1948–1957 (2008).

35. Agnarsson, I. *et al.* Supercontraction forces in spider dragline silk depend on hydration rate. *Zoology* **112**, 325–331 (2009).

36. Andersson, M. Mechanisms of Native and Artificial Spinning of Spider Silk (Thesis). (Swedish University of Agricultural Sciences, 2016).

37. Rising, A., Hjälm, G., Engström, W. & Johansson, J. N-terminal nonrepetitive domain common to dragline, flagelliform, and cylindriform spider silk proteins. *Biomacromolecules* **7**, 3120–3124 (2006).

38. Askarieh, G. *et al.* Self-assembly of spider silk proteins is controlled by a pH-sensitive relay. *Nature* **465**, 236–238 (2010).

39. Gaines, W. A., Sehorn, M. G. & Marcotte, W. R. Spidroin N-terminal domain

promotes a ph-dependent association of silk proteins during self-assembly. *J. Biol. Chem.* **285**, 40745–40753 (2010).

40. Hagn, F., Thamm, C., Scheibel, T. & Kessler, H. PH-dependent dimerization and salt-dependent stabilization of the N-terminal domain of spider dragline silk - Implications for fiber formation. *Angew. Chemie - Int. Ed.* **50**, 310–313 (2011).

41. Hedhammar, M. *et al.* Structural properties of recombinant nonrepetitive and repetitive parts of major ampullate spidroin 1 from Euprosthenops australis: Implications for fiber formation. *Biochemistry* **47**, 3407–3417 (2008).

42. Jaudzems, K. *et al.* pH-dependent dimerization of spider silk N-terminal domain requires relocation of a wedged tryptophan side chain. *J. Mol. Biol.* **422**, 477–487 (2012).

43. Jiang, W., Askarieh, G., Shkumatov, A., Hedhammar, M. & Knight, S. D. Structure of the N-terminal domain of Euprosthenops australis dragline silk suggests that conversion of spidroin dope to spider silk involves a conserved asymmetric dimer intermediate. *Acta Crystallogr. Sect. D Struct. Biol.* **75**, 618–627 (2019).

44. Ittah, S., Michaeli, A., Goldblum, A. & Gat, U. A model for the structure of the C-terminal domain of dragline spider silk and the role of its conserved cysteine. *Biomacromolecules* **8**, 2768–2773 (2007).

45. Strickland, M. *et al.* Conservation of a pH-sensitive structure in the C-terminal region of spider silk extends across the entire silk gene family. *Heredity (Edinb).* **120**, 1–7 (2018).

46. Chen, G. *et al.* Full-Length Minor Ampullate Spidroin Gene Sequence. *PLoS One* **7**, 1–11 (2012).

47. Cao, Y. & Wang, B. Biodegradation of silk biomaterials. *Int. J. Mol. Sci.* **10**, 1514–1524 (2009).

48. Vepari, C. & Kaplan, D. L. Silk as a biomaterial. *Prog. Polym. Sci.* **32**, 991–1007 (2007).

49. Venner, S., Pasquet, A., Leborgne, R. & Nancy, I. Web-building behaviour in the orb-weaving spider Zygiella x-notata: Influence of experience. *Anim. Behav.* **59**, 603–611 (2000).

50. Opell, B. D. Economics of spider orb-webs: The benefits of producing adhesive capture thread and of recycling silk. *Funct. Ecol.* **12**, 613–624 (1998).

51. Agnarsson, I., Boutry, C. & Blackledge, T. A. Spider silk aging: Initial improvement in a high performance material followed by slow degradation. *J. Exp. Zool. Part A Ecol. Genet. Physiol.* **309**, 494–504 (2008).

52. Peakall, D. B. Conservation of web proteins in the spider, Araneus diadematus. *J. Exp. Zool.* **176**, 257–264 (1971).

53. Scharff, N. *et al.* Phylogeny of the orb-weaving spider family Araneidae (Araneae: Araneoidea). *Cladistics* **0**, 1–21 (2019).

54. Blackledge, T. A. *et al.* Reconstructing web evolution and spider diversification in the molecular era. *Proc. Natl. Acad. Sci.* **106**, 5229–5234 (2009).

55. Fox, L. R. Cannibalism in Natural Populations. *Annu. Rev. Ecol. Syst.* **6**, 87–106 (1975).

56. Work, R. W. & Emerson, P. D. An apparatus and technique for the forcible silking of spiders. *J. Arachnol.* **10**, 1–10 (1982).

57. Rosano, G. L. & Ceccarelli, E. A. Recombinant protein expression in Escherichia coli: Advances and challenges. *Front. Microbiol.* **5**, 1–17 (2014).

58. Andersson, M. *et al.* Biomimetic spinning of artificial spider silk from a chimeric minispidroin. *Nat. Chem. Biol.* **13**, 262–264 (2017).

59. Xia, X.-X. *et al.* Native-sized recombinant spider silk protein produced in metabolically engineered Escherichia coli results in a strong fiber. *Proc. Natl. Acad. Sci.* **107**, 14059–14063 (2010).

60. Hedhammar, M. *et al.* Sterilized recombinant spider silk fibers of low pyrogenicity. *Biomacromolecules* **11**, 953–959 (2010).

61. Harris, J. L. *et al.* Rapid and general profiling of protease specificity by using combinatorial fluorogenic substrate libraries. *Proc. Natl. Acad. Sci.* **97**, 7754–7759 (2000).

62. Furlong, S. T. *et al.* Synthesis and Physical Characterization of a P1 Arginine Combinatorial Library, and Its Application to the Determination of the Substrate Specificity of Serine Peptidases. *Bioorganic Med. Chem.* **10**, 3637–3647 (2002).

63. Petrassi, H. M. *et al.* A strategy to profile prime and non-prime proteolytic substrate specificity. *Bioorganic Med. Chem. Lett.* **15**, 3162–3166 (2005).

64. Le Bonniec, B. F. *et al.* Characterization of the P2′ and P3′ Specificities of Thrombin Using Fluorescence-Quenched Substrates and Mapping of the Subsites by Mutagenesis. *Biochemistry* **35**, 7114–7122 (1996).

65. Jastrzebska, K. *et al.* The method of purifying bioengineered spider silk determines the silk sphere properties. *Sci. Rep.* **6**, 1–15 (2016).

66. Wohlrab, S. *et al.* Cell adhesion and proliferation on RGD-modified recombinant spider silk proteins. *Biomaterials* **33**, 6650–6659 (2012).

67. Heidebrecht, A. *et al.* Biomimetic Fibers Made of Recombinant Spidroins with the Same Toughness as Natural Spider Silk. *Adv. Mater.* **27**, 2189–2194 (2015).

68. Huemmerich, D. *et al.* Primary Structure Elements of Spider Dragline Silks and Their Contribution to Protein Solubility †. *Biochemistry* **43**, 13604–13612 (2004).

69. Schacht, K. & Scheibel, T. Controlled hydrogel formation of a recombinant spider silk protein. *Biomacromolecules* **12**, 2488–2495 (2011).

70. DeSimone, E., Aigner, T. B., Humenik, M., Lang, G. & Scheibel, T. Aqueous electrospinning of recombinant spider silk proteins. *Mater. Sci. Eng. C* **106**, 1–7 (2020).

71. Spiess, K., Lammel, A. & Scheibel, T. Recombinant spider silk proteins for applications in biomaterials. *Macromol. Biosci.* **10**, 998–1007 (2010).

72. Müller-Herrmann, S. & Scheibel, T. Enzymatic Degradation of Films, Particles, and Nonwoven Meshes Made of a Recombinant Spider Silk Protein. *ACS Biomater. Sci. Eng.* **1**, 247–259 (2015).

73. Thompson, K. & Rice, J. Comparing Spider Silk Production Technologies | Kraig Biocraft Laboratories. Available at: https://www.kraiglabs.com/comparison/. (Accessed: 29th July 2020)

74. Rising, A. & Johansson, J. Toward spinning artificial spider silk. *Nat. Chem. Biol.* **11**, 309–315 (2015).

75. Scheibel, T. Spider silks: Recombinant synthesis, assembly, spinning, and engineering of synthetic proteins. *Microb. Cell Fact.* **3**, 1–10 (2004).

76. Bini, E. *et al.* RGD-functionalized bioengineered spider dragline silk biomaterial. *Biomacromolecules* **7**, 3139–3145 (2006).

77. Li, C., Vepari, C., Jin, H.-J., Kim, H. J. & Kaplan, D. L. Electrospun silk-BMP-2 scaffolds for bone tissue engineering. *Biomaterials* **27**, 3115–3124 (2006).

78. Lin, W. H., Yu, J., Chen, G. & Tsai, W. B. Fabrication of multi-biofunctional gelatin-based electrospun fibrous scaffolds for enhancement of osteogenesis of mesenchymal stem cells. *Colloids Surfaces B Biointerfaces* **138**, 26–31 (2016).

79. Saravanan, D. Spider Silk - Structure, Properties and Spinning. *J. Text. Apparel,*

Technol. Manag. **5**, 1–20 (2006).

80. Lin, C. B., Lee, Y. T. & Liu, C. Y. Optimal photonic nanojet beam shaping by mesoscale dielectric dome lens. *J. Appl. Phys.* **127**, 243110–243117 (2020).

81. Illingworth, C. A Short History of Surgery with particular reference to Sutures. *Med. Hist.* **17**, 158–168 (1973).

82. Gulrajani, M. L. Degumming of silk. *Rev. Prog. Color.* **22**, 79–89 (1992).

83. Harvey, D., Bardelang, P., Goodacre, S. L., Cockayne, A. & Thomas, N. R. Antibiotic Spider Silk: Site-Specific Functionalization of Recombinant Spider Silk Using "Click" Chemistry. *Adv. Mater.* **29**, 1–5 (2017).

84. Brown, J., Lu, C., Coburn, J. & Kaplan, D. L. Impact of silk biomaterial structure on proteolysis. *Acta Biomater.* **11**, 212–221 (2015).

85. Jao, D., Xue, Y., Medina, J. & Hu, X. Protein-based drug-delivery materials. *Materials (Basel).* **10**, 1–24 (2017).

86. Seib, F. P. & Kaplan, D. L. Silk for drug delivery applications: Opportunities and challenges. *Isr. J. Chem.* **53**, 756–766 (2013).

87. Nguyen, T. P. *et al.* Silk Fibroin-Based Biomaterials for Biomedical Applications: A Review. *Polymers (Basel).* **11**, 1–25 (2019).

88. Thurber, A. E., Omenetto, F. G. & Kaplan, D. L. In vivo bioresponses to silk proteins. *Biomaterials* **71**, 145–157 (2015).

89. Arai, T., Freddi, G., Innocenti, R. & Tsukada, M. Biodegradation of Bombyx mori silk fibroin fibers and films. *J. Appl. Polym. Sci.* **91**, 2383–2390 (2004).

90. Fredriksson, C. *et al.* Tissue response to subcutaneously implanted recombinant spider silk: An in vivo study. *Materials (Basel).* **2**, 1908–1922 (2009).

91. Teuschl, A. H., van Griensven, M. & Redl, H. Sericin removal from raw Bombyx mori silk scaffolds of high hierarchical order. *Tissue Eng. Part C Methods* **20**, 431–439 (2014).

92. More, S. V. Review Article Proteases for Degumming : a Novel , Green and Ecofriendly Way To Quality Silk Production. *Int. J. Curr. Res.* **7**, 23032–23038 (2015).

93. Lammel, A., Schwab, M., Slotta, U., Winter, G. & Scheibel, T. Processing conditions for the formation of spider silk microspheres. *ChemSusChem* **1**, 413–416 (2008).

94. Lammel, A., Schwab, M., Hofer, M., Winter, G. & Scheibel, T. Recombinant spider silk particles as drug delivery vehicles. *Biomaterials* **32**, 2233–2240 (2011).

95. Florczak, A., Mackiewicz, A. & Dams-Kozlowska, H. Functionalized spider silk spheres as drug carriers for targeted cancer therapy. *Biomacromolecules* **15**, 2971–2981 (2014).

96. Blüm, C. & Scheibel, T. Control of drug loading and release properties of spider silk sub-microparticles. *Bionanoscience* **2**, 67–74 (2012).

97. Kucharczyk, K. *et al.* Bioengineering the spider silk sequence to modify its affinity for drugs. *Int. J. Nanomedicine* **13**, 4247–4261 (2018).

98. Numata, K., Subramanian, B., Currie, H. A. & Kaplan, D. L. Bioengineered silk protein-based gene delivery systems. *Biomaterials* **30**, 5775–5784 (2009).

99. Numata, K., Hamasaki, J., Subramanian, B. & Kaplan, D. L. Gene Delivery Mediated by Recombinant Silk Proteins Containing Cationic and Cell Binding Motifs. *J. Control. Release* **146**, 136–143 (2010).

100. Gomes, S. C., Leonor, I. B., Mano, J. F., Reis, R. L. & Kaplan, D. L. Antimicrobial functionalized genetically engineered spider silk. *Biomaterials* **32**, 4255–4266

(2011).

101. Allmeling, C. *et al.* Spider silk fibres in artificial nerve constructs promote peripheral nerve regeneration. *Cell Prolif.* **41**, 408–420 (2008).

102. Radtke, C. *et al.* Spider Silk Constructs Enhance Axonal Regeneration and Remyelination in Long Nerve Defects in Sheep. *PLoS One* **6**, e16990 (2011).

103. Koeppel, A. & Holland, C. Progress and Trends in Artificial Silk Spinning: A Systematic Review. *ACS Biomater. Sci. Eng.* **3**, 226–237 (2017).

104. Aigner, T. B., DeSimone, E. & Scheibel, T. Biomedical Applications of Recombinant Silk-Based Materials. *Adv. Mater.* **30**, 1–28 (2018).

105. Lewicka, M., Hermanson, O. & Rising, A. U. Recombinant spider silk matrices for neural stem cell cultures. *Biomaterials* **33**, 7712–7717 (2012).

106. Harvey, D. *et al.* Cyclo(RGDfK) Functionalized Spider Silk Cell Scaffolds: Significantly Improved Performance in Just One Click. *Macromol. Biosci.* **20**, 1–9 (2020).

107. Gholipourmalekabadi, M. *et al.* Silk fibroin/amniotic membrane 3D bi-layered artificial skin. *Biomed. Mater.* **13**, 1–12 (2018).

108. Liebsch, C. *et al.* Preliminary investigations of spider silk in wounds in vivo — Implications for an innovative wound dressing. *Burns* **44**, 1829–1838 (2018).

109. Gholipourmalekabadi, M. *et al.* 3D Protein-Based Bilayer Artificial Skin for the Guided Scarless Healing of Third-Degree Burn Wounds in Vivo. *Biomacromolecules* **19**, 2409–2422 (2018).

110. Chouhan, D. *et al.* Recombinant Spider Silk Functionalized Silkworm Silk Matrices as Potential Bioactive Wound Dressings and Skin Grafts. *ACS Appl. Mater. Interfaces* **10**, 23560–23572 (2018).

111. Dinjaski, N. *et al.* Osteoinductive recombinant silk fusion proteins for bone regeneration. *Acta Biomater.* **49**, 127–139 (2017).

112. Schacht, K. *et al.* Biofabrication of cell-loaded 3D spider silk constructs. *Angew. Chemie - Int. Ed.* **54**, 2816–2820 (2015).

113. Zhao, L., Chen, D., Yao, Q. & Li, M. Studies on the use of recombinant spider silk protein/polyvinyl alcohol electrospinning membrane as wound dressing. *Int. J. Nanomedicine* **12**, 8103–8114 (2017).

114. McNaught, A. D. & Wilkinson, A. *IUPAC. Compendium of Chemical Terminology, 2nd ed. (the 'Gold Book').* (Blackwell Scientific Publications, 1997).

115. IUPAC Compendium of Chemical Technology. Polymer definition. *The Gold Book* 1151 (2019). doi:10.1351/goldbook.P04735

116. Feizi, T. & Chai, W. Oligosaccharide microrrays to decipher the glyco code. *Nat. Rev. Mol. Cell Biol.* **5**, 582–588 (2004).

117. Lucas, N. *et al.* Polymer biodegradation: Mechanisms and estimation techniques - A review. *Chemosphere* **73**, 429–442 (2008).

118. Haider, T. P., Völker, C., Kramm, J., Landfester, K. & Wurm, F. R. Plastics of the Future? The Impact of Biodegradable Polymers on the Environment and on Society. *Angew. Chemie - Int. Ed.* **57**, 2–15 (2018).

119. Müller, R.-J. Biodegradability of Polymers: Regulations and Methods for Testing. in *Biodegradability of Polymers* 365–374 (2005). doi:10.1002/3527600035.bpola012

120. Reineke, W. Fundementals of Aerobic & Anaerobic Biodegradation Process - Aerobic and Anaerobic Biodegradation. *PolimerNET* 1–7 (2009). doi:10.1007/10508767_1

121. Wu, C.-S. S. Physical properties and biodegradability of maleated-

polycaprolactone/starch composite. *Polym. Degrad. Stab.* **80**, 127–134 (2003).

122. Lendlein, A. & Langer, R. Biodegradable , Elastic Shape-Memory Polymers for Potential Biomedical Applications. *Science (80-.).* **1673**, 1673–1677 (2009).

123. Stadelmann, W., Digenis, A. & Tobin, G. Physiology and healing dynamics of chronic cutaneous wounds. *Plast. Reconstr. Surg.* **79**, 657 (1987).

124. Vroman, I. & Tighzert, L. Biodegradable polymers. *Materials (Basel).* **2**, 307–344 (2009).

125. Nair, L. S. & Laurencin, C. T. Biodegradable polymers as biomaterials. *Prog. Polym. Sci.* **32**, 762–798 (2007).

126. Moses, O. *et al.* Biodegradation of Three Different Collagen Membranes in the Rat Calvarium: A Comparative Study. *J. Periodontol.* **79**, 905–911 (2008).

127. Rothamel, D. *et al.* Biodegradation of differently crosslinked collagen membranes: An experimental study in the rat. *Clin. Oral Implants Res.* **16**, 369–378 (2005).

128. Jabłońska-Trypuć, A., Matejczyk, M. & Rosochacki, S. Matrix metalloproteinases (MMPs), the main extracellular matrix (ECM) enzymes in collagen degradation, as a target for anticancer drugs. *J. Enzyme Inhib. Med. Chem.* **31**, 177–183 (2016).

129. Blanco, N. M., Edwards, J. & Zamboni, W. A. Dermal substitute (Integra) for open nasal wounds. *Corresp. Br. Commun.* **113**, 2224–2225 (2004).

130. Integra LifeSciences Corporation. Dermal regeneration information portfolio. **1**, 1–20 (2016).

131. Purna, S. K. & Babu, M. Collagen based dressings - a review. *Burns* **26**, 54–62 (2000).

132. Olsen, D. *et al.* Recombinant collagen and gelatin for drug delivery. *Adv. Drug Deliv. Rev.* **55**, 1547–1567 (2003).

133. Chandra, R. & Rustgi, R. Biodegradable polymers. *Prog. Polym. Sci.* **23**, 1273–1335 (1998).

134. Klemm, D., Schmauder, H. & Heinze, T. Biopolymers, vol 6. Polysaccharides II. in *Biopolymers* (eds. De Baets, S., Vandamme, E. & Steinbüchel, A.) 275–319 (Wiley-VCH, 2002).

135. Béguin, P. & Aubert, J.-P. The biological degradation of cellulose. *FEMS Microbiol. Rev.* **13**, 25–58 (1994).

136. Puls, J., Wilson, S. A. & Hölter, D. Degradation of Cellulose Acetate-Based Materials: A Review. *J. Polym. Environ.* **19**, 152–165 (2011).

137. Kotnis, M. A., O'Brien, G. S. & Willett, J. L. Processing and mechanical properties of biodegradable Poly(hydroxybutyrate-co-valerate)-starch compositions. *J. Environ. Polym. Degrad.* **3**, 97–105 (1995).

138. Sireesha, M., Jagadeesh Babu, V. & Ramakrishna, S. Biocompatible and biodegradable elastomer/fibrinogen composite electrospun scaffolds for cardiac tissue regeneration. *RSC Adv.* **5**, 103308–103314 (2015).

139. Ramkumar, D. H. S. & Bhattacharya, M. Steady shear and dynamic properties of biodegradable polyesters. *Polym. Eng. Sci.* **38**, 1426–1435 (1998).

140. Doi, Y. & Abe, C. Biosynthesis and Characterization of a New Bacterial Copolyester of 3-Hydroxyalkanoates and 3-Hydroxy-ω-chloroalkanoates. *Macromolecules* **23**, 3705–3707 (1990).

141. Ohbayashi, T. *et al.* Degradation of fibrinogen and collagen by staphopains, cysteine proteases released from Staphylococcus aureus. *Microbiology* **157**, 786–792 (2011).

142. Navone, L. & Speight, R. Understanding the dynamics of keratin weakening and

hydrolysis by proteases. *PLoS One* **13**, 1–21 (2018).

143. Yamamura, S., Morita, Y., Hasan, Q., Yokoyama, K. & Tamiya, E. Keratin degradation a cooperative action of two enzymes.pdf. **294**, 1138–1143 (2002).

144. Tork, S. E., Shahein, Y. E., El-Hakim, A. E., Abdel-Aty, A. M. & Aly, M. M. Production and characterization of thermostable metallo-keratinase from newly isolated Bacillus subtilis NRC 3. *Int. J. Biol. Macromol.* **55**, 169–175 (2013).

145. Brandelli, A. Bacterial keratinases: Useful enzymes for bioprocessing agroindustrial wastes and beyond. *Food Bioprocess Technol.* **1**, 105–116 (2008).

146. Onifade, A. A., Al-Sane, N. A., Al-Musallam, A. A. & Al-Zarban, S. A review: Potentials for biotechnological applications of keratin-degrading microorganisms and their enzymes for nutritional improvement of feathers and other keratins as livestock feed resources. *Bioresour. Technol.* **66**, 1–11 (1998).

147. Shavandi, A., Silva, T. H., Bekhit, A. A. & Bekhit, A. E.-D. A. Keratin: Dissolution, extraction and biomedical application. *Biomater. Sci.* **5**, 1699–1735 (2017).

148. Gurtner, G. C., Werner, S., Barrandon, Y. & Longaker, M. T. Wound repair and regeneration. *Nature* **453**, 314–321 (2008).

149. McCarty, S. M. & Percival, S. L. Proteases and Delayed Wound Healing. *Adv. Wound Care* **2**, 438–447 (2013).

150. Enoch, S. & Price, P. Cellular, molecular and biochemical differences in the pathophysiology. *World Wide Wounds* 1–12 (2004).

151. Las Heras, K., Igartua, M., Santos-Vizcaino, E. & Hernandez, R. M. Chronic wounds: Current status, available strategies and emerging therapeutic solutions. *J. Control. Release* **328**, 532–550 (2020).

152. Velnar, T. *et al.* The Wound Healing Process : an Overview of the Cellular and Molecular Mechanisms. *J. Int. Med. Res.* **37**, 1528–1542 (2016).

153. Dellapelle, P. *et al.* Fibronectin and fibrin provide a provisional matrix for epidermal cell migration during wound reepithelialization. *J. Invest. Dermatol.* **79**, 264–269 (1982).

154. Grinnell, F., Billingham, R. E. & Burgess, L. Distribution of fibronectin during wound healing in vivo. *J. Invest. Dermatol.* **76**, 181–189 (1981).

155. Leibovich, S. J. & Ross, R. The Role of the Macrophage in Wound Repair. *Am. J. Pathol.* **78**, 71–100 (1975).

156. Lazarus, G. S. *et al.* Definitions and Guidelines for Assessment of Wounds and Evaluation of Healing Background: Chronic wounds represent a worldwide. *Arch. Dermatol. Res.* **130**, 489–493 (1994).

157. Coleman, S. *et al.* A new pressure ulcer conceptual framework. *J. Adv. Nurs.* **70**, 2222–2234 (2014).

158. Defloor, T. The risk of pressure sores: A conceptual scheme. *J. Clin. Nurs.* **8**, 206–216 (1999).

159. Braden, B., Bergstrom, N., Ms, R. N. & Bergstrom, N. A conceptual schema for the study of the etiology of pressure sores. *Rehabil. Nurs.* **12**, 8–12 (1987).

160. Dealey, C., Posnett, J. & Walker, A. The cost of pressure ulcers in the United Kingdom. *J. Wound Care* **21**, 261–266 (2012).

161. Schoonhoven, L., Bousema, M. T. & Buskens, E. The prevalence and incidence of pressure ulcers in hospitalised patients in The Netherlands: A prospective inception cohort study. *Int. J. Nurs. Stud.* **44**, 927–935 (2007).

162. Hankin, C. S., Knispel, J., Lopes, M., Bronstone, A. & Maus, E. Clinical and cost efficacy of advanced wound care matrices for venous ulcers. *J. Manag. Care Pharm.* **18**, 375–384 (2012).

163. Yager, D. R., Zhang, L. Y., Liang, H. X., Diegelmann, R. F. & Cohen, I. K. Wound fluids from human pressure ulcers contain elevated matrix metalloproteinase levels and activity compared to surgical wound fluids. *J. Invest. Dermatol.* **107**, 743–748 (1996).

164. Ladwig, G. P. *et al.* Ratios of activated matrix metalloproteinase-9 to tissue inhibitor of matrix metalloproteinase-1 in wound fluids are inversely correlated with healing of pressure ulcers. *Wound Repair Regen.* **10**, 26–37 (2002).

165. Desmoulire, A. *et al.* Apoptosis mediates the decrease in cellularity during the transition between granulation tissue and scar. *Am. J. Pathol.* **146**, 56–66 (1995).

166. Zamboni, P. *et al.* Serum iron and matrix metalloproteinase-9 variations in limbs affected by chronic venous disease and venous leg ulcers. *Am. Soc. Dermatologic Surg.* **31**, 644–649 (2005).

167. Trengove, N. J. *et al.* Analysis of the acute and chronic wound environments: The role of proteases and their inhibitors. *Wound Repair Regen.* **7**, 442–452 (1999).

168. Nicoletti, G. *et al.* Versatile use of dermal substitutes: A retrospective survey of 127 consecutive cases. *Indian J. Plast. Surg.* **51**, 46–53 (2018).

169. Wiegand, C. *et al.* Protease and pro-inflammatory cytokine concentrations are elevated in chronic compared to acute wounds and can be modulated by collagen type i in vitro. *Arch. Dermatol. Res.* **302**, 419–428 (2010).

170. Schultz, G. S. & Mast, B. A. Molecular analysis of the environments of healing and chronic wounds: cytokines, proteases and growth factors. *Wounds* **2**, 7–14 (1999).

171. Miyashita, T., Maezono, Y. & Shimazaki, A. Silk feeding as an alternative foraging tactic in a kleptoparasitic spider under seasonally changing environments. *J. Zool.* **262**, 225–229 (2004).

172. Eckhard, U. *et al.* Active site specificity profiling of the matrix metalloproteinase family: Proteomic identification of 4300 cleavage sites by nine MMPs explored with structural and synthetic peptide cleavage analyses. *Matrix Biol.* **49**, 37–60 (2016).

173. Turk, B. E., Huang, L. L., Piro, E. T. & Cantley, L. C. Determination of protease cleavage site motifs using mixture-based oriented peptide libraries. *Nat. Biotechnol.* **19**, 661–667 (2001).

174. Kasserra, H. P. & Laidler, K. J. Mechanisms of action of trypsin and chymotrypsin. *Can. J. Chem.* **47**, 4031–4039 (1969).

175. Hedstrom, L. Serine protease mechanism and specificity. *Chem. Rev.* **102**, 4501–4523 (2002).

176. Fernandez-patron, C. *et al.* Vascular Matrix Metalloproteinase-2–Dependent Cleavage of Calcitonin Gene-Related Peptide Promotes Vasoconstriction. *Circ. Res.* **87**, 670–676 (2000).

177. Nagase, H. & Woessner, F. Matrix Metalloproteinases. *J. Biol. Chem.* **274**, 21491–21494 (1999).

178. Senior, R. M. *et al.* Human 92- and 72-kilodalton type IV collagenases are elastases. *J. Biol. Chem.* **266**, 7870–7875 (1991).

179. Proost, P., Von Damme, J. & Opdenakker, G. Leukocyte Gelatinase B cleavage releases Encephalitogens from Human Myelin Basic Protein. *Biochem. Biophys. Res. Commun.* **192**, 1175–1181 (1993).

180. Birkedal-Hansen, H. *et al.* Matrix metalloproteinases: A review. *Crit. Rev. Oral Biol. Med.* **4**, 197–250 (1993).

181. Birkedal-hansen, H. Proteolytic remodeling of extracellular matrix. *Curr. Opin. Cell Biol.* **7**, 728–735 (1995).

182. Baldassarre, M. *et al.* Dynamin Participates in Focal Extracellular Matrix Degradation by Invasive Cells. *Mol. Biol. Cell* **14**, 1074–1084 (2003).

183. Vu, T. H. *et al.* MMP-9/Gelatinase B Is a Key Regulator of Growth Plate Angiogenesis and Apoptosis of Hypertrophic Chondrocytes. *Cell* **93**, 411–422 (1998).

184. Vasilevskaya, T., Khrenova, M. G., Nemukhin, A. V. & Thiel, W. Mechanism of proteolysis in matrix metalloproteinase-2 revealed by QM/MM modeling. *J. Comput. Chem.* **36**, 1621–1630 (2015).

185. Crabbe, T. *et al.* Mutation of the active site glutamic acid of human gelatinase A: effects on latency, catalysis, and the binding of tissue inhibitor of metalloproteinases-1. *Biochemistry* **33**, 6684–6690 (1994).

186. Challis, R. J., Goodacre, S. L. & Hewitt, G. M. Evolution of spider silks: Conservation and diversification of the C-terminus. *Insect Mol. Biol.* **15**, 45–56 (2006).

187. Garb, J. E., Ayoub, N. A. & Hayashi, C. Y. Untangling spider silk evolution with spidroin terminal domains. *BMC Evol. Biol.* **10**, (2010).

188. Price, R. *et al.* In vivo evaluation of matrix metalloproteinase responsive silk-elastinlike protein polymers for cancer gene therapy. *J. Control. release* **213**, 48–56 (2016).

189. Farina, A. R. & Mackay, A. R. Gelatinase B/MMP-9 in tumour pathogenesis and progression. *Cancers (Basel).* **6**, 240–296 (2014).

190. Katoh, K., Rozewicki, J. & Yamada, K. D. MAFFT online service: multiple sequence alignment, interactive sequence choice and visualization. *Brief. Bioinform.* 1–7 (2017). doi:10.1093/bib/bbx108

191. Waterhouse, A. M., Procter, J. B., Martin, D. M. A., Clamp, M. & Barton, G. J. Jalview Version 2-A multiple sequence alignment editor and analysis workbench. *Bioinformatics* **25**, 1189–1191 (2009).

192. Chen, E. I. *et al.* A unique substrate recognition profile for matrix metalloproteinase-2. *J. Biol. Chem.* **277**, 4485–4491 (2002).

193. Kawabata, K., Moore, A. R. & Willoughby, D. A. Impaired activity of protease inhibitors towards neutrophil elastase bound to human articular cartilage. *Ann. Rheum. Dis.* **55**, 248–252 (1996).

194. NEB. NEBaseChanger. (2018). Available at: https://nebasechanger.neb.com/.

195. Dinjaski, N. *et al.* Predicting rates of in vivo degradation of recombinant spider silk proteins. *J. Tissue Eng. Regen. Med.* **12**, e97–e105 (2018).

196. Dao, A. T. N., Shimokata, J., Takeuchi, K., Nakayama, K. & Taniike, T. Stabilization of recombinant spider silk in thermo-oxidative degradation: High-throughput screening for antioxidants. *Polym. Degrad. Stab.* **153**, 37–46 (2018).

197. Liu, B. *et al.* Silk structure and degradation. *Colloids Surfaces B Biointerfaces* **131**, 122–128 (2015).

198. Zhang, L., Liu, X., Li, G., Wang, P. & Yang, Y. Tailoring degradation rates of silk fibroin scaffolds for tissue engineering. *J. Biomed. Mater. Res. - Part A* **107**, 104–113 (2019).

199. Moore, A. M. F. & Tran, K. Material properties of cobweb silk from the black widow spider Latrodectus hesperus. *Int. J. Biol. Macromol.* **24**, 277–282 (1999).

200. Garrison, N. L. *et al.* Spider phylogenomics: untangling the Spider Tree of Life. *PeerJ* **4**, e1719 (2016).

201. Santos, A. J. A phylogenetic analysis of the nursery-web spider family Pisauridae, with emphasis on the genera Architis and Staberius (Araneae: Lycosoidea). *Zool. Scr.* **36**, 489–507 (2007).

202. Tso, I. M. & Severinghaus, L. L. Silk stealing by Argyrodes lanyuensis (Araneae: Theridiidae): A unique form of kleptoparasitism. *Anim. Behav.* **56**, 219–225

(1998).

203. Vollrath, F. Kleptobiosis in Spiders. in *Ecophysiology of Spiders* (ed. Nentwig, W.) 274–286 (Springer Berlin Heidelberg, 1987). doi:10.1007/978-3-642-71552-5_20

204. Lombardi, S. J. & Kaplan, D. L. The amino acid composition of major ampullate gland silk (dragline) of Nephila clavipes (Araneae, Tetragnathidae). *J. Arachnol.* **18**, 297–306 (1990).

205. Shao, Z. & Vollrath, F. The effect of solvents on the contraction and mechanical properties of spider silk. *Polymer (Guildf).* **40**, 1799–1806 (1999).

206. Kridel, S. J. *et al.* Substrate Hydrolysis by Matrix Metalloproteinase-9. *J. Biol. Chem.* **276**, 20572–20578 (2001).

207. Witt, P. N., Levine, V. D., Peakall, D. B. & Breed, A. L. The fate of the intact orb web of the spider Araneus Diadematus Cl. *Behaviour* **23**, 43–60 (1963).

208. Cohn, J. & Christenson, T. E. Utilization of resources by the male golden orb-weaving spider *Nephila clavipes* (Araneae). *J. Arachnol.* **15**, 185–192 (1987).

209. Higgins, L. E. & Buskirk, R. E. Spider-web kleptoparasites as a model for studying producer-consumer interactions. *Behav. Ecol.* **9**, 384–387 (1998).

210. Whitehouse, M. *et al.* Argyrodes: Phylogeny, Sociality and Interspecific Interactions—a Report on the Argyrodes Symposium, Badplaas 2001. *J. Arachnol.* **30**, 238–245 (2002).

211. Johansson, J., Norling, K. & Rising, A. Monomeric N-terminal spider silk protein domain and uses thereof - EP2644619A1. 1–87 (2013).

212. Johansson, J., Rising, A. & Hedhammar, M. Methods of producing polymers of spider silk proteins - EP2243792A1. 1–58 (2010).

213. Rising, A., Kronqvist, N., Nordling, K. & Johansson, J. Charge-reversed N-terminal spider silk protein domain and uses thereof - EP3168228A1. 1–128 (2017).

214. Collin, M. A., Clarke, T. H., Ayoub, N. A. & Hayashi, C. Y. Genomic perspectives of spider silk genes through target capture sequencing: Conservation of stabilization mechanisms and homology-based structural models of spidroin terminal regions. *Int. J. Biol. Macromol.* **113**, 829–840 (2018).

215. Han, L., Zhang, L., Zhao, T., Wang, Y. & Nakagaki, M. Analysis of a new type of major ampullate spider silk gene, MaSp1s. *Int. J. Biol. Macromol.* **56**, 156–161 (2013).

216. Ackerschott, C., Huemmerich, D. & Scheibel, T. Recombinant spider silk proteins. (2008).

217. Tai, P. L., Hwang, G. Y. & Tso, I. M. Inter-specific sequence conservation and intra-individual sequence variation in a spider silk gene. *Int. J. Biol. Macromol.* **34**, 237–243 (2004).

218. Johansson, J. *et al.* Spider silk proteins and methods for producing spider silk proteins - WO2007/078239A2. 1–97 (2007).

219. Johansson, J., Rising, A., Nygren, P.-Å. & Hedhammar, M. Spider silk fusion protein structures for binding to an organic target - EP3178843A1. 1–108 (2011).

220. Chinali, A. *et al.* Containment of Extended Length Polymorphisms in Silk Proteins. *J. Mol. Evol.* **70**, 325–338 (2010).

221. Gaines, W. & Marcotte Jr, W. Identification and characterization of multiple Spidroin 1 genes encoding major ampullate silk proteins in Nephila clavipes. *Insect Mol. Biol.* **17**, 465–474 (2008).

222. Gatesy, J., Hayashi, C., Motriuk, D., Woods, J. & Lewis, R. Extreme Diversity , Conservation , and Convergence of Spider Silk Fibroin Sequences. *Science (80-.).* **291**, 2603–2605 (2001).

223. Zhang, Y. *et al.* The molecular structures of major ampullate silk proteins of the wasp spider , Argiope bruennichi : A second blueprint for synthesizing de novo silk. *Comp. Biochem. Physiol. Part B* **164**, 151–158 (2013).

224. Song, J. *et al.* PROSPER : An Integrated Feature-Based Tool for Predicting Protease Substrate Cleavage Sites. *PLoS One* **7**, e50300 (2012).

225. Kargozar, S., Ramakrishna, S. & Mozafari, M. Chemistry of biomaterials: future prospects. *Curr. Opin. Biomed. Eng.* **10**, 181–190 (2019).

226. Langer, R., Cima, L. G., Tamada, J. A. & Wintermantel, E. Future directions in biomaterials. *Biomaterials* **11**, 738–745 (1990).

227. Day, W. H. E. & Mcmorris, F. R. Critical comparison of consensus methods for molecular sequences. *Nucleic Acids Res.* **20**, 1093–1099 (1992).

228. Malay, A. D., Arakawa, K. & Numata, K. Analysis of repetitive amino acid motifs reveals the essential features of spider dragline silk proteins. *PLoS One* **12**, 1–16 (2017).

229. An, B. *et al.* Reproducing natural spider silks' copolymer behavior in synthetic silk mimics. *Biomacromolecules* **13**, 3938–3948 (2012).

230. Bergström, J. Birefringence. in *Mechanics of Solid Polymers* (ed. Andrew, W.) 19–114 (Elsevier Inc., 2015). doi:10.1016/B978-0-323-31150-2.00002-9

231. Cambridge Polymer Group. The Theory of Birefringence. *Cambridge Polymer Group* 1–5 (2004).

232. Savage, K. N. & Gosline, J. M. The effect of proline on the network structure of major ampullate silks as inferred from their mechanical and optical properties. *J. Exp. Biol.* **211**, 1937–1947 (2008).

233. Phoenix, J. *et al.* Full polarization control of fiber-delivered light in a dilution refrigerator. *Rev. Sci. Instrum.* **91**, 083107 (2020).

234. Sobuj, S. R. Birefringence | Fiber Birefringence | Textile Study Center. (2018). Available at: https://textilestudycenter.com/fiber-birefringence/. (Accessed: 11th November 2020)

235. Honda, R. *et al.* Simple multi-wavelength imaging of birefringence:case study of silk. *Sci. Rep.* **8**, 1–9 (2018).

236. Founda, I. M. & El-Tonsy, M. M. Birefringence behaviour of annealed silk fibres. *J. Mater. Sci.* **25**, 4752–4757 (1990).

237. Liu, Y., Shao, Z. & Vollrath, F. Relationships between supercontraction and mechanical properties of spider silk. *Nat. Mater.* **4**, 901–905 (2005).

238. Vollrath, F., Madsen, B. & Zhengzhong, S. The effect of spinning conditions on the machanics of a spiders dragline silk. *R. Soc.* **268**, 2339–2346 (2001).

239. Elettro, H., Vollrath, F., Antkowiak, A. & Neukirch, S. Coiling of an elastic beam inside a disk: A model for spider-capture silk. *Int. J. Non. Linear. Mech.* **75**, 59–66 (2015).

240. Page-mccaw, A., Serano, J., Sante, J. M. & Rubin, G. M. Drosophila Matrix Metalloproteinases Are Required for Tissue Remodeling , but Not Embryonic Development. *Dev. Cell* **4**, 95–106 (2003).

241. Page-McCaw, A. Remodeling the model organism: Matrix metalloproteinase functions in invertebrates. *Semin. Cell Dev. Biol.* **19**, 14–23 (2008).

242. Ratner, B. D., Hoffman, A. S., Schoen, F. J. & Lemons, Jack, E. *Biomaterial Science - An Introduction to Materials 2nd Edition*. (Elsevier Inc., 2004).

243. Deshayes, S. & Kasko, A. M. Polymeric biomaterials with engineered degradation. *J. Polym. Sci. Part A Polym. Chem.* **51**, 3531–3566 (2013).

244. Ielasi, A., Cortese, B. & Steffenino, G. Late Structural Discontinuity as a Possible Cause of Very Late Everolimus-Eluting Bioresorbable Scaffold Thrombosis. *JACC Cardiovasc. Interv.* **8**, e171–e172 (2015).

245. Brisbois, E. J. Novel Nitric Oxide (NO)-Releasing Polymers and their Biomedical Applications. *Thesis* (University of Michigan, 2014).

246. Horbett, T. A. Principles Underlying the Role of Adsorbed Plasma Proteins in Blood Interactions With Foreign Materials. *Cardiovasc. Pathol.* **2**, 137–148 (1993).

247. Wang, L. *et al.* Biomechanical studies on biomaterial degradation and co-cultured cells: mechanisms, potential applications, challenges and prospects. *J. Mater. Chem. B* **7**, 7439–7459 (2019).

248. Rajkumar, K., Ramraji, K., Namratha, G., Manoj, S. & Gnanavelbabu, A. A study of bio and tribo modifier on degradation of magnesium-calcium carbonate biomaterial. *Mater. Today Proc.* **27**, 691–695 (2020).

249. Wissing, T. B. *et al.* Macrophage-driven biomaterial degradation depends on scaffold microarchitecture. *Front. Bioeng. Biotechnol.* **7**, 1–20 (2019).

250. Doblhofer, E. & Scheibel, T. Engineering of recombinant spider silk proteins allows defined uptake and release of substances. *J. Pharm. Sci.* **104**, 988–994 (2015).

251. Armstrong, D. G. & Jude, E. B. The role of matrix metalloproteinases in wound healing. *J. Am. Podiatr. Med. Assoc.* **92**, 12–18 (2002).

252. Nguyen, T. T., Mobashery, S. & Chang, M. Roles of Matrix Metalloproteinases in Cutaneous Wound Healing. in *Wound Healing - New insights into Ancient Challenges* 37–71 (2016). doi:10.5772/64611

253. Mohan, R. *et al.* Matrix Metalloproteinase Gelatinase B (MMP-9) Coordinates and Effects Epithelial Regeneration. *J. Biol. Chem.* **277**, 2065–2072 (2002).

254. Zhang, H., Chang, M., Hansen, C. N., Basso, D. M. & Noble-haeusslein, L. J. Role of Matrix Metalloproteinases and Therapeutic Benefits of Their Inhibition in Spinal Cord Injury. *Am. Soc. Exp. Neurother.* **8**, 206–220 (2011).

255. Madlener, M., Parks, W. C. & Werner, S. Matrix metalloproteinases (MMPS) and their physiological inhibitors (TIMPs) are differentially expressed during excisional skin wound repair. *Exp. Cell Res.* **242**, 201–210 (1998).

256. Ågren, M. S. Gelatinase activity during wound healing. *Br. J. Dermatol.* **131**, 634–640 (1994).

257. Rayment, E. A., Upton, Z. & Shooter, G. K. Increased matrix metalloproteinase-9 (MMP-9) activity observed in chronic wound fluid is related to the clinical severity of the ulcer. *Br. J. Dermatol.* **158**, 951–961 (2008).

258. Wang, W. *et al.* MicroRNA-129 and -335 Promote Diabetic Wound Healing by Inhibiting Sp1-Mediated MMP-9 Expression. *Diabetes* **67**, 1627–1638 (2018).

259. Zhang, Y. I-TASSER server for protein 3D structure prediction. *BMC Bioinformatics* **8**, 1–8 (2008).

260. Hagen, L., Harvey, D. & Thomas, N. R. *I-Tasser model of 4RepCT (Unpublished)*. (2019).

261. McGill, M., Holland, G. P. & Kaplan, D. L. Experimental Methods for Characterizing the Secondary Structure and Thermal Properties of Silk Proteins. *Macromol. Rapid Commun.* **40**, 1–14 (2019).

262. Grip, S., Johansson, J. & Hedhammar, M. Engineered disulfides improve mechanical properties of recombinant spider silk. *Protein Sci.* **18**, 1012–1022 (2009).

263. Chanmugam, A. *et al.* Relative Temperature Maximum in Wound Infection and Inflammation as Compared with a Control Subject Using Long-Wave Infrared Thermography. *Adv. Ski. Wound Care* **30**, 406–414 (2017).

264. Dini, V. *et al.* Correlation Between Wound Temperature Obtained With an Infrared Camera and Clinical Wound Bed Score in Venous Leg Ulcers. *Wounds* **27**, 274–8 (2015).

265. Thusberg, J. & Vihinen, M. Bioinformatic Analysis of Protein Structure–Function Relationships: Case Study of Leukocyte Elastase (ELA2) Missense Mutations. *Hum. Mutat.* **27**, 1230–1243 (2006).

266. Budisa, N. *et al.* High-level Biosynthetic Substitution of Methionine in Proteins by its Analogs 2-Aminohexanoic Acid, Selenomethionine, Telluromethionine and Ethionine in Escherichia coli. *Eur. J. Biochem.* **230**, 788–796 (1995).

267. Vasilyeva, E. M. *et al.* The System of Neutrophil Elastase and Plasma Level of MMP-7 in Children with Pulmonary Arterial Hypertension and Chronic Cor Pulmonale. *Int. J. Biomed.* **3**, 269–273 (2013).

268. Jia, L. *et al.* Amyloidogenicity and Cytotoxicity of a Recombinant C-Terminal His 6 -Tagged Aβ 1-42. *ACS Chem. Neurosci.* **10**, 1251–1262 (2019).

269. Jansson, R. *et al.* Recombinant spider silk genetically functionalized with affinity domains. *Biomacromolecules* **15**, 1696–1706 (2014).

270. Kenney, J. M., Knight, D., Wise, M. J. & Vollrath, F. Amyloidogenic nature of spider silk. *Eur. J. Biochem.* **269**, 4159–4163 (2002).

271. Howie, A. J., Brewer, D. B., Howell, D. & Jones, A. P. Physical basis of colors seen in Congo red-stained amyloid in polarized light. *Lab. Investig.* **88**, 232–242 (2008).

272. Ratner, B. D. & Bryant, S. J. BIOMATERIALS : Where We Have Been and Where We Are Going. *Annu. Rev. Biomed. Eng.* **6**, 41–75 (2004).

273. Fomete, B., Saheeb, B. & Obiadazie, A. A prospective clinical evaluation of the longevity of resorbable sutures in oral mucosa. *Niger. J. Clin. Pract.* **16**, 334–338 (2013).

274. Vigen, M., Ceccarelli, J. & Putnam, A. J. Protease-sensitive PEG hydrogels regulate vascularization in vitro and in vivo. *Macromol. Biosci.* **14**, 1368–1379 (2014).

275. Jiang, L. *et al.* An electrospun poly(ϵ-caprolactone) scaffold modified with matrix metalloproteinase for cellularization and vascularization. *J. Mater. Chem. B* **6**, 2795–2802 (2018).

276. Phelps, E. A., Landázuri, N., Thulé, P. M., Taylor, W. R. & García, A. J. Bioartificial matrices for therapeutic vascularization. *Proc. Natl. Acad. Sci.* **107**, 3323–3328 (2010).

277. Raeber, G. P., Lutolf, M. P. & Hubbell, J. A. Molecularly engineered PEG hydrogels: A novel model system for proteolytically mediated cell migration. *Biophys. J.* **89**, 1374–1388 (2005).

278. Lutolf, M. P. *et al.* Synthetic matrix metalloproteinase-sensitive hydrogels for the conduction of tissue regeneration: Engineering cell-invasion characteristics. *Proc. Natl. Acad. Sci.* **100**, 5413–5418 (2003).

279. Zhu, J., He, P., Lin, L., Jones, D. R. & Marchant, R. E. Biomimetic Poly(ethylene glycol)-Based hydrogels as scaffolds for inducing endothelial adhesion and capillary-like network formation. *Biomacromolecules* **13**, 706–713 (2012).

280. Lu, P., Takai, K., Weaver, V. M. & Werb, Z. Extracellular matrix degradation and remodeling in development and disease. *Cold Spring Harb Perspect Biol* **3**, 1–24 (2011).

281. Ito, A. *et al.* Optimum temperature for extracellular matrix production by articular chondrocytes. *Int. J. Hyperth.* **30**, 96–101 (2014).

282. Mirastschijski, U. *et al.* Matrix metalloproteinase inhibition delays wound healing and blocks the latent transforming growth factor-β1-promoted myofibroblast

formation and function. *Wound Repair Regen.* **18**, 223–234 (2010).

283. Lazarus, G. S. *et al.* Definitions and Guidelines for Assessment of Wounds and Evaluation of Healing. *Arch. Dermatol. Res.* **130**, 489–493 (1994).

284. Castorena-Torres, F., Penuelas-Urquides, K. & Bermúdez de León, M. Site-Directed Mutagenesis by Polymerase Chain Reaction. in *Polymerase Chain Reaction for Biomedical Applications* (ed. Samadikuchaksaraei, A.) 159–173 (Intech, 2016). doi:10.5772/66429

285. Altschup, S. F., Gish, W., Miller, W., Myers, E. W. & Lipman, D. J. Basic Local Alignment Search Tool. *J. Mol. Biol.* **215**, 403–410 (1990).

286. Camacho, C. *et al.* BLAST+: Architecture and applications. *BMC Bioinformatics* **10**, 1–9 (2009).

287. Gottesman, S. Proteases and Their Targets in Escherichia Coli . *Annu. Rev. Genet.* **30**, 465–506 (1996).

288. Noble, J. E. & Bailey, M. J. A. Chapter 8 Quantitation of Protein. in *Methods in Enzymology* **463**, 73–95 (Elsevier Inc., 2009).

289. Congdon, R. W., Muth, G. W. & Splittgerber, A. G. The Binding Interation of Coomassie Blue with Proteins. *Anal. Biochem.* **213**, 407–413 (1993).

290. Georgiou, C. D., Grintzalis, K., Zervoudakis, G. & Papapostolou, I. Mechanism of Coomassie brilliant blue G-250 binding to proteins: A hydrophobic assay for nanogram quantities of proteins. *Anal. Bioanal. Chem.* **391**, 391–403 (2008).

291. Li, X. *et al.* Water-stable silk fibroin nerve conduits with tunable degradation prepared by a mild freezing-induced assembly. *Polym. Degrad. Stab.* **164**, 61–68 (2019).

292. Nakayama, K., Dao, A. T. N., Takeuchi, K., Shimokata, J. & Taniike, T. Chemiluminescence from recombinant spider silk under thermo-oxidative degradation. *Polym. Degrad. Stab.* **144**, 264–269 (2017).

293. Zhu, J. & Marchant, R. E. Design properties of hydrogel tissue-engineering scaffolds. *Expert Rev. Med. Devices* **8**, 607–626 (2011).

294. Horan, R. L. *et al.* In vitro degradation of silk fibroin. *Biomaterials* **26**, 3385–3393 (2005).

295. Liu, T., Qiu, C., Ben, C., Li, H. & Zhu, S. One-step approach for full-thickness skin defect reconstruction in rats using minced split-thickness skin grafts with Pelnac overlay. *Burn. Trauma* **7**, 1–13 (2019).

296. Simman, R., Mari, W., Younes, S. & Wilson, M. Use of Hyaluronic Acid–Based Biological Bilaminar Matrix in Wound Bed Preparation: A Case Series. *Eplasty* **18**, 151–161 (2018).

297. Schwarze, H. *et al.* Suprathel, a new skin substitute, in the management of partial-thickness burn wounds: Results of a clinical study. *Ann. Plast. Surg.* **60**, 181–185 (2008).

8. Appendix

8.1 Identifying silk for degradation

Using the protease map, seen in **Figure 63**, any degradation seen could be matched to the corresponding protease. The quantity of silk reeled from each spider dictated how many different proteases could be investigated on a single silk slide, with a negative water control with each species. ELNE and α-chymotrypsin were also applied to silks to compare with recombinant 4RepCT films and fibres (see **Section 4.3.1**).

The majority of *N. madagascarensis* silk was collected from a sub adult female, while the silk denoted (★) was collected from an adult female to investigate the effect of sexual maturity on silk degradation. However, no difference in degradation was observed between the two silk types.

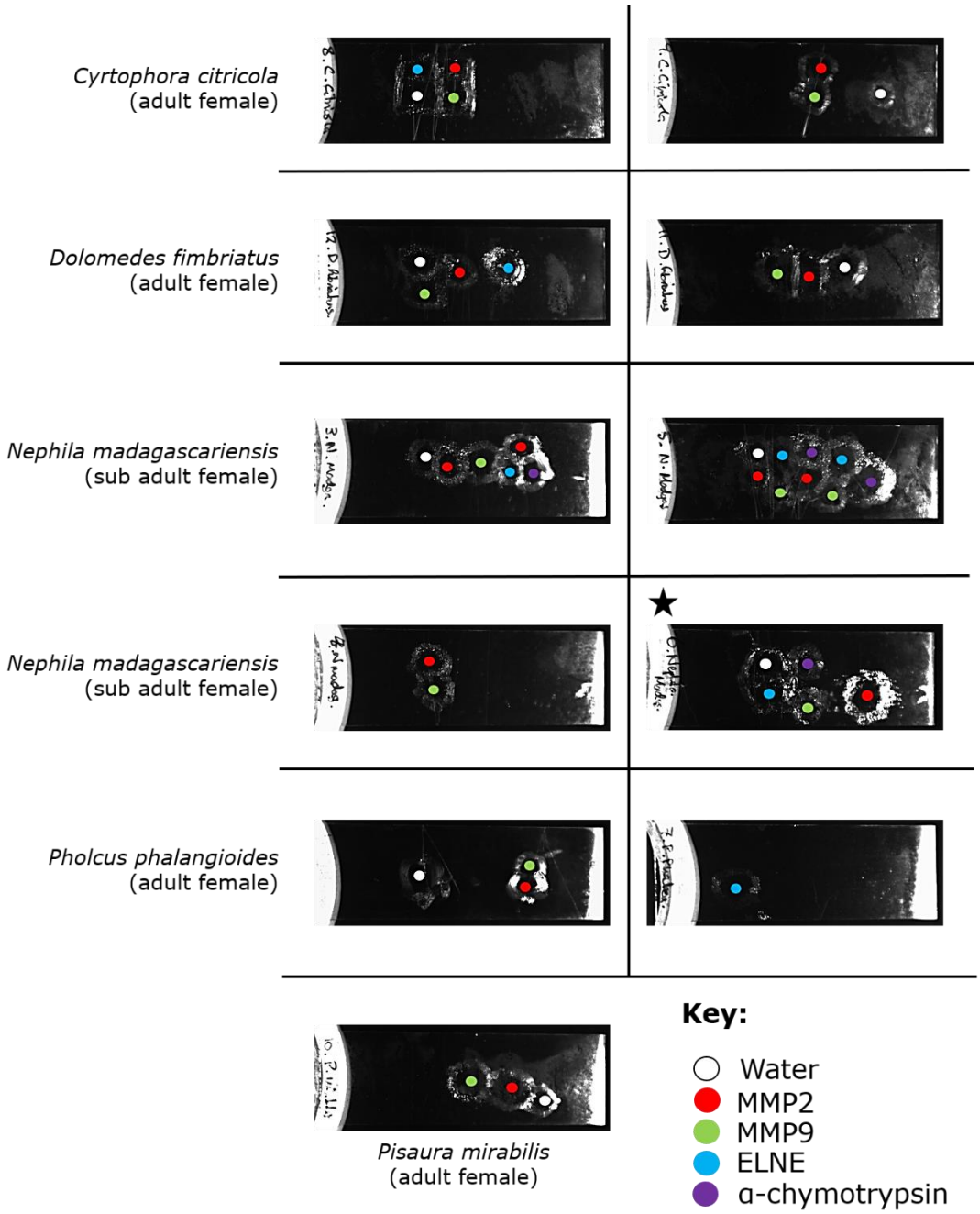

Figure 63. Once silica grease had been applied to each slide at the positions of the anticipated degradation, the slides were imaged with low magnification. The resulting images were used to produce a map of each protease. Silk from an adult female N. *madagascarensis* was also collected, indicated by (★). Microscope slide length = 7.5 cm, image scale factor = 1.79.

8.2 pJ401Express–TRX_4RepCT plasmid map

TRX_4RepCT was located within a pJ401 Express plasmid vector containing kanamycin resistance, T5 promoter and terminator and inducible lac operon control. The inserted sequence was flanked by *Xho1* and *Nde1* restriction sites to allow insertion and removal of the sequence.

The complete plasmid contained 5205 base pairs and was stored in XL1b *E. coli* after plasmid preparation. Protein expression was induced by the IPTG-controlled lac operon and T5 polymerase.

Figure 64. pJ401Express-TRX_4RepCT was viewed using SnapGene and shows the various T5 controlled reading frames as well as the inherent kanamycin selectivity and lac operon within the plasmid.

8.3 Growth of 4RepCT mutants on LB agar plates

XL1b and DL41 E. coli

After plasmid electro-transformation, cell growth of both XL1b and DL41 *E. coli* was seen suggesting the mutated plasmid had successfully been taken up, enabling antibiotic resistance. Similar cell size and number was observed with both *E. coli* strains compared to the positive control that contained the normal TRX_4RepCT plasmid construct, suggesting that the introduction of mutants had not affected cellular growth significantly. However, if mutant TRX_4RepCT expression was problematic to the cells, it would be likely be seen after protein induction as a result of the inducible T5 promoter.

As no phenotypic differences were seen with XL1b and DL41 *E. coli*, this process was not repeated with the T7 controlled constructs.

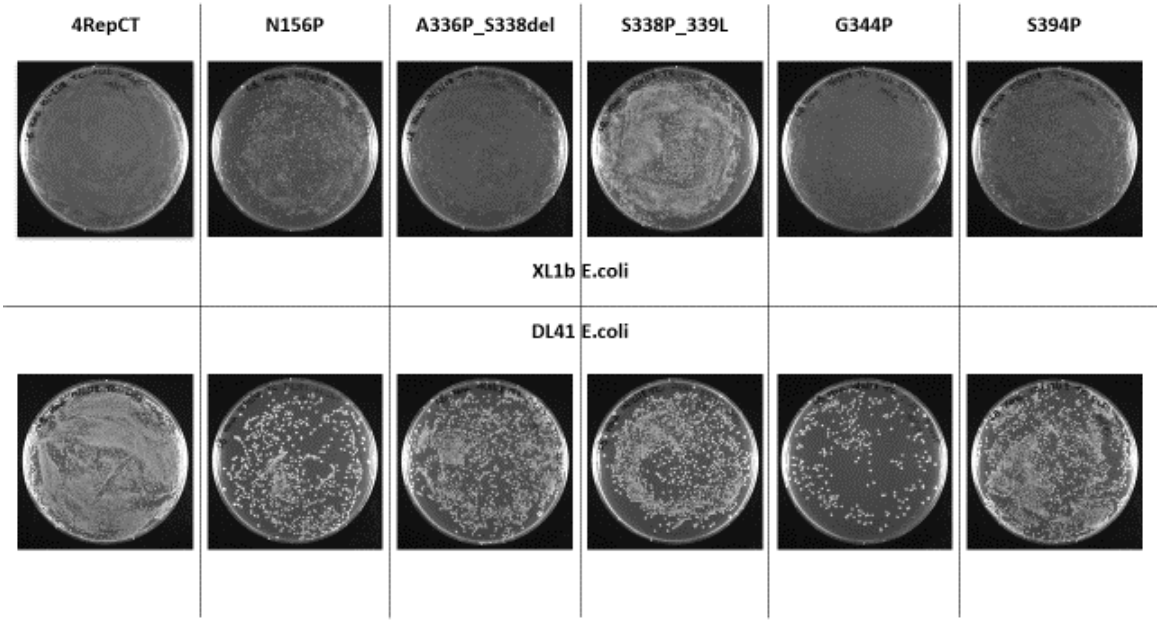

Figure 65. Successful cell growth was seen for all mutants although G344P DL41 displayed a lower number of colonies when compared to the positive control (normal TRX_4RepCT). However, the inducible control of the T5 promoter prevented protein expression so little differences in phenotype were likely if caused by the expression of the mutant proteins.

8.4 pET22b-TRX_4RepCT plasmid map

TRX_4RepCT was mutated into the pET22b(+) expression plasmid containing ampicillin resistance, T7 promoter and terminator and inducible lac operon control. As with pJ401Express, the inserted sequence was flanked by *Xho1* and *Nde1* restriction sites to allow insertion and removal.

The full plasmid contained 6767 base pairs and was stored in Neb5α *E. coli after* plasmid preparation. As before, protein expression was induced by IPTG-controlled lab operon but this time inducing the T7 polymerase.

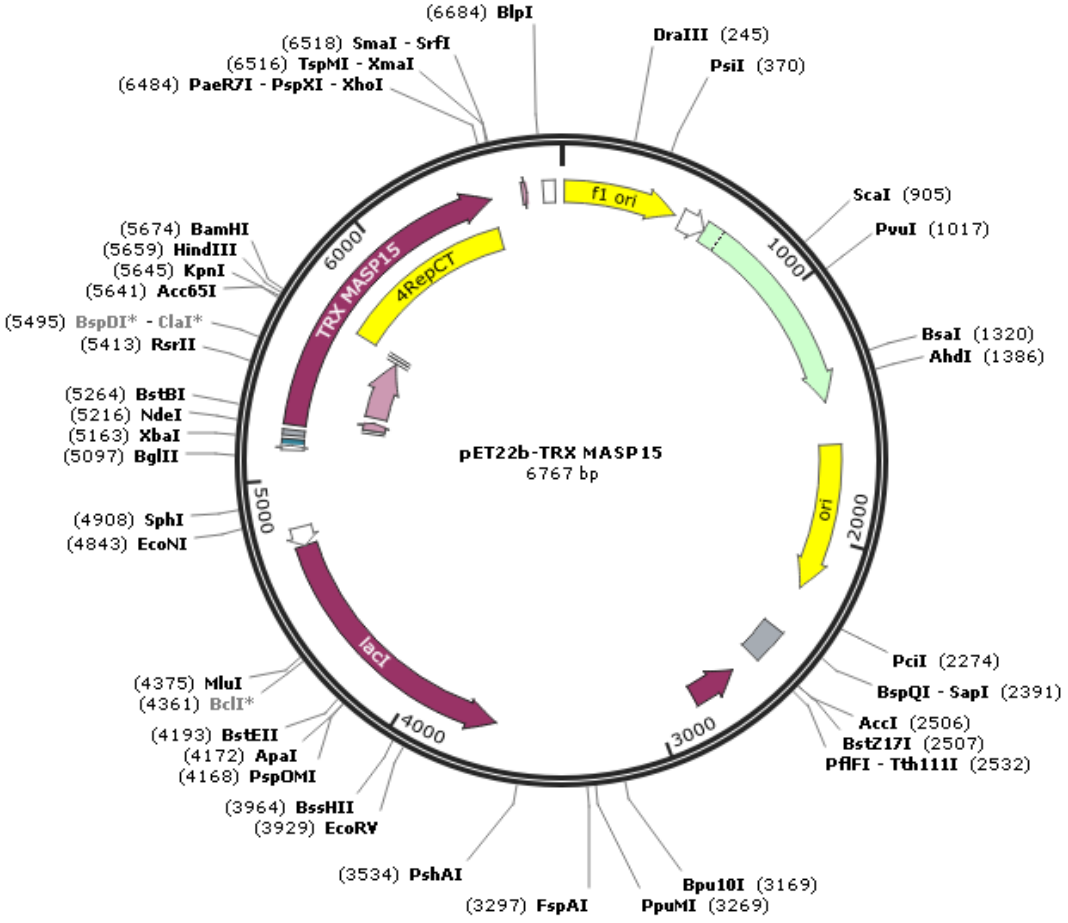

Figure 66. pET22b-TRX_4RepCT was viewed using SnapGene displaying the T7 controlled reading frames. The pET22b vector contained the antibiotic resistance gene for ampicillin compared to kanamycin resistance provided by the pJ401Express plasmid vector.

8.5 Unsuccessful expression and purification of insoluble TRX_4RepCT mutants

Unlike the N156P mutant, which was successfully expressed and purified from DL41 *E. coli*, Ni^{2+} IMAC purification failed to produce purified recombinant proteins of the remaining pJ401Express mutant proteins. Before induction, culture growth speeds were similar to those observed from TRX_N156P-expressing cells suggesting that plasmid transformation had not affected the cell's growth rate. Cell density was also not affected by protein induction with final cell density readings of approximately 1.2 after 15 hrs expression at 20 °C, similar to that achieved by TRX_4RepCT. However, no protein was eluted from IMAC purification, as seen by 15% (w/v) SDS-PAGE in **Figure 67**, suggesting that expression had not occurred.

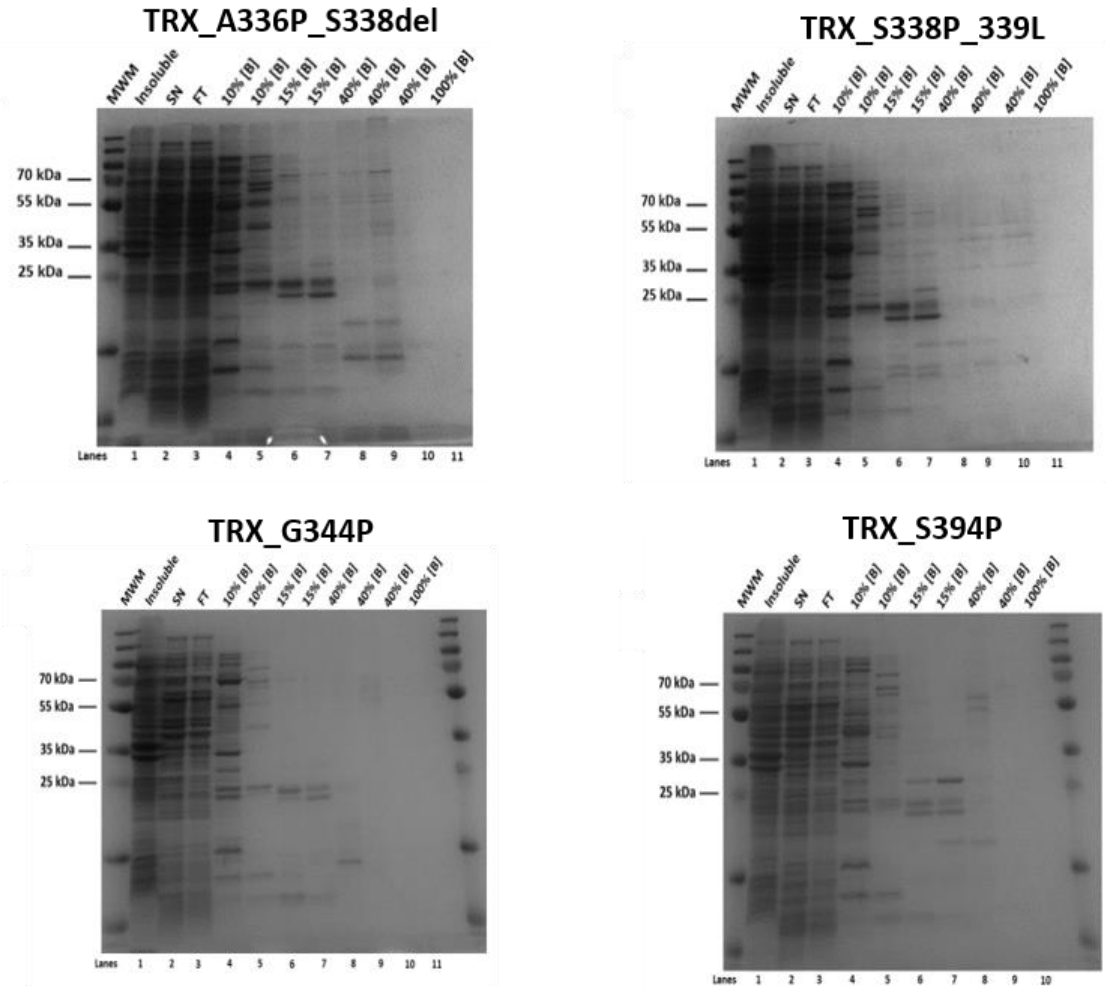

Figure 67. Ni^{2+} IMAC purification for A336P_S338del, S338P_339L, G344P and S394P mutants after growth and expression in 1L supplemented M9 minimal media and analysed by 15% (w/v) SDS-PAGE. The purifications were considered unsuccessful as no protein was eluted at any concentration of imidazole.

8.5.1 Time point expression test of insoluble 4RepCT mutants

A time point expression test of S338P_339L, G344P and S394P mutations was carried out to explore if the protein was initially expressed before becoming insoluble. Samples were taken at 1 hr, 1.5 hr, 2 hr, 2.5 hr, 3 hr and 4 hrs. Once lysed by CelLytic protocol as seen in **Methods 2.12**, the insoluble and soluble fractions were analysed by SDS-PAGE.

As no protein was seen in soluble or insoluble fractions, it was suggested that inserting the genes into a T7 controlled plasmid, such as pET22b would allow expression in *E. coli* strains that encouraged expression of difficult to express proteins such as BL21 Rosetta *E. coli* and BL21 DE3 C41 *E. coli.*

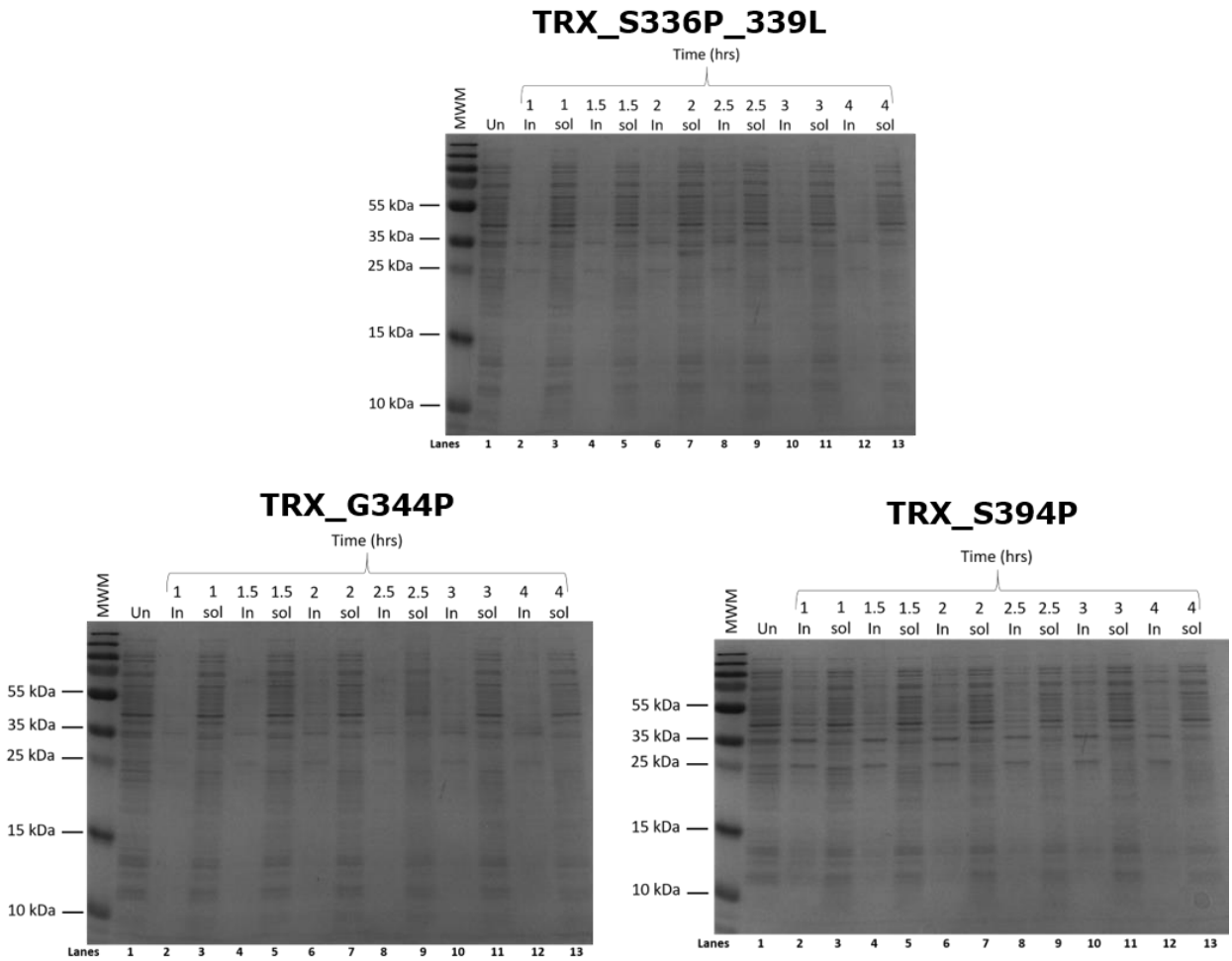

Figure 68. Insoluble and soluble fractions at time points of 1 - 4 hrs of mutant TRX_4RepCT were analysed by 15% (w/v) SDS-PAGE to determine the location of any mutant protein that had been expressed. No protein was observed so the relevant gene constructs were mutated into pET22b plasmid vectors.

8.5.2 Purification of insoluble mutant pellets

Before the decision to transfer the mutant constructs was made, the insoluble pellets of previous mutant protein purification attempts were dialysed in decreasing concentrations of urea (from 8M) to encourage correct refolding of mutant proteins that had been expressed. The refolded protein was then purified by the same increasing imidazole step increment IMAC purification method before being analysed by SDS-PAGE.

Upon staining, it was clear that the majority of the insoluble fraction had been successfully resolubilised apart from some cellular proteins as the IN lane (**lane 1**) was mostly clear in all gels. However, as the majority of the now soluble protein did not bind to the affinity column, the resulting flow through (**lane 3**) was often overloaded.

As no protein was successfully eluted at any concentration of imidazole, the plasmid constructs were transferred to a pET22b plasmid.

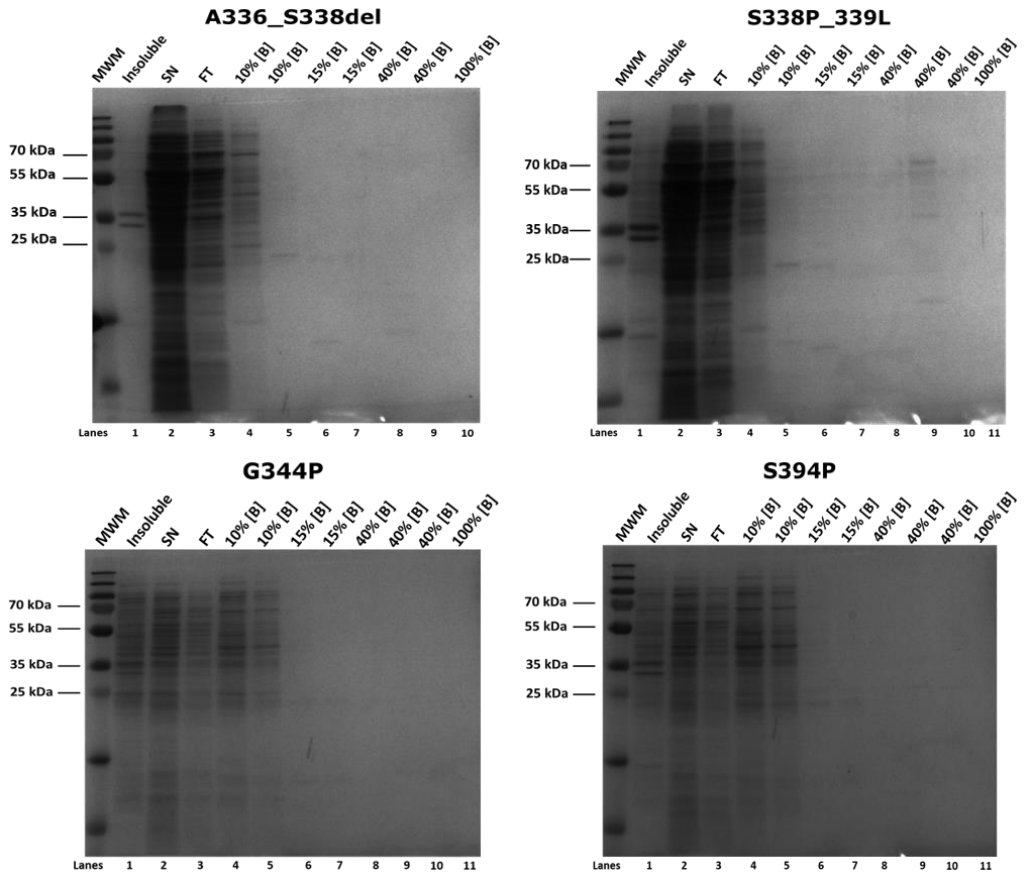

Figure 69. Unsuccessful IMAC purifications were analysed by 15% (w/v) SDS-PAGE. Insoluble cell pellets from previous purifications were resuspended in denaturing 8M urea before the urea was removed by dialysis in the original binding buffer (20 mM Tris, 300 mM NaCl, 15 mM imidazole). After removal of the urea the dialysed protein was purified by Ni^{2+} IMAC but no protein was eluted at any concentration of imidazole.

8.5.3 Mutant protein expression investigations

To investigate the reason behind the lack of mutant protein expression, a number of different approaches were attempted during purification. Although these approaches were attempted with all low expressing mutants (A336P_S338del, S338_339L, G344P and S394P), only A336P_S338del results are shown in **Figure 70a – d**.

Figure 70a) Insoluble pellets of previous mutant protein purification attempts were dialysed in decreasing concentrations of urea (from 8M) into Buffer A to encourage correct refolding of mutant proteins that had been expressed. After purification by step-increment IMAC purification, the majority of the insoluble fraction was successfully resolubilised apart from some cellular proteins, shown as an almost clear insoluble lane (**Figure 70a, lane 1**). However, as the majority of the now soluble protein did not bind to the affinity column, the resulting supernatant (**Figure 70a, lane 2**) and flow through (**Figure 70a, lane 3**) were often overloaded. As no protein was eluted at higher concentrations of imidazole, resolubilisation was not considered effective.

Figure 70b) A time point expression test was also carried out to explore if protein was initially expressed and later lost to the insoluble fractions. Samples were taken at 1hr, 1.5hr, 2hr, 2.5 hr, 3 hr and 4 hrs. Once lysed by CelLytic protocol (see **Methods 2.12**), the insoluble and soluble fractions were analysed by SDS-PAGE. Although many cellular protein bands were visible at all time points, no 40 kDa protein expression band was seen after induction suggesting a problem with the bacterial expression strain.

Figure 70c and **Figure 70d**) IMAC purification was also attempted using binding buffers supplemented with non-denaturing and denaturing components (5% (v/v) glycerol (**Figure 70c**) and 8M urea (**Figure 70d**) respectively). Lysate preparation was carried out in the same method as previously described before being loaded onto a 5 mL Histrap column. Elution buffers were also supplemented with the same components to allow elution of target proteins if present. Although a <25 kDa band was seen in both conditions (**Figure 70c, lanes 5 – 6** and

Figure 70d, lanes 5 – 10 respectively) at increasing concentrations of imidazole, the expected full length 40 kDa band was not observed. As no band was seen in the flow-through, it suggested that the issue lay with the *E. coli* expression system, rather than a failure to purify once expressed.

As no protein could be expressed throughout that experiments, it was suggested that inserting the genes into a T7 controlled plasmid, such as pET22b would allow expression in *E. coli* strains that encouraged expression of difficult to express proteins such as Rosetta and C41 *E. coli***.**

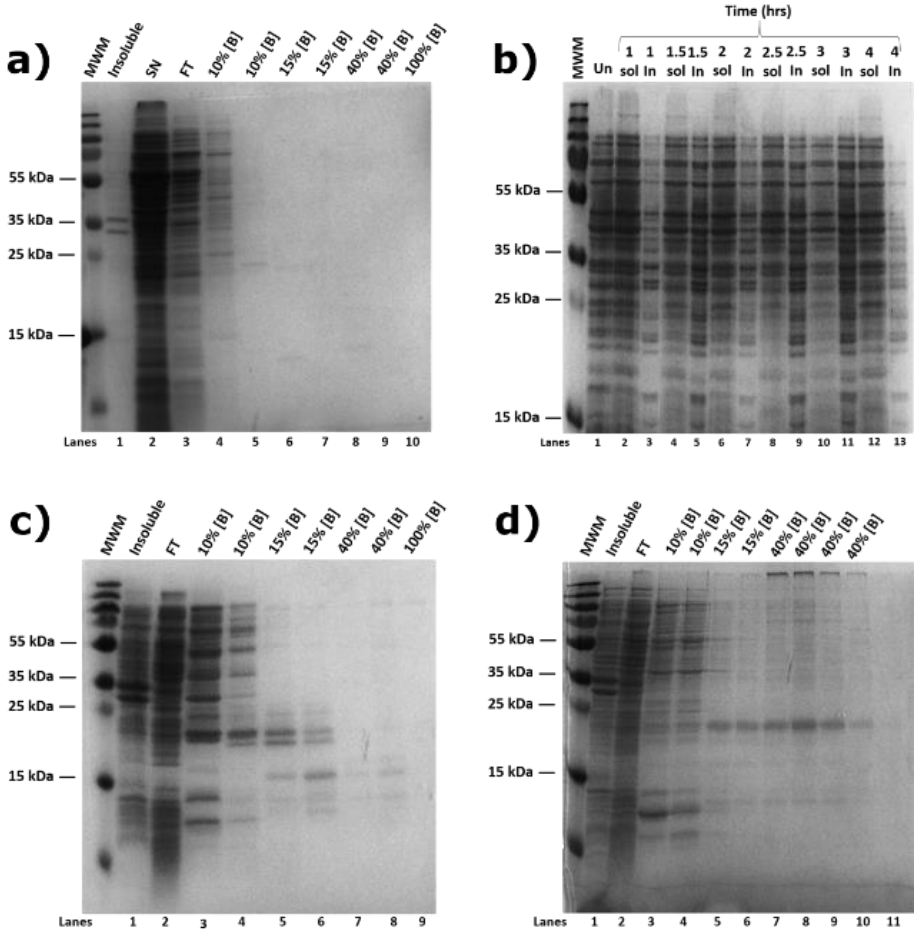

Figure 70. In an attempt to increase protein expression of mutant TRX_4RepCT, different purification protocols were carried out, included insoluble pellet purification (**a**), time point expression tests (**b**) and elution buffers containing non-denaturing (**c**) and denaturing (**d**) components. **a**) Insoluble cell pellets from previous purifications were resuspended in denaturing 8M urea before the urea was removed by dialysis in the original binding buffer. After removal of the urea the dialysed protein was purified by Ni^{2+} IMAC but no protein was eluted at any concentration of imidazole. **b**) Insoluble and soluble fractions at time points of 1 - 4 hrs of mutant 4RepCT were analysed by 15% (w/v) SDS-PAGE to determine the location of any mutant protein that had been expressed. No protein was observed so the relevant gene constructs were mutated into pET22b plasmid vectors. **c**), **d**) Standard binding and elution buffers were supplemented with 5% (v/v) glycerol **c**) and 8M urea **d**) respectively. Cells were lysed and purified by the same method as described and analysed by 15% (w/v) SDS-PAGE. As no 40 kDa protein was observed at any imidazole concentration, it was concluded that the cells were failing to express the mutant protein at any point.

8.6 Additional images of recombinant fibre *in vitro* degradation

In vitro degradation of recombinant fibres was performed as described in **Methods 2.16.5 4RepCT and mutant fibre degradation** Methods and images collected by bright field, dark field and birefringence microscopy, as described in **Figure 41**, **Figure 42**, **Figure 43**, **Figure 60**, **Figure 61** and **Figure 62**. The additional images from these experiments are collected and shown here.

8.6.1.1 4RepCT fibres after 0 min viewed with bright field microscopy

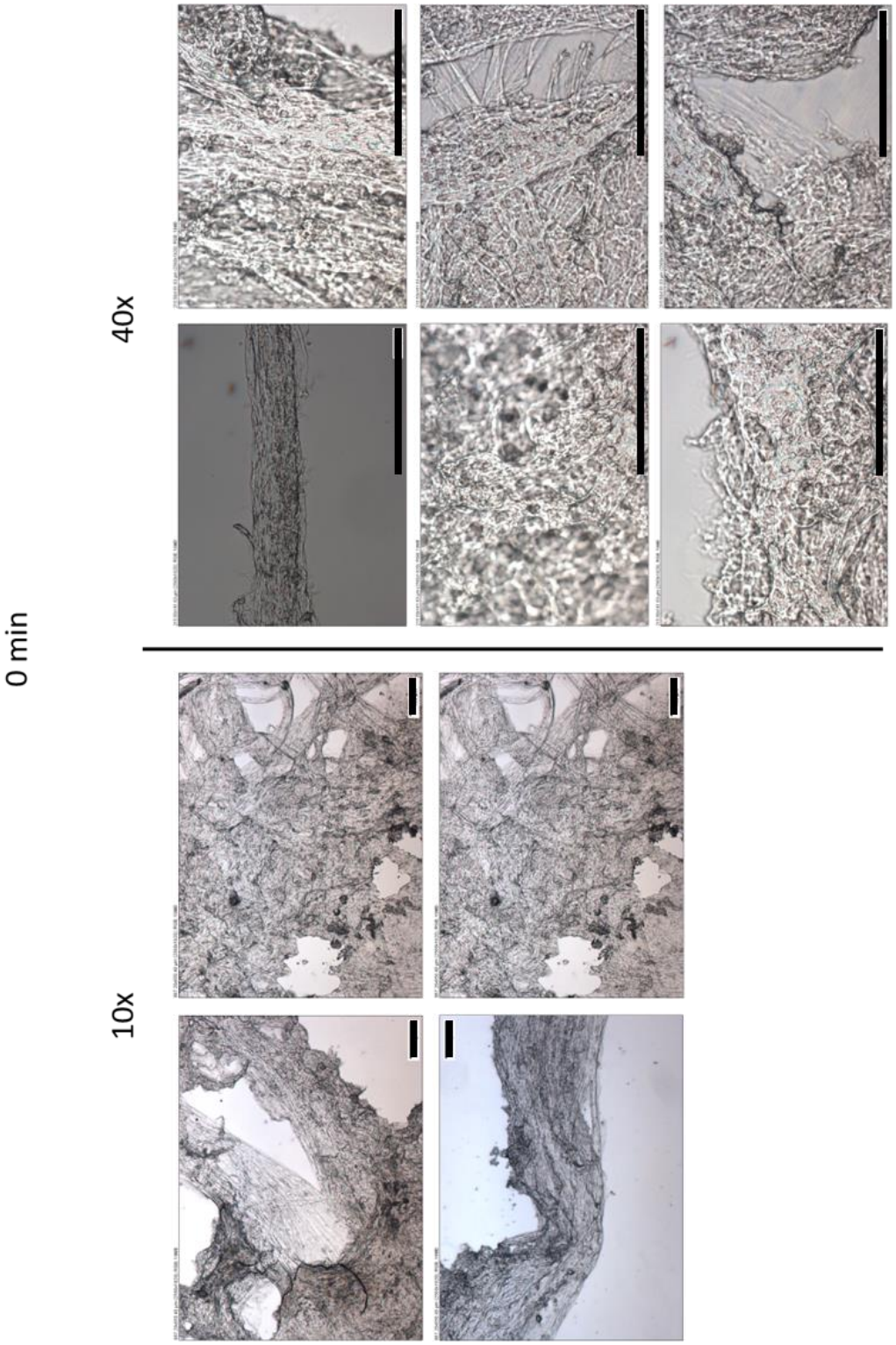

Figure 71. Representative images of 4RepCT fibres by MMP2 using bright field light microscopy at 10X and 40X magnification after 0 min as seen in **Figure 39**. Scale bar = 100 μm.

8.6.1.2 4RepCT fibres after 0 min with dark field and birefringence microscopy

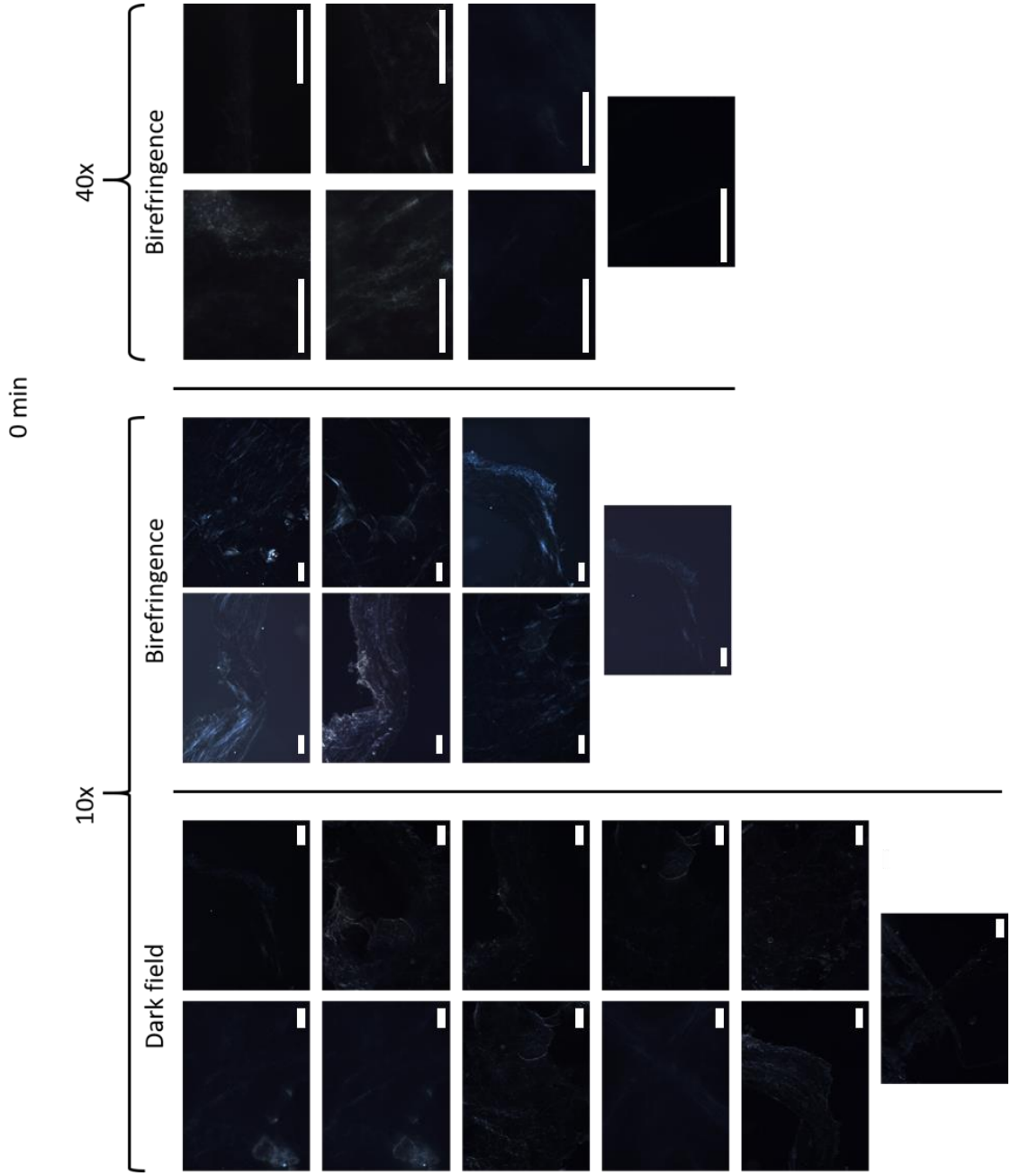

Figure 72. Representative images of 4RepCT fibres by MMP2 using dark field and birefringence microscopy at 10X (dark field and birefringence) and 40X (birefringence) magnification after 0 min as seen in **Figure 41**. Scale bar = 100 µm.

8.6.1.3 4RepCT fibres after 30 min viewed with bright field microscopy

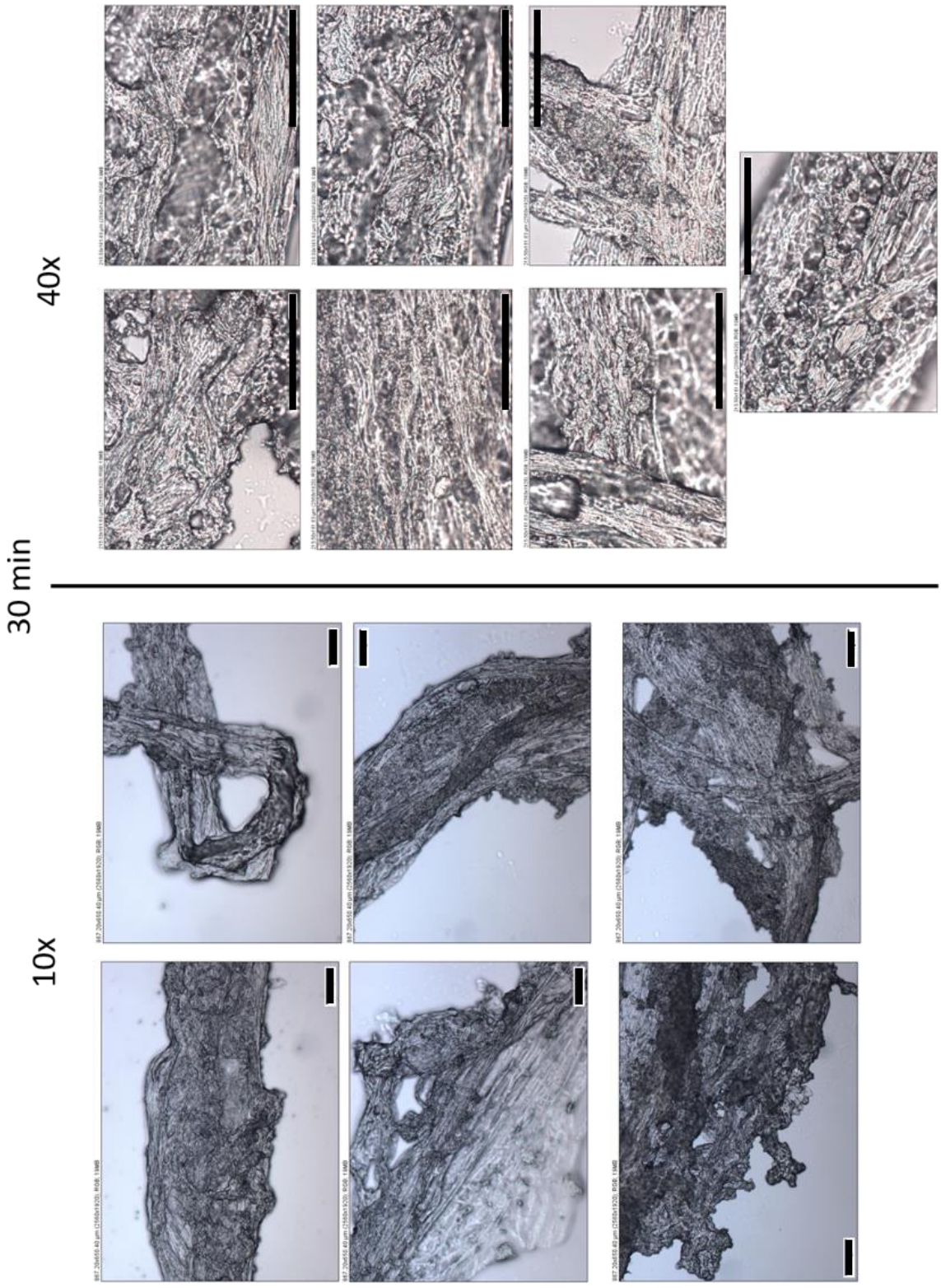

Figure 73. Representative images of 4RepCT fibres by MMP2 using bright field light microscopy at 10X and 40X magnification after 30 min as seen in **Figure 39**. Scale bar = 100 μm.

8.6.1.4 4RepCT fibres after 30 min viewed with dark field and birefringence microscopy

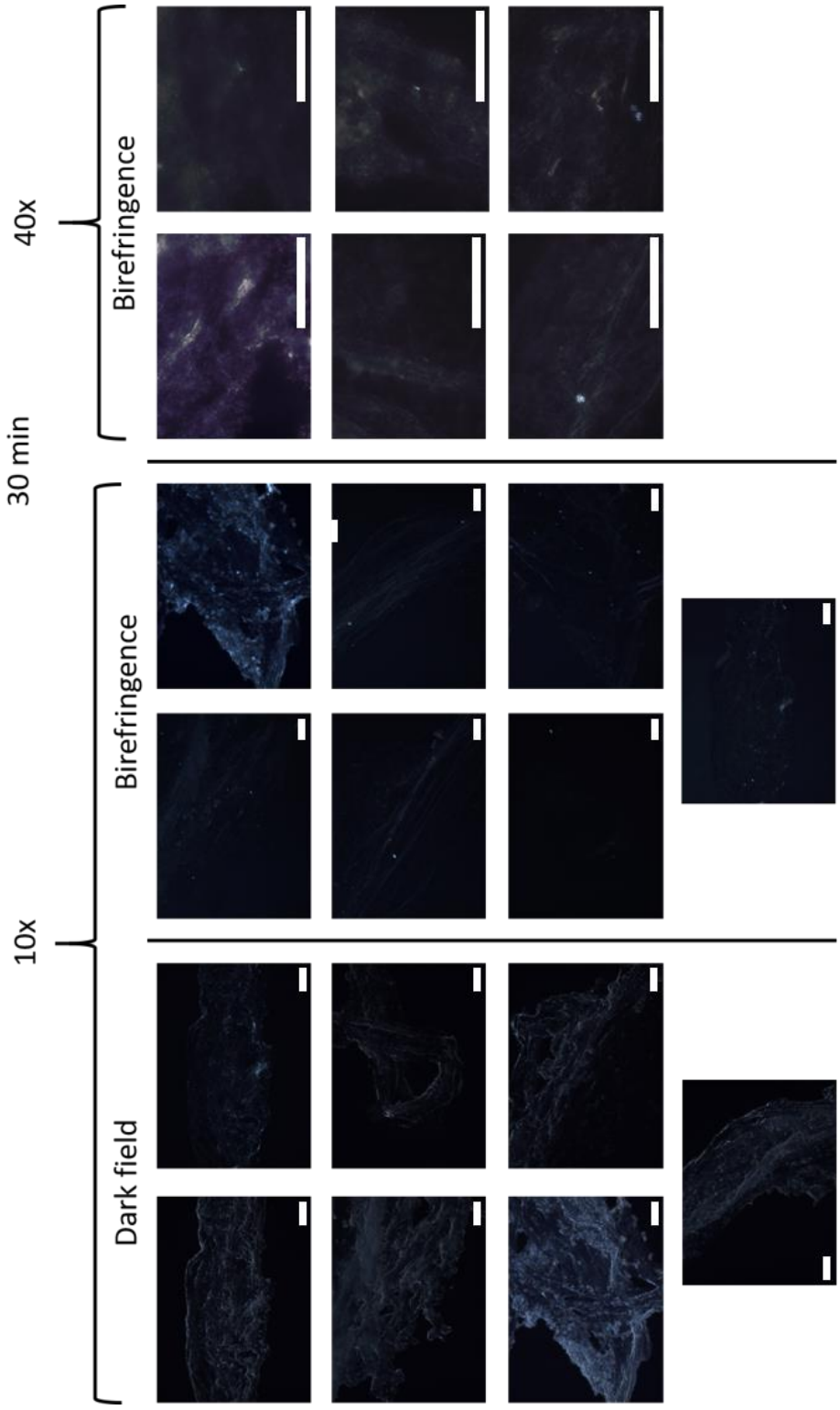

Figure 74. Representative images of 4RepCT fibres by MMP2 using dark field and birefringence microscopy at 10X (dark field and birefringence) and 40X (birefringence) magnification after 30 min as seen in **Figure 41**. Scale bar = 100 µm.

8.6.1.5 4RepCT fibres after 60 min viewed with bright field microscopy

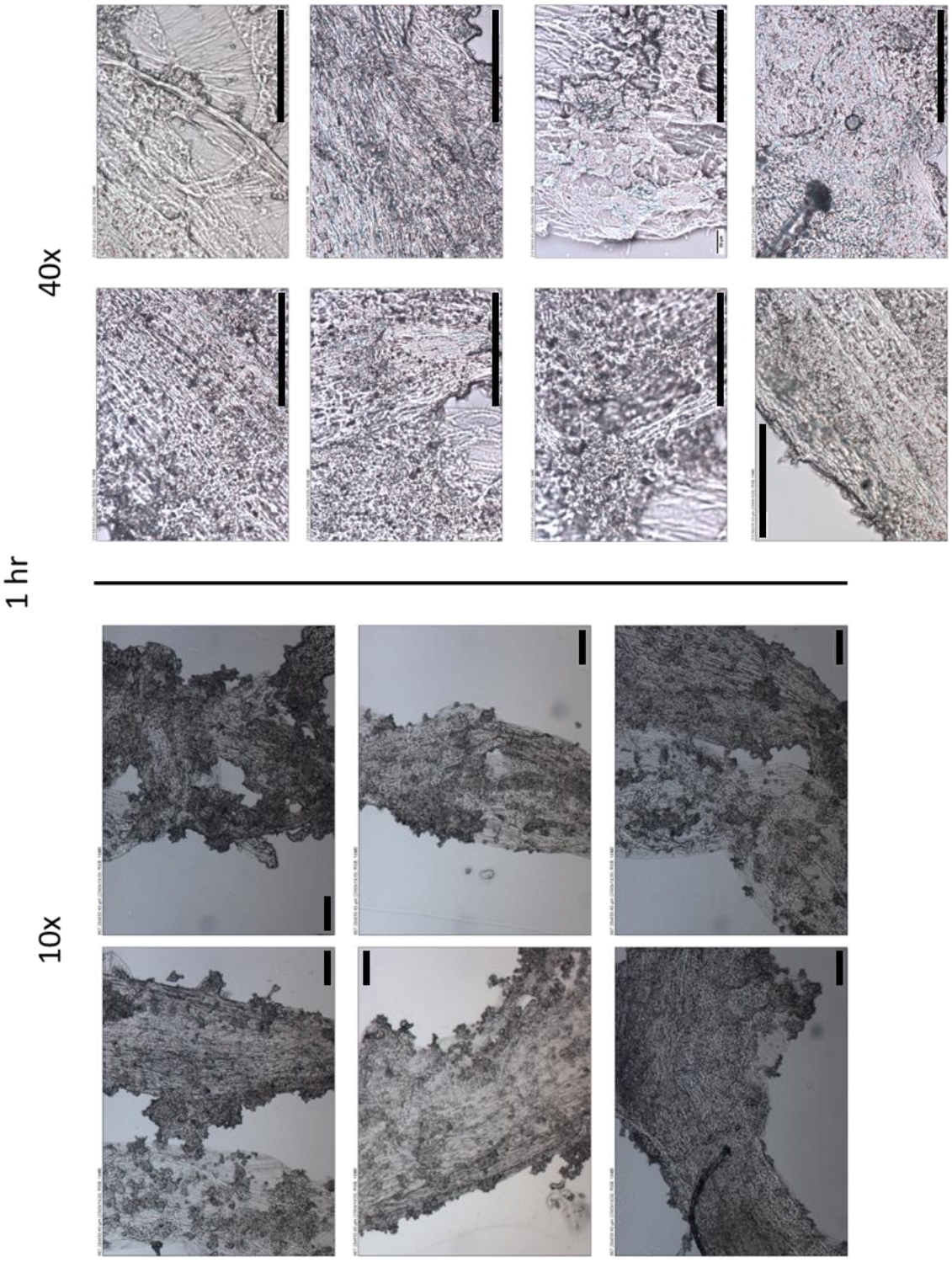

Figure 75. Representative images of 4RepCT fibres by MMP2 using bright field light microscopy at 10X and 40X magnification after 60 min as seen in **Figure 39**. Scale bar = 100 µm.

8.6.1.6 4RepCT fibres after 60 min viewed with dark field and birefringence microscopy

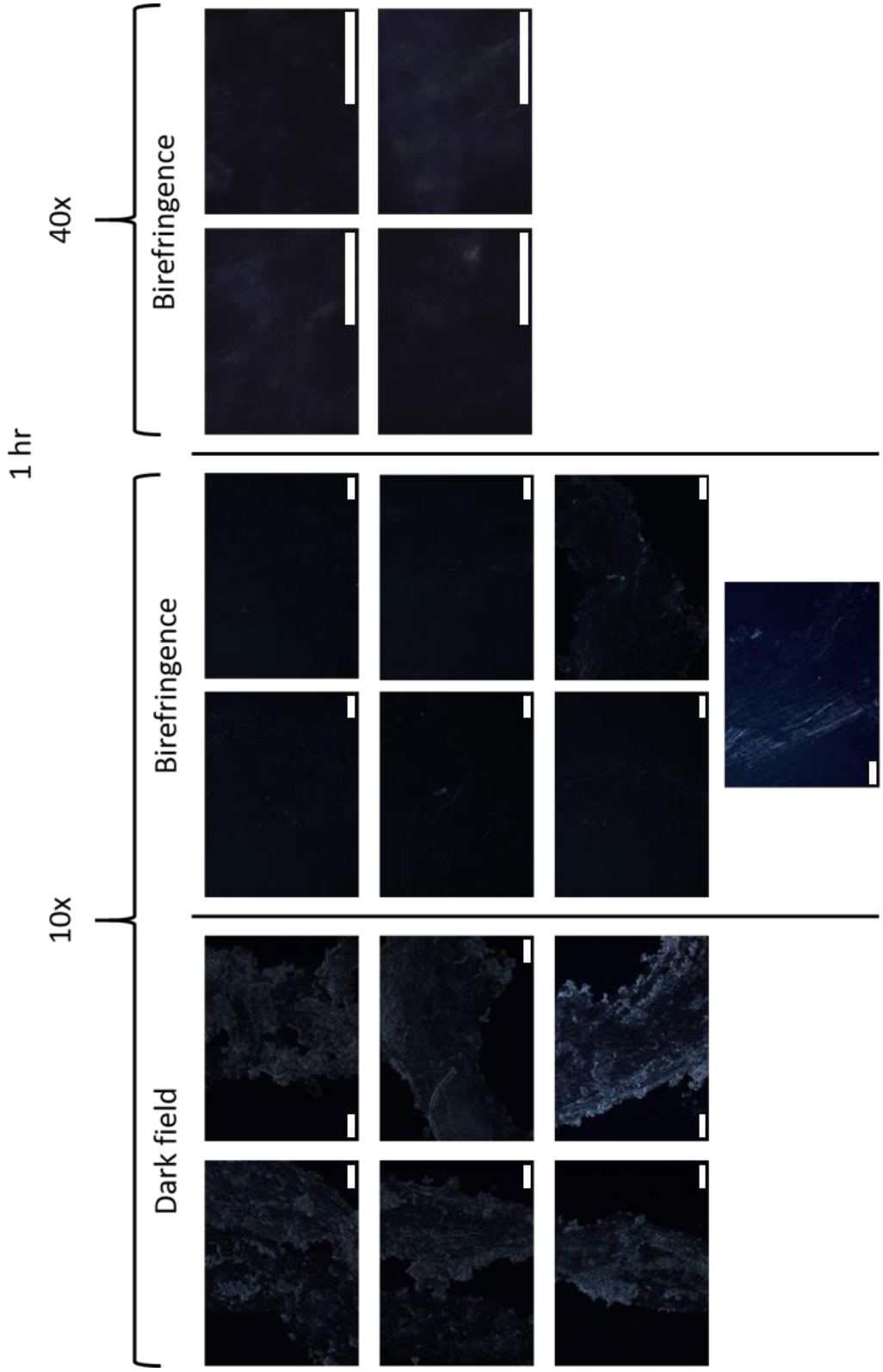

Figure 76. Representative images of 4RepCT fibres by MMP2 using dark field and birefringence microscopy at 10X (dark field and birefringence) and 40X (birefringence) magnification after 60 min as seen in **Figure 41**. Scale bar = 100 μm.

8.6.1.7 4RepCT fibres after 120 min viewed with bright field microscopy

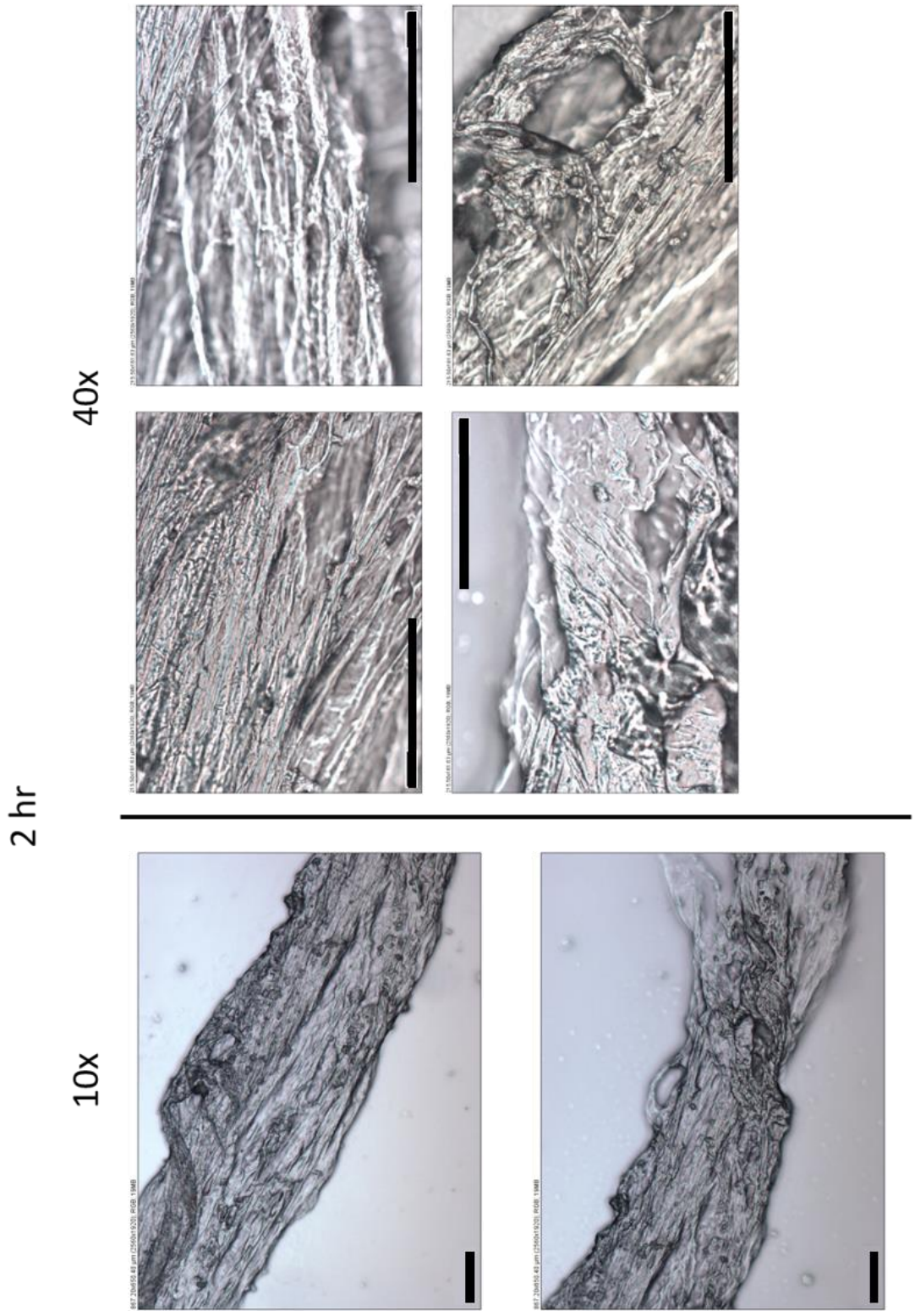

Figure 77. Representative images of 4RepCT fibres by MMP2 using bright field light microscopy at 10X and 40X magnification after 120 min as seen in **Figure 39**. Scale bar = 100 µm.

8.6.1.8 4RepCT fibres after 120 min viewed with dark field and birefringence microscopy

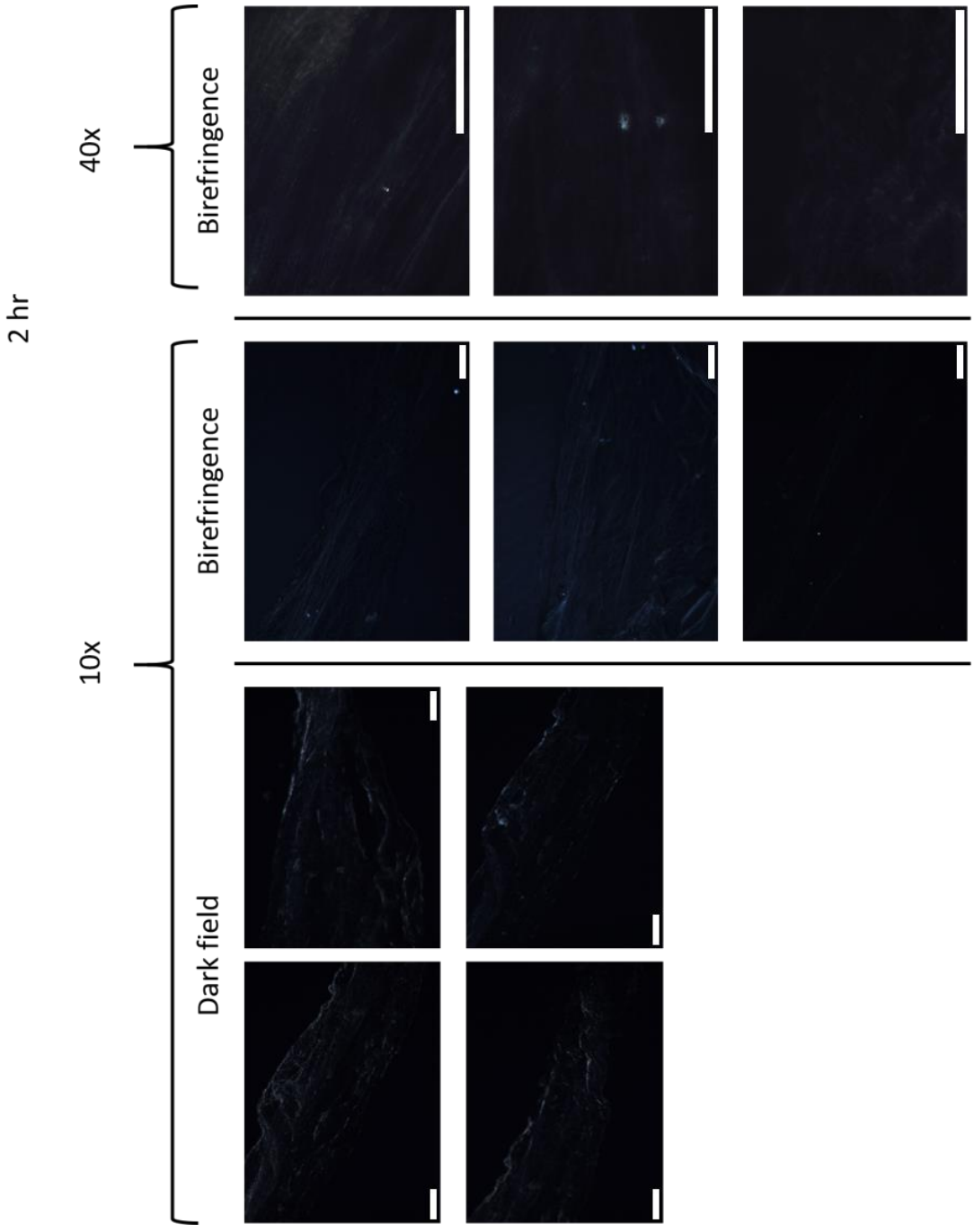

Figure 78. Representative images of 4RepCT fibres by MMP2 using dark field and birefringence microscopy at 10X (dark field and birefringence) and 40X (birefringence) magnification after 120 min as seen in **Figure 41**. Scale bar = 100 μm.

8.6.1.9 4RepCT fibres after 240 min viewed with bright field microscopy

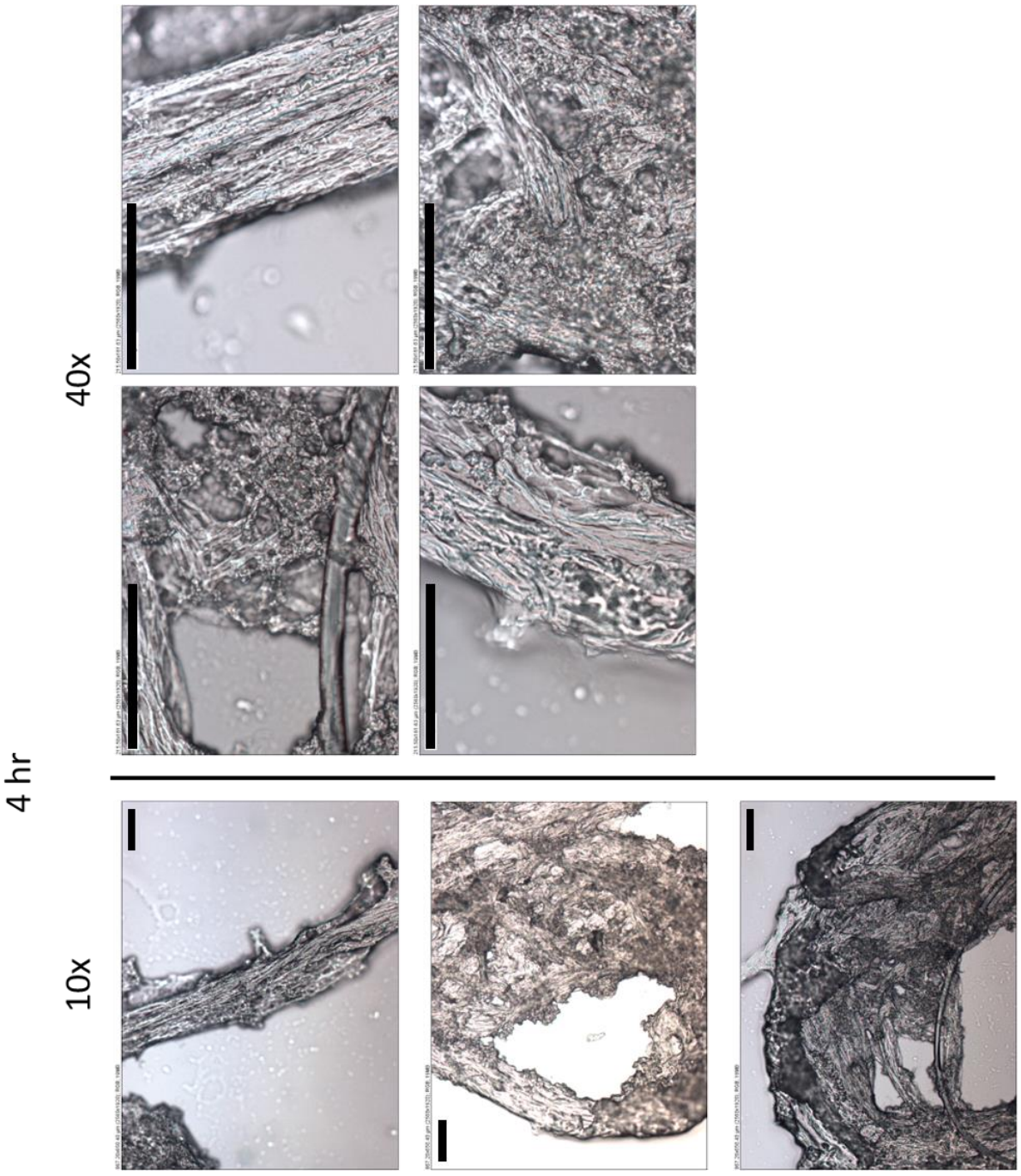

Figure 79. Representative images of 4RepCT fibres by MMP2 using bright field light microscopy at 10X and 40X magnification after 240 min as seen in **Figure 39**. Scale bar = 100 μm.

8.6.1.10 4RepCT fibres after 240 min viewed with dark field and birefringence microscopy

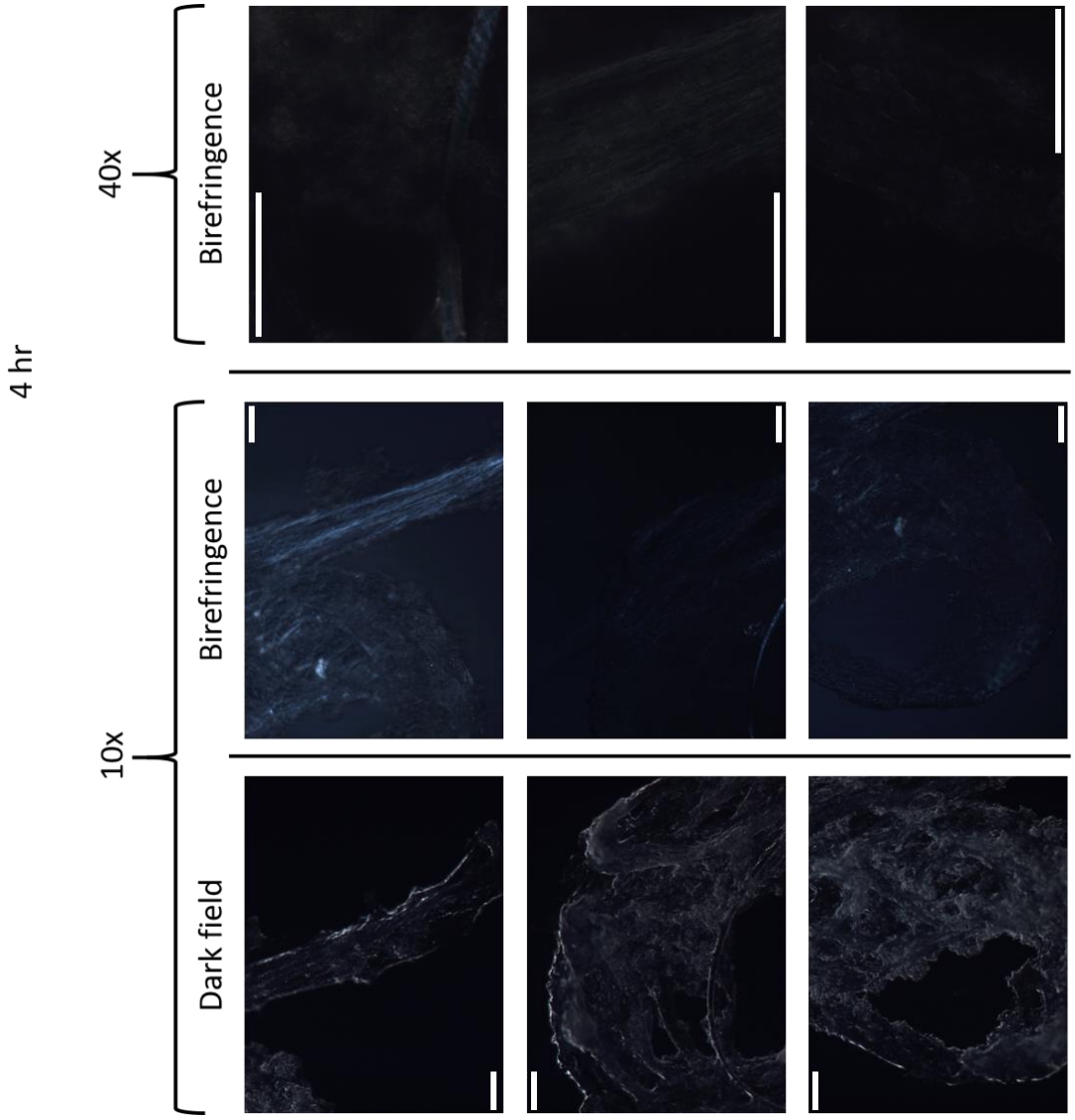

Figure 80. Representative images of 4RepCT fibres by MMP2 using dark field and birefringence microscopy at 10X (dark field and birefringence) and 40X (birefringence) magnification after 240 min as seen in **Figure 41**. Scale bar = 100 µm.

8.6.1.11 4RepCT fibres after 24 hr viewed with bright field microscopy

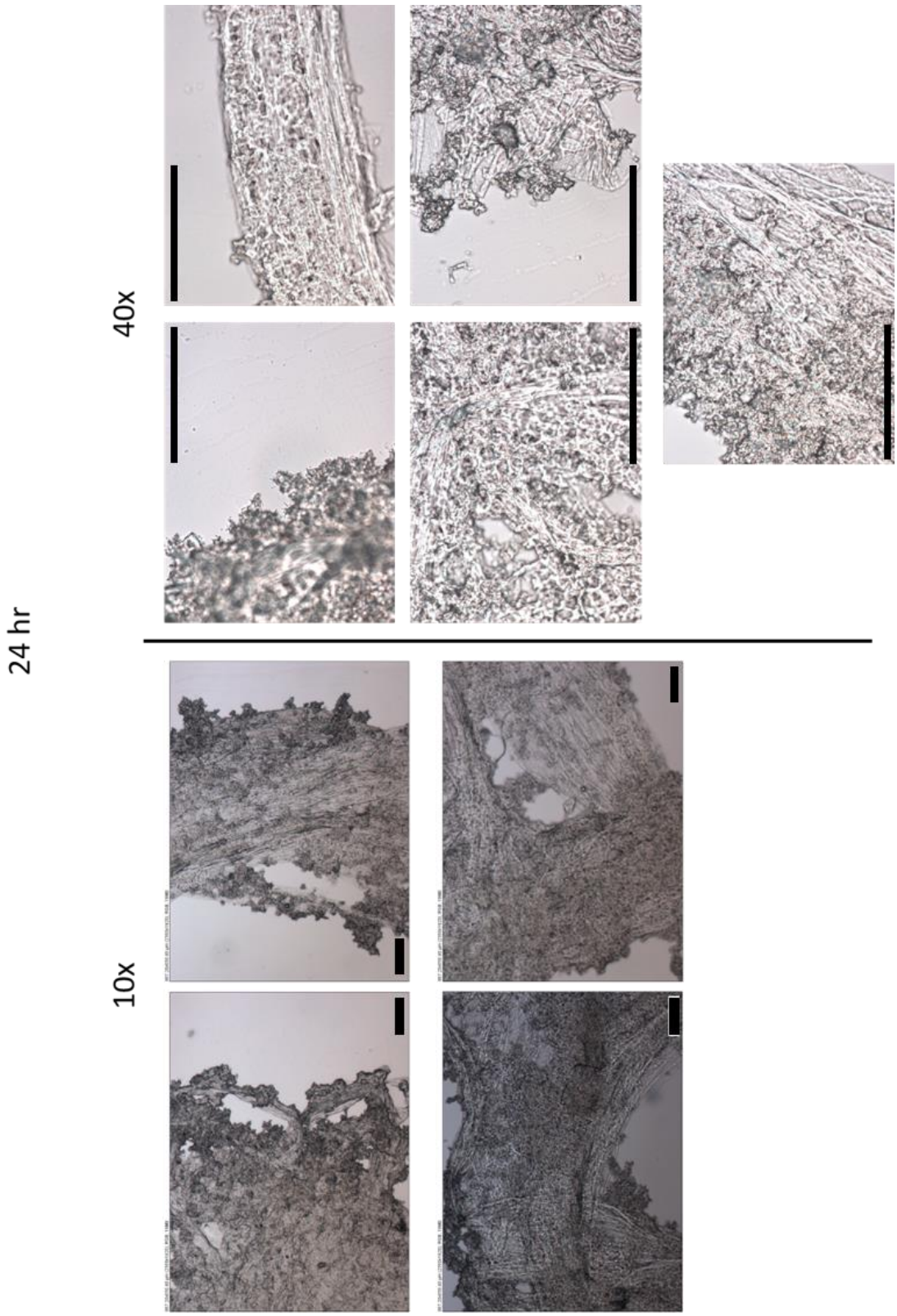

Figure 81. Representative images of 4RepCT fibres by MMP2 using bright field light microscopy at 10X and 40X magnification after 24 hr as seen in **Figure 40**. Scale bar = 100 µm.

8.6.1.12 4RepCT fibres after 24 hr viewed with dark field and birefringence microscopy

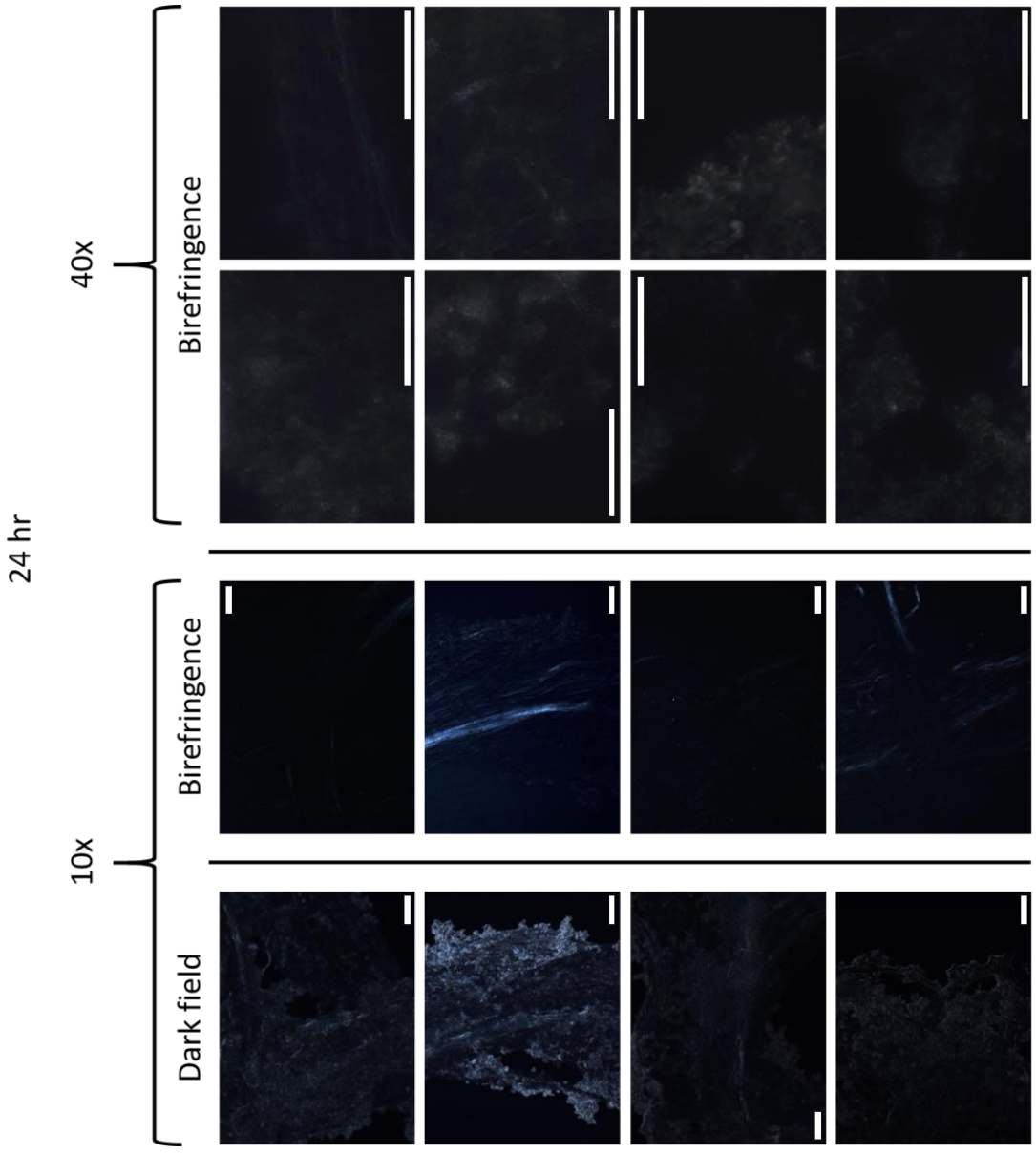

Figure 82. Representative images of 4RepCT fibres by MMP2 using dark field and birefringence microscopy at 10X (dark field and birefringence) and 40X (birefringence) magnification after 24 hr as seen in **Figure 41**. Scale bar = 100 μm.

8.6.1.13 4RepCT fibres after 1 week viewed with bright field microscopy

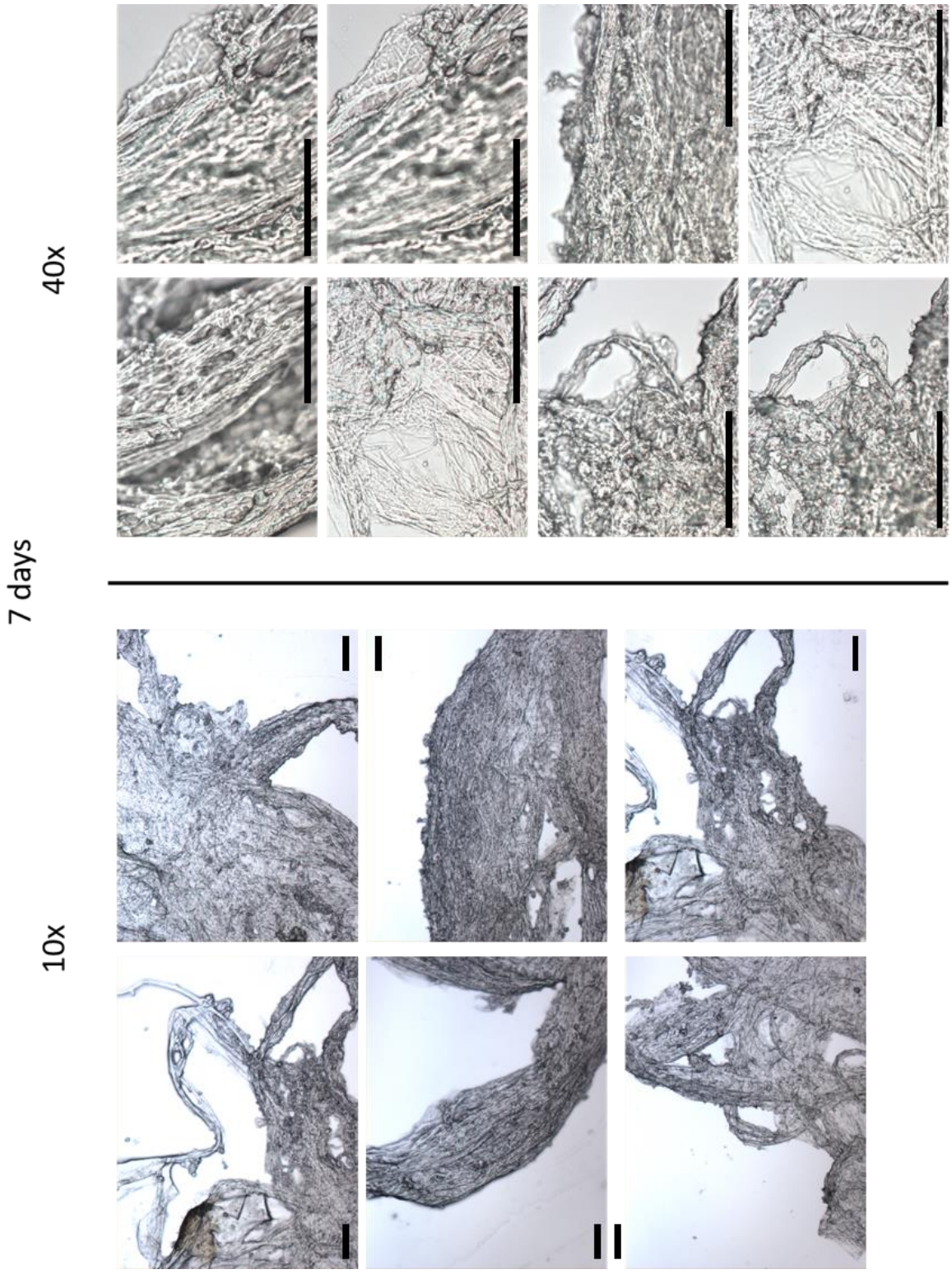

Figure 83. Representative images of 4RepCT fibres by MMP2 using bright field light microscopy at 10X and 40X magnification after 1 week as seen in **Figure 40**. Scale bar = 100 μm.

8.6.1.14 4RepCT fibres after 1 week viewed with dark field and birefringence microscopy

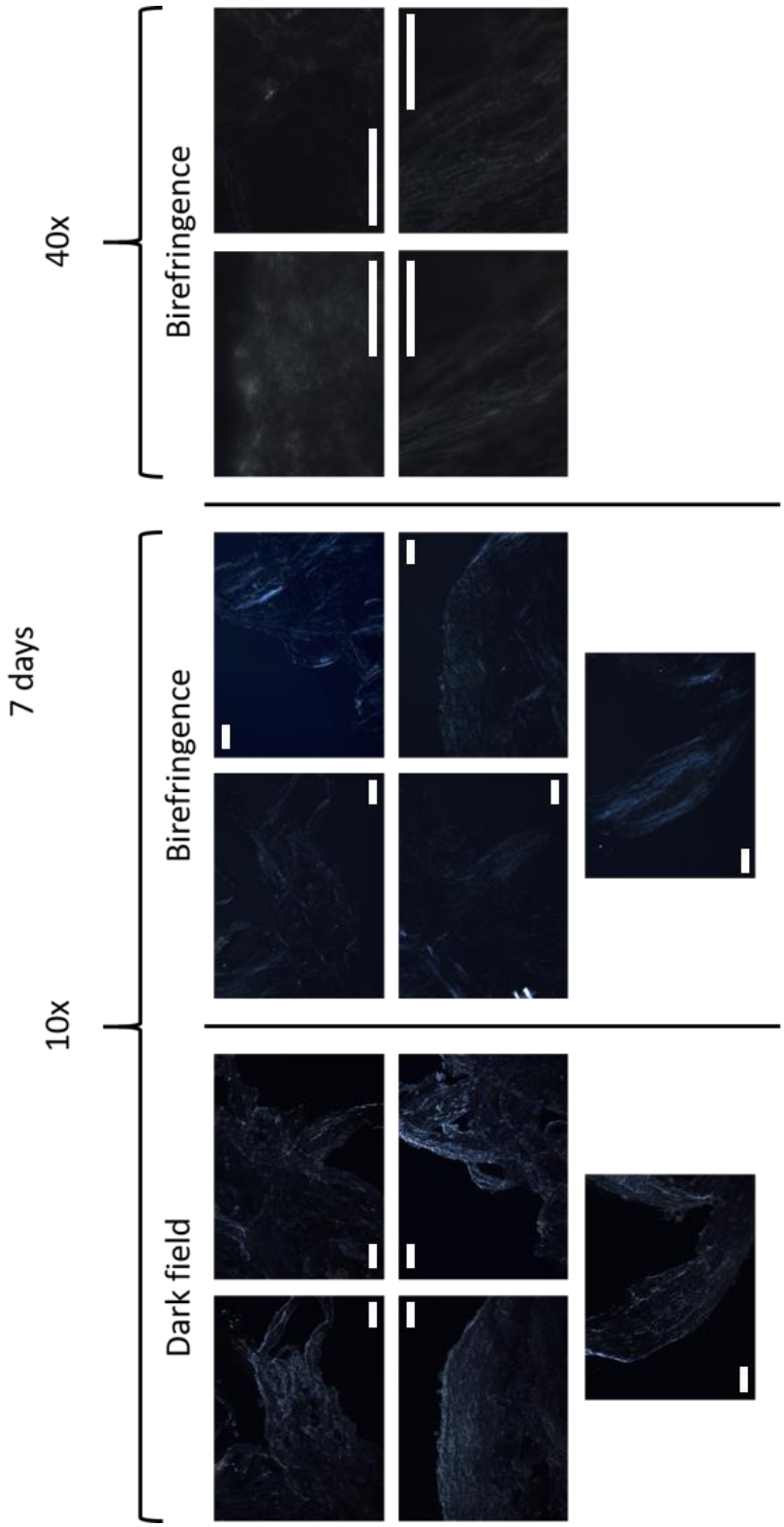

Figure 84. Representative images of 4RepCT fibres by MMP2 using dark field and birefringence microscopy at 10X (dark field and birefringence) and 40X (birefringence) magnification after 1 week as seen in **Figure 41**. Scale bar = 100 μm.

8.6.2.1 N156P fibres after 0 min viewed with bright field microscopy

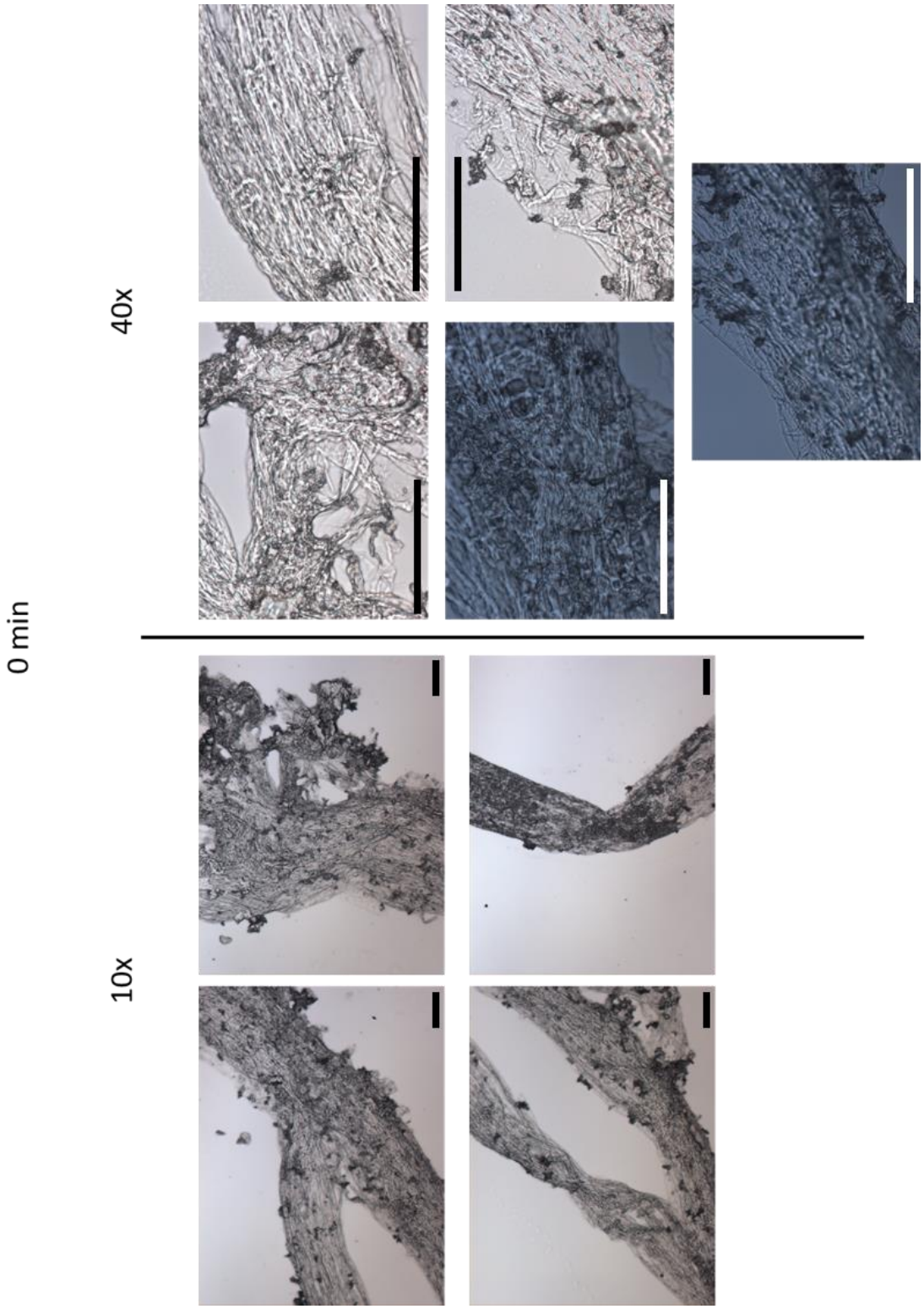

Figure 85. Representative images of N156P fibres by MMP2 using bright field light microscopy at 10X and 40X magnification after 0 min as seen in **Figure 58**. Scale bar = 100 μm.

8.6.2.2 N156P fibres after 0 min with dark field and birefringence microscopy

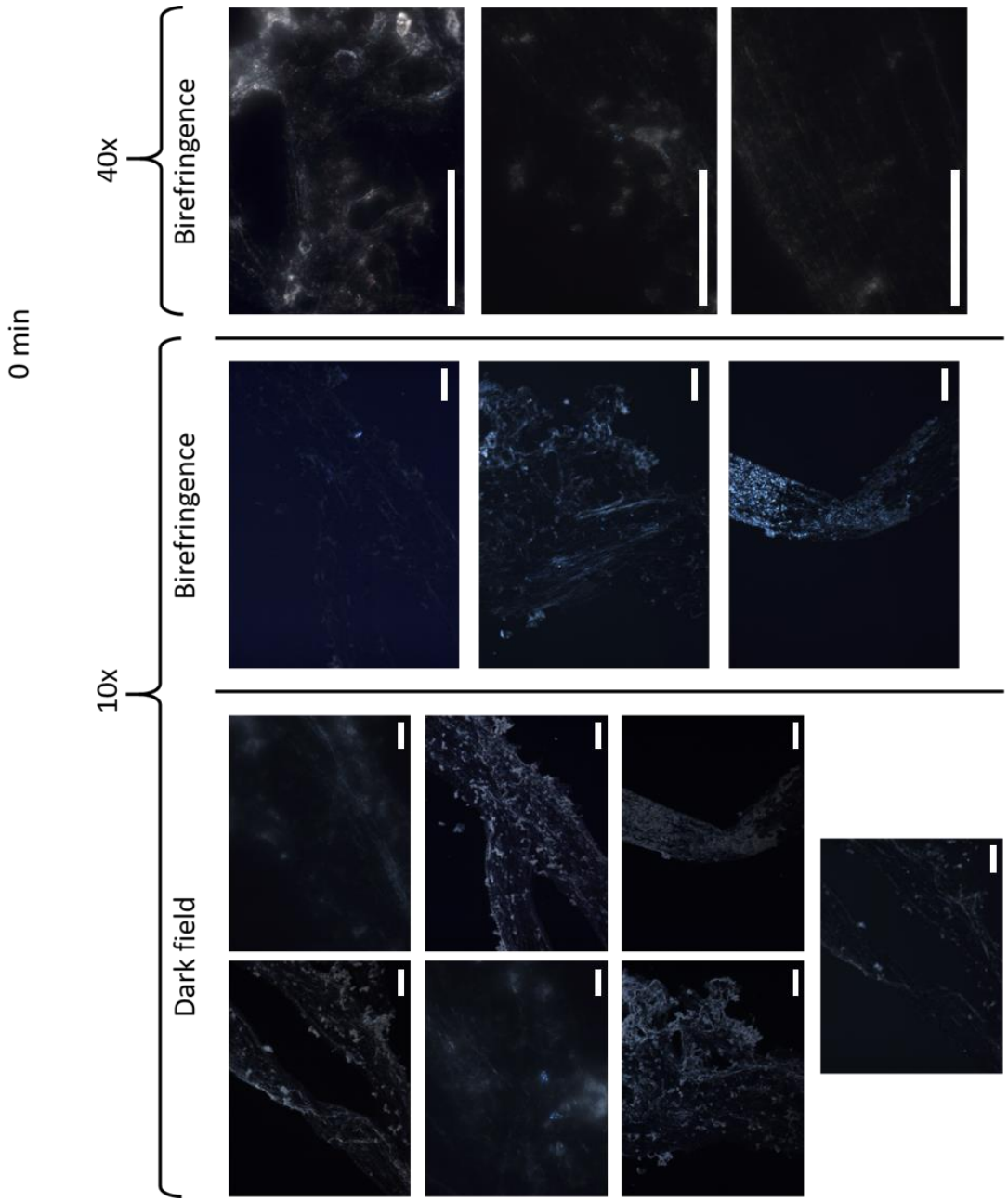

Figure 86. Representative images of N156P fibres by MMP2 using dark field and birefringence microscopy at 10X (dark field and birefringence) and 40X (birefringence) magnification after 0 min as seen in **Figure 60**. Scale bar = 100 μm.

8.6.2.3 N156P fibres after 30 min viewed with bright field microscopy

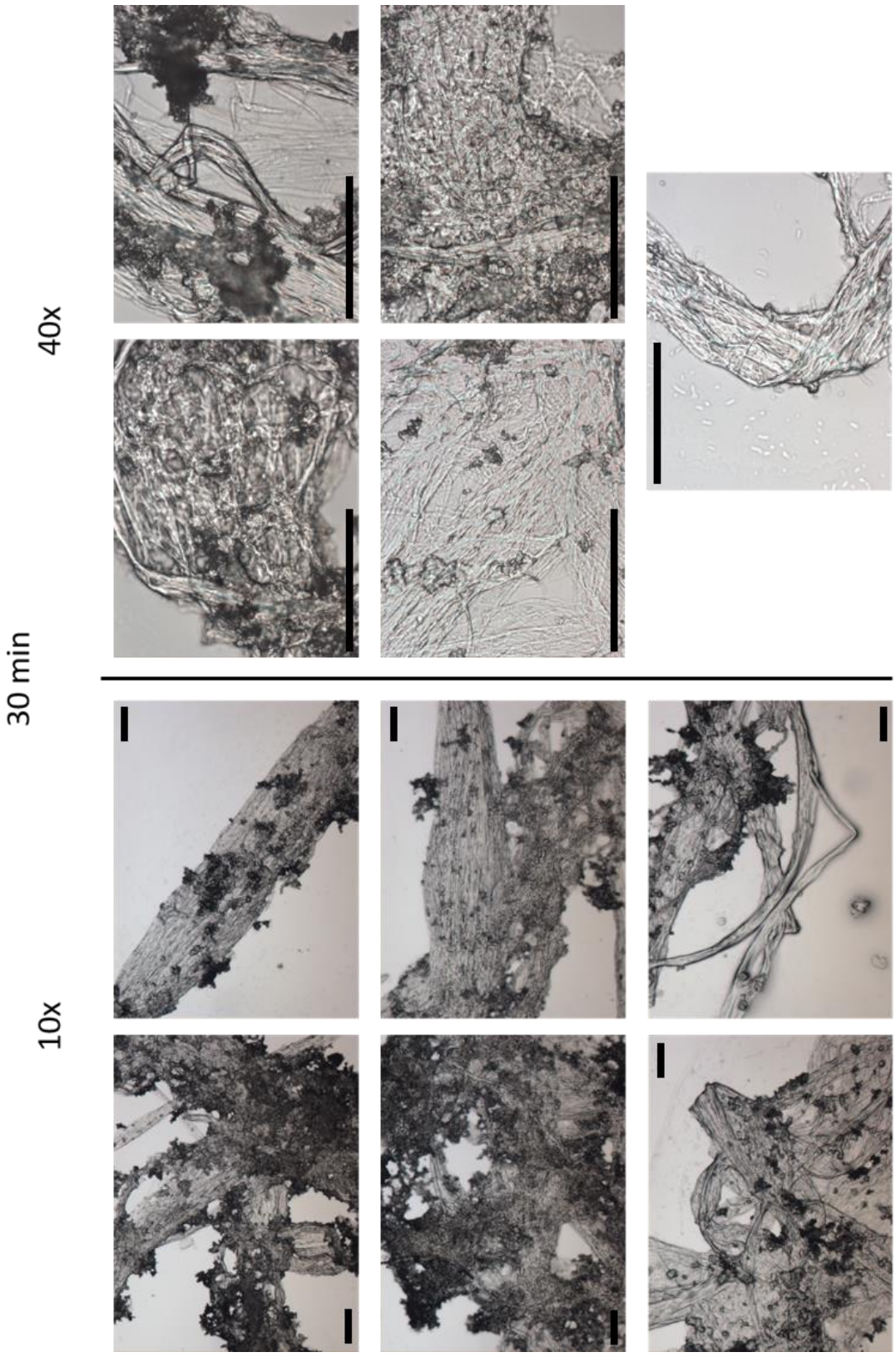

Figure 87. Representative images of N156P fibres by MMP2 using bright field light microscopy at 10X and 40X magnification after 30 min as seen in **Figure 58**. Scale bar = 100 μm.

8.6.2.4 N156P fibres after 30 min viewed with dark field and birefringence microscopy

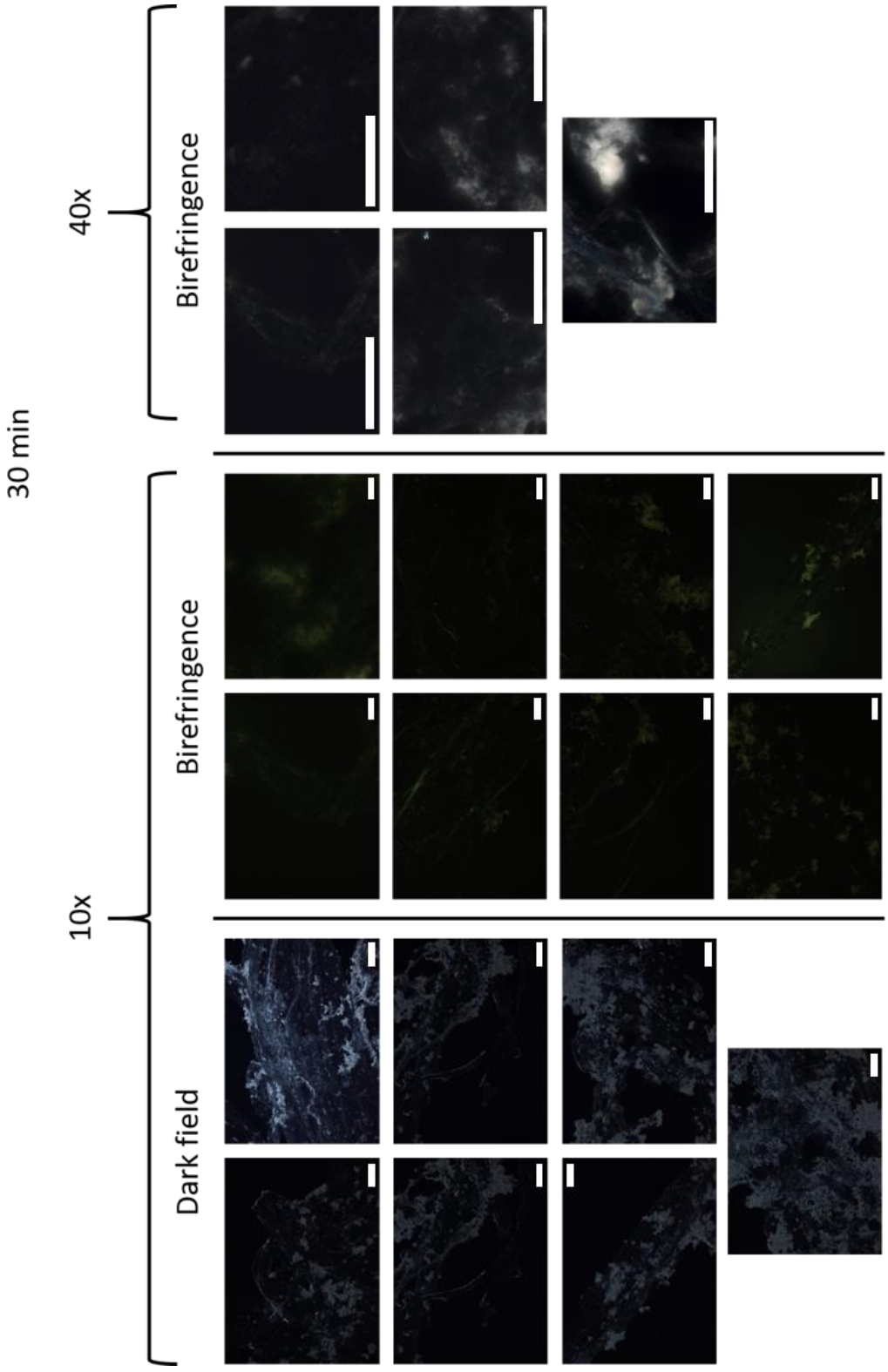

Figure 88. Representative images of N156P fibres by MMP2 using dark field and birefringence microscopy at 10X (dark field and birefringence) and 40X (birefringence) magnification after 30 min as seen in **Figure 60**. Scale bar = 100 μm.

8.6.2.5 N156P fibres after 60 min viewed with bright field microscopy

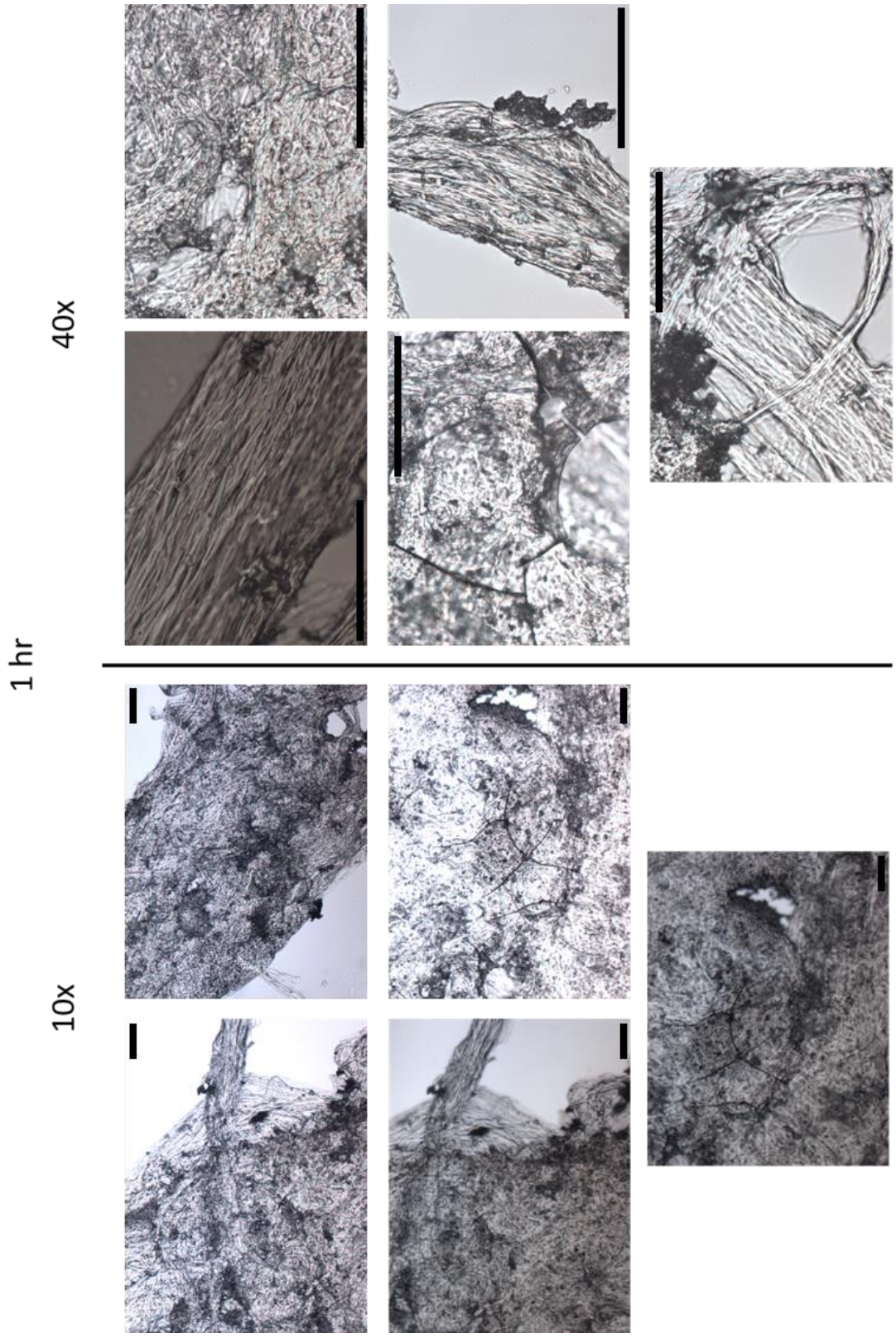

Figure 89. Representative images of N156P fibres by MMP2 using bright field light microscopy at 10X and 40X magnification after 60 min as seen in **Figure 58**. Scale bar = 100 μm.

8.6.2.6 N156P fibres after 60 min viewed with dark field and birefringence microscopy

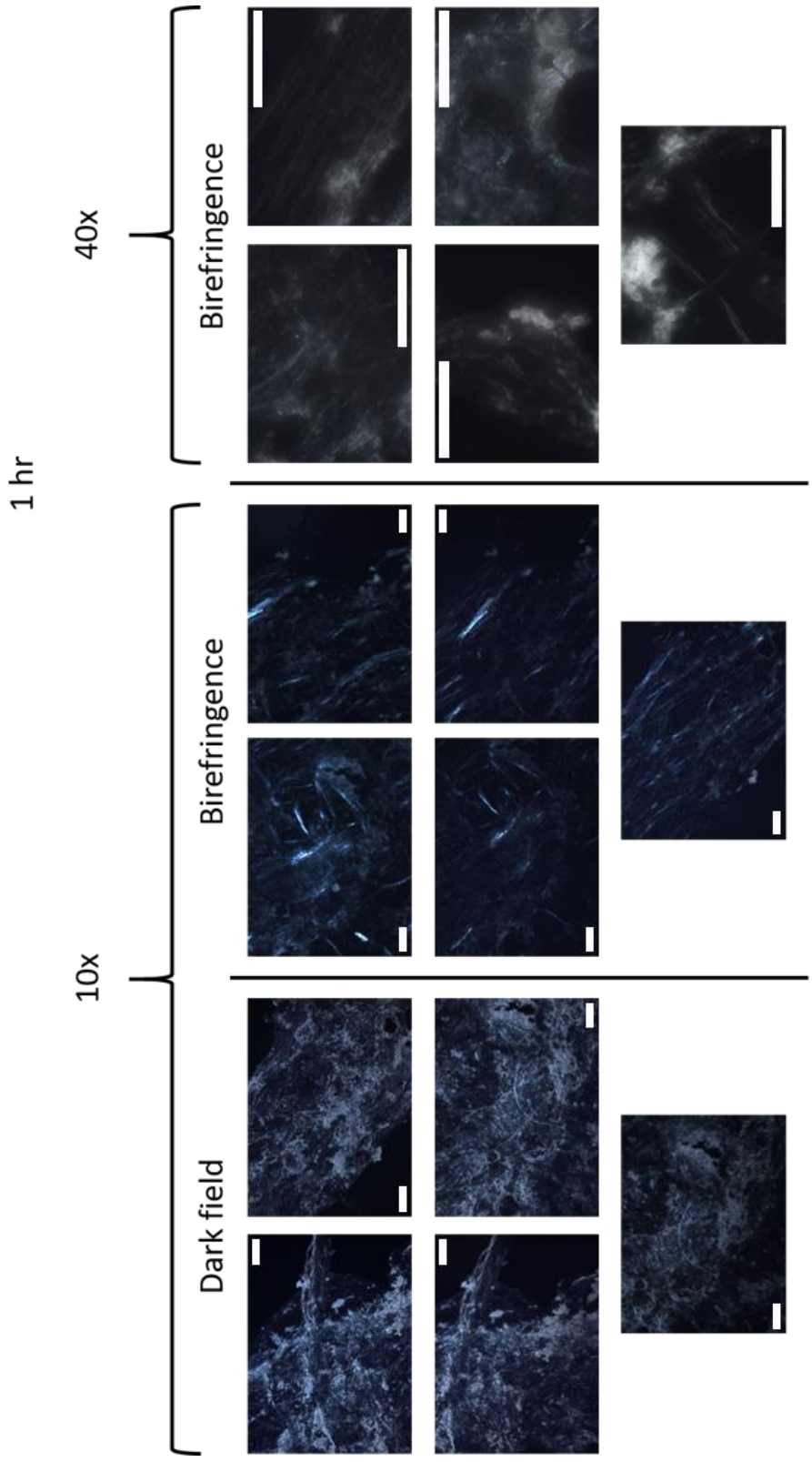

Figure 90. Representative images of N156P fibres by MMP2 using dark field and birefringence microscopy at 10X (dark field and birefringence) and 40X (birefringence) magnification after 60 min as seen in **Figure 60**. Scale bar = 100 μm.

8.6.2.7 N156P fibres after 120 min viewed with bright field microscopy

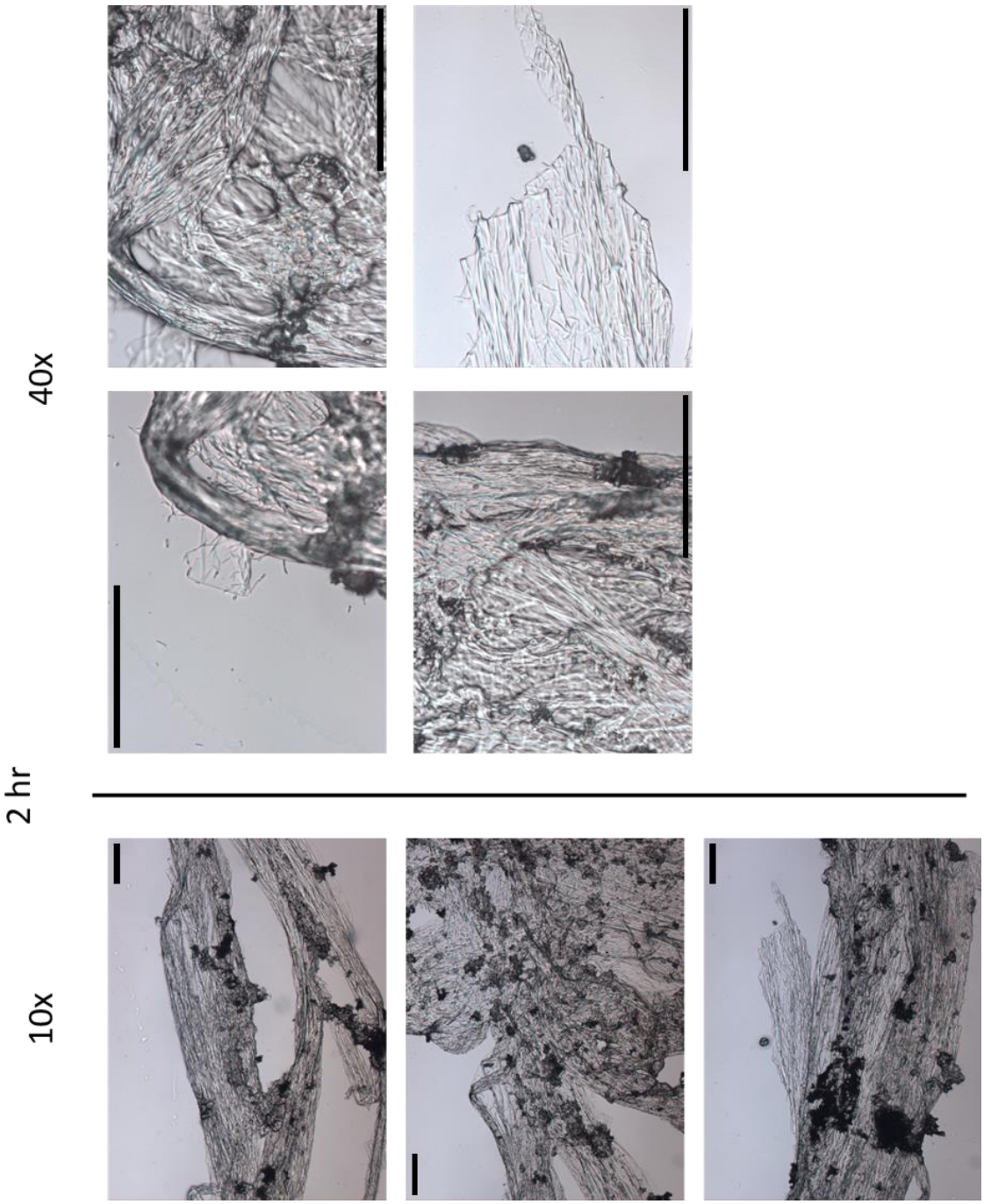

Figure 91. Representative images of N156P fibres by MMP2 using bright field light microscopy at 10X and 40X magnification after 120 min as seen in **Figure 58**. Scale bar = 100 μm.

8.6.2.8 N156P fibres after 120 min viewed with dark field and birefringence microscopy

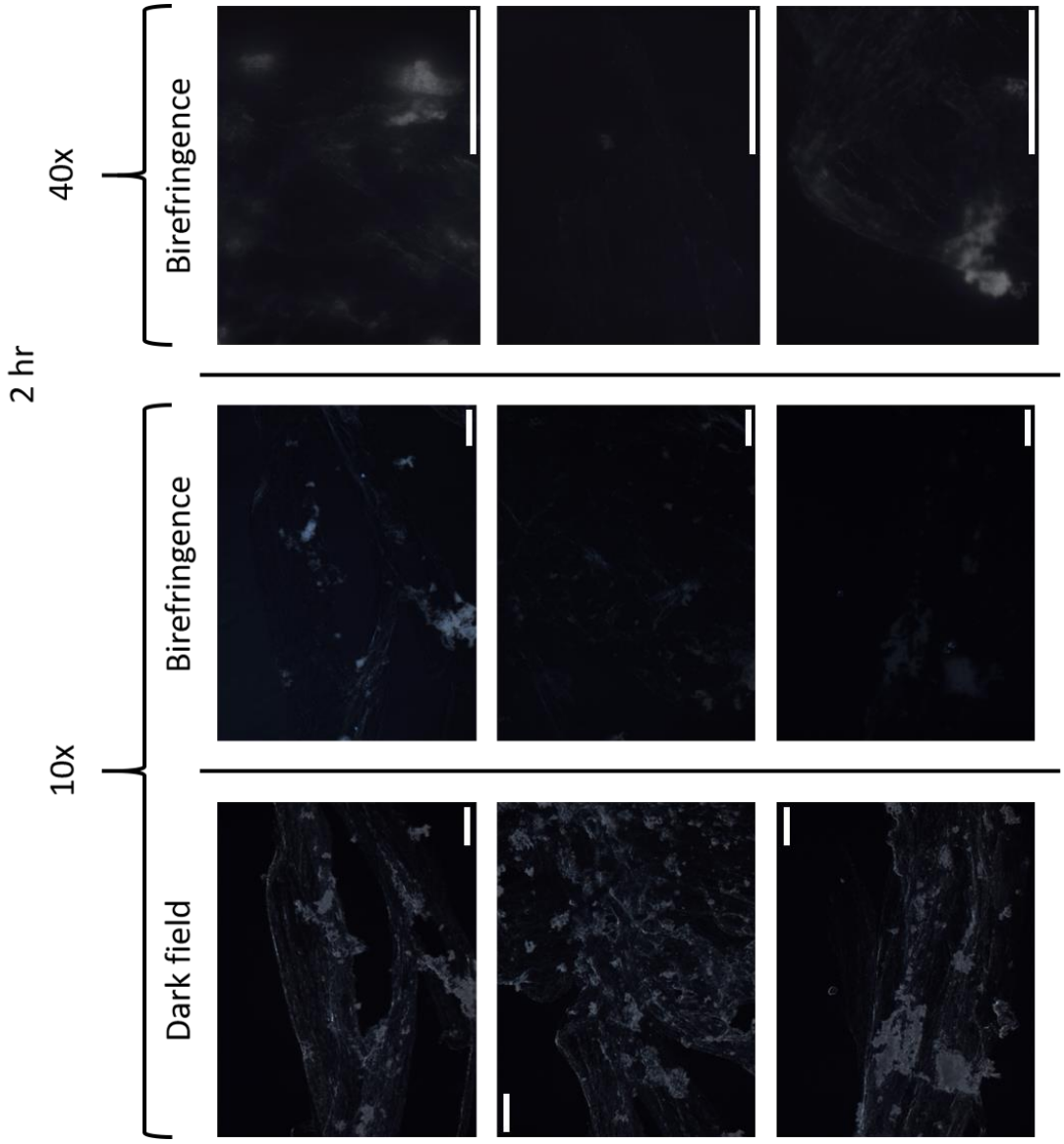

Figure 92. Representative images of N156P fibres by MMP2 using dark field and birefringence microscopy at 10X (dark field and birefringence) and 40X (birefringence) magnification after 120 min as seen in **Figure 60**. Scale bar = 100 μm.

8.6.2.9 N156P fibres after 240 min viewed with bright field microscopy

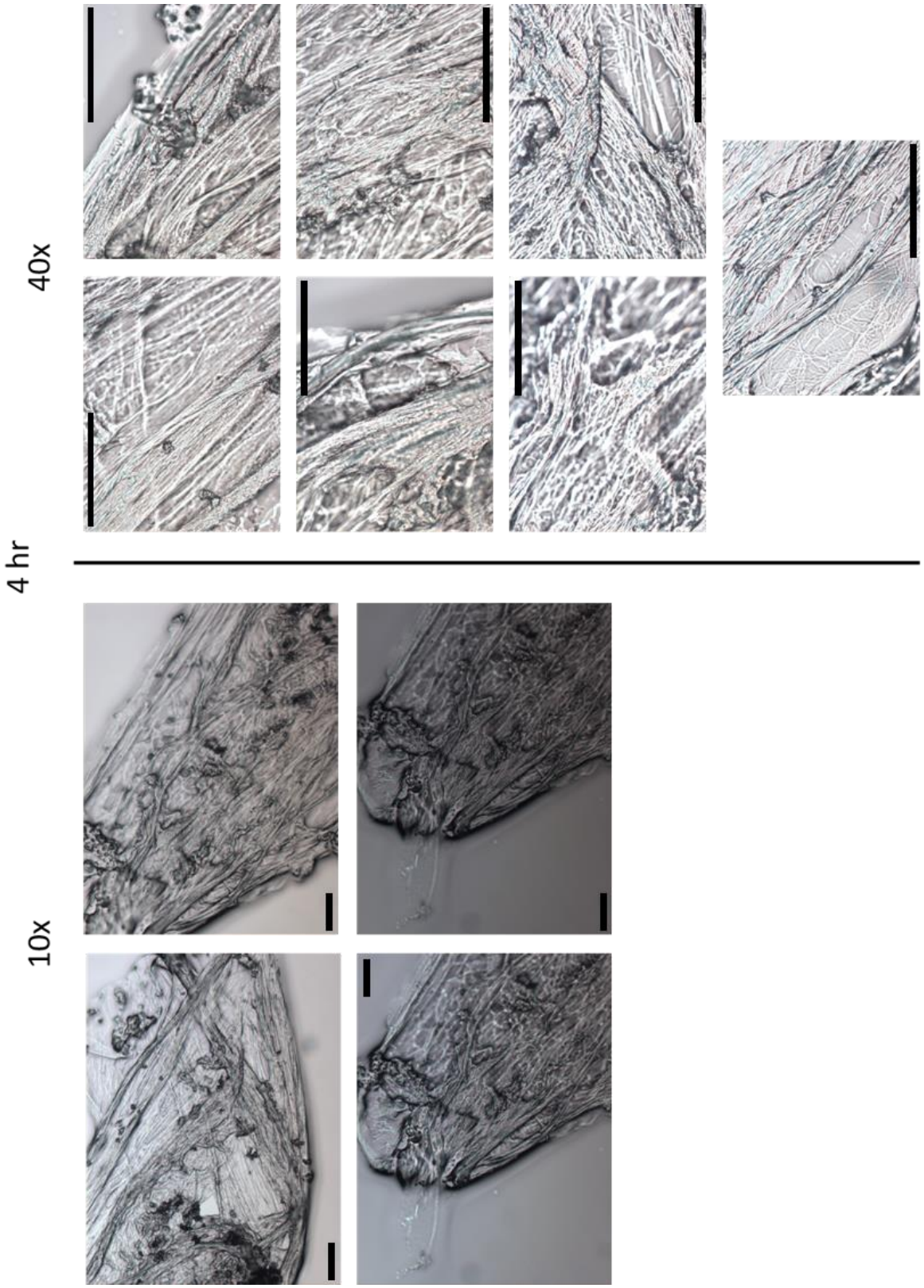

Figure 93. Representative images of N156P fibres by MMP2 using bright field light microscopy at 10X and 40X magnification after 240 min as seen in **Figure 58**. Scale bar = 100 μm.

8.6.2.10 N156P fibres after 240 min viewed with dark field and birefringence microscopy

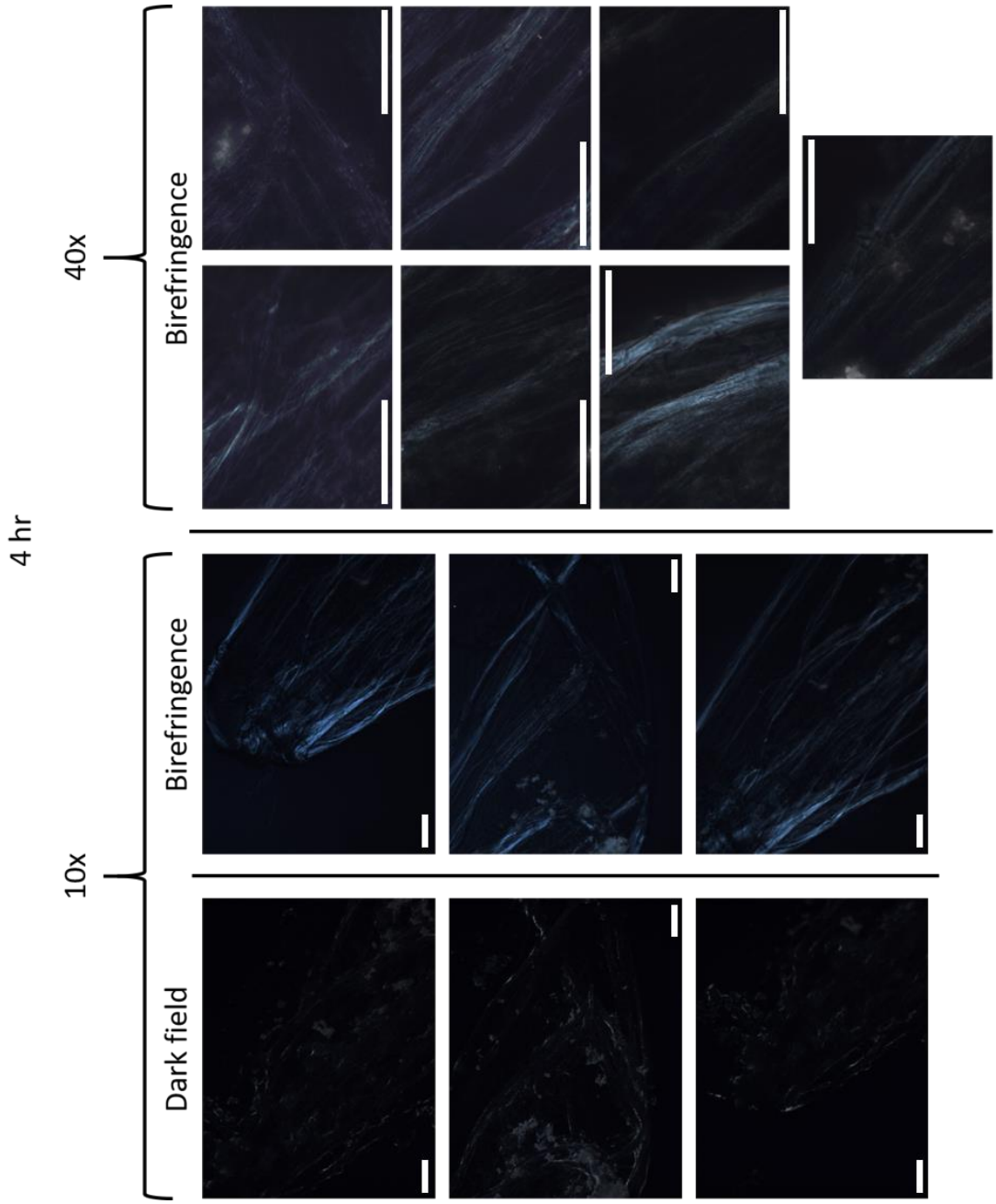

Figure 94. Representative images of N156P fibres by MMP2 using dark field and birefringence microscopy at 10X (dark field and birefringence) and 40X (birefringence) magnification after 240 min as seen in **Figure 60**. Scale bar = 100 μm.

8.6.2.11 N156P fibres after 24 hr viewed with bright field microscopy

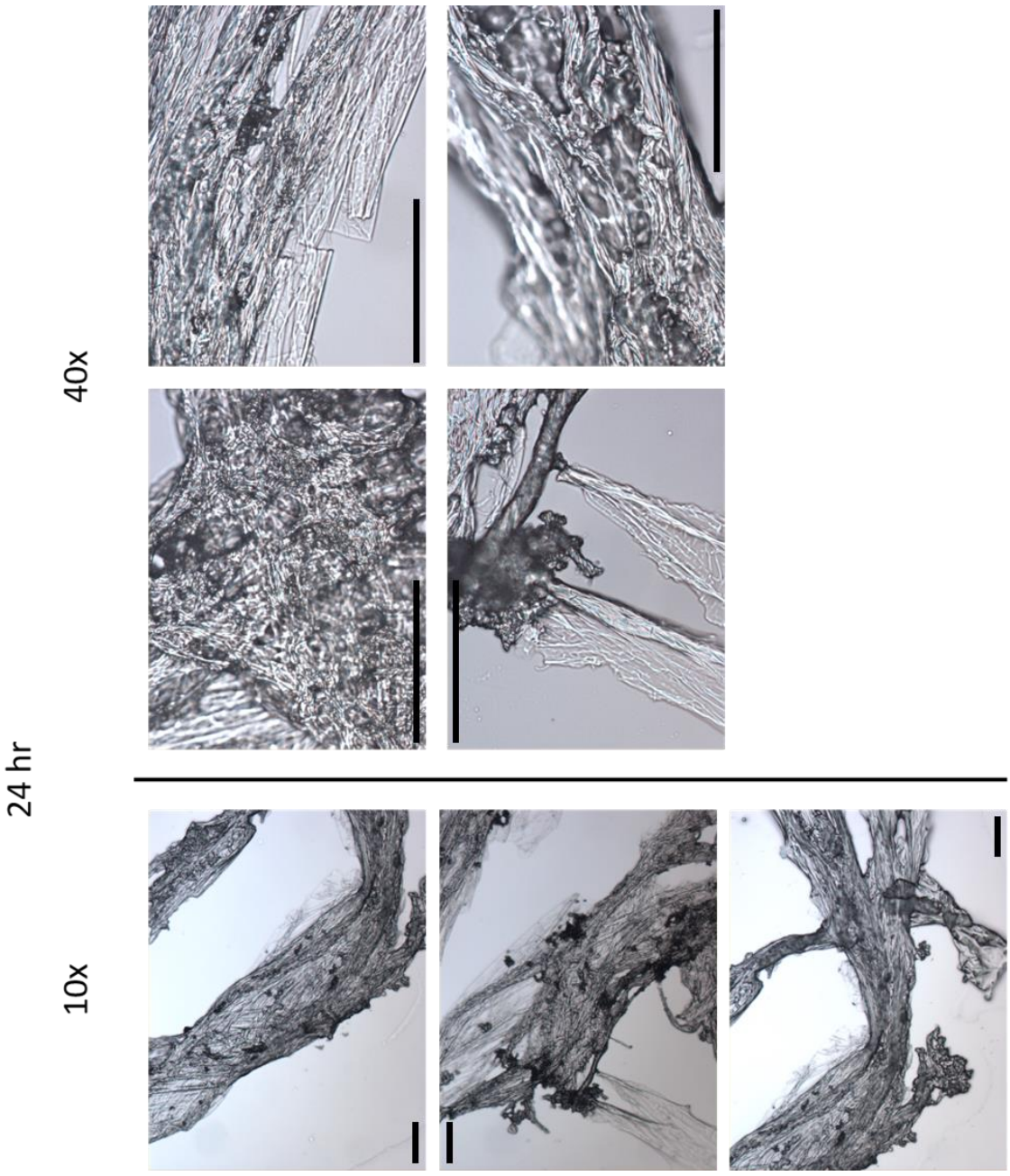

Figure 95. Representative images of N156P fibres by MMP2 using bright field light microscopy at 10X and 40X magnification after 24 hr as seen in **Figure 59**. Scale bar = 100 μm.

8.6.2.12 N156P fibres after 24 hr viewed with dark field and birefringence microscopy

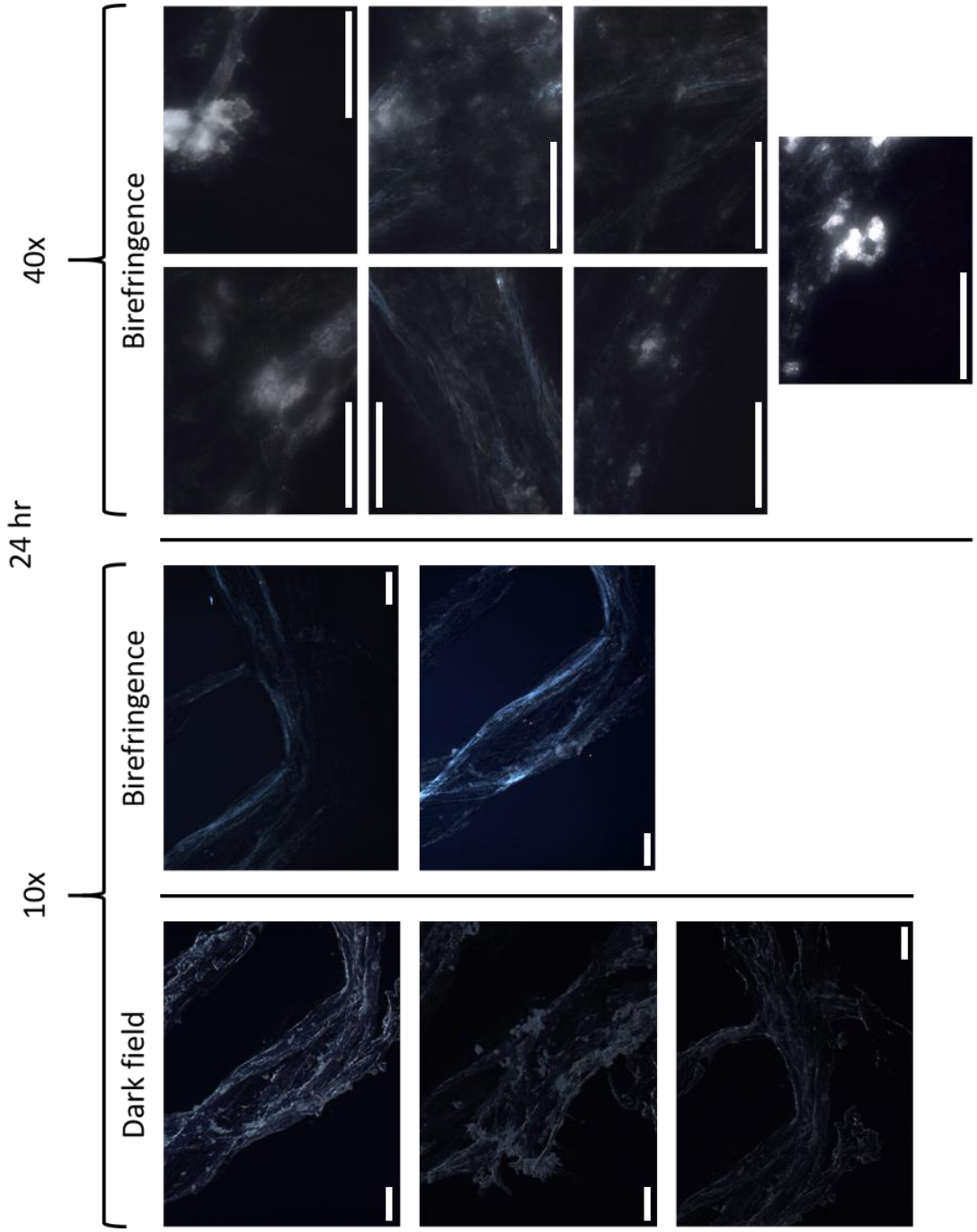

Figure 96. Representative images of N156P fibres by MMP2 using dark field and birefringence microscopy at 10X (dark field and birefringence) and 40X (birefringence) magnification after 24 hr as seen in **Figure 60**. Scale bar = 100 μm.

8.6.2.13 N156P fibres after 1 week viewed with bright field microscopy

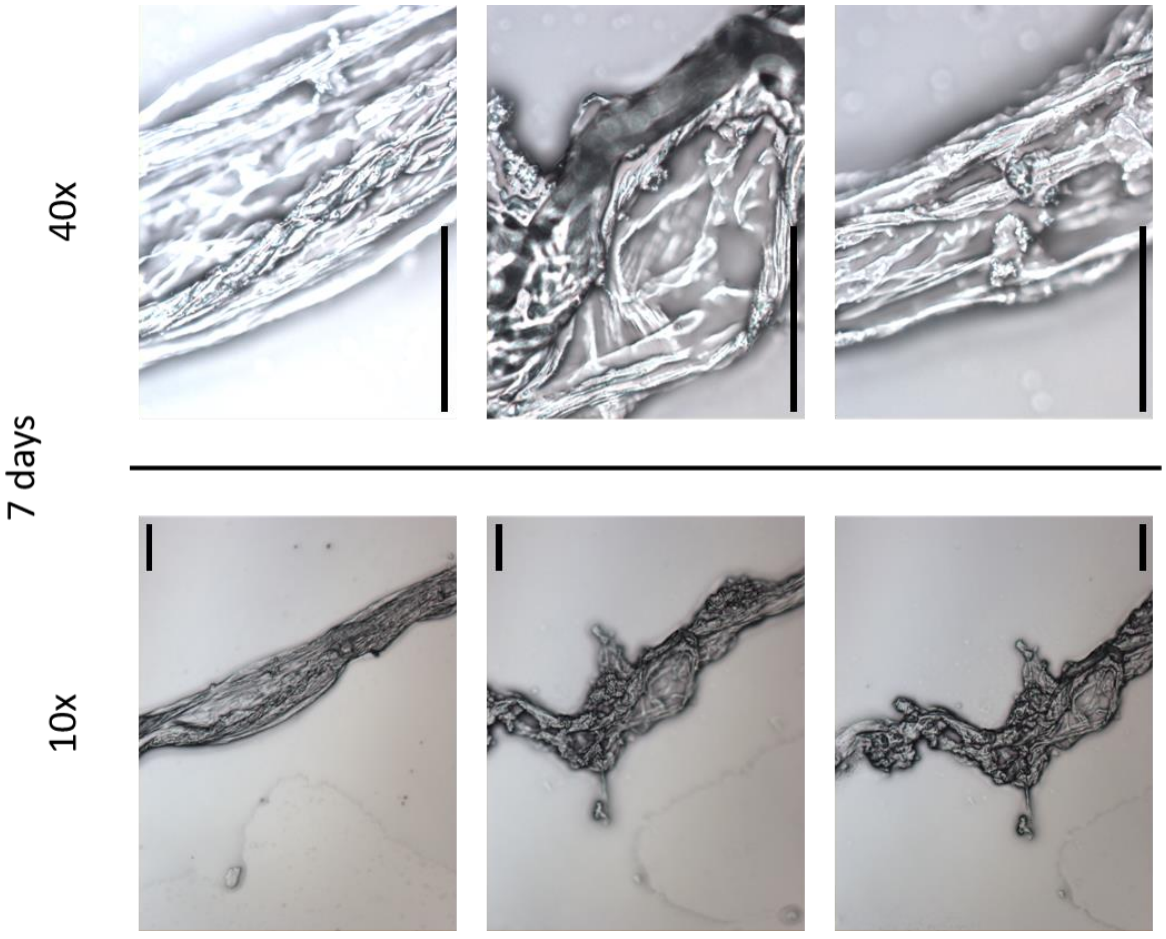

Figure 97. Representative images of N156P fibres by MMP2 using bright field light microscopy at 10X and 40X magnification after 1 week as seen in **Figure 59**. Scale bar = 100 μm.

8.6.2.14 N156P fibres after 1 week viewed with dark field and birefringence microscopy

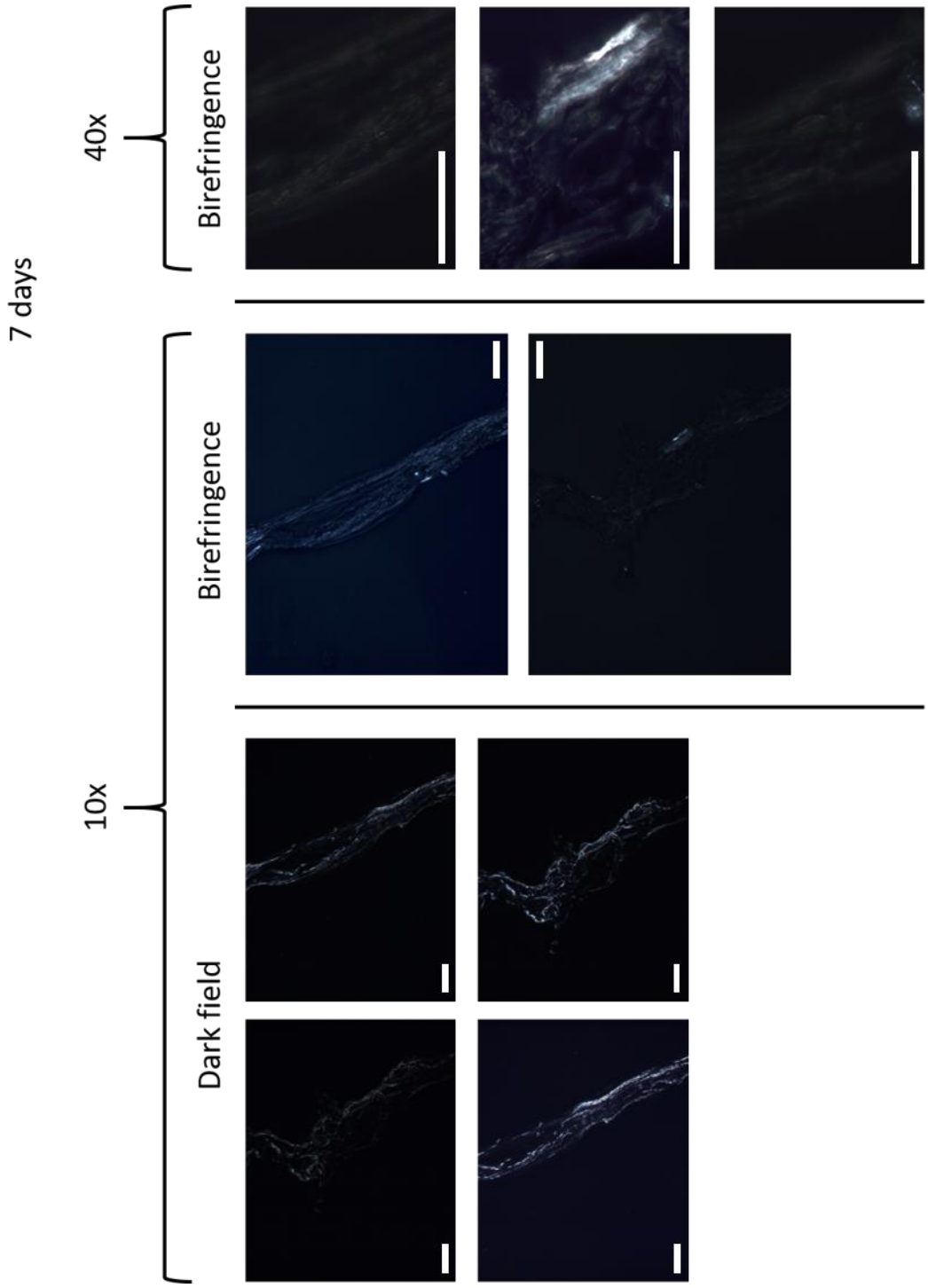

Figure 98. Representative images of N156P fibres by MMP2 using dark field and birefringence microscopy at 10X (dark field and birefringence) and 40X (birefringence) magnification after 1 week as seen in **Figure 60**. Scale bar = 100 μm.

8.7 PhD industrial placement report (Ignite Futures!)

As part of the doctoral training programme I undertook a three month industrial placement separate from my research project. I undertook this placement at the science communication and outreach charity Ignite Futures! based in Nottingham City centre with Rick, Sarah and Megan. Based in the heart of the city, the small team at Ignite! coordinate public outreach activities in addition to visiting primary schools to engage the curiosity of young people.

During my time at Ignite! I was involved in a number of projects, experiencing the full breadth of the charity's involvements. In addition to planning meetings for the upcoming Festival of Science which is coordinated by Ignite and attracted 7500 participants in February 2019, I worked as part of Lab_13, an initiative to allow primary school children to investigate science of their choosing. Based at Dovecote primary school, I acted as an interim Scientist-in-Residence (SiR) for the three months before a permanent scientist could be found to fill the role. As SiR, I was tasked with exploring and facilitating the investigations that the lab members wanted to investigate. This role was also run at Henry Whipple alongside an afternoon of science teaching for each year group. As a result, I developed my ability to plan and deliver science lessons and principles that reflected the range of audience ages and abilities over the three month placement.

In addition to Lab_13, I was also involved in a Royal Society of Chemistry initiative to evaluate the effect of science intervention with young people during their secondary education on the likelihood of continuing into science at University. At the end of a 5-year scheme, the so-called 'Creative Sparks' consisted of 11 children from five schools between the ages of 15 – 17. Over the course of the placement and subsequent year, Ignite! sought to encourage pair of students to investigate a topic of science through their own prerogative and creativity. During my placement I was involved in beginning their projects, encouraging their ideas and establishing their lines of investigation for the coming year. My role also included acting as a

mentor during my time with Ignite! although this was difficult to develop in the short time frame.

Overall I thoroughly enjoyed my experience with Ignite Futures! and would be thrilled to work alongside them again. The placement provided me with a new and exciting outlook on science outreach and a different environment from that of the research bench. Although the placement did not impact my research project directly, it allowed me to rest, away from the PhD project and return refreshed. It has also encouraged me to pursue a career with aspects of public science outreach.